Mathematical modelling of glycolysis in skeletal muscle cells

By

Jacobus Barend van Dyk

Dissertation presented for the degree of

Doctor of Philosophy
Science

at

Stellenbosch University
Department of Biochemistry, Faculty of Science

The financial assistance of the National Research Foundation (NRF) towards this research is hereby acknowledged. Opinions expressed and conclusions arrived at are those of the author and are not necessarily to be attributed to the NRF.

Supervisor: Prof. Jacky L. Snoep

Co-supervisor: Dr. Dawie D. van Niekerk

March 2020

Declaration:

By submitting this dissertation electronically, I declare that the entirety of the work contained therein is my own, original work, that I am the sole author thereof (save to the extent explicitly otherwise stated) that reproduction and publication thereof by Stellenbosch University will not infringe any third party rights and that I have not previously in its entirety or in part submitted it for obtaining any qualification.

Date:

Summary

Diabetes is a term used to describe a group of metabolic diseases characterised by high blood glucose levels. Regulation of blood glucose levels is facilitated by the insulin stimulation of target tissues, such as skeletal muscle tissue and fat cells. A decrease in the effective working of insulin on target tissues can lead to a variety of symptoms, including damage or dysfunction of organs, such as the eyes, kidneys, nerves, and the heart and ultimately leads to the development of type 2 diabetes. Blood glucose homeostasis is predominately regulated by the metabolic activity of skeletal muscle fibres (70 – 80%). Therefore, there is an interest to investigate the dysfunctions caused by insulin resistance in skeletal muscle cells.

In this thesis we present the kinetic characterisation of the glycolytic enzymes in C_2C_{12} skeletal muscle fibres. The kinetic rate equations, describing the dynamic behaviour of each enzyme, was compiled into a kinetic model. The development of a novel HPLC analytical technique for the separation and quantification of glycolytic intermediates and cofactors was also presented in the thesis. This HPLC technique enables the separation and quantification of the glycolytic cofactors; ATP, ADP, AMP, NAD^+ and NADH via UV/Vis detection, along with the separation and quantification of 13 glycolytic species derived from glucose, including ACA and ETOH, as well as GLY and G3P via the use and detection of ^{14}C-radioactive labelling. The novel HPLC technique was used to validate the kinetic model describing glycolysis in C_2C_{12} skeletal muscle cells by comparing model simulations to experimental data. 3 incubations of C_2C_{12} skeletal muscle extract was analysed under different concentrations of GLC, FBP, ATP and NAD^+ via the HPLC technique and compared to the corresponding model simulations. A good comparison between experimental data and model simulations was obtained, validating the glycolytic model describing glycolysis in C_2C_{12} skeletal muscle extract.

Metabolic control analysis was performed on the validated model and showed that the majority of flux control was held by the demand for ATP, described by the ATPase reaction (99.4%). This is in comparison with what is found in literature.

Opsomming

Diabetes is `n term wat gebruik word om `n groep metaboliese siektes, gekenmerk deur hoë bloed glukose vlakke te beskryf. Regulasie van bloed glukose vlakke word gehandhaaf deur die werking van insulien op teiken weefsels, soos spierweefsel en vetselle. `n Afname in the effektiewe werking van insulin op teikenweefsels lei tot `n wye verskeidenheid van simptome, insluitend skade of versaking van organe soos die oë, niere, senuwees en die hart en lei tot die ontwikkeling van tipe 2 diabetes. Die regulasie van bloed glukose homeostase word oorwegend deur die metaboliese aktiwiteit van skelet spierweefsel (70 – 80%) genhandhaaf. Daarom is daar groot belang in die ondersoek van die versaking van insulin werking, afkomstig van insulien weerstandbediendheid in skelet spierweefsel.

In hierdie tesis lê ons die biochemiese karakterisering van die glikolitiese ensieme in C_2C_{12} skelet spiervesels voor. Die kinetiese tempovergelykings, wat die dinamiese gedrag van elke ensiem beskryf, was in `n kinetiese model saamgestel. Die ontwikkeling van `n nuwe HPLC analise tegniek vir die skeiding en kwantifisering van glikolitiese intermediate en kofaktore in selekstrak word ook in hierdie tesis voorgelê. Dié HPLC tegniek handhaaf die skeiding en kwantifisering van die glikolitiese kofaktore; ATP, ADP, AMP, NAD^+ en NADH d.m.v. UV/Vis opname, sowel as die skeiding en kwantifisering van 13 glikolitiese spesies afgelei van glukose, insluited ACA en ETOH, saam met GLY en G3P d.m.v. die gebruik en opsporing van ^{14}C- radioaktiewe etikettering. Die nuwe HPLC tegniek was gebruik vir die validering van die kinetiese model wat glikoliese in C_2C_{12} skelet spierselle beskryf, deurom model simulasies met ekserimentele data te vergelyk. 3 inkubasies van C_2C_{12} skelet spierveselekstrak onder verskeie konsentrasies van GLC, FBP, ATP en NAD^+ was d.m.v die HPLC tegniek geanaliseer en vergelyk met die ooreenstemende model simulasies. `n goeie ooreensteming tussen eksperimentele data en model simulasies was bevind en valideer die glikolities model van C_2C_{12} skelet spierveselekstrak.

Metaboliese kontrole analise van die gevalideerde model was onderneem en dui tot `n meerderheids fluksie kontrolle wat deur die aanvraag van ATP, beskryf deur die ATPase reaksie (99.4%) gehandhaaf word. Dit is in ooreenstemming met wat in die literatuur aangedui is.

This dissertation is dedicated to
My Wife and Family

Acknowledgements

I wish to express my sincere gratitude and appreciation to the following persons and institutions:

My supervisor Prof. Jacky Snoep

My co-supervisor Dr. Dawie van Niekerk

The NRF for funding

The department of Biochemistry, Stellenbosch University

My Laboratory colleagues and support staff

My Wife Meagan van Dyk

My Family

Table of Contents

Chapter 1
General introduction

The term diabetes is used to describe a group of metabolic diseases characterised by hyperglycaemia that results from defective insulin action to control blood glucose concentrations. Chronic hyperglycaemia is associated with numerous health risks and can lead to damage and failure of organs, including the eyes, kidneys, nerves, heart and blood vessels. Insufficient insulin action can arise from defects in insulin secretion, insulin stimulation, or both. Autoimmune destruction of the β-cells of the pancreas leads to decreased insulin secretion, whereas a resistance to insulin in tissues such as skeletal muscle and adipocytes leads to a decreased efficacy of insulin stimulation. The deficient action of insulin on target tissues leads to abnormalities in the metabolism of carbohydrates, fats and proteins[1]. Failing of insulin secretion by the β-cells of the pancreas is referred to as type 1 diabetes and often results from an autoimmune pathologic process that occurs in the pancreatic islets. Type 2 diabetes on the other hand, is caused by a combination of insulin resistance in target tissues and an inadequate secretion of insulin in response. Type 2 diabetes accounts for 90 – 95% of diabetes patients and the onset is generally in the later stages of life[1]. The majority of patients that suffer from type 2 diabetes are obese, and obesity is therefore related to insulin resistance[2]. The regulation of blood glucose homeostasis is predominantly dependent on the metabolic activity of skeletal muscle cells[3,4]. Therefore, it is of critical importance to investigate the dysfunctions caused by insulin resistance in skeletal muscle cells.

We investigated the mechanistic behaviour of skeletal muscle cells under basal conditions to define the reference state of C_2C_{12} skeletal muscle metabolism. The focus of the project was to elucidate the defects associated with insulin resistance in skeletal muscle cells and to contribute to a mechanistic understanding of the cellular processes that are affected by insulin resistance. The elucidation of insulin stimulated metabolism of skeletal muscle can be broken up into 3 subsections: Investigation of the insulin dependent stimulation of GLUT4 translocation in a time- and dose dependent manner, quantification of the glucose uptake rate under various insulin-stimulated conditions, and investigation of the control and regulatory behaviour of glycolysis in skeletal muscle cells. This thesis forms part of our greater objective to understand insulin resistance in target tissues and how this relates to changes in the physiology observed in type 2 diabetic patients. A sister study, undertaken by Stefan Kuhn, focussed on the investigation of the insulin signalling cascade, GLUT4 translocation dynamics

and glucose uptake. The primary objective of our joined endeavours was to construct a metabolic model describing basal and insulin stimulated glucose metabolism in skeletal muscle cells. This metabolic model will then be expanded to describe muscle metabolism under an insulin resistant state.

Within the scope of this thesis we will be focussing on the metabolism of glucose inside the cell using a molecular systems biology bottom-up approach. This will entail a detailed kinetic characterisation of each enzyme present in glycolysis. Furthermore, the dynamic behaviour of each enzyme will be integrated with the other enzymes in the pathway by constructing a detailed kinetic model of glycolysis in C_2C_{12} skeletal muscle cell extract. To test whether the detailed kinetic model accurately describes the pathway in C_2C_{12} skeletal muscle extract, a new method was developed for the quantification of metabolite dynamics to correlate these results with the detailed kinetic model and to test the predictive accuracy of the kinetic model.

The aim of this study was to construct and validate a detailed kinetic model of glycolysis in non-diabetic skeletal muscle cells to characterise the reference state. The objectives of this study are listed below.

- Develop a metabolomic technique for the separation and quantification of the glycolytic intermediates and cofactors present in glycolysis.
- Characterisation of the glycolytic enzymes in differentiated C_2C_{12} skeletal muscle cells.
- Construction of a detailed kinetic model to describe glycolysis in differentiated C_2C_{12} skeletal muscle cells from the kinetic characterisation of the glycolytic enzymes.
- Validation of the glycolytic model by comparing model simulations with experimental data.
- Analysis of the kinetic model by performing metabolic control analysis.

The thesis is divided into three research chapters (Chapter 3 -5) that are presented in paper format. In addition to the research chapters I present an overview of the current literature on type 2 diabetes in the context of the broader project in **Chapter 2**, and skeletal muscle metabolism and metabolomics in the context of this study. The general discussion of the outcomes of this thesis is discussed in **Chapter 6.** In **Chapter 3** I present the development of a novel metabolomics technique for the identification and quantification of the glycolytic intermediates and cofactors present in glycolysis. In **Chapter 4** the construction of a detailed

kinetic model that describes glycolysis in skeletal muscle extract is presented. In **Chapter 5** I focus on the validation and analysis of the detailed kinetic model, using metabolic control analysis and the novel metabolomics technique developed in Chapter 3.

1. 1. References

1 **American diabetes association.**, Diagnosis and classification of diabetes mellitus., *Diabetes Care*, 33:S62-S69, 2010

2 **Simoneau JA and Kelley DE.**, Altered glycolytic and oxidative capacities of skeletal muscle contribute to insulin resistance in NIDDM., *J. Appl. Physiol*. 83:166–171, 1997

3 **DeFronzo RA, Jacot E, Jequier E, Maeder E, Wahren J and Felber JP.**, The effect of insulin on the disposal of intravenous glucose. Results from indirect calorimetry and hepatic and femoral venous catheterization., *Diabetes* 30: 1000–1007, 1981

4 **Nuutila P, Knuuti MJ, Raitakari M, Ruotsalainen U, Teras M, Voipio-Pulkki LM, Haaparanta M, Solin O, Wegelius U and Yki-Jarvinen H.**, Effect of antilipolysis on heart and skeletal muscle glucose uptake in overnight fasted humans., *Am. J. Physiol. Endocrinol. Metab.* 267: E941–E946, 1994

Chapter 2
Literature Review of the regulation of glucose metabolism in mammalian tissue

2. 1. Preamble

The literature review presented in this chapter discusses the relevant literature associated with glucose transport and insulin signalling (Sections 2.3 – 2.5) within the scope of the broader focus of this study. This is required for the research topics discussed in Chapter 6 of this thesis. The relevant literature pertaining to this study is discussed in Sections 2.6 – 2.10.

2. 2. Background

Within the body, the regulation of glucose homeostasis is of critical importance to maintain a normal and healthy physiology. After a meal, the majority of the glucose introduced into the body (70 – 80%) is consumed via the metabolic activity of skeletal muscle cells[1,2]. Alterations to the blood glucose levels have a direct effect on the physiology of the body and can lead to chronic hyperglycaemia, the predominant metabolic state associated with type 2 diabetes mellitus. The development of this progressive metabolic disorder has been attributed to both environmental lifestyle factors along with undetermined genetic factors[3]. This involves defective action in the major organs associated with metabolic control including; skeletal muscle, adipose tissue, the liver and β-cells. An early defect in type 2 diabetic patients is the impairment of insulin to activate an increase in the metabolic rate of skeletal muscle. Intrinsic impairment of insulin activity on skeletal muscle has been established by clinical trials that focussed on the relatives of type 2 diabetic patients who showed a resistance to insulin action, relating the progression of type 2 diabetes to genetic factors[4 - 6]. Moreover, hyperglycaemia, hyperinsulinemia, altered lipid profiles, and other metabolic abnormalities can also aggravate the defective disposal of glucose in insulin-regulated tissues by interfering with the insulin mechanism regulating glucose transport and thus disrupting glucose uptake[7,8].

Traditional biochemical and physiological techniques have delivered several essential findings on muscle biology, for example, the discovery of glycolysis regulation by fructose-2,6-bisphosphate[9,10], the description of mechanisms of glucose transport into myofibres[10], and many others. Thus far, conclusions on muscle biology were based on the analysis of the activity,

cellular localization and/or biological functions of only a limited number of enzymes or proteins. To have a concise understanding of the mechanistic interactions related to maintaining blood glucose homeostasis in the body, a standardised study of the glucose metabolism of skeletal muscle myofibres is required. This includes the transport of glucose into the muscle fibres, the regulation of glucose transport through insulin dependent and insulin independent mechanisms and a thorough kinetic understanding of how glucose is metabolised via glycolysis in muscle fibres.

To further our understanding of the biological framework in which insulin operates, specifically with regards to skeletal muscle, a detailed investigation of the literature available on this topic will be discussed in this chapter.

2. 3. Glucose transporters in muscle cells

The rate at which glucose is taken up by cellular tissue from the extracellular fluids, is a crucial regulating step in the control of glucose and glucose metabolism within the cell. The uptake of glucose occurs via glucose transporters in the plasma membrane of animal cells[11,12]. These carrier-mediated facilitated diffusion glycoproteins are a family of structurally related glucose transport proteins. The type of glucose transporters expressed is tissue-specific and differ in their transcriptional and posttranscriptional regulation[13 - 15]. Apart from liver cells, skeletal muscle is the most intensely studied tissue regarding metabolism and protein composition. Studies on the physiology, histochemistry and enzymology of muscle cells in the late 1970's have resulted in a framework describing muscle metabolism[16 - 18]. Within this framework, insulin has been shown to accelerate glucose transport into the cell through the cell membrane[19 - 22]. Furthermore, Randle and Smith[23] demonstrated that an increase in glucose uptake is also observed under anoxic conditions. They attributed this observation to the acceleration of the glucose transport process over the cell membrane induced by anoxia itself, as later confirmed by Morgan *et al.*[24]. Through a kinetic investigation of the glucose transport in rat heart muscle, Morgan *et al.*[25] examined the behaviour of glucose transport under basal-, insulin stimulated- and anoxic conditions. Under basal conditions, glucose flux is controlled by glucose transport. However, under both insulin-stimulated, and anoxic conditions, glucose transport is upregulated and glucose phosphorylation, holds most of the control over glucose flux. Moreover, Morgan *et al.*[25] concluded that anoxia stimulated glucose phosphorylation, the first step in glycolysis.

Within skeletal muscle cells glucose transport is facilitated predominantly by the GLUT1 and GLUT4 glucose transporters, two members of the glucose transporter family[11]. The GLUT1 glucose transporter is universally distributed in the plasma membrane of various cell types, including skeletal muscle, and is responsible for basal glucose transport over the plasma membrane[26]. The expression of GLUT4 is excessive in insulin-stimulated cell types, such as skeletal muscle, cardiac muscle and adipocytes[27]. The concentration of the GLUT4 isoform in the plasma membrane is low under basal conditions, with high concentrations of the GLUT4 isoform located within the intracellular compartments of the cell. Under activated conditions, resulting from insulin stimulation, muscle contraction or hypoxia, the translocation of the GLUT4 transporter from the intracellular compartments to the plasma membrane is promoted. The increase of GLUT4 glucose transporters on the cell surface results in an increase in the uptake of glucose by the cell[28]. The insulin-resistant characteristics of type 2 diabetes can be attributed to defects in the insulin-induced GLUT4 translocation process in skeletal muscle[29].

2. 4. Insulin dependent GLUT4 translocation

The insulin signalling pathway in skeletal muscle cells plays a crucial regulatory role in several cellular processes, such as: glucose metabolism, protein synthesis and gene expressing. The insulin-induced GLUT4 translocation process is predominantly dependent on phosphatidylinositol (PI) 3-kinase in both adipocytes and skeletal muscle[30]. The insulin signalling cascade is facilitated by a series of phosphorylation reactions starting with the initial activation of the tyrosine kinase, insulin receptor (IR), through the binding of insulin to IR. The insulin signal is then carried through the insulin-receptor substrate (IRS), a regulatory docking protein. The tyrosine phosphorylation of IRS by the IR is central to the differentiation of the insulin signal towards either metabolic events or gene regulatory events[3].

Tyrosine phosphorylation of the IRS enables this regulatory docking protein to recruit signalling molecules containing SH2 domains to form active signalling complexes. PI 3-kinase is one such protein, which catalyses the conversion of phosphatidylinositol-4,5-bisphosphate (PI2P) to phosphatidylinositol-3,4,5-triphosphate (PI3P) upon active signalling complex formation. This is a crucial step in the insulin stimulated GLUT4 translocation process. PI3P is an allosteric regulator of phosphoinositide-dependent kinase (PDK), a downstream target of PI 3-kinase. PDK was originally described as a phosphoinositide-dependent serine/threonine kinase PKB/Akt activator[31], However, PDK was later found to be an activator of other molecules in the AGC serine/ threonine kinase super-family, comprising the prototypes protein

kinase A (PKA), G (PKG), and C (PKC) associated with regulating glucose uptake[32]. The insulin signal is carried forward through the phosphorylation of Akt by PDK at the Ser-473 and Thr-308 residues[33]. After activation of Akt, the insulin signal is carried forward through the phosphorylation of Akt Substrate (AS) 160, which contains GTPase-activating proteins (GAP) for Rabs. AS160 is sometimes also abbreviated as TBC1D4 relating to its Tre-2/Bub2/Cdc16 (TBC) domain, a highly conserved domain responsible for GAP activity[34,35]. Rabs are small G proteins that are directly associated with the membrane trafficking of, in this case GLUT4[35]. A schematic representation of the insulin signalling cascade in given in Figure 2.1.

It has been noted that the insulin induced PI 3-kinase activation does not sufficiently account for the metabolic activity observed under insulin stimulated conditions[36,37]. This suggests that there are novel cascades that contribute to the amplification of insulin stimulated GLUT4 translocation which are independent of the PI 3-kinase cascade. Even though several regulatory reactions running in tandem have been elucidated, there is still many unknowns in the complete workings of the insulin stimulated GLUT4 translocation process.

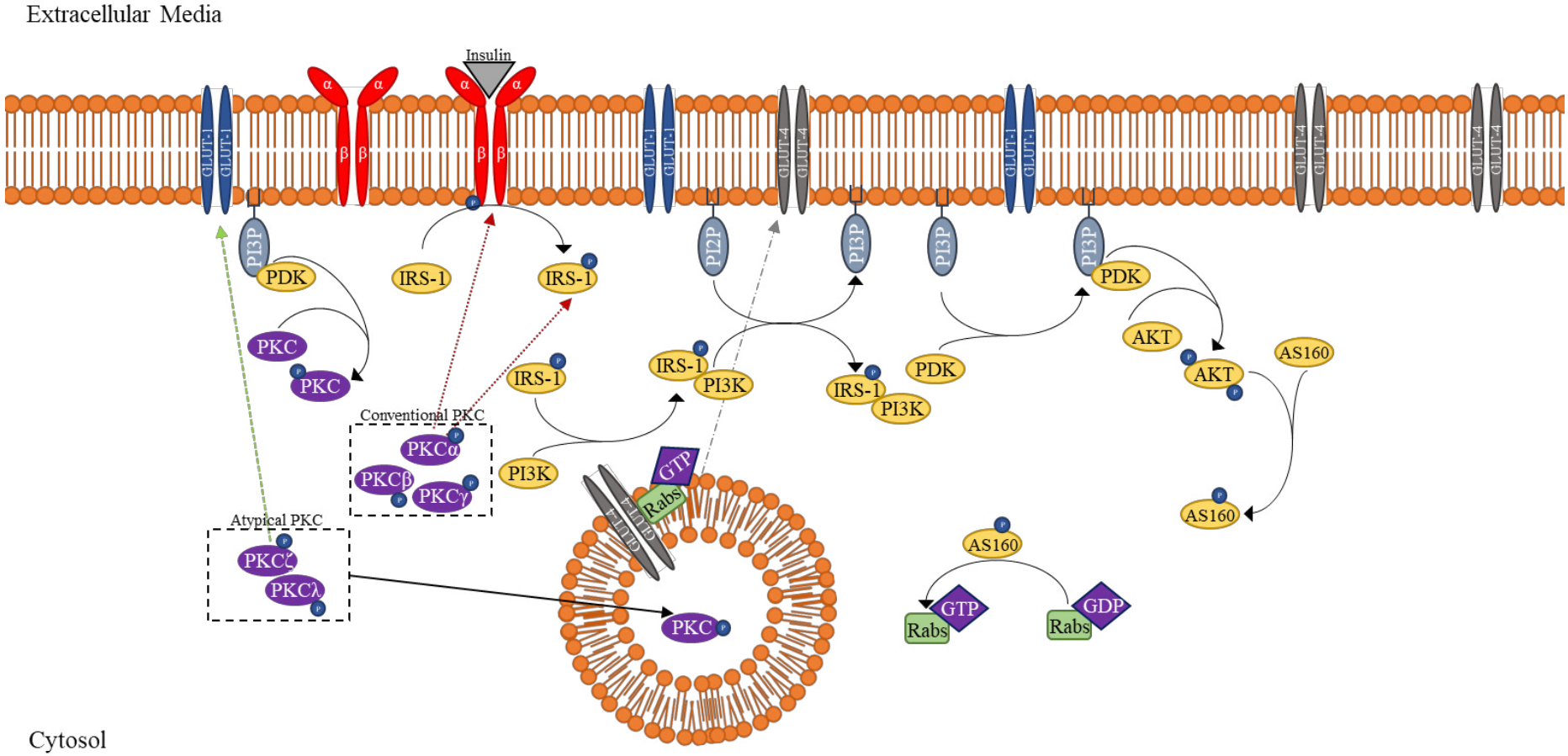

***Figure 2.1**: A schematic illustration of the insulin-signalling cascade. This scheme illustrates the series of phosphorylation reactions initialised by the binding of insulin to the IR and ending with translocation of the GLUT4 transporter to the cell membrane as discussed in the text above. This first step is the binding of insulin to the insulin receptor (IR) resulting in phosphorylation of the IR. This results in the phosphorylation of the insulin receptor substrate (IRS-1) and binding of IRS-1 to PI3-kinase (PI3 K). The subsequent step involves the phosphorylation of PI2P to PI3P and binding of PDK to PI3P. The PI3P/PDK complex phosphorylates AKT, resulting in the phosphorylation of Akt substrate 160 (AS 160). AS160 activates Rabs proteins which results in the trafficking of the GLUT4 vesicles from the cytosol to the cell membrane*

2. 5. AMPK activation of GLUT4 translocation

The insulin-independent activation of GLUT4 translocation is thought to be facilitated by the activation of 5'-AMP-activated protein kinase (AMPK), independent from the PI 3-kinase signalling pathway [38,39]. The insulin-independent AMPK activation of glucose uptake facilitates the enhanced translocation of the GLUT4 glucose transporter to the plasma membrane in response to metabolic stress[3]. AMPK phosphorylates key targets in diverse metabolic pathways, such as hepatic lipid metabolism and adipocyte lipolysis as well as fatty acid oxidation and glucose transport in skeletal muscle through the phosphorylation of Acetyl CoA Carboxylase (ACC)-β, thereby acting as a metabolic switch[40]. Several studies done on AMPK regulation noted that the signal is sensitive to increased energy demands by the skeletal muscle cells[41 - 44]. The regulation of the AMPK contribution to glucose uptake is thought to be dependent on the balance between ATP demand (*e.g.* muscle contraction) and ATP supply from substrate oxidation (*e.g.* glycolysis)[45]. It is of interest to note that AMPK may also be involved in mitochondrial biogenesis and chronic adaptions to the skeletal muscle cells seen with exercise training and fitness[46 - 48].

The heterotrimeric AMPK enzyme consists of a catalytic α-subunit along with regulatory β- and γ- subunits which can be activated both allosterically and covalently. Covalent phosphorylation of AMPK is mediated by the up-stream AMPK kinase (AMPKK) which activates AMPK, via phosphorylation[45]. *In-vitro* studies investigating the allosteric regulation of AMPK concluded that AMP and creatine (Cr) act as activators of AMPK, whereas ATP and phosphocreatine (PCr) act as inhibitors of AMPK[49,50]. Moreover, AMP may also be an allosteric activator to AMPKK, and an allosteric inhibitor of protein phosphatase-2A (PP-2A), the protein responsible for the de-phosphorylation, and thus inactivation of AMPK[51,52]. Therefore, both allosteric and covalent regulation of AMPK is extremely sensitive to changes in the concentration of metabolites related to the cellular energy state of skeletal muscle cells (AMP, ATP, Cr and PCr)[53,54].

The concentrations of the allosteric regulators of AMPK namely, AMP and ATP along with ADP, is primarily dictated by the enzyme catalysed adenylate kinase (AK) reaction. During the AK reaction, phosphate (P_i) transfer from one ADP molecule to another ADP molecule occurs, resulting in the formation of AMP and ATP. In skeletal muscle, the activity of AK is noted to be extremely high, even at high energy demands. Therefore, it can be expected that the AK reaction is always at equilibrium and the concentration of AMP becomes a function

of ADP concentration dictated by the cellular energy state[55 - 57]. Furthermore, the reaction creatine kinase (CK) regulates ATP concentration during transitions in energy demands, through a P_i transfer reaction between ADP and PCr, resulting in the formation of ATP and Cr. With an increase in muscle contraction CK will regulate the formation of ATP in accordance with the demands, resulting in a decrease in PCr concentrations and an increase in Cr concentrations, further contributing to the allosteric activation of AMPK[44,58,59]. Similarly, to AK, the activity of CK in skeletal muscle cells is extremely high and is accepted to be at equilibrium under most energy demands. In summary, an increase in muscle contraction results in a higher demand for ATP. The resulting increase in ADP concentration is regulated through the enzymes AK and CK, resulting in the reduction of ADP and PCr and the formation of AMP, ATP and Cr. The formation of ATP further drives muscle metabolism, whereas the formation of AMP within the cell subsequently activates AMPKK and deactivates PP-2A, resulting in the covalent activation of AMPK[54,60]. Furthermore, allosteric activators (AMP, Cr) of AMPK are increased and allosteric inhibitors (ATP, PCr) of AMPK are decreased. The elevated activity of AMPK facilitates the translocation of the GLUT4 glucose transporter to the cell surface, resulting in an enhanced glucose transport rate.

Similar to AS160, TCB1D1 contains a TBC Domain for the GTPase activation of Rabs that facilitates trafficking to the GLUT4 transporter to the cell membrane. There is a significant structural similarity between AS160 and TCB1D1 specifically with regards to the Rab-GAP domain. However, the distribution of AS160 and TCB1D1 varies significantly between different tissue types. AS160 is expressed to a similar degree in a multiple of mammalian tissue types, whereas the expression of TCB1D1 is several times higher is skeletal muscle compared to other muscle types[61,62]. A study performed by An *et. al.*[63] to elucidate the functionality and role of TCB1D1 in the insulin-stimulated and AMPK activated GLUT 4 translocation process found that TCB1D1 plays a role in both insulin-stimulated GLUT4 translocation and AMPK activated GLUT 4 translocation. TCB1D1 can act as an analogue of AS160 that can be phosphorylated by Akt. Furthermore, TCB1D1 also acts as a substrate of AMPK to facilitate the AMPK activated GLUT 4 translocation process. A schematic illustration of the AMPK activation of GLUT4 translocation is shown in Figure 2.2.

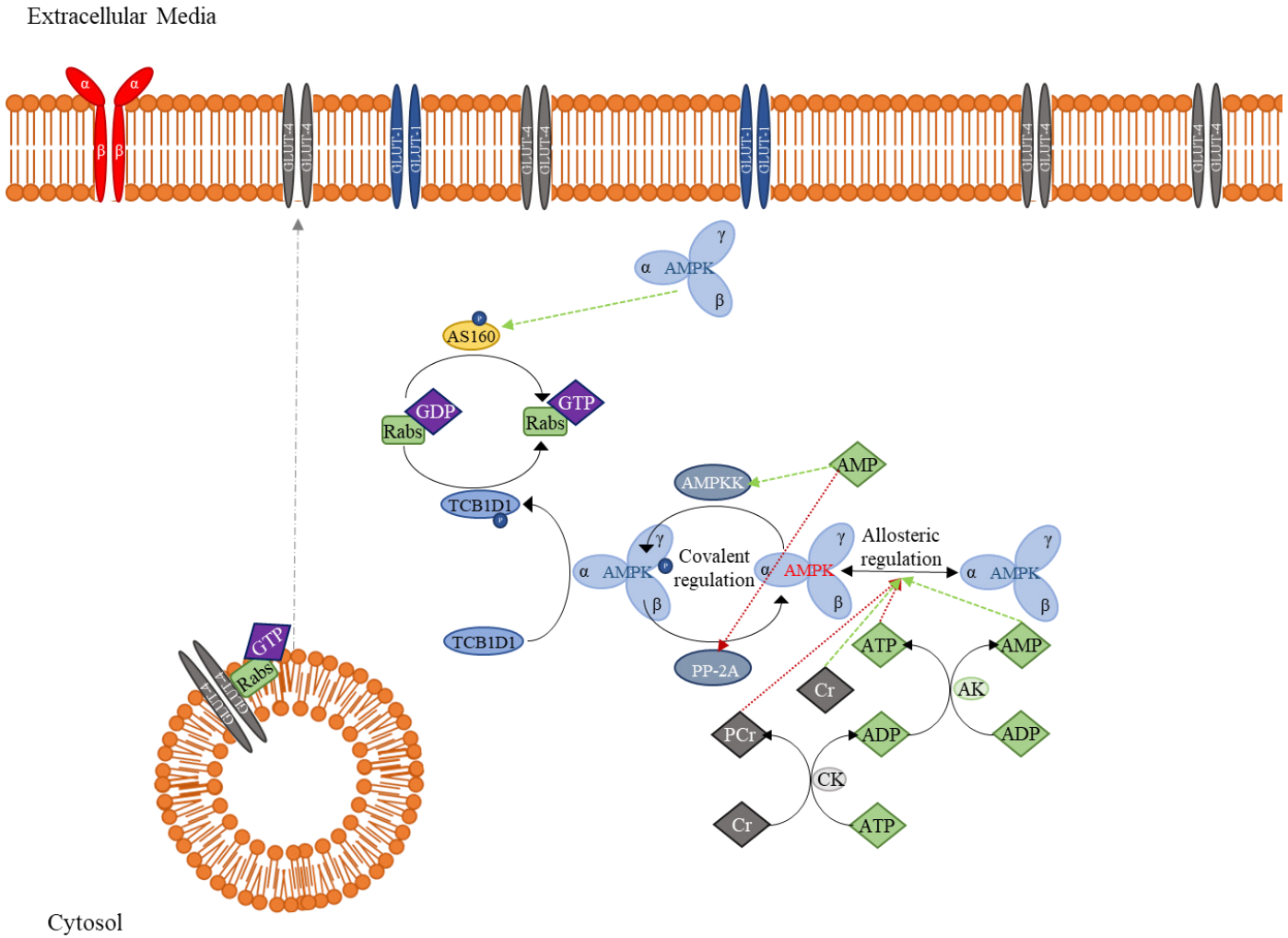

***Figure 2.2**: A schematic illustration of AMPK signalling pathway. This scheme illustrates the allosteric regulation of AMPK by AMP, ATP, creatine (Cr) and phosphocreatine (PCr), and the covalent activation of AMPK via AMPK kinase (AMPKK) and deactivation by protein phosphatase 2A (PP-2A). The activated form of AMPK phosphorylates TCB1D1 which in turn activates Rabs proteins resulting in trafficking of the GLUT4 vesicles from the cytosol to the cell membrane The AMPK pathway is stimulated under conditions of high metabolic activity resulting in the translocation of the GLUT4 transporter to the cell membrane as discussed in the text above.*

2. 6. Glycolysis

Glycolysis plays a central role in metabolism as an important production process for ATP and key metabolites in all cell types[64,65]. Apart from the biochemical understanding of carbohydrate utilization, studying the regulation of glycolysis has found applications in biotechnological processes[66] and in biomedical research, *e.g.* drug development for cancer therapies[67]. The term glycolysis describes the series of connected reactions which forms a pathway that systematically converts glucose to pyruvate. Pyruvate can then be further metabolised to CO_2 via oxidative phosphorylation in the tricarboxylic acid (TCA) cycle or to lactate via glucose fermentation[68]. Glycolysis can be divided into 2 parts namely upper- and lower glycolysis. Upper glycolysis comprises the enzymes hexokinase (HK), phosphoglucoisomerase (PGI), phosphofructokinase (PFK), aldolase (ALD) and triosephosphate isomerase (TPI), which utilises ATP as a substrate (HK and PFK) for the phosphorylation of glucose (GLC) and fructose-6-phosphate (F6P). Lower glycolysis comprises the enzymes glyceraldehyde-3-phosphate (GAPDH), 3-phosphoglycerate kinase (PGK), 3-phosphglycerate mutase (PGM), enolase (ENO) and pyruvate kinase (PK), which produces ATP as a product during the formation of 3-phosphoglycerate (P3G) via PGK and pyruvate (PYR) via PK. There are several branch pathways that flow out of glycolysis, such as the conversion of glucose-6-phosphate (G6P) to glucose-1-phosphate (G1P) catalysed by the enzyme phosphoglucomutase (PGLM) for the synthesis of glycogen. Another branched pathway is the conversion of dihydroxyacetone phosphate (DHAP) to form glycerol (GLY). A schematic representation of glycolysis is shown in Figure 2.3 illustrating the conversion of GLC to PYR (Glycolysis) and the branched pathway leading from glycolysis (glycogen synthesis, glycerol synthesis and the TCA cycle).

The traditional biochemistry approach to understanding the dynamic behaviours of metabolic pathways, such as glycolysis, relies on studying the properties of each enzyme in isolation[69]. However, the *in vivo* properties of enzymatic reactions can differ significantly from the *in vitro* measurements[70]. The regulation of enzyme activity by metabolites arising from unrelated metabolic process, the effects of molecular crowding, pH and temperature, and the spatial distribution and compartmentalisation of enzymes within the cell contribute to discrepancies between the *in vitro* measurement of enzyme activities and their *in vivo* realised activities[70]. To address these concerns van Eunen *et. al.*[71] have developed a protocol for the measurement of *in vitro* enzyme activities. This includes measuring enzyme activity at a

physiological pH and temperature, in a buffer matrix that mimics the chemical composition of the cytosol. Several investigations on the characterisation glycolysis is specified cell lines have successfully been performed[69,72]. A study performed by Teusink *et. al.*[69] investigated whether *in vivo* glycolysis can be understood from the *in vitro* characterisation of the glycolytic enzymes in yeast. Teusink *et. al.*[69] concluded that some enzymatic reactions showed a satisfactory comparison between *in vitro* description and *in vivo* activity, whereas other enzymes did not compare so favourably. Another study performed by Penkler et. al.[72] used a similar approach as mentioned above[69] to investigate the activity of glycolytic enzymes in *plasmodium falciparum* for the identification of novel antimalarial drug targets.

2. 7. Glycolysis in skeletal muscle cells

With regards to mammalian cells, glycolytic and glycogenolytic regulation studies have predominantly focussed on skeletal muscle as a key experimental model. This is because of the glycogenolytic ATP production flux increase of two orders of magnitude that can be observed during transitions between the resting state and the activated state of skeletal muscle within the seconds timescale[66,73,74]. The activated state of skeletal muscle that arises from performing exercise results in a rapid increase in ATP utilization that is buffered and balanced through multiple ATP synthetic pathways, including glycolysis and oxidative phosphorylation[73,74]. To compensate for the increased utilization of ATP an increased production of ATP is required to uphold a cellular energy balance for prolonged muscle activity[75]. Therefore, it is anticipated that the exceptionally rapid and large operational range of ATP utilization will result in stringent control mechanisms in place for regulating the flux through the glycolytic pathway[76].

Insulin exposure to muscle cells increases the rate of glycogen synthesis to produce glycogen inside the cell[77]. The discussion surrounding the importance of insulin-stimulated glycogen synthesis compared to GLUT4 mediated glucose transport remains controversial[78]. A 2-fold increase in the rate of glycogen synthesis was observed upon insulin exposure of C_2C_{12} skeletal muscle[77]. Several studies[79 - 82] focussed on evaluating the effect of insulin stimulation of mammalian cells on the activity of glycolytic enzymes have been published. Printz *et. al.*[79] investigated the regulation of the hexokinase isoform, HK II, by insulin in the 3T3-F442A adipose cell line and observed a 4-fold increase of HK II activity when cells were treated with 100 nM insulin. A follow-up study established that insulin increases the rate of HK II gene transcription[80]. An investigation performed by Elstrom *et. al.*[81] into the activation of glycolysis by Akt, suggested that Akt activity, regulated by insulin stimulation, directly stimulates the

cellular rate of glycolysis. Furthermore, the exposure of cultured rat hepatocytes to insulin resulted in a 4-fold increase in the activity of 6-phosphofructo-2-kinase and its product fructose-2,6-bisphosphate[82]. Fructose-2,6-bisphosphate is a potent PFK activator and it is postulated that the higher levels of fructose-2,6-bisphosphate present in insulin stimulated cell will lead to increase PFK activity.

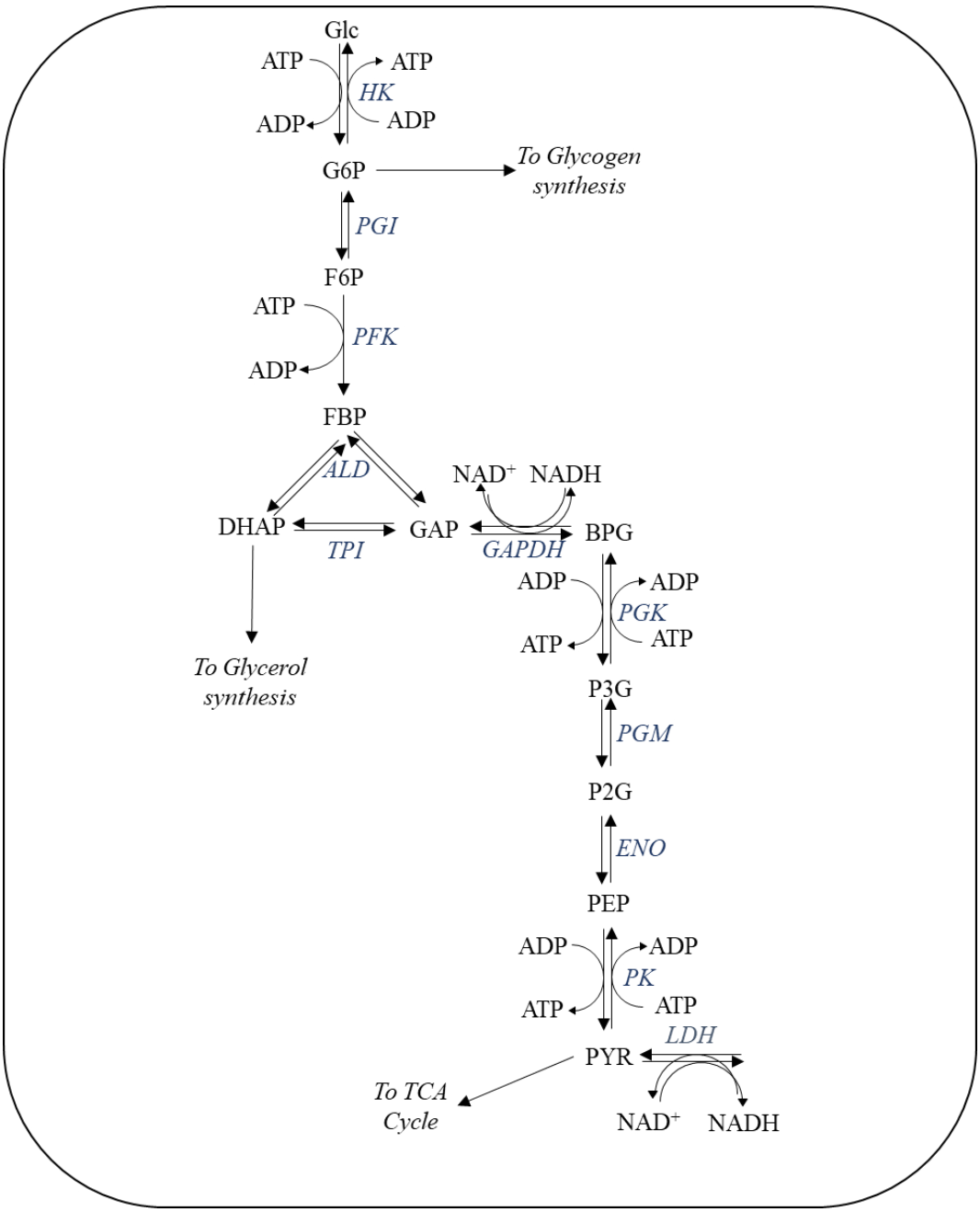

***Figure 2.3**: Schematic representation of glycolysis as discussed in the text above. The conversion of GLC to PYR (Glycolysis) is shown along with the branched pathways (glycogen synthesis, glycerol synthesis and the TCA cycle) leading from glycolysis. The glycolytic enzymes are shown in blue.*

Considering the characteristics of heterogeneous skeletal muscle, the distinct mechanical and energetic properties under activated conditions is of note when investigating the metabolic workings of skeletal muscle. Metabolically, fast twitch muscle (type II) relies heavily on glycolysis for ATP generation, whereas slow twitch muscle (type I) predominantly relies on oxidative phosphorylation to generate ATP to drive contractile activation of the muscle[83]. The difference in ATP production mechanisms observed in type I and II muscle is further supported by the measured enzyme activities and protein isoforms present in the different muscle types[84 - 87]. Furthermore, the rates of glycolysis and ATPase in type I and type II muscle are identical at rest. However, under actively contracting conditions the rates of ATPase and glycolysis are significantly higher in type I fibres compared to type II fibres[88]. Vinnakota *et al.*[88] measured the concentrations of ATP, phosphocreatine (PCr) and inorganic phosphate (Pi) as a function of time using ^{31}P nuclear magnetic resonance (^{31}P NMR) spectroscopy. Swiss Webster mice were dissected, and type I and type II muscle were harvested. ^{31}P-NMR measurements were performed on the muscle biopsies, along with pH measurements, following the induction of anoxia by replacing the oxygen rich environment with nitrogen. The difference measured in the rates of ATPase and lactate production in type I muscle were reported to be a factor of 3 – 4 times higher compared to type II muscle.

Extensive detailed studies of the ATP synthetic pathways and its kinetic regulation have been done by several research groups and several *in silico* models have been constructed for cellular ATP synthesis and regulation[75,89 - 92]. Vicini and Kushmerick[75] constructed a minimal mechanistic model to describe the cellular energy balance regulation processes studied in individuals as they transition from the resting state to the activated state and back to the resting state. The minimal model focussed on the interplay between the reactions of oxidative phosphorylation, ATP utilization (ATPase) and creatine kinase activity and successfully described the time dependent intracellular concentrations of PCr and Pi as obtained from the test subjects using ^{31}P-NMR. Lambeth and Kushmeric[89] constructed a detailed kinetic model of glycolysis in skeletal muscle using kinetic parameters obtained in literature from predominantly mammalian cell lines and biopsies. The kinetic parameters were later updated to better reflect the parameters determined in mammalian skeletal muscle in a follow-up publication[93]. Their model findings indicated that the flux control through glycolysis is predicated solely on the ATPase reaction describing ATP demand within the system (95 – 99% of control). As noted by Lambeth and Kushmeric[89] several limitations to their *in-situ* investigations were present. The lack of standardised kinetic data in a specified cell line for the

construction of a glycolytic model will be required to improve the model. Furthermore, several simplifications to the mechanistic descriptions of the enzymes were included due to a lack of literature data available. However, modifications to the model included in the follow-up publication[93] have improved on the above-mentioned limitations and the predictive capabilities of the model and was tested using time dependent concentrations of PCR and Pi obtained with ^{31}P-NMR. The research performed by Selivanov *et al.*[91] focussed on the changes observed to glycolytic flux under different exercise regimes. The kinetic parameters for this study were obtained from work published by Parra *et al.*[94]. Interestingly Parra *et al.*[94] have observed a 2-fold increase in phosphofructo-kinase (PFK) activity measured after training as compared to the PFK activity before training (at rest). However, this increase in PFK activity did not correlate with fructose-1,6-bisphosphate (FBP) concentrations measured at rest. In both simulation cases performed by Selivanov *et al.*[91] the FBP concentration at rest was under predicted eluding to a wrongful measurement of PFK activity at rest[91]. The model simulations performed by Selivanov *et al.*[91] support the findings of Lambeth and Kushmeric[89] that glycolytic regulation is almost exclusively controlled by ATP demand. An *in-silico* investigation conducted by Schmitz et. al.[92] illustrated the important role that the regulation of PFK and PK activity play in silencing glycolytic flux in resting skeletal muscle. The *in-silico* models in literature[75,89 - 92] discussed here focus exclusively on the regulation of skeletal muscle metabolism under exercise conditions where the predominant driving force of metabolism is the generation of ATP for muscle activity. In the case of insulin stimulation of skeletal muscle, the predominant driving force of skeletal muscle is not the generation of ATP but rather the consumption and processing of glucose. Therefore, we can speculate that the regulatory effects observed during exercise will be significantly different in comparison to the regulatory effects required to deal with the increased demand for glucose processing afforded by insulin stimulation.

2. 8. Metabolic syndrome

Extensive *in-vivo* and *in-silico* investigations into the development and metabolic behaviour of metabolic syndrome has been conducted by Rozendaal *et. al.*[95,96]. Their endevours resulted in the successful description of metabolic changes that arise from the development of metabolic syndrome[95,96]. This resulted in a model capable of describing the development of pathophysiological symptoms relevant to clinical identification for the onset of metabolic syndrome[95].

Metabolic syndrome is a common metabolic disease that arise from an increasing incidence of obesity and characterised by insulin resistance, hypertension and glucose intolerance, among other symptoms[97]. Lillioja *et al.* [98] have observed a positive correlation between the presence of insulin resistance and the percentage of type I muscle fibres vs. type II muscle fibres obtained from muscle biopsies. Their study suggests that in the presence of decreased insulin sensitivity, the higher glycolytic activity of type I muscle is favoured compared to the oxidative activity of type II muscle. Furthermore, a shift to higher glycolytic activity has also been observed to occur during aging and physical inactivity[99]. In contrast, physical exercise enhances the expression of oxidative enzymes in relation to glycolytic enzymes associated with an increased sensitivity to insulin[99]. The metabolic capacity of skeletal muscle does not necessarily rely on fibre type distribution per se, but rather on the oxidative and glycolytic capacity of skeletal muscle. A study performed by Simoneau *et al.*[100] identified a strong relationship between the presence of insulin resistance and increased glycolytic enzyme activity and decreased oxidative enzyme activity in the skeletal muscle of obese women. Furthermore, the oxidative enzyme capacity of individuals suffering from non-insulin dependent diabetes mellitus (NIDDIM) is measurably lower compared to healthy individuals[101]. Another study performed by Simoneau *et al.*[101] measured the activities of glycolytic and oxidative marker enzymes in lean non-diabetic, obese non-diabetic and NIDDIM patients. The activities of glycolytic enzymes (HK, GAPDH, PFK) showed higher activity in obese non-diabetic patients compered to lean non-diabetic patients, with the highest activity measured in NIDDIM patients. The inverse trend was observed for oxidative enzymes (citrate synthase (CS), cytochrome c oxidase (COx), creatine kinase (CK)) with the lowest activities measured in NIDDIM patients and the highest activities measured in lean non-diabetic patients[101]. This suggests that the ratio of glycolytic vs. oxidative activities strongly correlates with the metabolic capabilities of skeletal muscle, with increased glycolytic to oxidative activities observed in obese and NIDDIM patients[101]. However, a mechanism responsible for the increased glycolytic to oxidative ratio remains unelucidated.

There has been significant debate amongst researchers whether the development of insulin resistance and type 2 diabetes results from the diminished activity of glucose transport or the defective glucose metabolism of skeletal muscle[102 - 105]. Several studies performed by the research group of Youn[106 - 109] have focussed on the hypothesis that impaired intracellular glucose metabolism precedes the observed suppression of insulin stimulated glucose transport in skeletal muscle. Kim *et al.*[106] have shown that insulin stimulated glycolysis is suppressed in

rats reared on a high-fat diet prior to the onset of insulin resistance. A significant reduction of approximately 30% in the whole-body glucose metabolism, under insulin stimulated conditions, was measured after 2 days of starting the high fat diet, whereas an insignificant decrease in the insulin stimulated glucose uptake was measured within this timeframe and the onset of insulin resistance was only observable on day 7 of the experiment. Furthermore, the suppression of glycolysis (via intralipid infusion) or glycogen synthesis (via amylin infusion) under insulin stimulated conditions in conscious rats resulted in a decreased glucose uptake rate of approximately 30%[107]. A further study also reported that during growth hormone infusion, the onset of diminished glycogen synthesis activity occurred prior to the development of insulin resistance[108]. The hypothesis that defective glucose metabolism leads to insulin resistance was further tested by Lombardi *et al.*[110] through an investigation of the inhibitory effects of lactate on glycolysis and how this relates to insulin resistance. Chronic lactate infusion over a 24h period in rat biopsies have shown no difference in glucose utilization compared to the control. However, when the biopsies were treated with insulin a 72% reduction in glucose utilization was observed when compared to the control. This observation suggests that lactate inhibition of glycolysis is correlated with skeletal muscle's inability to dispose of glucose effectively under insulin stimulated conditions[110]. The cause of lactate induced insulin resistance is hypothesised to occur via feedback inhibition of glycolysis through the inhibition of PFK-1 thereby decreasing the glucose flux through glycolysis[109]. Correlations between PFK-1 deficiencies and insulin resistance has also been observed in human studies by Ristow et al.[111,112]. Furthermore, lactate induced insulin resistance is associated with a significant decrease in the extent of IRS-1 – and IRS-2 associated PI 3-kinase activities along with down-stream Akt phosphorylation. However, the mechanism correlating lactate inhibition of glycolysis and decreased insulin signalling is still unclear[109]. A detailed study performed by Choi *et al.*[109] on the effect of lactate infusion on insulin signalling in rats showed that lactate infusion under hyperinsulinemic conditions did not result in changes in the extent of IR, IRS-1 and IRS-2 phosphorylation. However, IRS-1 – and IRS-2 associated PI 3-kinase activities were significantly lower in the presence of lactate infusions, translated with a measured reduction in Akt phosphorylation[109]. The study performed by Choi *et al.* strongly suggests that lactate can induce insulin resistance in skeletal muscle.

2. 9. Molecular systems biology

As laid out by J. C. Smuts in his book 'Holism and Evolution'[113] the animated does not differ from the unanimated in terms of structure, but in terms of functionality. Within the field of biology, organisms can be considered from both the perspective of the components that the organism is comprised of (structure) as well as the activities that these components perform (function). The cell can be perceived as a system of co-operation among the constituent components leading to function. Therefore, investigation of the components in isolation will not give a clear indication of its functionality within the whole, hence the term 'Holism'. However, the cell exists in a seemingly directionless state. Each component operates with little to no comprehension of the other components surrounding it. The functionality aspect observed in living states that arises from a seemingly chaotic assembly of components is governed by a system of organic regulation and co-ordination among these components. The organism is maintained in an active state with all its innumerable components finely constrained and adjusted to one another to form a harmonious, balanced process, which maintains a balanced functionality, not only in the life-span of a single individual, but improves and increases in complexity in the duration of its future generations. This is what we conceptualise as "life". This active, balanced state that governs life can be seen in all levels of complexity in an organism, from the intake of food as fuel and the excretion of by-products, to the chemical reactions mediated by enzymes. Therefore, to maintain the proper working of an organism all these processes must be maintained in a balanced state within each level and across different levels. Systems biology operates within this framework and is focussed on elucidating the functional and regulatory characteristics of each component in order to understand its role within a greater whole. This process occurs over several levels and utilizes different techniques and strategies with an ultimate goal of describing and understanding the whole. The levels that comprise an organism from a systems biology perspective is illustrated in Figure 2.4.

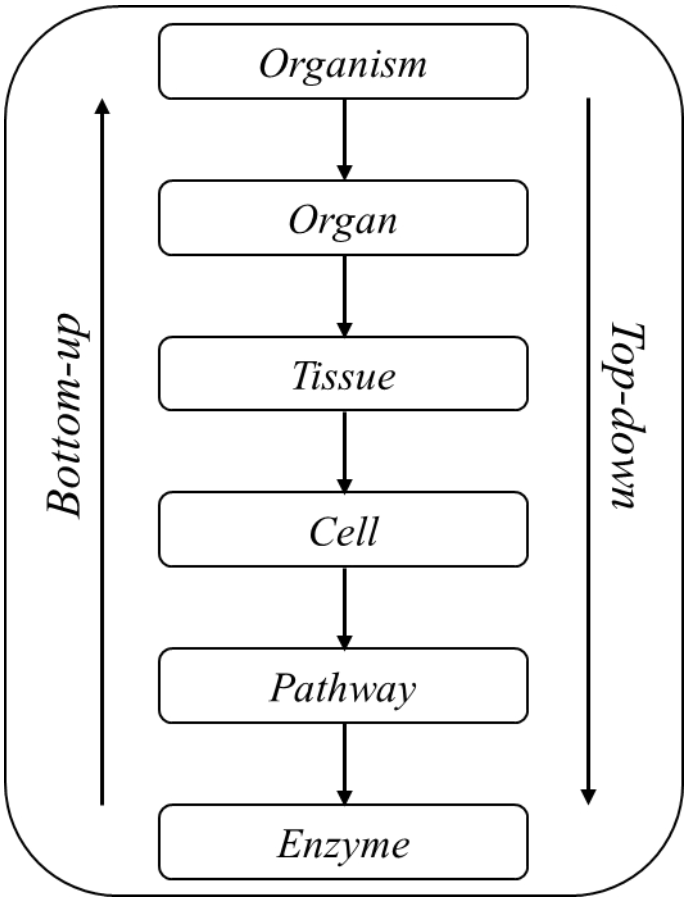

***Figure 2.4**: Representation of the modelling approaches of systems biology across different levels. A top-down modelling approach relies on starting at a higher level and moving down to describe lower levels of complexity. A bottom-up approach entails starting at a lower level and building up the higher levels of complexity.*

There are 2 main approaches that systems biologists use, namely; top-down and bottom-up. The top-down approach emerged as the dominant method for systems biology with the introduction of new omics analysis. With the ability to measure genome-wide experimental data, top-down modelling infers a bird's eye view of the behaviour of the system. Therefore, the aim of top-down systems biology is to discover and characterise biological mechanisms at the bottom level using an iterative cycle of analysis between experimental data and data analysis to identify correlations between concentrations of molecules. This enables the formulation of hypotheses regarding the regulation of groups of molecules. These hypotheses can then be tested experimentally to generate further data about the regulation of groups of molecules within the system. Top-down modelling approaches aims to discover patterns of behaviour that are generic enough to accurately predict biological mechanisms present in the system[114 - 116], or, to uncover functionally related processes under the control of a common set of transcription factors[117 - 119]. The strengths of top-down systems biology approaches arise from having a near complete overhead view of the system that addresses the metabolome, fluxome, transcriptome

and proteome. Therefore, top-down modelling is faced with analysing large experimental datasets for a single organism under specified conditions[120]. The conditions can be genetic (knockout studies, gene overexpression), environmental (changes in nutrients) or as a result of RNA interference. However, it is difficult to obtain a large number of perturbations to accurately elucidate the correlative regulatory processes present in the system. This results in a perception of large insight into the mechanistic workings of a living organism, but generally yields only fractional increases in our understanding of how these living systems are organised and regulated. Due to a lack of mechanistic data, top-down systems biology is phenomenological, describing the correlations between molecular components rather than the mechanistic relationship between those molecular components. These correlations are mapped onto a virtual mechanism which describes the correlation but could be far from reality. As such top-down modelling approaches are mostly used in cellular systems that lack a high level of mechanistic characterisation[121].

In contrast to top-down systems biology approaches, which give insights into correlations between components through induction, bottom-up systems biology investigates the functional properties of a system that could arise by having a high level of mechanistic detail about the molecular processes involved. Thus, bottom-up modelling addresses the elucidation of a system from the bottom, looking at the interactive behaviour of the components involved in each process. This is typically accomplished through the use of rate equations that describe the mechanistic behaviour of each component and integrating these rate equations to predict the behaviour of the whole system. The ultimate aim of the bottom-up modelling approach is to combine the components present in a system into a model that describes the whole system. Therefore, the main concern of bottom-up modelling is accuracy between model predictions and reality[121]. Bottom-up models are mechanism based rather than phenomenological. However, there are difficulties regarding parameter estimation. Due to the simplification of mechanistic models, along with the inability to measure enzyme activities *in situ*, the mechanistic description of the enzyme along with kinetic parameter determination can vary from the biologically concise parameters of the enzyme. Therefore, model validation to ensure that model predictions accurately reflect the reality of the system is imperative. It should be noted that bottom-up model behaviour is not fitted but predicted. Bottom-up models allow for the prediction of changes in the concentrations of system variables based on a mechanistic understanding of the components involved and how these components interact. Model validation is thus used to determine how accurately the model predicts the system in reality.

The typical bottom-up modelling approach reflects the actual stoichiometric relationship between variables, along with an accurate reflection of the structure of allosteric regulation. However, this is dependent on the complexity of the experimental efforts required to determine precise kinetic parameters and enzyme mechanisms under standardised conditions that mimic the complexity of the cytosolic environment in which the enzyme is active. The complexity of bottom-up modelling approaches is often alleviated by obtaining kinetic parameters from literature, measured under non-cytosolic-like conditions, or by fitting kinetic parameters to simplified catalytic mechanisms. This brings in question the accuracy of some bottom-up studies. Therefore, a strong emphasis should be placed on model validation, *i.e.* determining the predictive accuracy of bottom-up models.

This has led to the development of the silicon cell program[122]. The explicit aim of the silicon cell program is to construct computer-based models that replicate the mechanistic behaviour of cellular pathways. This includes the experimentally determined properties of all molecular components[123]. The silicon cell programs bring together groups globally to construct precise biological models which, after the peer-review process by associated journals, are then made available on model databases and simulation platforms, such as Biomodels[124] and JWS online[125]. JWS online aims to provide curated models constructed from experimentally determined parameter values, refereed by scientific journals to enable in silico simulation-based experimentation. The silicon cell approach has shown significant advancements in understanding the metabolic behaviour of organisms such as *Plasmodium falciparum* in red blood cells[126] and bloodstream form *Trypanosoma brucei* [127 - 129]. Similarly, using detailed kinetic models on metabolism, EGF receptor signal transduction and the eukaryotic life cycle in *Saccharomyces cerevisiae* have demonstrated the silicon cell program[122].

Validation and determination of the predictive accuracy of bottom-up models relies heavily on the availability of analytical techniques that offer metabolomic data of the biological system in question. Metabolome analysis allows for direct access to the metabolic phenotype expressed under specific environmental conditions. The outcome of cellular regulatory processes present at different levels of expression is reflected in the metabolic phenotype of the cell[130,131]. This has significant value to molecular systems biology in terms of both a top-down phenomenological approach, identifying potential metabolic bottlenecks and elucidating new regulatory processes present in a pathway, as well as bottom-up mechanistic modelling to compare model predictions with metabolome data to validate models.

Metabolic control analysis (MCA) allows for the quantitative identification of how control over the flux through a metabolic pathway is distributed over the components (*e.g.* enzymes) in the pathway. MCA was developed by Kacser and Burns[132], and Heinrich and Rapoport[133]. The control exerted by each model component over the flux of the substrate or systematic parameter (*e.g.* metabolite concentration) results in quantification of control each component has over the pathway as control coefficients. Control coefficients describe the fractional control each component has over the pathway[134]. Refer to the review by Cascante *et. al.*[134]for further information on MCA and its application in drug discovery and disease.

2. 10. Metabolomics

The completion of the human genome sequence[135], has increased efforts to determine the function of orphan genes as molecular targets for therapeutic intervention, and the search for biological markers as indicators of disease response or progression[136]. This post genomic era has increasingly shown the need for analytical methods to quantify the concentrations of intracellular and extracellular metabolites of living organisms and continues to be more apparent as advances in our detailed understanding of metabolic processes in biological systems progress[137]. Analytical approaches in the fields of gene sequencing (genomics), gene expression (transcriptomics) and protein translation (proteomics) have become important tools for understanding and quantifying the regulation of biological systems, but a similar approach to metabolomics has remained problematic. Development of the polymerase chain reaction (PCR) and automated sequencing for genomic analysis[138,139] and array-based proteomics[140] offers an automated analytical strategy for the elucidation of the genome or proteome of a biological system. In contrast, the chemical complexity and heterogeneity of metabolites make it impossible to develop an automated analytical strategy for the quantification of all possible metabolites in a cellular system[136].

Analysis of a biological system at the transcriptomic, proteomic and metabolomic level in conjunction with a systems biology approach offers a method of bridging the genotype-to-phenotype gap[141]. However, the staggering number of metabolites in any given system and their relationship and interactions with other metabolites (metabolism) and biochemical species makes this a dauting challenge. The major effort of metabolomic investigations aims to qualitatively and/ or quantitatively identify the phenotypic expression and biological function biochemical species[142]. Metabolomics, in particular, is of importance to systems biologists as it

is the result of gene expression and it is expected that changes to the metabolome will be amplified in conjunction to changes in the transcriptome and proteome[143].

The metabolome is an overarching term that includes many different biomolecules and there is active discussion in the research community on what exactly constitutes the term 'Metabolome'[136]. The term was first defined by Oliver *et. al.*[144] as the concentration profile of all low molecular weight molecules present in cells at a specific physiological state at a given time. However, the wide ranges of physiochemical properties associated with the metabolome makes the determination of the metabolic profile complicated. This has allowed for the development of different metabolomic strategies with varying degrees of quantitative ability, and number of metabolites included in the analysis, depending on the study and the need.

Untargeted metabolomic studies, or metabolic profiling is focussed on acquiring analytical data in relation to a wide range of metabolites in the metabolome and is applied in inductive studies. Therefore, untargeted metabolomic techniques are developed for the detection of hundreds to thousands of metabolites in a single analysis at the cost of lower precision and accuracy in comparison to targeted studies. Untargeted metabolomic studies are often carried out on samples with a lack of metabolite composition beforehand and the large number of metabolites under analysis mean that sample preparation is limited to reduce metabolite losses. This typically results in the acquisition qualitative or semi quantitative data that measures relative changes in the metabolome as opposed to concentrations, since the technical difficulty of preparing standards and setting up calibration curves for each metabolite is impossible[142]. This metabolomics approach does offer a large amount of data on the metabolites present in a sample, which makes it ideal for quality control applications, for example the measurement of flavonols and anthocyanins present in grapes[145]. Another example of an untargeted study is the investigation carried out by Lisec et. al.[146] on the metabolic profile of plants in which gas chromatography mass spectrometry (GC-MS) was employed for the routine determination of relative levels of between 300 and 500 metabolites.

Targeted metabolomic studies is placed on the other side of the metabolomic analytical spectrum and emphasises high specificity, precision and accuracy to quantify metabolite concentrations of a select number of metabolites[142]. Targeted metabolomic studies rely on traditional analytical biochemical methods applied to deductive studies where the metabolites of interest are known. Sample preparation is typically more extensive to separate the

metabolites of interest from the sample matrix. Furthermore, calibration curves and internal standards are used to ensure that quantitative data is obtained[142].

Recent metabolomic studies, such as the study performed by Sabatine *et. al.*[147] for the identification of novel biomarkers of coronary heart disease, have resulted in an intermediate strategy to metabolomic analysis, sometimes referred to as semi-targeted metabolomic analysis. The experimental methodologies employed offers higher specificity, precision and accuracy compared to untargeted metabolomics and provide quantitative or semi-quantitative concentrations of metabolites[142].

2. 11. References

1 **DeFronzo RA, Jacot E, Jequier E, Maeder E, Wahren J and Felber JP.**, The effect of insulin on the disposal of intravenous glucose. Results from indirect calorimetry and hepatic and femoral venous catheterization., *Diabetes* 30: 1000–1007, 1981

2 **Nuutila P, Knuuti MJ, Raitakari M, Ruotsalainen U, Teras M, Voipio-Pulkki LM, Haaparanta M, Solin O, Wegelius U and Yki-Jarvinen H.**, Effect of antilipolysis on heart and skeletal muscle glucose uptake in overnight fasted humans., *Am. J. Physiol. Endocrinol. Metab.* 267: E941–E946, 1994

3 **Krook A, Wallberg-Henriksson H and Zierath JR.**, Sending the signal: molecular mechanisms regulating glucose uptake., *Med. Sci. Sports. Exerc.* 36: 1212–1217, 2004

4 **Eriksson J, Koranyi L, Bourney R, Schalin-Jäntti C, Widèn E, Meuckler M, Permutt AM and Groop LC.**, Insulin resistance in type 2 (non-insulin-dependent) diabetic patients and their relatives is not associated with a defect in the expression of the insulin responsive glucose transporter (GLUT4) gene in human skeletal muscle., *Diabetologia* 35:143–147, 1992

5 **Henriksen JE, Alford F, Handberg A, Vaag A, Ward GM, Kalfas A and Beck-Nielsen H.**, Increased glucose effectiveness in normoglycemic but insulin-resistant relatives of patients with non-insulin-dependent diabetes mellitus., *J. Clin. Invest.* 94:1196–1204, 1994

6 **Vaag A, Henriksen JE and Beck-Nielsen H.**, Decreased insulin activation of glycogen synthase in skeletal muscle in young nonobese Caucasian first-degree relatives of patients with noninsulin-dependent diabetes mellitus., *J. Clin. Invest.* 89:782–788, 1992

7 **Davidson MB, Bouch C, Venkatesan N and Karjala RG.**, Impaired glucose transport in skeletal muscle but normal GLUT-4 tissue distribution in glucose-infused rats., *Am. J. Physiol. Endocrinol. Metab.* 267: E808–E813, 1994

8 **Hager SR, Pastorek D, Jochen AL and Meier D.**, Divergence between GLUT4 mRNA and protein abundance in skeletal muscle of insulin resistant rats., *Biochem. Biophys. Res. Comm.* 181: 240–245, 1991

9 **Pilkis SJ, El-Maghrabi MR, Pilkis J, Claus TH and Cumming DA.**, Fructose 2,6-bisphosphate. A new activator of phosphofructokinase., *J. Biol. Chem.* 256: 3171–3174, 1981

10 **Van Schaftingen E and Hers HG.**, Inhibition of fructose-1,6-bisphosphatase by fructose 2,6-biphosphate., *Proc. Natl. Acad. Sci. USA* 78: 2861–2863, 1981

11 **Mueckler M.**, Family of glucose transporter genes: implications for glucose homeostasis and diabetes., *Diabetes* 39:6-11, 1990

12 **Kasanicki MA and Pilch PF.**, Regulation of glucose-transporter function., *Diabetes Care* 13:219-27, 1990

13 **Kahn BB and Flier JS.**, Regulation of glucose-transporter gene expression in vitro and in vivo., *Diabetes Care* 13:548-64, 1990

14 **Fukumoto H, Kayano T, Buse JP, Edwards Y, Pilch PF, Bell GI and Seino S.**, Cloning and characterization of the major insulin-responsive glucose transporter expressed in human skeletal muscle and other insulin-responsive tissues., *J. Biol. Chem.* 264:7776-79, 1989

15 **Tordjman KM, Leingang KA, James DE and Meuckler MM.**, Differential regulation of two distinct glucose transporter species expressed in 3T3-L1 adipocytes: effect of chronic insulin and tolbutamide treatment., *Proc. Natl. Acad. Sci. USA* 86:7761-65, 1989

16 **Barnard RJ, Edgerton VR, Furukawa T and Peter JB.**, Histochemical, biochemical, and contractile properties of red, white, and intermediate fibres., *Am. J. Physiol.* 220: 410–414, 1971

17 **Peter JB, Barnard RJ, Edgerton VR, Gillespie CA and Stempel KE.**, Metabolic profiles of three fibre types of skeletal muscle in guinea pigs and rabbits., *Biochemistry* 11:2627–2633, 1972

18 **Gollnick PD, Sjödin B, Karlsson J, Jansson E and Saltin B.**, Human soleus muscle: A comparison of fibre composition and enzyme activities with other leg muscles., *Pflug. Arch.* 348: 247–255, 1974

19 **Park CR, Bornstein J and Post RL.**, Effect of Insulin on Free Glucose Content of Rat Diaphragm in Vitro., *Am. J. Physiol.* 182:12-16, 1955

20 **Park CR and Johnson LH.**, Effect of Insulin on Transport of Glucose and Galactose into Cells of Rat Muscle and Brain., *Am. J. Physiol.* 182:17-23, 1955

21 **Levine R, Goldstein MS, Klein S and Huddlestun B.**, The action of insulin on the distribution of galactose in eviscerated nephrectomized dogs., *J. Biol. Chem.* 179:985–986, 1949

22 **Levine R, Goldstein MS, Huddlestun B and Klein S.**, Action of Insulin on the 'Permeability' of Cells to Free Hexose, As Studied by its Effect on the Distribution of Galactose., *Am. J. Physiol.* 163:70-76, 1950

23 **Randle PJ and Smith GH.**, Regulation of glucose uptake by muscle. 1. The effects of insulin, anaerobiosis and cell poisons on the uptake of glucose and release of potassium by isolated rat diaphragm., *Biochem. J.* 3:490-500, 1958

24 **Morgan HE, Randle PJ, and Regen DM.**, Regulation of glucose uptake by muscle. 3. The effects of insulin, anoxia, salicylate and 2:4-dinitrophenol on membrane transport and intracellular phosphorylation of glucose in the isolated rate heart., *Biochem.. J.* 73:573-579, 1959

25 **Morgan HE, Henderson MJ, Regen DM and Park CR.**, The effects of insulin and anoxia on glucose transport and phosphorylation in the isolated, perfused heart on normal rats., *J. Biol. Chem.* 236:253-261, 1961

26 **Mueckler M.**, Facilitative glucose transporters., *Eur. J. Biochem.* 219:713–725, 1994

27 **Watson RT, Shigematsu S, Chiang SH, Mora S, Kanzaki M, Macara IG, Saltiel AR and Pessin JE.**, Lipid raft microdomain compartmentalization of TC10 is required for insulin signaling and GLUT4 translocation., *J. Cell. Biol.* 154:829–840, 2001

28 **Watson RT and Pessin JE.**, Intracellular organization of insulin signaling and GLUT4 translocation., *Recent. Prog. Horm. Res.* 56:175–193, 2001

29 **Koistinen HA and Zierath JR.**, Regulation of glucose transport in human skeletal muscle., *Ann. Med.* 34:410–418, 2002

30 **Itani SI, Saha AK, Kurowski TG, Coffin HR, Tornheim K and Ruderman NB.**, Glucose autoregulates its uptake in skeletal muscle: involvement of AMP-activated protein kinase., *Diabetes* 52:1635–1640, 2003

31 **Alessi DR, James SR, Downes CP, Holmes AB, Gaffney PRJ, Reese CB and Cohen P.**, Characterization of a 3-phosphoinositide-dependent protein kinase which phosphorylates and activates protein kinase Bα., *Curr. Biol.* 7:261–269, 1997

32 **Stokoe D, Stephens LR, Copeland T, Gaffney PRJ, Reese CB, Painter GF, Holmes AB, McCormick F and Hawkins PT.**, Dual role of phosphatidylinositol-3,4,5-trisphosphate in the activation of protein kinase B., *Science* 277:567–570, 1997

33 **Mora A, Komander D, van Aalten DM and Alessi DR.**, PDK1, the master regulator of AGC kinase signal transduction., *Semin. Cell. Dev. Biol*. 15:161–170, 2004

34 **Fukuda M.**, "TBC proteins: GAPs for mammalian small GTPase Rab?"., *Bioscience Reports* 31:159–168, 2011

35 **Kane S, Sano H, Liu SC, Asara JM, Lane WS, Garner CC and Lienhard GE.**, A method to identify serine kinase substrates. Akt phosphorylates a novel adipocyte protein with a Rab GTPase-activating protein (GAP) domain., *J. Biol. Chem.* 277:22115–22118, 2002

36 **Baumann CA, Ribon V, Kanzaki M, Thurmond DC, Mora S, Shigematsu S, Bickel PE, Pessin JE and Saltiel AR.**, CAP defines a second signalling pathway required for insulin-stimulated glucose transport., *Nature* 407:147–148, 2000

37 **Krook A, Whitenead JP, Dobson SP, Griffiths MR, Ouwens M, Baker C, Hayward AC, Sen SK, Maassen JA, Siddle K, Tavarè JM and O'Rahilly S.**, Two naturally occurring insulin receptor tyrosine kinase domain mutants provide evidence that phosphatidylinositol 3-kinase activation alone is not sufficient for the meditation of insulin's metabolic and mitogenic effects., *J. Biol. Chem.* 272:30208–30214, 1997

38 **Hayashi T, Hirshman MF, Kurth EJ, Winder WW and Goodyear LJ.**, Evidence for 5AMP-activated protein kinase mediation of the effect of muscle contraction on glucose transport., *Diabetes* 47:1369–1373, 1998

39 **Kurth-Kraczek EJ, Hirshman MF, Goodyear LJ and Winder WW.**, 5AMP-activated protein kinase activation causes GLUT4 translocation in skeletal muscle., *Diabetes* 48:1667–1671, 1999

40 **Mu J, Brozinick JT Jr, Valladares O, Bucan M and Birnbaum MJ.**, A role for AMP-activated protein kinase in contraction- and hypoxia-regulated glucose transport in skeletal muscle., *Mol. Cell.* 7:1085–1094, 2001

41 **Aschenbach WG, Sakamoto K, and Goodyear LJ.**, 5 Adenosine monophosphate- activated protein kinase, metabolism and exercise., *Sports Med.* 34:91–103, 2004

42 **Carling D, Fryer LG, Woods A, Daniel T, Jarvie SL and Whitrow H.**, Bypassing the glucose/fatty acid cycle: AMP-activated protein kinase., *Biochem. Soc. Trans.* 31:1157–1160, 2003

43 **Hardie DG**., AMP-activated protein kinase: a key system mediating metabolic responses to exercise., *Med. Sci. Sports Exerc.* 36:28–34, 2004

44 **Winder WW.** Energy-sensing and signaling by AMP-activated protein kinase in skeletal muscle. *J. Appl. Physiol.* 91:1017–1028, 2001

45 **Hancock CR, Janssen E and Terjung RL.**, Contraction-mediated phosphorylation of AMPK is lower in skeletal muscle of adenylate kinase-deficient mice., *J. Appl. Physiol.* 100:406–413, 2006

46 **Holmes BF, Kurth-Kraczek EJ and Winder WW.**, Chronic activation of 5-AMP-activated protein kinase increases GLUT-4, hexokinase, and glycogen in muscle., *J. Appl. Physiol.* 87:1990–1995, 1999

47 **Winder WW, Holmes BF, Rubink DS, Jensen EB, Chen M and Holloszy JO.**, Activation of AMP-activated protein kinase increases mitochondrial enzymes in skeletal muscle., *J. Appl. Physiol.* 88:2219–2226, 2000

48 **Zong H, Ren JM, Young LH, Pypaert M, Mu J, Birnbaum MJ and Shulman GI.,** AMP kinase is required for mitochondrial biogenesis in skeletal muscle in response to chronic energy deprivation., *Proc. Natl. Acad. Sci. USA* 99:15983–15987, 2002

49 **Carling D, Clarke PR, Zammit VA and Hardie DG.**, Purification and characterization of the AMP-activated protein kinase. Copurification of acetyl-CoA carboxylase kinase and 3-hydroxy-3-methylglutaryl-CoA reductase kinase activities., *Eur. J. Biochem.* 186:129–36, 1989

50 **Ponticos M, Lu QL, Morgan JE, Hardie DG, Partridge TA and Carling D.**, Dual regulation of the AMP-activated protein kinase provides a novel mechanism for the control of creatine kinase in skeletal muscle., *EMBO. J.* 17:1688–1699, 1998

51 **Davies SP, Helps NR, Cohen PT and Hardie DG.**, 5-AMP inhibits dephosphorylation, as well as promoting phosphorylation, of the AMP activated protein kinase. Studies using bacterially expressed human protein phosphatase-2C alpha and native bovine protein phosphatase-2AC., *FEBS. Lett.* 377:421–425, 1995

52 **Scott JW, Hawley SA, Green KA, Anis M, Stewart G, Scullion GA, Norman DG and Hardie DG.**, CBS domains form energy-sensing modules whose binding of adenosine ligands is disrupted by disease mutations., *J. Clin. Invest.* 113:274–284, 2004

53 **Salt I, Celler JW, Hawley SA, Prescott A, Woods A, Carling D and Hardie DG.**, AMP-activated protein kinase: greater AMP dependence, and preferential nuclear localization, of complexes containing the alpha2 isoform., *Biochem. J.* 334:177–187, 1998

54 **Weekes J, Hawley SA, Corton J, Shugar D and Hardie DG.**, Activation of rat liver AMP-activated protein kinase by kinase kinase in a purified, reconstituted system. Effects of AMP and AMP analogues., *Eur. J. Biochem.* 219:751–757, 1994

55 **Lawson JW and Veech RL.**, Effects of pH and free Mg2+ on the Keq of the creatine kinase reaction and other phosphate hydrolyses and phosphate transfer reactions., *J. Biol. Chem.* 254:6528–6537, 1979

56 **McGilvery RW and Murray TW.**, Calculated equilibria of phosphocreatine and adenosine phosphates during utilization of high energy phosphate by muscle., *J. Biol. Chem.* 249:5845–5850, 1974

57 **Meyer RA and Foley JM.**, Cellular processes integrating the metabolic response to exercise. In: Handbook of Physiology. Exercise: Regulation and Integration of Multiple Systems. Bethesda, MD: *Am. Physiol. Soc.*, 1996, sect. 12, chapt. 18, p. 841–869

58 **Hardie DG.**, Minireview: the AMP-activated protein kinase cascade: the key sensor of cellular energy status., *Endocrinology* 144:5179–5183, 2003

59 **Hardie DG, Carling D and Carlson M.**, The AMP-activated/SNF1 protein kinase subfamily: metabolic sensors of the eukaryotic cell., *Annu. Rev. Biochem.* 67:821–855, 1998

60 **Moore F, Weekes J and Hardie DG.**, Evidence that AMP triggers phosphorylation as well as direct allosteric activation of rat liver AMP activated protein kinase. A sensitive mechanism to protect the cell against ATP depletion., *Eur. J. Biochem.* 199:691–697, 1991

61 **Roach WG, Chavez JA, Miinea CP and Lienhard GE.**, Substrate specificity and effect on GLUT4 translocation of the Rab GTPase-activating protein Tbc1d1., *Biochem. J.* 403:353–358, 2007

62 **Taylor EB, An D, Kramer HF, Yu H, Fujii NL, Roeckl KS, Bowles N, Hirshman MF, Xie J, Feener EP and Goodyear LJ.**, Discovery of TBC1D1 as an insulin-, AICAR-, and contraction-stimulated signaling nexus in mouse skeletal muscle., *J. Biol. Chem.* 283:9787–9796, 2008

63 **An D, Toyoda T, Taylor EB, Yu H, Fujii N, Hirshman MF and Goodyear LJ.**, TBC1D1 Regulates Insulin- and Contraction-Induced Glucose Transport in Mouse Skeletal Muscle., *Diabetes* 59:1358-1365, 2010

64 **Fothergill-Gilmore LA and Michels PA.**, Evolution of glycolysis., *Prog. Biophys. Mol. Biol.* 59:105–235, 1993

65 **Romano AH and Conway T.**, Evolution of carbohydrate metabolic pathways., *Res. Microbiol.* 147:448–455, 1996

66 **Schuster S, Fell DA and Dandekar T.**, A general definition of metabolic pathways useful for systematic organization and analysis of complex metabolic networks., *Nat. Biotechnol.* 18:326–332, 2000

67 **Pelicano H, Martin DS, Xu RH and Huang P.**, Glycolysis inhibition for anticancer treatment., *Oncogene* 25:4633–4646, 2006

68 **Lunt SY and Vander Heiden MG.**, Aerobic glycolysis: meeting the metabolic requirements of cell proliferation., *Annu. Rev. Cell. Dev. Bi.* 1:441-464, 2011

69 **Teusink B, Passarge J, Reijenga CA, Esgalhado E, van der Weijden CC, Schepper M, Walsh MC, Bakker BM, van Dam K, Westerhoff HV and Snoep JL.**, Can yeast glycolysis be understood in terms of in vitro kinetics of the constituent enzymes? Testing biochemistry., *Eur. J. Biochem.* 267:5313-5329, 2000

70 **Ovadi J and Srere PA.**, Metabolic consequences of enzyme interactions., *Cell. Biochem. Funct.* 14:249-258, 1996

71 **van Eunen K, Bouwman J, Daran-Lapujade P, Postmus J, Canelas AB, Mensonides FIC, Orij R, Tuzuns I, van den Brink J, Smits GJ, van Gulik WM, Brul S, Heijnen JJ, de Winde JH, de Mattoss MJT, Kettner C, Nielsen J, Westerhoff HV and Bakker BM.**, Measuring enzyme activities under standardized in vivo-like conditions for systems biology., *FEBS Journal* 277:749–760, 2010

72 **Penkler G, du Toit F, Adams W, Rautenbach M, Palm DC, van Niekerk DD and Snoep JL.**, Construction and validation of a detailed kinetic model of glycolysis in *plasmodium falciparum.*, *FEBS Journal* 282:1481-1511, 2015

73 **Blei ML, Conley KE and Kushmerick MJ.**, Separate measures of ATP utilization and recovery in human skeletal muscle., *J. Physiol.* 465:203–222, 1993

74 **Walter G, Vandenborne K, Elliott M and Leigh JS.**, In vivo ATP synthesis rates in single human muscles during high intensity exercise., *J. Physiol.* 519:901–910, 1999

75 **Vicini P and Kushmerick MJ.**, Cellular energetics analysis by a mathematical model of energy balance: estimation of parameters in human skeletal muscle., *Am. J. Physiol. Cell. Physiol.* 279:C213–C224, 2000

76 **Schmitz JPJ, Groenendaal W, Wessels B, Wiseman RW, Hilbers PAJ, Nicolay K, Prompers JJ, Jeneson JAL and van Riel NAW.**, Combined in vivo and in silico investigations of activation of glycolysis in contracting skeletal muscle., *Am. J. Physiol. Cell. Physiol.* 304: C180–C193, 2013

77 **Schmitz-Peiffer C, Craig DL and Biden TJ.**, Ceramide generation is sufficient to account for the inhibition of the insulin-stimulated PKB pathway in C_2C_{12} skeletal muscle cells pre-treated with palmitate., *J. Biol. Chem.* 274:24202-24210, 1999

78 **Lawrence JC and Roach PJ.**, New insights into the role and mechanism of glycogen synthase activation by insulin., *Diabetes* 46:541-547, 1997

79 **Printz RL, Koch S, Potter LR, O`Doherty RM, Tiesinga JJ, Moritz S and Granner DK.**, Hexokinase II mRNA and gene structure, regulation by insulin, and evolution., *J. Biol. Chem.* 268:5209-5219, 1993

80 **Osawa H, Sutherland C, Robey RB, Printz RL and Granner DK.**, Analysis of the signalling pathway involved in the regulation of hexokinase II gene transcription by insulin., *J. Biol. Chem.* 271:16690-16694, 1996

81 **Elstrom RL, Bauer DE, Buzzai M, Karnauskas R, Harris MH, Plas DR, Zhuang H, Cinalli RM, Alavi A, Rudin CM and Thompson CB.**, Akt stimulates aerobic glycolysis in cancer cells., *Cancer Res.* 64:3892-3899, 2004

82 **Probst I and Unthan-Fechner K.**, Activation of glycolysis by insulin with a sequential increase of a 6-phosphofructo-2-kinase activity, fructose-2,6-bisphosphate level and pyruvate kinase activity in culture rate hepatocytes., *Eur. J. Biochem.* 153:347-353, 1985

83 **Close RI.**, Dynamic properties of mammalian skeletal muscle., *Physiol. Revs.* 52:129–197, 1972

84 **Barany M.**, ATPase activity of myosin correlated with speed of muscle shortening., *J. Gen. Physiol.* 50:197–218, 1967

85 **Nemeth P, Hofer HW and Pette D.**, Metabolic heterogeneity of muscle fibres., *Histochemistry* 63:191–201, 1979

86 **Pette D and Staron RS.**, The molecular diversity of mammalian muscle fibres., *News Physiol. Sci.* 8:153–157, 1993

87 **Hughes SM, Chi MM, Lowry OH and Gundersen K.**, Myogenin induces a shift of enzyme activity from glycolytic to oxidative metabolism in muscles of transgenic mice., *J. Cell. Biol.* 145:633–642, 1999

88 **Vinnakota KC, Joshua Rusk J, Palmer L, Shankland E and Kushmerick MJ.**, Common phenotype of resting mouse extensor digitorum longus and soleus muscles: equal ATPase and glycolytic flux during transient anoxia., *J. Physiol.* 588:1961–1983, 2010

89 **Lambeth MJ and Kushmerick MJ.**, A Computational Model for Glycogenolysis in Skeletal Muscle., *Ann. Biomed. Eng.* 30:808–827, 2002

90 **Dash RK, Li Y, Kim J, Beard DA, Saidel GM and Cabrera ME.**, Metabolic dynamics in skeletal muscle during acute reduction in blood flow and oxygen supply to mitochondria: in-silico studies using a multi-scale, top-down integrated model., *Plos. One* 3:e3168, 2008

91 **Selivanov VA, de Atauri P, Centelles JJ, Cadefau J, Parra J, Cuss oR, Carreras J and Cascante M.**, The changes in the energy metabolism of human muscle induced by training., *J. Theor. Biol.* 252:402–410, 2008

92 **Schmitz JPJ, van Riel NAW, Nicolay K, Hilbers PAJ and Jeneson JAL.**, Silencing of glycolysis in muscle: experimental observation and numerical analysis., *Exp. Physiol.* 95:380-397, 2010

93 **Lambeth MJ, Kushmerick MJ, Marcinek DJ and Conley KE.**, Basal glycogenolysis in mouse skeletal muscle: in vitro model predicts in vivo fluxes., *Mol. Biol. Rep.* 29:135-139, 2002

94 **Parra J, Cadefau JA, Rodas G, Amigo N and Cusso R.**, The distribution of rest periods affects performance and adaptations of energy metabolism induced by high-intensity training in human muscle., *Acta Physiol. Scand.* 169:157–165, 2000

95 **Rozendaal YJW, Wang Y, Paalvast Y, Tambyrajah LL, Li Z, Willems van Dijk K, Rensen PCN, Kuivenhoven JA, Groen AK, Hilbers PAJ and van Riel NAW.**, *in vivo* and *in silico* dynamics of the development of metabolic syndrome., *PLoS. Comput. Biol.* 14:e1006145, 2018

96 **Rozendaal YJW, Wang Y, Hilbers PAJ and van Riel NAW.**, Computational modelling of energy balance in individuals with metabolic syndrome., *MBC Syst. Biol.* 13:24, 2019

97 **Eckel RH, Grundy SM and Zimmet PZ.**, The metabolic syndrome., *Lancet.* 365:1415-1428, 2005

98 **Lillioja, S, Young A, Cutler C, Ivy JL, Abbott WG, Zawadzki JK, Yki-Jarvinen H, Christin L, Secomb TW and Bogardus C.**, Skeletal muscle capillary density, and fibre type are possible determinants of in vivo resistance in man., *J. Clin. Invest.* 80:415–424, 1987

99 **Papa S.**, Mitochondrial oxidative phosphorylation changes in the life span. Molecular aspects and physiological implications., *Biochim. Biophys. Acta.* 1276:87–105, 1996

100 **Simoneau JA, Colberg SR, Thaete FL and Kelley DE.**, Skeletal muscle glycolytic and oxidative enzyme capacities are determinants of insulin sensitivity and muscle composition in obese women., *Faseb. J.* 9:273–278, 1995

101 **Simoneau JA and Kelley DE.**, Altered glycolytic and oxidative capacities of skeletal muscle contribute to insulin resistance in NIDDM., *J. Appl. Physiol.* 83:166–171, 1997

102 **Cline GW, Petersen KF, Krssak M, Shen J, Hundal RS, Trajanoski Z, Inzucchi S, Dresner A, Rothman DL and Shulman GI.**, Impaired glucose transport as a cause of decreased insulin-stimulated muscle glycogen synthesis in type 2 diabetes., *N. Engl. J. Med.* 341:240–246, 1999

103 **Rothman DL, Magnusson I, Cline G, Gerard D, Kahn CR, Shulman RG and Shulman GI.**, Decreased muscle glucose transport/phosphorylation is an early defect in the pathogenesis of non-insulin-dependent diabetes mellitus., *Proc. Natl. Acad. Sci. USA* 92:983–987, 1995

104 **Schalin-Jantti C, Harkonen M and Groop LC.**, Impaired activation of glycogen synthase in people at increased risk for developing NIDDM., *Diabetes* 41:598–604, 1992

105 **Vaag A, Henriksen JE and Beck-Nielsen H.**, Decreased insulin activation of glycogen synthase in skeletal muscles in young nonobese Caucasian first-degree relatives of patients with non-insulin-dependent diabetes mellitus., *J. Clin. Invest.* 89:782–788, 1992

106 **Kim JK, Wi JK and Youn JH.**, Metabolic impairment precedes insulin resistance in skeletal muscle during high fat feeding in rats., *Diabetes* 45:651–658, 1996

107 **Kim JK and Youn JH.**, Prolonged suppression of glucose metabolism causes insulin resistance in rat skeletal muscle., *Am. J. Physiol. Endocrinol. Metab.* 272:E288–E296, 1997

108 **Kim JK, Choi CS and Youn JH.**, Acute effect of growth hormone to induce peripheral insulin resistance is independent of FFA and insulin levels in rats., *Am. J. Physiol. Endocrinol. Metab.* 277:E742–E749, 1999

109 **Choi SC, Kim Y, Lee FN, Zabolotny JM, Kahn BB and Youn JH.**, Lactate induces insulin resistance in skeletal muscle by suppressing glycolysis and impairing insulin signalling., *Am. J. Physiol. Endocrinol. Metab.* 283:E233–E240, 2002

110 **Lombardi AM, Fabris R, Bassetto F, Serra R, Leturque A, Federspil G, Girard J and Vettor R.**, Hyperlactatemia reduces muscle glucose uptake and GLUT-4 mRNA while increasing (E1)PDH gene expression in rat., *Am. J. Physiol. Endocrinol. Metab.* 276:E922–E929, 1999

111 **Ristow M, Vorgerd M, Mohlig M, Schatz H and Pfeiffer A.**, Deficiency of phosphofructo-1-kinase/muscle subtype in humans impairs insulin secretion and causes insulin resistance., *J. Clin. Invest.* 100:2833–2841, 1997

112 **Ristow M, Vorgerd M, Mohlig M, Schatz H and Pfeiffer A.**, Insulin resistance and impaired insulin secretion due to phosphofructo-1-kinase-deficiency in humans., *J. Mol. Med.* 77:96–103, 1999

113 **Smuts, Jan Christiaan.**, Holism and Evolution 2nd Edition. Macmillan and Co. (1927)

114 **Goodacre R, Vaidyanathan S, Dunn WB, Harrigan GG and Kell DB.**, Metabolomics by numbers: acquiring and understanding global metabolite data., *Trends Biotechnol.* 22:245–252, 2004

115 **Ihmels JH and Bergmann S.**, Challenges and prospects in the analysis of large-scale gene expression data., *Brief. Bioinform.* 5:313–327, 2004

116 **Taylor CF, Patton NW, Garwood KL, Kirby PD, Stead DA, Yin Z, Deutsch EW, Selway L, Walker J, Riba-Garcia I, Mohammed S, Deery MJ, Howard JA, Dunkley T, Aebersold R, Kell DB, Lilley KS, Roepstorff P, Yates JR, Brass A, Brown AJP, Cash P, Gaskell SJ, Hubbard SJ and Oliver SG.**, A systematic approach to modeling, capturing, and disseminating proteomics experimental data., *Nat. Biotechnol.* 21:247–254, 2003

117 **Eisen MB, Spellman PT, Brown PO and Botstein D.**, Cluster analysis and display of genome-wide expression patterns., *Proc. Natl. Acad. Sci. USA* 95:14863–14868, 1998

118 **Tanay A, Sharan R, Kupiec M and Shamir R.**, Revealing modularity and organization in the yeast molecular network by integrated analysis of highly heterogeneous genome wide data., *Proc. Natl. Acad. Sci. USA* 101:2981–2986, 2004

119 **Beyer A, Workman C, Hollunder J, Radke D, Möller U, Wilhelm T and Ideker T.**, Integrated assessment and prediction of transcription factor binding., *Plos. Comput. Biol.* 2:e70, 2006

120 **Selinger DW, Wright MA and Church GM.**, On the complete determination of biological systems., *Trends Biotechnol*. 21:251–254, 2003

121 **Bruggeman FJ and Westerhoff HV.**, The nature of systems biology., *Trends Microbiol.* 15:45–50, 2006

122 **Snoep JL.**, The Silicon Cell initiative: working towards a detailed kinetic description at the cellular level., *Curr. Opin. Biotechnol*. 16:336–343, 2005

123 **Westerhoff HV.**, The silicon cell, not dead but live!, *Metab. Eng.* 3:207–210, 2001

124 **Le Novère N, Bornstein B, Broicher A, Courtot M, Donizelli M, Dharuri H, Li L, Sauro H, Schilstra M, Shapiro B, Snoep J.L and Hucka M.**, BioModels Database: A free, centralized database of curated, published, quantitative kinetic models of biochemical and cellular systems., *Nucleic. Acids. Res*. 34:D689-D691, 2006

125 **Snoep JL and Olivier BG.**, Java web simulation (JWS); a web based database of kinetic models., *Mol. Biol. Rep*. 29:259-263, 2002

126 **Penkler G, du Toit F, Adams W, Rautenbach M, Palm DC, van Niekerk DD and Snoep JL.**, Construction and validation of a detailed kinetic model of glycolysis in *Plasmodium falciparum*., FEBS. 282:1481-1511, 2015

127 **Bakker BM, Michels PAM, Opperdoes FR and Westerhoff HV.**, Glycolysis in bloodstream form *Trypanosoma brucei* can be understood in terms of the kinetics of the glycolytic enzymes., *J. Biol. Chem*. 272:3207-3215, 1997

128 **Bakker BM, Michels PAM, Opperdoes FR and Westerhoff HV.**, What controls glycolysis in bloodstream form *Trypanosoma brucei?, J. Biol. Chem.* 274:14551-14559, 1999

129 **Alberts M, Haanstra JR, Hannaert V, van Roy J, Opperdoes FR, Bakker BM and Michels PAM.**, Experimental and in silico analysis of glycolytic flux control in bloodstream form *Trypanosoma brucei*., *J. Biol. Chem.* 280:28306-28315, 2005

130 **Nielsen J.**, It is all about metabolic fluxes., *J Bacteriol*. 185:7031–7035, 2003

131 **Krömer JO, Sorgenfrei O, Klopprogge K, Heinzle E and Wittmann C.**, In-depth profiling of lysine-producing Corynebacterium glutamicum by combined analysis of the transcriptome, metabolome, and fluxome., *J. Bacteriol*. 186:1769–1784, 2004

132 **Kacser H and Burns JA.**, The control of flux., *Symp. Soc. Exp. Biol*. 27:65-104, 1973

133 **Heinrich R and Rapoport TA.**, A linear steady-state treatment of enzymatic chains: general properties, control and effector strength., *Eur. J. Biochem*. 42:89-95, 1974

134 **Cascante M, Boros LG, Comin-Anduix B, de Atauri P, Centelles JJ and Lee PWN.**, Metabolic control analysis in drug discovery and disease., *Nat. Biotechnol*. 20:243-249, 2002

135 **Venter JC, Adams MD, Myers EW, Li PW, Mural RJ, Sutton GG, Smith HO, Yandell M, Evans CA, Holt RA, Gocayne JD, Amanatides P, Ballew RM, Huson DH, Wortman JR, Zhang Q, Kodira CD, Zheng XH, Chen L, Skupski M, Subramanian G, Thomas PD, Zhang J, Gabor Miklos GL, Nelson C, Broder S, Clark AG, Nadeau J, McKusick VA, Zinder N, Levine AJ, Roberts RJ, Simon M, Slyman C, Hunkapiller M, Bolanos R, Delcher A, Dew I, Fasulo D, Flanigan M, Floreaq L, Halpern A, Hannenhalli S, Kravitz S, Levy S, Mobarry C, Reinert K, Remington K, Abu-Threideh J, Beasley E, Biddick K, Bonnazi V, Brandon R, Cargill M, Chandramouliswaran I, Charlab R, Chaturvedi K, Deng Z, Di Francesco V, Dunn P, Eilbeck K, Evangelista C, Gabrielian AE, Gan W, Ge W, Gong F, Gu Z, Guan P, Heiman TJ, Higgins ME, Ji R, Ke Z, Ketchum KA, Lai Z, Lei Y, Li Z, Li J, Liang Y, Lin X, Lu F, Merkulov GV, Milshina M, Moore HM, Naik AK, Narayan VA, Neelam B, Nusskern D, Rusch DB, Salzberg S, Shao W, Shue B, Sun J, Wang ZY, Wang A, Wang X, Wang J, Wei M, Wides R, Xiao C, Yan C, Yao A, Ye J, Zhan M, Zhang W, Zhang H, Zhao Q, Zheng L, Zhong F, Zhong W, Zhu SC, Zhao S, Gilbert D, Baumhueter S, Spier G, Carter C, Cravchik A, Woodage T, Ali F, An H, Awe A, Baldwin D, Baden H, Barnstead M, Barrow I, Beeson K, Busam D, Carven A, Center A, Cheng LM, Curry L, Danaher S, Davenport L, Desilets R, Dietz S, Dodson K, Doup L, Ferriera S, Garg N, Hostin D, Houck J, Howland T, Ibegwan C, Johnson J, Kalush F, Kline L, Koduru S, Love A, Mann F, May D, McCawley S, McIntosh T, McMullen I, Moy M, Moy L, Murphy B, Nelson K, Pfannkoch C, Pratts E, Puri V, Qureshi H, Reardon M, Rodriguez R, Rogers Y, Romblad D, Ruhfel B, Scott R, Sitter C, Smallwood M, Steward E, Strong R, Suh E, Thomas R, Tint N, Tse S, Vech C, Wang G, Wetter J, Williams S, Williams M, Windsor S, Winn-Deen E, Wolfe K, Zaveri J, Zaveri K, Abril JF, Guigo R, Campbell MJ, Sjolander KV, Karlak B, Kejariwal A, Mi H, Lazareva B, Hatton T, Narechania A, Diemer K, Muruganujan A, Guo N, Sato S, Bafna V, Istrail S, Lippert R, Schwartz R, Walenz B, Yooseph S, Allen D, Basu A, Baxendale J, Blick L, Caminha M, Carnes-Stine J, Caulk P, Chiang Y, Coyne M, Fosler C, Gire H, Glanowski S, Glasser K, Glodek A, Gorokhov M, Graham K, Gropman B, Harris M, Heil J, Henderson S, Hoover J, Jennings G, Jordan C, Jordan J, Kasha J, Kagan L, Kraft C, Levitsky A, Lewis M, Liu X, Lopez J, Ma D, Majoros W, McDaniel J, Murphy S, Newman M, Nguyen N, Nodell M, Pan S, Peck J, Peterson M, Rowe W, Sanders R, Scott J, Simpson M, Smith T, Sprague A, Stockwell T, Turner R, Venter E, Wang M, Wen M, Wu D, Wu M, Xia A, Zandieh A and Zhu X.**, The sequence of the human genome., *Science* 291:1304-1351, 2001

136 **Goodacre R, Vaidyanathan S, Dunn WB, Harrigan GG and Kell DB.**, Metabolomics by numbers: acquiring and understanding global metabolite data., *Trends. Biotechnol*. 22:245-252, 2004

137 **Schaub J and Reuss M.**, In Vivo Dynamics of Glycolysis in Escherichia coli Shows Need for Growth-Rate Dependent Metabolome Analysis., *Biotechnol. Prog*. 24:1402-1406, 2008

138 **Shoemaker DD and Linsley PS.**, Recent developments in DNA microarrays., *Curr. Opin. Microbiol*. 5:334–337, 2002

139 **Tong AH, Evangelista M, Parsons AB, Xu H, Bader GD, Page N, Robinson M, Raghibizadeh S, Hogue CWV, Bussey H, Andrews B, Tyers M and Boone C.**, Systematic genetic analysis with ordered arrays of yeast deletion mutants., *Science* 294:2364-2368, 2001

140 **Tyers M and Mann M.**, From genomics to proteomics., *Nature* 422:193-197, 2003

141 **Fiehn, O.**, Metabolomics – the link between genotypes and phenotypes., *Plant. Mol. Biol*. 48:155–171, 2002

142 **Dunn WB, Broadhurst DI, Atherton HJ, Goodacre R and Griffin JL.**, Systems level studies of mammalian metabolomes: the roles of mass spectrometry and nuclear magnetic resonance spectroscopy., *Chem. Soc. Rev*. 40:387-426, 2011

143 **Urbanczyk-Wochniak E, Luedemann A, Kopka J, Selbig J, Roessner-Tunali U, Willmitzer L and Fernie AR.**, Parallel analysis of transcript and metabolic profiles: a new approach in system biology., *EMBO Rep*. 4:989–993, 2003

144 **Oliver SG, Winson MK, Kell DB and Baganz F.**, systematic functional analysis of the yeast genome., *Trends Biotechnol.* 16:373–378, 1998

145 **Mattivi F, Guzzon R, Vrhovsek U, Stefanini M and Velasco R.**, Metabolite profiling in grapes: flavonols and anthocyanins., *J. Agric. Food. Chem*. 54:7692-7702, 2006

146 **Lisec J, Schauer N, Kopka J, Willmitzer J and Fernie AR.**, Gas-chromatography mass spectrometry-based metabolic profiling in plants., *Nat. Protoc.* 1:387-396, 2006

147 **Sabatine MS, Liu E, Morrow DA, Heller E, McCarroll R, Wiegand R, Berriz GF, Roth FP and Gerszten RE.**, Metabolomic identification of novel biomarkers of myocardial ischemia., *Circulation* 112:3868-3875, 2005

Chapter 3

Development of an ion pairing reverse phase liquid chromatography method for the quantification of glycolytic intermediates and cofactors.

3.1 Preamble

To validate the glycolytic model that was constructed in this study we needed a method to dynamically follow glycolytic intermediates. Here we present how that method was developed.

3.2 Introduction

The need for analytical methods to quantify the concentrations of intracellular and extracellular metabolites of living organisms is becoming more apparent as advances in our detailed understanding of metabolic processes in biological systems increase[1]. Analytical approaches in the fields of genomics, transcriptomics and proteomics have become important tools for understanding and quantifying the regulation of biological systems, but a similar approach to metabolomics has remained problematic. Due to the chemical complexity and heterogeneity of the metabolites present in a biological sample, it is impossible to develop a simple automated analytical strategy to quantify all the possible metabolites in such a sample[2].

Metabolome analysis allows for direct access to the metabolic phenotype expressed under specific environmental conditions and therefore, reflect the outcome of cellular regulatory processes present at different levels of expression, *e.g.* at the transcriptional or translational level[3 - 5]. This has significant value to molecular systems biology as knowledge of intracellular metabolite concentrations enables identification of potential metabolic bottlenecks and provides the basis for a quantitative understanding of intracellular reaction rates and the control of metabolic fluxes[6]. The ability of utilizing a metabolomic approach in tandem with dynamic metabolic models allows for the identification and elucidation of new metabolic pathways and a better understanding of the metabolic regulation of new and existing metabolic pathways[7,8].

Targeted studies focussed on the quantification of specific metabolites in a metabolic pathway, such as glycolysis, are also of interest for the validation of metabolic models. The ability to compare model predictions to experimentally obtained metabolite concentrations increases confidence in the use of such models. Various approaches attempting to analyse

multiple metabolites simultaneously have been published including thin-layer chromatography[9,10], nuclear magnetic resonance spectroscopy[11 - 13], capillary electrophoreses tandem mass spectrometry (MS)[14] and high-performance liquid chromatography (LC) with various modes of detection[15 - 19]. An extensive analysis of LC-MS approaches to metabolomics conducted by Bajad *et. al.*[20] found that ionic interactions on the column are required to obtain sufficient separation of water-soluble cellular metabolites[21]. Among their trails, amino-column based separations in HILIC mode performed best whereas C-18 reverse phase separations showed little to no separation efficiency. However, with the aid of an ion-pairing agent, the separation efficiency of C-18 reverse phase columns are greatly improved. Lu *et. al.*[22] developed a reverse phase LC method, assisted with tributylamine as ion pairing agent, followed by the stand-alone analysis via orbitrap mass spectrometry for the separation of water-soluble species involved in the core metabolism of Baker's yeast, including several of the glycolytic species of interest to this study.

Within the field of metabolomics, NMR and MS has become the methods of choice. This is in part, due to the uniform detection obtained for a specific NMR active nucleus, regardless of chemical structure[5]. However, poor sensitivity is a drawback to using NMR. In contrast, MS offers high sensitivity to select classes of analytes, but the technique is prone to matrix effects[2]. Both techniques mentioned above have their advantages for screening large amounts of metabolites, but alternative methods of detection exist for targeted studies. Radio-isotope detection offers high sensitivity to labelled metabolites with no interference from matrix effects and makes a good alternative technique for targeted metabolomic studies. The metabolism of montelukast, a potent cysteinyl leukotreine$_1$ receptor antagonist, was investigated using a RPLC- radioactivity detector to analyse human bile[23].

In this chapter we present a new method for the quantitative detection of glycolytic intermediates and cofactors. A novel ion-pairing reverse phase LC (IP-RPLC) method with UV-Vis and radio-labelled detection was developed for targeted metabolomic studies of glycolytic intermediates and tested in yeast extract. This method offers the advantages of robustness from RPLC analysis with the high sensitivity and limited matrix interference from radio-isotope detection.

3.3 Materials and Methods

3.3.1. Materials

Water used for the preparation of mobile phases was prepared via reverse osmosis filtration. HPLC grade acetonitrile was obtained from *Romil*. Tetrabutylammonium (TBA) bisulfate, formic acid, metabolites, purified enzymes and all additional media components were sourced from *Sigma-Aldrich*. ^{14}C- glucose, ^{14}C-pyruvate and ^{14}C-glycerol was obtained from *American Radiolabelled Chemicals Inc. (ARC)*.

3.3.2. HPLC instrumentation and methodology

All chromatographic analysis was performed on a *SpectraSYSTEM* HPLC setup containing the following instrumental components; *SpectraSYSTEM* P4000 pump with low pressure mixing of the mobile phase reservoirs, *SpectraSYSTEM* AS3000 Autosampler, connected to a *SpectraSYSTEM* UV6000LP UV-Vis detector followed by a *LabLogic* β-RAM model 5 radio-labelled detector. A reverse phase Phenomenex Luna C_{18} column (5 µm) was used for all chromatographic separations.

The ion-pairing RPLC (IP-RPLC) method was optimized through a trial and error approach. The mobile phase composition is as follow: Solvent A is 25 mM TBA in water adjusted to a pH of 7.3 (± 0.1); Solvent B is 97.5% Acetonitrile and 2.5% water; Solvent C is 0.1% formic acid in water and was used for a routine wash after every set of samples. The total run time is 20 min at a flow rate of 1 mL/ min. A gradient is employed to expedite the analysis by lowering the retention of the late eluting chemical species. The gradient is as follow: at 0 - 4.5 min 95% A and 5% B; 5 - 12 min 70% A and 30% B; 13 - 20 min 95% A and 5% B. UV-Vis detection of the column effluent was measured at 254 nm. The radiolabelled detector is set to start at a runtime of 1 min and is terminated at a runtime of 13 min. Scintillation fluid is mixed with the column effluent in a 3:1 ratio.

3.3.3. Quantification of the glycolytic intermediates via IP-RPLC-radiolabelled detection.

The retention times of the glycolytic intermediates were determined by radiolabelled detection of the IP-RPLC eluent. Radiolabelled measurement was initialised 1 min after injection. Therefore, the radiolabelled chromatographic traces have a 1 min offset in comparison to the UV/Vis chromatographic traces. The ^{14}C-labeled glycolytic intermediates

were synthesised from ^{14}C-glucose (^{14}C-GLC), ^{14}C-glycerol (^{14}C-GLY) and ^{14}C-pyruvate (^{14}C-PYR) through a series of enzymatic reactions. The stepwise conversion of the ^{14}C-labeled starting materials allowed for the synthesis of all required glycolytic intermediates, with the exception of bisphosphoglycerate (BPG). The synthesised ^{14}C-labelled glycolytic intermediates were separated via IP-RPLC analysis and detected with the radiolabelled detector connected to the column. The resulting chromatographic traces were integrated to determine the relative concentrations of the metabolites associated with the peaks present in each of the chromatographic traces.

Integration of the chromatographic traces were done via an in-house developed script in *Wolfram Mathematica*. Tailing of the peaks were present in the chromatographic traces and as a result the peaks were described by skewed normal distribution functions, rather than normal- or gaussian distribution functions. The function describing the probability density of a skewed normal distribution, which represents an estimation of the area under the peak, is given in Eq. 3.1 and Eq. 3.2 and includes a shape parameter that relates to the slant of the peak. Each peak obtained in the chromatographic trace was described by 1 or more skewed normal distribution functions. In the case where more than 1 skewed normal distribution was required, the function was described as the summation of multiple skewed normal distribution functions with independent parameters for each skewed normal distribution function.

$$\text{Probability density (x)} = \left(1 + \text{erf}\left(\frac{\alpha(\text{x} - \mu)}{\sqrt{2} \cdot \sigma}\right)\right) \cdot e^{\left(-\frac{(\text{x}-\mu)^2}{2\sigma^2}\right)} \qquad \text{(Eq. 3.1)}$$

$$\text{erf(z)} = \frac{2}{\sqrt{\pi}} \int_0^{\text{z}} e^{-\text{t}^2}\, dt \qquad \text{(Eq. 3.2)}$$

The function for a skewed normal distribution described in Eq. 3.1 and Eq. 3.2 determines the probability density (x), for an optimised set of parameters. The following parameters dictate the description of the skewed normal distribution:

μ - represents the retention time of the peak.

σ - represents the scale parameter or standard deviation of the peak.

α - represents the shape parameter or slant of the peak.

t – dictates the retention time boundaries of the peak.

The *Nonlinearmodelfit* function of *Wolfram Mathematica* was used to fit skewed normal distribution functions to the chromatographic traces by optimising the parameters (μ, σ, α) over the defined retention time range. In the majority of cases, the retention time had to be constrained to obtain an accurate description of the peaks in the chromatographic trace. Integration of the skewed normal distribution functions yielded the area corresponding to each metabolite.

3.3.4. Quantification of the adenosine and nicotinamide metabolites via IP-RPLC-UV/Vis detection.

Calibration standards of the metabolites ATP, ADP, AMP, NAD^+ and NADH were prepared by dissolving 1 mM of each of the metabolites in a 100 mM phosphate buffer. A dilution series over the range of 1 mM – 0.05 mM was prepared and analysed via the IP-RPLC method. The chromatographic traces obtained for the adenosine and nicotinamide calibration standards were integrated using the *ChromSolve* integration software associated with the HPLC analysis software package. Calibration curves for each of the adenosine and nicotinamide moieties were constructed from the integration of the chromatographic traces obtained from the calibration standards. The areas under each peak obtained for the calibration standards were plotted against the corresponding known concentration of each adenosine and nicotinamide metabolite yielding a calibration curve for each chemical species over the range of 1 mM – 0.05 mM.

The limit of detection (LOD) and limit of quantification (LOQ) of the adenosine and nicotinamide metabolites were determined from the standard error (SE) of the intercept by using Eq. 3.3 – 3.5, where *N* refers to the amount of readings used for the construction of each calibration curve (*N* = 6). The linear calibration curves were used to determine the unknown concentrations of the adenosine and nicotinamide moieties in the biological samples using Eq. 3.6.

$$\text{Standard deviation (SD) of intercept} = \text{SE of intercept} \times \sqrt{N} \qquad \text{(Eq. 3.3)}$$

$$\text{LOD} = 3.3 \times \left(\frac{\text{SD of intercept}}{\text{Gradient}}\right) \qquad \text{(Eq. 3.4)}$$

$$\text{LOQ} = 10 \times \left(\frac{\text{SD of intercept}}{\text{Gradient}}\right) \qquad \text{(Eq. 3.5)}$$

$$\text{Concentration} = \frac{(\text{Peak area} - \text{intercept})}{\text{gradient}} \qquad \text{(Eq. 3.6)}$$

3.3.5. Quantification of the total GLC concentration in the ^{14}C-GLC starting material.

To determine the GLC concentration present in the ^{14}C-starting material, a GLC calibration curve was constructed. Standards containing unlabelled GLC at concentrations of 1 mM, 0.5 mM, 0.25 mM, 0.125mM and 0mM were prepared and treated with HK and G6PDH in the presence of excess ATP and NAD^+. In the presence of HK and G6PDH, GLC is converted to phosphor-D-glucono-1,5-lactone (PGL) with the corresponding conversion of NAD^+ to NADH at a stoichiometric ratio of 1:1. The NADH was visualised spectrophotometrically at 340 nm, resulting in a linear relationship between the concentration of the GLC standards and the absorbance at 340 nm as shown in Figure 3.1.

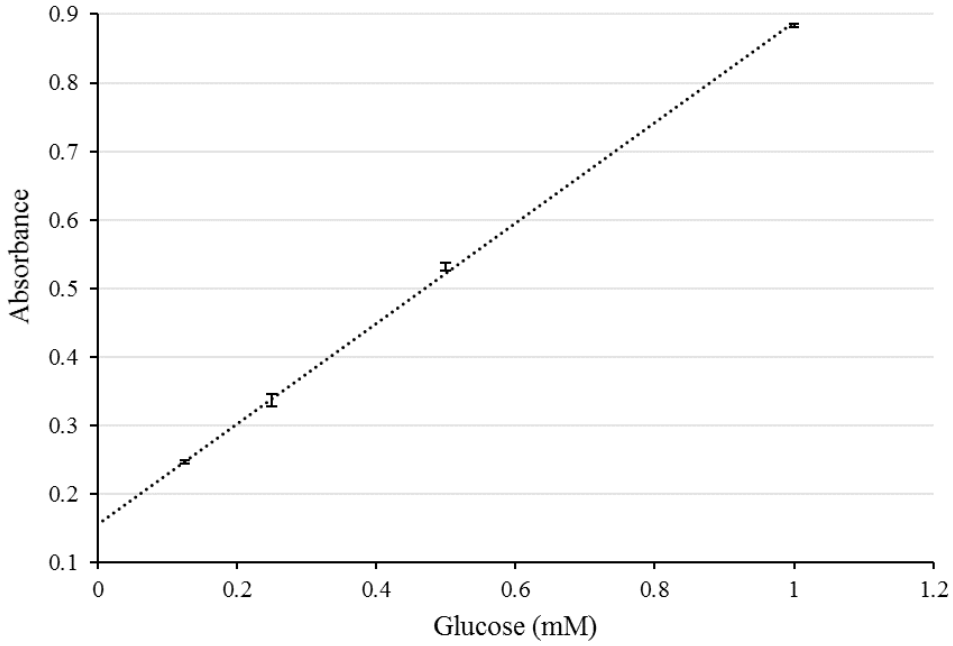

Figure 3.1: *Plot of GLC standards vs. absorbance The calibration curve constructed for the quantification of GLC in unknown samples. The calibration curve was constructed by treating GLC samples of known concentrations with HK and G6PDH in the presence of excess ATP and NAD^+ and measuring the absorbance at 340 nm. (Gradient = 0.735, Intercept = 0.154, r^2 = 0.9996)*

The dilution samples prepared from the ^{14}C-GLC stock solution were treated with HK and G6PDH in the presence of excess ATP and NAD^+ and the absorbance was measured at 340 nm via UV-Vis spectroscopy. The total concentration of GLC present in the ^{14}C-GLC starting

material was determined by relating the measured absorbance to concentration using the calibration curve constructed for GLC in Figure 3.1.

3.3.6. Preparation of yeast extract and quantification of the glycolytic intermediates via enzyme coupled assays.

Yeast strain X2180 was cultured under aerobic conditions in a gyratory shaker at 30ºC in a yeast nitrogen base. Growth was monitored by measuring the optical density at 600 nm to ensure that growth is in the log phase. The yeast culture was harvested in the log growth phase and pelleted via centrifugation. Yeast lysate was prepared via glass bead extraction. Lysis was performed by resuspending the yeast cells and vortexing the cell suspension, in the presence of 100mg glass beads/ 1 ml of cell suspension, for 1 minute followed by resting the suspension on ice for 15 seconds and repeating this cycle 6 times. The cell solution was then centrifuged at 20 800 x *g* at 4ºC for 15 minutes to pellet the cell debris. After centrifugation the supernatant was removed and stored on ice.

The concentrations of ATP, DHAP and FBP were determined via enzyme coupled assays to compare to concentrations obtained via the novel IP-RPLC technique. For DHAP determination, time course samples were treated with G3PDH in the presence of excess NAD^+ for the conversion of DHAP to G3P associated with the conversion of NAD^+ to NADH. The concentration of DHAP was determined by measuring the amount of NADH formed by UV-Vis spectroscopy at 340 nm. For FBP determination, samples were treated with ALD in the presence of excess NAD^+ after conversion of DHAP to G3P. The concentration of FBP was quantified by measuring the further increase in NADH concentration, considering the NADH resulting from the DHAP. The concentration of ATP was determined via coupled assay technique by treating samples with commercially obtained HK and G6PDH in the presence of excess GLC and $NADP^+$. The conversion of ATP to ADP via HK is equivalent to the conversion of $NADP^+$ to NADPH and the ATP concentration was determined from the increased absorbance as a result of NADPH production.

3.4 Results

3.4.1. IP-RPLC separation and quantification of the adenosine and nicotinamide metabolites via UV-Vis detection

To determine the retention times of the adenosine and nicotinamide moieties, commercially available ATP, ADP, AMP, NAD^+ and NADH salts were analysed via IP-RPLC separation in tandem with UV-Vis detection. A series of samples, each containing a single adenosine or nicotinamide compound, were injected onto the column. To match the sample preparation protocol used for the biological samples, 50 µL samples for each of the adenosine and nicotinamide standards were collected and treated with 7.5 µL of a 50% PCA solution, followed by neutralisation with 42.5 µL of a 1 M K_2CO_3 solution. IP-RPLC analysis of the standards resulted in a chromatographic trace corresponding to the specific compound in each standard. The chromatographic traces for ATP, ADP, AMP and NAD^+ resulted in a single peak corresponding to that species. However, the chromatographic trace for NADH resulted in 3 related peaks. NADH is known to degrade in acidic solutions to form related UV-Vis active chemical species and we suspect that the 3 peaks observed for NADH arise from the acid-degradation of NADH[24,25]. Therefore, the area under the 3 peaks corresponding to NADH was summed to give the chromatographic signal for NADH. The retention times of the adenosine and nicotinamide moieties are listed in Table 3.1.

Calibration curves for the quantification of the adenosine and nicotinamide moieties were constructed. Standards of the adenosine and nicotinamide moieties were made by preparing samples containing 1 mM, 0.75 mM, 0.5 mM, 0.25 mM, 0.1 mM and 0.05 mM of each of the 5 chemical species. The calibration standards were treated with PCA and neutralised with K_2CO_3 prior to IP-RPLC analysis. 10 µl of each standard was injected onto the column and the resulting chromatographic traces obtained for the IP-RPLC analysis of the calibration standards are illustrated in Figure 3.2 and calibration curves are illustrated in Figure 3.3.

***Table 3.1**: Summary of the retention times of the adenosine and nicotinamide moieties as separated by the IP-RPLC method developed here and quantified via UV-Vis detection.*

Retention Times	
Chemical Species	Retention Time (seconds)
NAD^+	199
NADH (1)	440
NADH (2)	454
NADH (3)	476
AMP	375
ADP	521
ATP	712

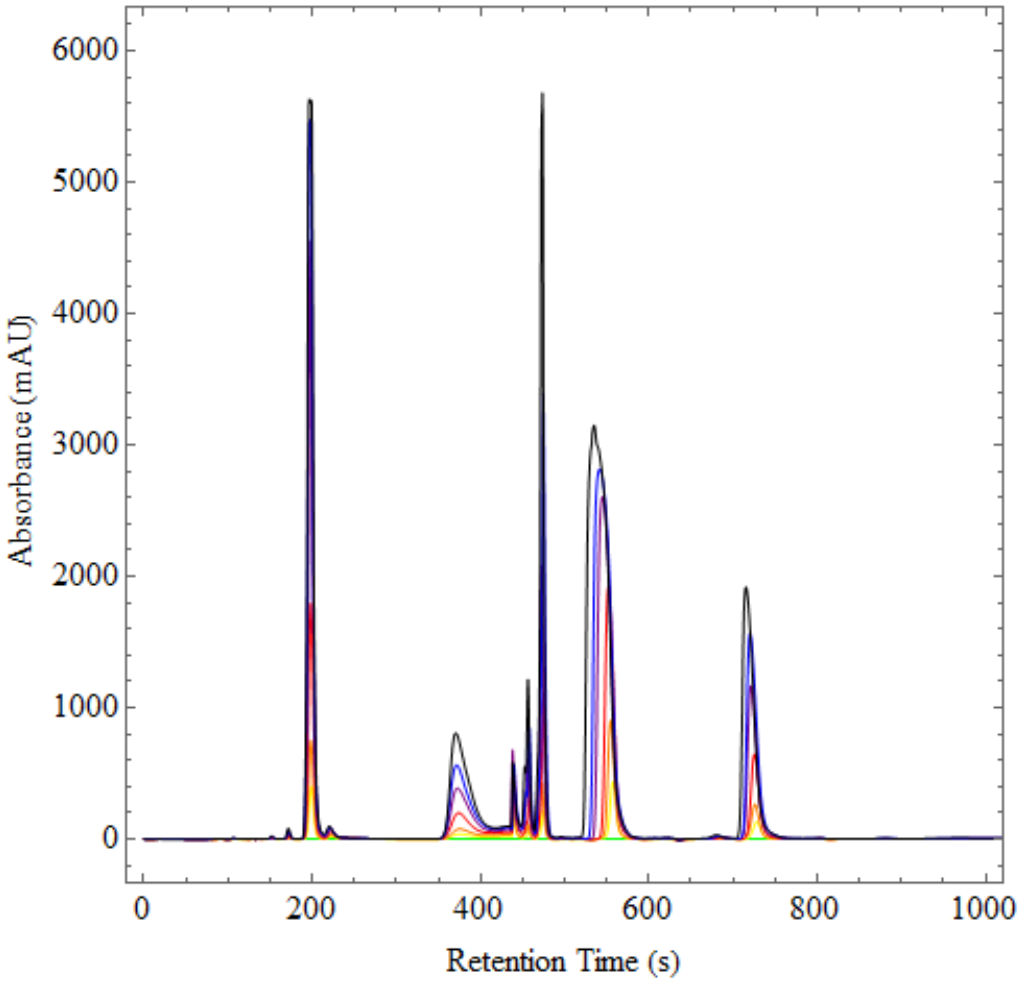

***Figure 3.2**: Chromatographic traces of the adenosine and nicotine moieties obtained from the IP-RPLC analysis of the calibration standards via UV-Vis detection at 254 nm. Standards containing 1.0 mM (Black), 0.75 mM (Blue), 0.5 mM (Purple), 0.25 mM (Red), 0.1 mM (Orange) and 0.05 mM (Green) of each of the adenosine and nicotinamide moieties were prepared and injected into the column.*

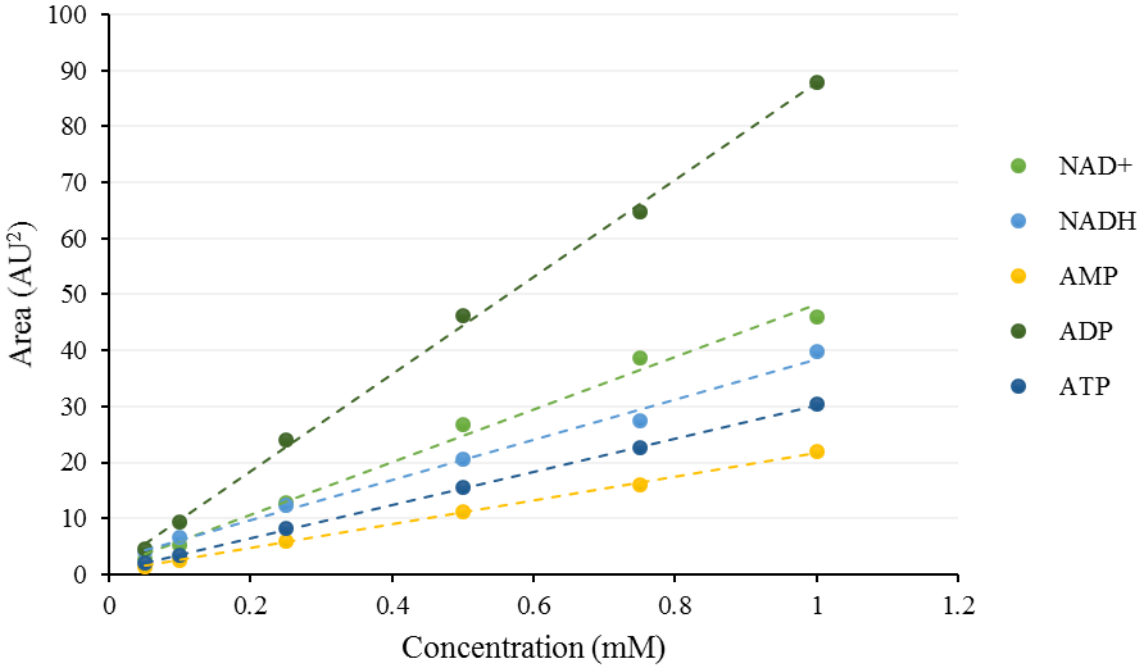

***Figure 3.3**: Calibration curves for each of the adenosine and nicotinamide moieties constructed from prepared standards at known concentrations of 1.0 mM, 0.75 mM, 0.5 mM, 0.25 mM, 0.1 mM and 0.05 mM of each of the species. Areas were obtained by integrating the chromatographic traces measured via UV-Vis detection at 254 nm and plotting the resulting area against the corresponding known concentration of each chemical species.*

A linear relationship between the measured areas and concentrations of each adenosine and nicotinamide moiety described the calibration data well ($r^2 > 0.99$). The resulting gradient and intercept of each calibration curve describes the relationship between peak area and concentration for each of the corresponding adenosine and nicotinamide moiety. The LOD and LOQ for each of the adenosine and nicotinamide metabolites were determined as described in Section 3.3.4. The values for the description of the calibration function (gradient and intercept) and the LOD and LOQ calculated for each of the adenosine and nicotinamide moiety are reported in Table 3.2.

***Table 3.2**: Description of the calibration curves used for quantification of the unknown concentrations of the adenosine and nicotinamide moieties. The tabulated gradient and intercept values describe the relationship between peak area and concentration for each of the species. The LOD and LOQ values were determined for each of the adenosine and nicotinamide moieties.*

Species	Gradient	Intercept	r^2	LOD (mM)	LOQ (mM)
NAD^+	47069.36	1268.82	0.9902	0.225	0.683
NADH	35752.62	2653.08	0.9929	0.192	0.582
ATP	29689.95	606.68	0.9998	0.062	0.187
ADP	86660.53	1209.04	0.9986	0.084	0.255
AMP	21383.56	421.91	0.9993	0.030	0.091

3.4.2. IP-RPC separation of the glycolytic intermediates prepared from ^{14}C-Glucose for the determination of retention times

A sample containing ^{14}C-GLC and an excess amount of ATP was prepared for the stepwise synthesis of the ^{14}C-labeled glycolytic intermediates as illustrated in Figure 3.4. IP-RPLC analysis of the sample containing ^{14}C-GLC resulted in a chromatographic trace with a peak at 38 second, corresponding to GLC, along with a peak at 90 seconds suspected to be an impurity present in the commercially obtained ^{14}C-GLC stock solution. The peak at a retention time of 38 seconds is close to the dead time of the column and shows that GLC is not retained by the IP-RPLC separation method. HK was added to the sample to convert the ^{14}C-GLC to ^{14}C-G6P and injected onto the column. This resulted in a peak at a retention time of 157 seconds that we assigned to be G6P. The sample was subsequently treated with PGI to convert the ^{14}C-G6P to ^{14}C-F6P. IP-RPLC analysis of a representative sample showed incomplete conversion of ^{14}C-G6P to ^{14}C-F6P, with the emergence of a peak at a retention time of 182 seconds corresponding to F6P. Due to the low equilibrium constant of PGI (Keq = 0.314)[26], incomplete conversion is expected. The chromatographic trace was integrated, and the ratio of the resulting areas were compared to the Keq for PGI. The ratio of the areas of the peaks assigned to G6P and F6P yielded a value of 0.292 which is close to the reported value of the Keq for PGI.

The sample containing ^{14}C-G6P and ^{14}C-F6P was treated with PFK for the enzymatic conversion of ^{14}C-F6P to ^{14}C-FBP. Due to the presence of PGI in the sample, near full conversion to ^{14}C-FBP was observed in the chromatographic trace obtained via IP-RPLC analysis. The resulting chromatographic trace resulted in the emergence of a peak at a retention time of 641 seconds assigned to FBP. ALD was added to the sample containing ^{14}C-FBP for the conversion of ^{14}C-FBP to ^{14}C-DHAP and ^{14}C-GAP. Only limited conversion of ^{14}C-FBP

associated with the emergence of a peak at a retention time of 195 seconds was observed. All attempts to convert the sample containing ^{14}C-FBP, ^{14}C-DHAP and ^{14}C-GAP to the lower glycolytic intermediates resulted in limited conversions and uncertainty surrounding the assignment of emerging peaks in the chromatographic trace. Therefore, the retention times of the lower glycolytic intermediates were determined by the enzymatic conversion of ^{14}C-GLY.The chromatographic traces and the integrated area corresponding to ^{14}C-GLC and the glycolytic intermediates derived from ^{14}C-GLC are shown in Figure 3.5

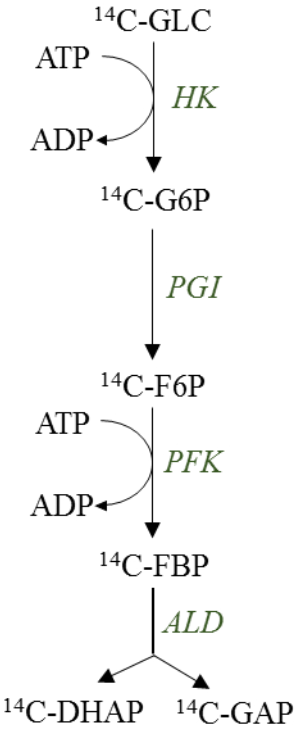

***Figure 3.4**: Schematic illustration of the enzymatic reactions used for the synthesis of the radiolabelled glycolytic intermediates. ^{14}C-GLC was converted to ^{14}C-G6P, ^{14}C-F6P, ^{14}C-FBP, ^{14}C-GAP and ^{14}C-DHAP and separation with the IP-RPLC method coupled to a radiolabelled detector for the determination of the corresponding retention times of each glycolytic intermediate. The corresponding retention rimes are listed in Table 3.3.*

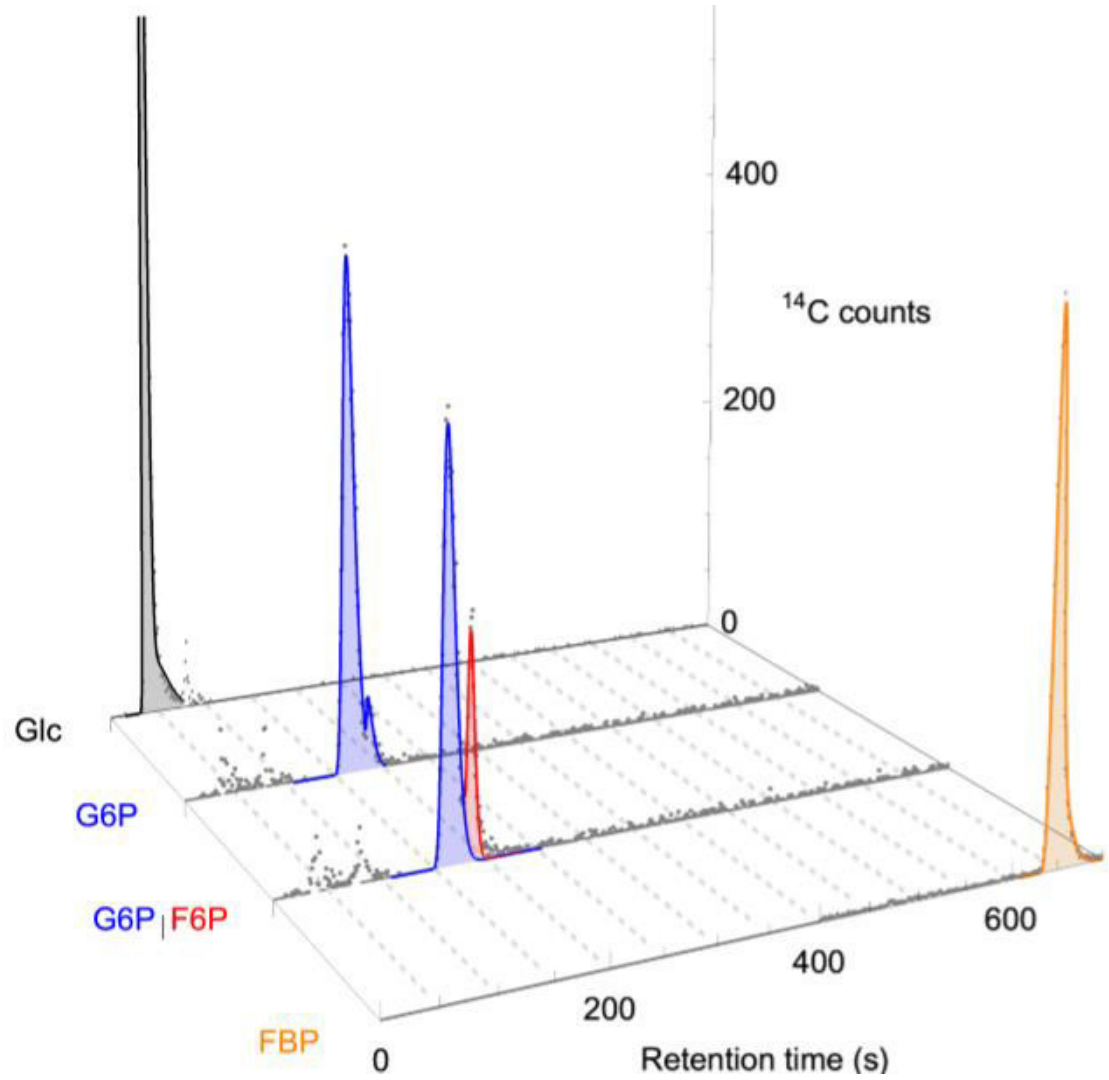

Figure 3.5: *Stacked plot of the chromatographic traces and integrated areas corresponding to the species; GLC, G6P, F6P and FBP synthesised by the step-wise enzymatic reaction of ^{14}C-GLC with HK, PGI and PFK as discussed in the text above. The grey dots represent the chromatographic traces. The black shaded area represents the integrated area corresponding to ^{14}C-GLC. The blue shaded area represents to integrated area corresponding to ^{14}C-G6P. The red shaded area represents to integrated area corresponding to ^{14}C-F6P. The orange shaded area represents to integrated area corresponding to ^{14}C-FBP.*

3.4.3. IP-RPC separation of the glycolytic intermediates prepared from ^{14}C-Glycerol for the determination of retention times

A sample containing ^{14}C-GLY and an excess amount of ATP and NAD^+ was prepared for the synthesis of radiolabelled glycolytic intermediates as illustrated in Figure 3.6. IP-RPLC analysis of the sample resulted in a single peak at 44 seconds assigned to GLY. The peak at a retention time of 44 seconds is close to the dead time of the column and shows that GLY is not retained by IP-RPLC separation method. The sample containing ^{14}C-GLY was treated with GK and a representative sample was injected onto the column. The resulting chromatographic trace

showed the emergence of a peak at a retention time of 202 seconds assigned to G3P with a near full conversion of ^{14}C-GLY to ^{14}C-G3P.

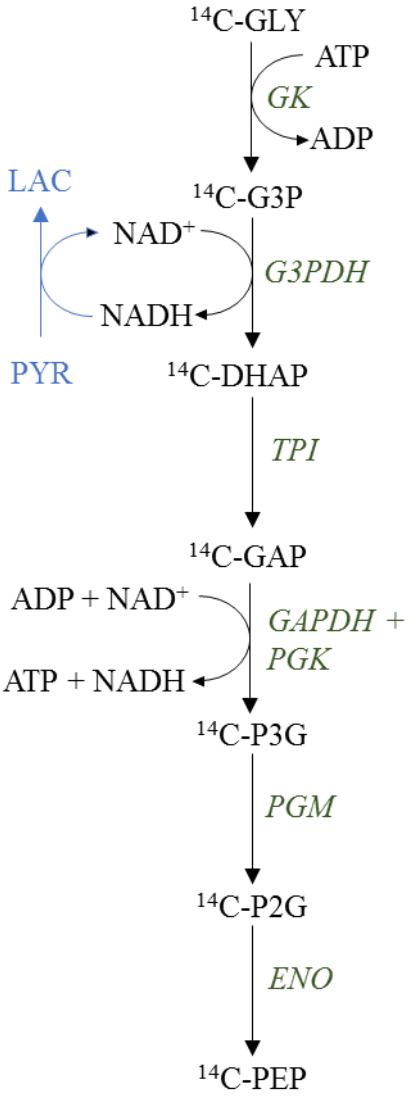

***Figure 3.6**: Schematic illustration of the enzymatic reactions used for the synthesis of the radiolabelled glycolytic intermediates. ^{14}C-GLY was converted to ^{14}C-G3P, ^{14}C-DHAP, ^{14}C-GAP, ^{14}C-P3G and ^{14}C-P2G and separation with the IP-RPLC method coupled to a radiolabelled detector for the determination of the corresponding retention times of each glycolytic intermediate. The corresponding retention rimes are listed in Table 3.3.*

The sample containing ^{14}C-G3P was subsequently treated with G3PDH for the conversion of ^{14}C-G3P to ^{14}C-DHAP. The presence of any NADH in the sample, produced by the enzymatic reaction of G3PDH, strongly inhibits G3PDH. Therefore, the reaction was coupled with LDH in the presence of unlabelled PYR to convert NADH back to NAD$^+$. The addition of G3PDH and LDH resulted in the formation of a peak at 195 seconds assigned to DHAP. The sample containing ^{14}C-DHAP was treated with TPI for the conversion of ^{14}C-DHAP to ^{14}C-

GAP and a representative sample was injected into the column. The resulting chromatographic trace showed the emergence of a very small peak at a retention time of 185 seconds assigned to GAP, along with a peak at a retention time of 195 seconds corresponding to DHAP. The chromatographic trace was integrated and the ratio of the areas of the peaks corresponding to GAP and DHAP yielded a value of 0.078 which compares well with the equilibrium constant reported for TPI (Keq = 0.089)[27] further supporting our assignment of the 2 chromatographic peaks to DHAP and GAP respectively. Due to the unfavourable equilibrium state of BPG the conversion of ^{14}C-GAP to ^{14}C-BPG was not attempted. ^{14}C-GAP was directly converted to ^{14}C-P3G by treating the sample containing ^{14}C-GAP and ^{14}C-DHAP with GAPDH and PGK. Additional ADP was added during this reaction step to ensure complete conversion of DHAP to P3G. The presence of TPI in the sample facilitated the conversion of ^{14}C-DHAP to ^{14}C-GAP and the resulting chromatographic trace showed the emergence of a peak at retention time of 445 seconds, assigned to P3G, and near full conversion of ^{14}C-DHAP and ^{14}C-GAP. The sample containing ^{14}C-P3G was treated with PGM for the conversion of ^{14}C-P3G to ^{14}C-P2G and a representative sample was injected into the column. The resulting chromatographic trace showed the emergence of a small peak at 482 seconds assigned to P2G. Due to the unfavourable Keq for PGM (Keq = 0.49)[27], full conversion is not expected and the ratio of the integrated areas for the peaks assigned to P3G and P2G yielded a value of 0.270 which is about half of the equilibrium constant reported for PGM. The sample containing 14C-P3G and ^{14}C-P2G was treated with ENO for the conversion of ^{14}C-P2G to ^{14}C-PEP and a representative sample was injected into the column. The conversion of ^{14}C-P2G to ^{14}C-PEP proved difficult. However, emergence of a small peak was observed at a retention time of 254 seconds. The chromatographic trace was integrated, and the ratio of the peak areas were correlated to the Keq values of PGM and ENO. The ratio of the peak areas corresponding to P3G and P2G yielded a value of 0.327 and is comparable to the Keq reported for PGM, but the ratio of the peak areas for P2G and PEP yielded a value of 0.450, which does not correlate to the equilibrium constant reported for ENO (Keq = 6.7)[28]. Therefore, the peak observed at a retention time of 254 seconds will be tentatively assigned to PEP however, further support for this assignment is necessary. Due to the presence of LDH and unlabelled PYR added for the conversion of ^{14}C-G3P to ^{14}C-DHAP the further conversion of the sample containing ^{14}C-P3G, ^{14}C-P2G and ^{14}C-PEP was not attempted and the determination of the retention times of the remaining glycolytic intermediates will be determined through the conversion starting with ^{14}C-PYR. The chromatographic traces and the integrated area corresponding to ^{14}C-GLY and the glycolytic intermediates derived from ^{14}C-GLY are shown in Figure 3.7.

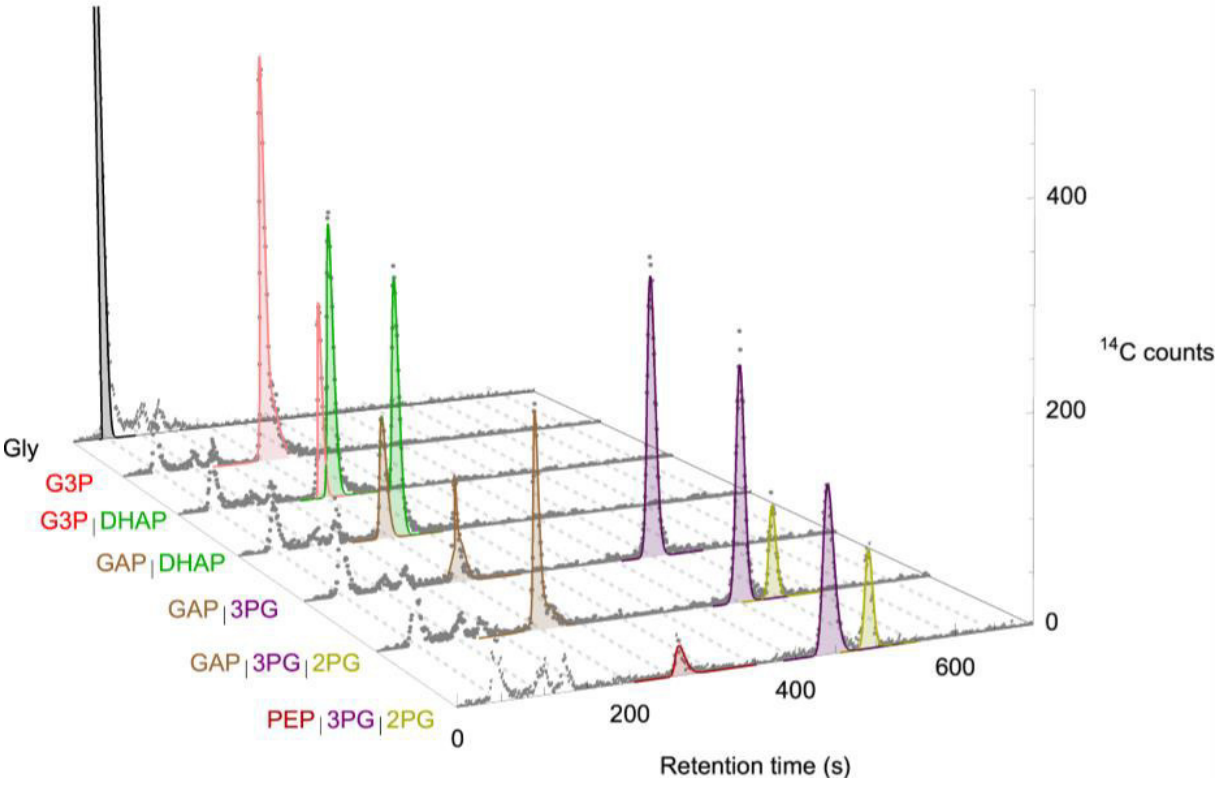

Figure 3.7: Stacked plot of the chromatographic traces and integrated areas corresponding to the species; GLY, G3P, DHAP, GAP, P3G, P2G and PEP synthesised by the step-wise enzymatic reaction of ^{14}C-GLY with GK, G3PDH, TPI, GAPDH, PGK, PGM and ENO as discussed in the text above. The grey dots represent the chromatographic traces. The black shaded area represents to integrated area corresponding to ^{14}C-GLY. The pink shaded area represents to integrated area corresponding to ^{14}C-G3P. The green shaded area represents to integrated area corresponding to ^{14}C-DHAP. The brown shaded area represents to integrated area corresponding to ^{14}C-GAP. The purple shaded area represents to integrated area corresponding to ^{14}C-P3G. The mustard shaded area represents to integrated area corresponding to ^{14}C-P2G. The red shaded area represents to integrated area corresponding to ^{14}C-PEP.

3.4.4. IP-RPC separation of the glycolytic intermediates prepared from ^{14}C-Pyruvate for the determination of retention times

A sample containing ^{14}C-PYR in the presence of excess NADH was prepared for the synthesis of the remaining radiolabelled glycolytic intermediates as illustrated in Figure 3.8. IP-RPLC analysis of a representative sample containing ^{14}C-PYR showed a large peak at a retention time of 210 seconds assigned to PYR, along with impurity peaks at retention times of 41, 302 and 401 seconds. The sample containing ^{14}C-PYR was treated with LDH and a representative sample was injected into the column. The chromatographic trace showed near full conversion of ^{14}C-PYR, resulting in the emergence of a peak at a retention time of 120 seconds assigned to LAC.

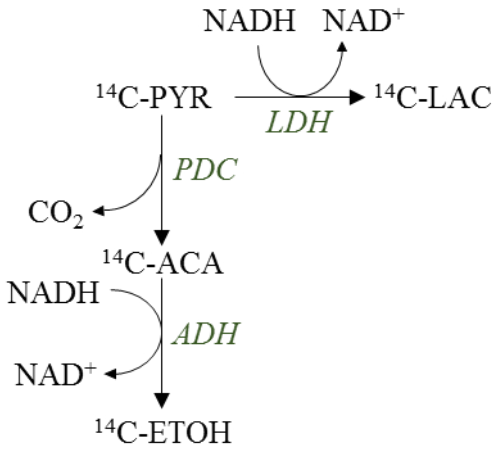

***Figure 3.8**: Schematic illustration of the enzymatic reactions used for the synthesis of the radiolabelled glycolytic intermediates. ^{14}C-PYR was converted to ^{14}C-LAC, ^{14}C-ACA and ^{14}C-ETOH and separation with the IP-RPLC method coupled to a radiolabelled detector for the determination of the corresponding retention times of each glycolytic intermediate. The corresponding retention rimes are listed in Table 3.3.*

For the conversion of ^{14}C-PYR to ^{14}C-acetaldehyde (ACA) and ^{14}C-ethanol (ETOH), a sample of ^{14}C-PYR containing an excess amount of NADH was prepared. The radioactive carbon atom is in the C_1 position of the^{14}C-Pyruvate and will be converted to ACA and ETOH and all CO_2 produced by pyruvate decarboxylase (PDC) is expected to be unlabelled. The sample containing ^{14}C-PYR was treated with yeast extract to convert the ^{14}C-PYR to ^{14}C-ACA and ^{14}C-ETOH. A sample was taken shortly after addition of yeast extract and the resulting chromatographic trace showed the emergence of 2 peaks at retention times of 76 seconds and 121 seconds. Another sample was taken after approximately an hour afterwards and the resulting chromatographic trace showed the emergence of a peak at a retention time of 76 seconds. Therefore, we have assigned the peak at 76 seconds to ETOH and the peak at 121 seconds to ACA. The chromatographic traces and the integrated area corresponding to ^{14}C-GLY and the glycolytic intermediates derived from ^{14}C-GLY are shown in Figure 3.9. The retention times determined for each of the glycolytic intermediates via the stepwise enzymatic conversion of ^{14}C-GLC, ^{14}C-GLY and ^{14}C-PYR are listed in Table 3.3.

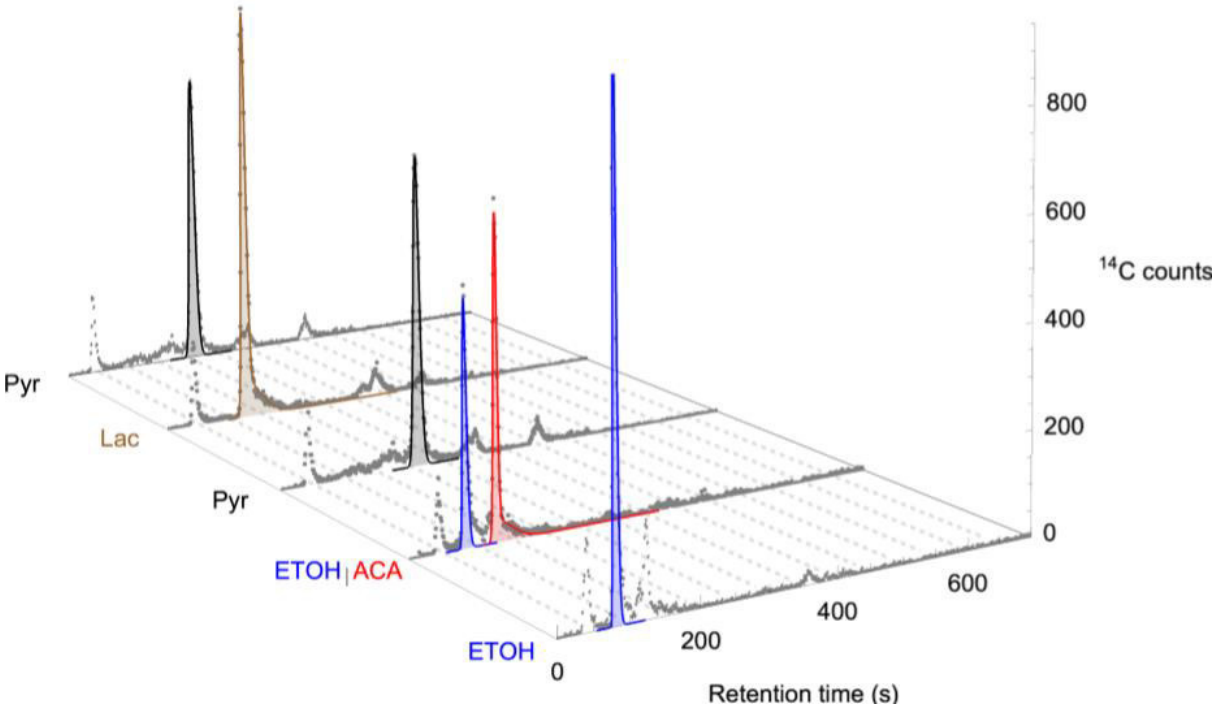

Figure 3.9: *Stacked plot of the chromatographic traces and integrated areas corresponding to the species; PYR, LAC, ACA and ETOH synthesised by the step-wise enzymatic reaction of ^{14}C-PYR with LDH obtained commercially, and PDC and ADH from yeast extract as discussed in the text above. The grey dots represent the chromatographic traces. The black shaded area represents to integrated area corresponding to ^{14}C-PYR. The brown shaded area represents to integrated area corresponding to ^{14}C-LAC. The red shaded area represents to integrated area corresponding to ^{14}C-ACA. The blue shaded area represents to integrated area corresponding to ^{14}C-ETOH.*

***Table 3.3**: Summary of the determined retention times of the glycolytic intermediated obtained through the IP-RPLC analysis coupled with radiolabelled detection. The glycolytic intermediates were synthesised by enzymatically converting ^{14}C-GLC, ^{14}C-GLY and ^{14}C-PYR to a subset of the glycolytic intermediates in a stepwise manner (see text for details).*

Glycolytic intermediate	Retention time (seconds)
GLC	38
G6P	157
F6P	182
FBP	641
GLY	44
G3P	202
DHAP	195
GAP	185
P3G	445
P2G	482
PEP	254
PYR	210
LAC	120
ACA	121
ETOH	76

3.4.5. IP-RPLC method application: Quantification of glucose in the ^{14}C-GLC starting material

The IP-RPLC method developed in this chapter, allows for the separation and quantification of the adenosine and nicotinamide moieties, summarised in Table 3.1, and the separation of the glycolytic intermediates, as summarised in Table 3.3. However, the chromatographic traces obtained from the radiolabelled detector represents the counts measured per second in response to the concentration of each glycolytic intermediate, as illustrated by Eq. 3.7. The ^{14}C-GLC starting material contains both ^{14}C-GLC and unlabelled GLC at unknown concentrations and the relative concentrations of ^{14}C-GLC and unlabelled GLC cannot be distinguished from one another. Therefore, a response factor (*rf*) needs to be calculated to correlate the ^{14}C-signal obtained in the chromatographic trace to concentration.

To determine the *rf* that relates the concentration of glycolytic intermediates to the corresponding area obtained from the chromatographic trace, both the concentration and the corresponding area must be known.

$$\text{Area} = rf \cdot \text{concentration} \qquad \text{(Eq. 3.7)}$$

The response factor that relates the area obtained from the chromatographic trace of GLC to the corresponding GLC concentration (see Section 3.3.5), was determined from a commercially obtained ^{14}C-GLC stock solution. The ^{14}C-GLC concentration of the stock solution was reported to be between 3.3 and 4.3 mM, whereas the concentration of unlabelled GLC in the stock solution was unknown. Samples from the ^{14}C-GLC stock solution was prepared at 2 times (x 2), 4 times (x 4) and 8 times (x 8) dilution. 5 µL of each dilution sample was injected into the column for IP-RPLC analysis and the chromatographic traces were integrated to yield the areas relating to each dilution sample, listed in Table 3.4.

To verify the measured GLC concentrations, the dilution samples prepared from the ^{14}C-GLC stock solution were treated with HK in the presence of excess ATP and 5µL of each sample was injected into the column. In the presence of HK, GLC is converted to G6P associated with a conversion of ATP to ADP at a stoichiometric ratio of 1:1. The corresponding conversion of ATP to ADP was quantified from the chromatographic traces obtained via UV-Vis detection, using an ADP calibration curve as discussed in Section 3.4.1 and the resulting concentrations are listed in Table 3.4. Furthermore, the chromatographic traces obtained via radiolabelled detection was integrated and the resulting areas are listed in Table 3.4.

Table 3.4: *Summary of the results obtained for the concentration determination of GLC in dilution samples of the ^{14}C-GLC stock solution. GLC concentration was determined spectrophotometrically with the aid of a GLC calibration curve (Figure 3.1). ADP concentration was determined from the chromatographic traces obtained via UV-Vis detection. The area describing the GLC peaks and the G6P peaks were obtained from the integration of the chromatographic traces obtained via radiolabelled detection.*

	^{14}C-GLC Stock solution (Total GLC Quantification)			
Dilution	GLC Concentration (mM)	ADP Concentration (mM)	GLC Area (cps)	G6P Area (cps)
x 2	5.90	5.66	85 467	85180
x 4	2.72	2.96	31 217	31541
x 8	1.46	1.38	15 815	15836

The concentrations measured via the 2 independent methods correlated well and the total concentration of GLC in the ^{14}C-GLC stock solution was determined to be 11.42 (± 0.42) mM. Determination of the area for the GLC and G6P peaks for each dilution sample also correlated well with each other. From the data summarised in Table 3.4 we can determine the *rf* for each dilution as given in Eq.3.7. The *rf* values were determined for each dilution sample and resulted in the values of 14 768 (± 355), 11 069 (± 544) and 11 154 (± 363) respectively. There is a

discrepancy between the *rf* value determined for the x 2 dilution sample in comparison with the lower dilutions. This is most likely due to an overestimation of the area obtained in this dilutions sample. Therefore, it is suggested that a *rf* value is determined for each experimental data set and not be taken as a constant for different ^{14}C-stock solutions. The reaction catalysed by ALD results in the fractionation of the 6-carbon FBP into the 3-carbon molecules of GAP and DHAP. Furthermore, TPI catalyses the reversible conversion of DHAP to GAP, resulting in a 2-fold increase in the concentration of lower down glycolytic intermediates. However, the number of ^{14}C-labeled molecules remains the same. This results in a 2-fold increase of the number of molecules leading to the same radiolabelled signal obtained as for upper glycolysis resulting in a *rf* value that is halved for the lower glycolytic intermediates.

3.4.6. IP-RPLC method application: Determining time-dependent metabolite concentrations of glycolytic intermediates and glycolytic flux in extracts of yeast strain X2180

The IP-RPLC method was tested in biological cell extracts in collaboration with Dr. Theresa Kouril[i]. Yeast strain X2180 was cultured and harvested during the log growth phase. Lysate of the yeast culture was prepared via glass bead extraction, as described in Section 3.3.6. The supernatant, containing the glycolytic enzymes of interest, was analysed at a final protein concentration of 5 mg/ mL in time course incubations. The cell lysate of the X2180 yeast strain was incubated at 30ºC in the presence of 2.4 mM ATP and 2.0 mM NAD^+. A mixture containing ^{14}C-GLC and unlabelled GLC was prepared with a final GLC concentration of approximately 10 mM. The time course experiment was initialised by adding this GLC solution to the cell lysate incubation, containing ATP and NAD^+. Samples were collected at timepoints; 0 min, 4 min, 8 min, 12 min, 16 min, 20 min, 25 min, 30 min and 40 min and quenched by adding the timepoint samples into a unlabelled solution of 50% perchloric acid (PCA) followed by neutralisation with a 1 M K_2CO_3 solution to pH 7 (method as described by Teusink *et. al.*[29]). Samples were centrifuged and the supernatant was injected into the column for IP-RPLC analysis. The integrated chromatographic trace of the yeast time-course sample at a timepoint of 20 min is shown in Figure 3.10.

i All culturing of yeast strain X2180 and the preparation and conduction of the required time course experiment was carried out by Dr. Theresa Kouril. Concentration determinations on the UV-Vis spectrometer was also conducted by her.

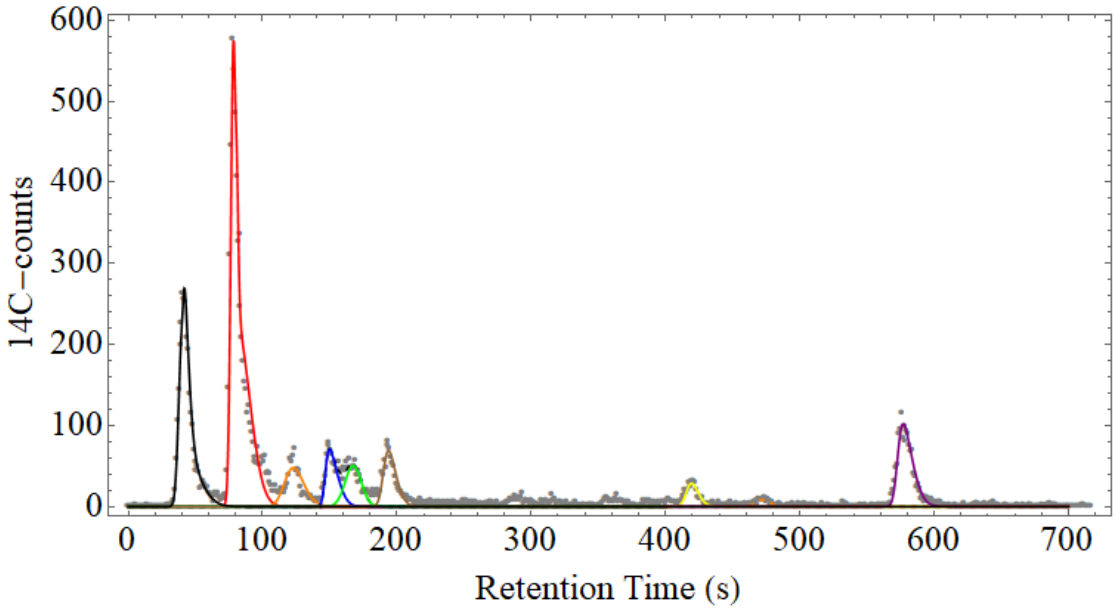

Figure 3.10: *Integrated ^{14}C-chromatographic trace of the time-course experiment conducted in yeast at a timepoint of 20 min. The grey dots represent the experimentally obtained chromatographic trace. The black line represents GLC, the red line represents ETOH, the orange line represents ACA, the blue line represents G6P, the green line represents F6P, the yellow line represents P3G, the purple line represents FBP. P2G is present at low levels represented by the orange-dashed line.*

The IP-RPLC analysis of the yeast time course samples resulted in chromatographic traces for the chemical species; GLC, G6P, F6P, FBP, DHAP, P3G, ACA and ETOH via radiolabelled detection and the chemical species NAD^+, NADH, AMP, ADP and ATP via UV-Vis detection. No peaks for the species GAP, PEP and PYR were detected in the chromatographic trace and these species are expected to be present at undetectable concentration levels. P2G is present at low levels but was not quantified. The chromatographic traces showed a clear time dependent decrease in GLC associated with an increase in the signal associated with ETOH. Of note was the appearance of large peaks associated with FBP and DHAP in the chromatographic traces. The chromatographic traces were quantified using the methods laid out in Sections 3.3.3 and 3.3.4 and the time dependent concentrations of each species was determined. The time dependent concentrations of the glycolytic intermediates and cofactors for the time course incubation of yeast extract are illustrated in Figure 3.11 and Figure 3.12.

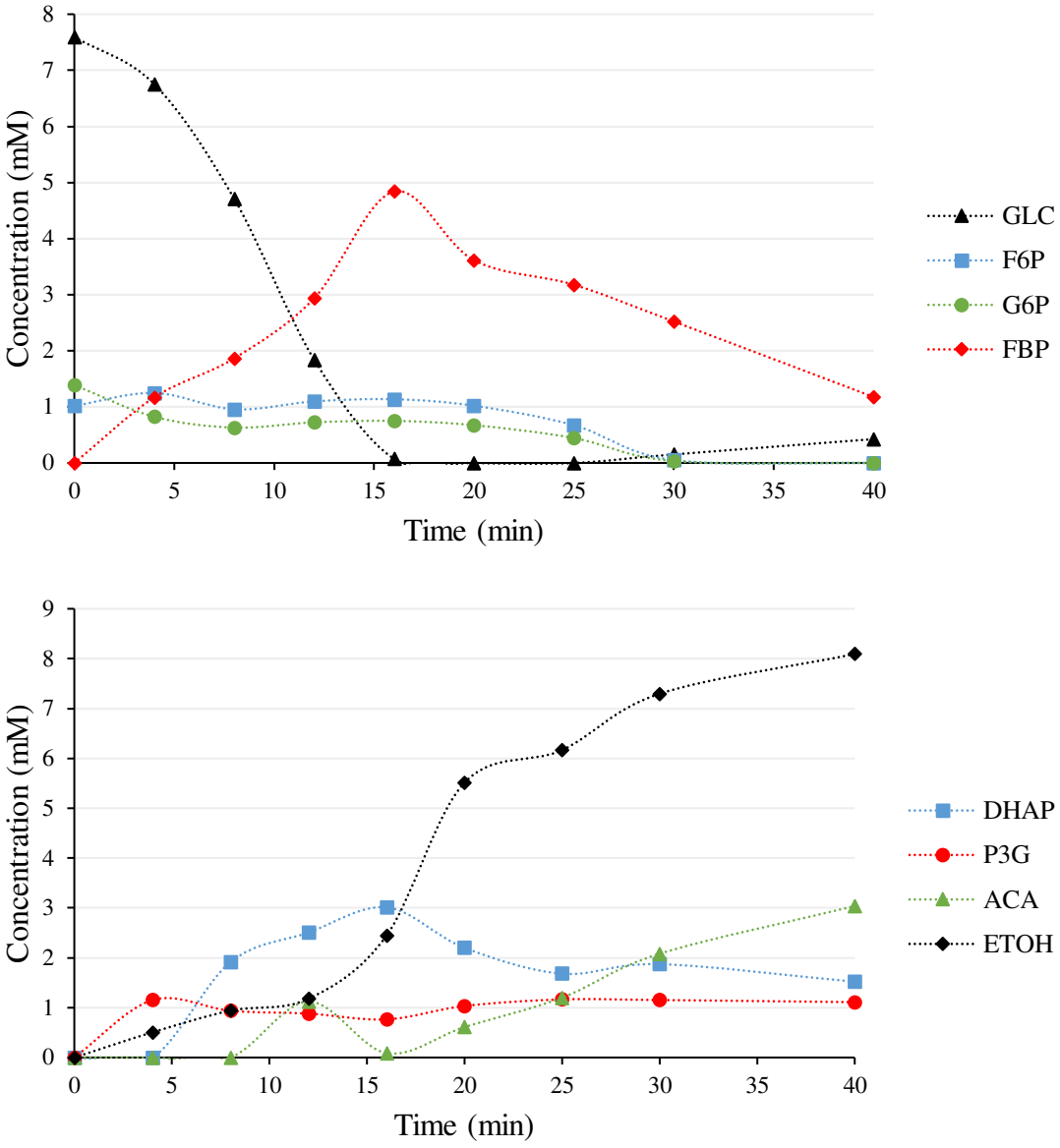

Figure 3.11: *Time dependent concentrations of the glycolytic intermediates separated via IP-RPLC and measured by radio-labelled detection in a yeast extract time course incubation.* ***Top:*** *Concentrations of the glycolytic intermediates of upper glycolysis; GLC, G6P, F6P and FBP as quantified by integration of the chromatographic traces obtained.* ***Bottom:*** *Concentrations of the glycolytic intermediates of lower glycolysis; DHAP, P3G, ACA and ETOH as quantified by integration of the chromatographic traces obtained.*

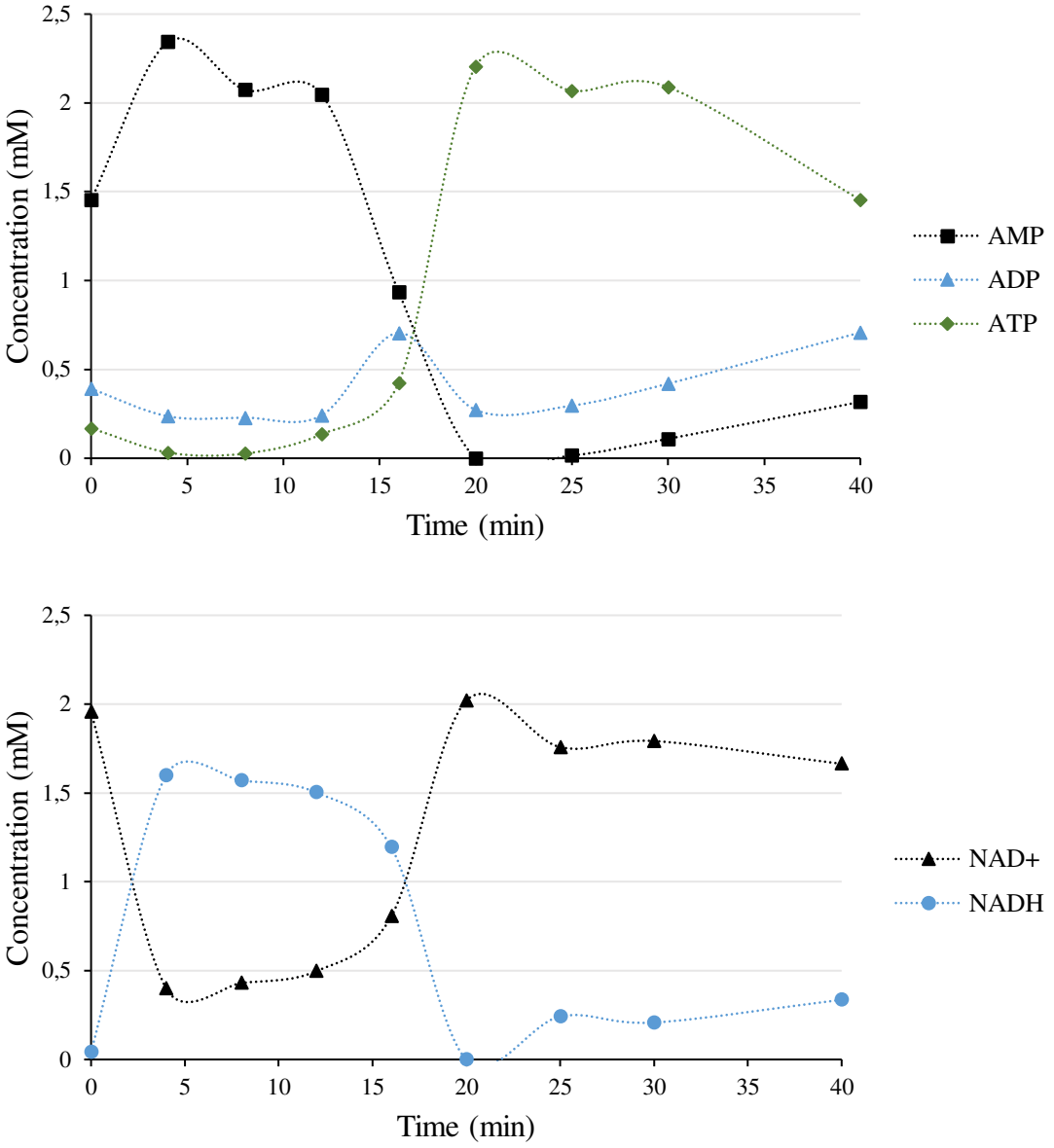

Figure 3.12: *Time dependent concentrations of the adenosine and nicotinamide moieties determined via IP-RPLC and measured by UV/Vis detection in a yeast extract time course incubation.* ***Top:*** *Concentrations of the cofactors; ATP, ADP and AMP quantified from the chromatographic traces obtained.* ***Bottom:*** *Concentrations of the cofactors; NAD^+ and NADH quantified from the chromatographic traces obtained.*

IP-RPLC analysis of the time dependent change in the concentrations of the glycolytic intermediates and cofactors (Figure 3.11 and Figure 3.12) clearly displays the analytical capacity of this technique. In total, 8 of the possible 12 glycolytic intermediates (Excluding the glycolytic intermediates; GAP, P2G, PEP and PYR) and the 5 cofactors could be quantified in the time-course samples. The relative high concentration of AMP in the initial half of the time-course experiment and the relative high concentration of FBP at t = 16 min is in correspondence

with the expected behaviour of glycolysis in yeast with relatively high activity in upper glycolysis in comparison to lower glycolysis[29]. After the consumption of GLC at t = 16 min, FBP gradually decreases with a corresponding increase in ATP and production of ETOH.

3.4.7. IP-RPLC method application: Comparing quantification via the novel IP-RPLC analytical technique to quantification using established coupled enzyme assay techniques

To test how well the IP-RPLC quantification of the glycolytic intermediates and adenosine and nicotinamide moieties compare to established methods, the concentrations of the chemical species were quantified via a UV-Vis coupled assay technique. The concentrations of ATP, DHAP and FBP were determined in representative samples of each time point in the yeast incubation experiment as described in Section 3.3.6. The concentrations of ATP, DHAP and FBP obtained by enzyme coupled assays and by IP-RPLC analysis were compared, as shown in Figure 3.13 to determine how well the novel IP-RPLC is able to quantify these chemical species.

The concentrations determined via the IP-RPLC analysis of the yeast extract time course samples compares well with the concentrations determined via the enzyme coupled assays using UV-Vis spectroscopy as illustrated in Figure 3.13. The concentrations determined for FBP and DHAP show a systematic increase in concentration to a maximum concentration measured at 16 min, followed by a systematic decrease in concentration. The concentrations measured for ATP in the initial phase of the time course incubation are very low and only increase after approximately 12 min. The very good correlation in the quantification of the chemical species using the 2 independent quantification techniques, suggests that the IP-RPLC quantification technique is on par with quantification of glycolytic intermediates using an enzyme coupled assay technique.

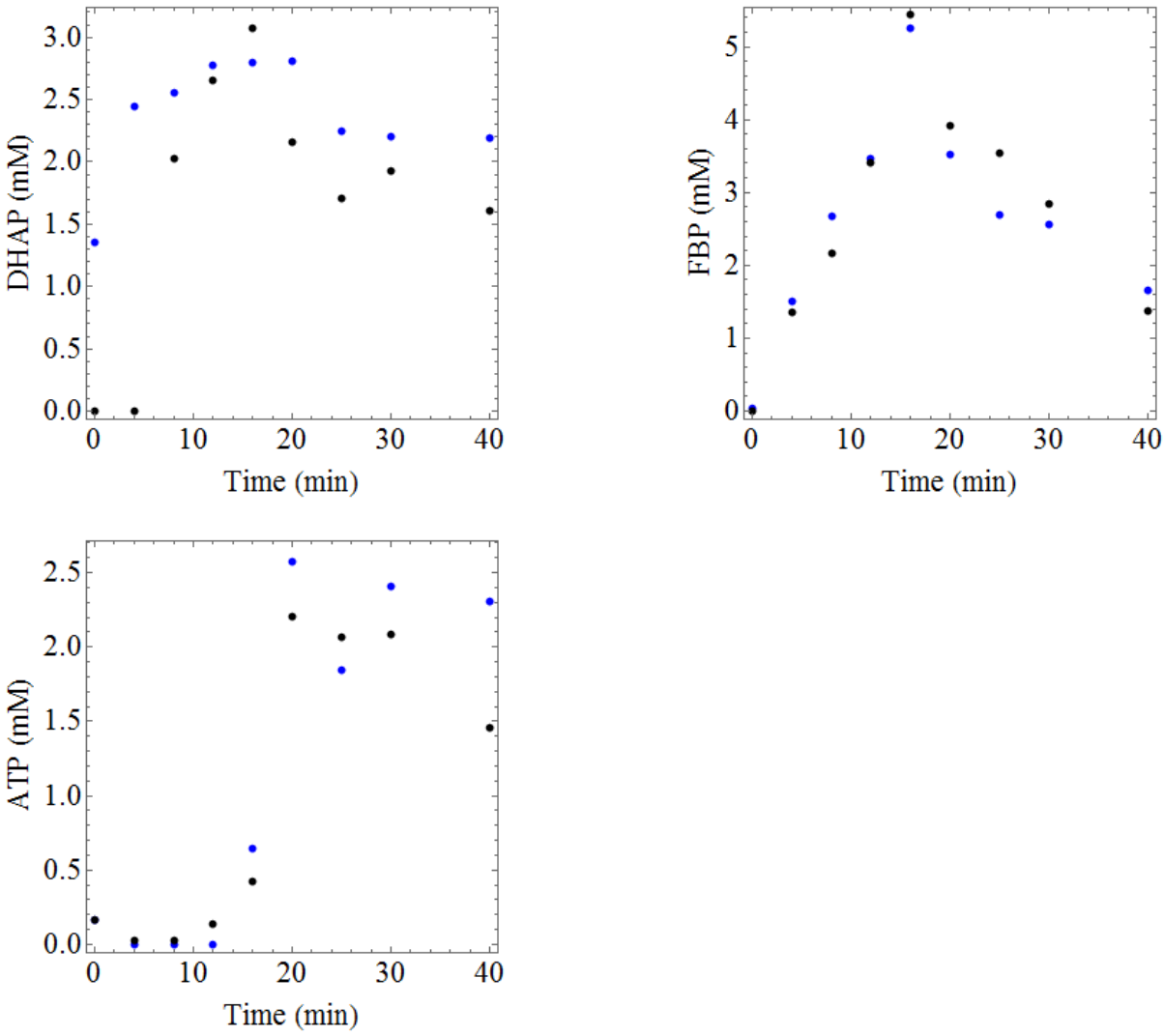

Figure 3.13: *Comparison of the concentrations determined for DHAP, FBP and ATP in yeast extract time course samples. The concentrations were determined via 2 independent methods. Concentrations determined via the IP-RPLC method developed in this chapter are illustrated in* ***Black****. Concentrations determined via coupled enzyme assay techniques using UV-Vis spectroscopy are illustrated in* ***Blue****.*

3.5 Discussion

There is a need for the development of metabolomic techniques to identify and investigate the regulation of metabolic pathways in biochemistry. Using metabolomic analysis in tandem with bottom-up modelling approaches creates a powerful tool to test our understanding of the regulatory processes associated with metabolic pathways. Furthermore, reliable data of the metabolome expressed under specific conditions allows for high resolution validation of bottom-up metabolic models. This allows for the determination of the predictive accuracy of metabolic models which increases the reliability and usefulness of such models. Previously, there has been some success in using an IP-RPLC technique for the gathering of metabolome

data[22] and we have set out to develop a similar technique tailored to our needs for investigating the metabolic regulation of glycolysis.

The IP-RPLC technique developed here relies on 2 modes of detection to quantify the chemical species present in glycolysis. The conserved adenosine and nicotinamide moieties are detected via UV-Vis spectroscopy with little to no interference observed from the glycolytic intermediates or cellular matrix and can be quantified with reasonable confidence. Quantification of the adenosine and nicotinamide moieties were done by means of calibration curves constructed for each moiety. From these calibration curves the LOD and LOQ for each conserved moiety was determined. The LOQ for the adenosine moieties are much lower than for the nicotinamide moieties. However, the IP-RPLC system is sensitive enough to quantify all conserved moieties within the concentration range of interest.

The glycolytic intermediates are quantified by using a ^{14}C-label and are detected via radiolabelled counting with no interference from the cellular matrix. The ^{14}C-label is sourced from a commercially obtained ^{14}C-GLC stock solution containing an unspecified amount of unlabelled GLC. The ^{14}C-GLC stock solution was analysed to quantify the total GLC concentration present in the stock solution and the *rf* value was determined by correlating the total GLC concentration to the signal obtained from the chromatographic trace. The GLC concentration was measured with 2 independent methods and resulted in a total GLC concentration of 11.42 (± 0.42) mM for the ^{14}C-GLC stock solution. The peak area described by the ^{14}C-GLC samples were determined in 2 independent ways from the GLC chromatographic trace and the G6P chromatographic trace which results from treating the GLC samples with HK. There was a good correlation between the area describing GLC and the area describing G6P for each dilution sample. However, determination of the *rf* values yielded different values for the different dilutions of the ^{14}C-GLC stock solution. It is therefore suggested that a *rf* value be determined for each experimental setup. This allows for some flexibility as the concentration of total GLC can be increased in analysis setups, without increasing the ^{14}C-GLC fraction by simply adding unlabelled GLC as required. The radiolabelled signal obtained in the chromatographic traces measures the ^{14}C-GLC but represent the total GLC concentration used and the relationship between the glycolytic intermediate concentration and chromatographic signal was determined by calculating a *rf* value for each experimental setup independently. The *rf* value remains constant for the different glycolytic

intermediates. However, the *rf* value is halved for the lower glycolytic intermediates due to the fractionation of FBP into GAP and DHAP catalysed by ALD.

The IP-RPLC metabolomics technique developed here can separate and quantify 20 chemical species, present in glycolysis. However, some chemical species do show peak overlap in the chromatographic traces. Significant overlap of the chromatographic traces obtained for F6P and GAP, as well as G3P, DHAP and PYR are present. These chemical species show similar retention behaviours and it is not possible to deconvolute the peaks from one another. Assuming that the enzymes of PGI and TPI have reached equilibrium in each sample, the concentrations of the overlapping species of F6P and GAP can be determined from the concentrations of G6P and DHAP. PYR can be determined by subtracting the estimated concentration of DHAP from the experimentally obtained peak.

The novel IP-RPLC method developed here, was applied to the investigation of glycolysis in the extract of yeast strain X2180. The time dependent change in the concentrations of the glycolytic intermediates and conserved adenosine and nicotinamide moieties were measured by analysing time course samples taken at different time points of a yeast extract incubation. The resulting concentration obtained from the chromatographic traces of the time point samples are shown in Figure 3.11 and Figure 3.12. There is a near instantaneous decrease in the concentration of ATP to almost zero. This decrease in ATP is associated with an increase in the concentration of AMP. This rapid conversion of ATP to AMP can be attributed to the high activity of adenylate kinase (AK) in yeast[30]. AK catalyses the conversion of ADP to form ATP and AMP via a phosphate transfer from one molecule of ADP to another molecule of ADP. The adenosine conversion catalysed by AK increases the effective concentration of ATP that is required for upper glycolysis and the conversion of GLC to FBP. The rapid formation of additional ATP, and consumption of ATP via upper glycolysis, continues until the total adenosine pool is converted to AMP. The IP-RPLC dynamics shown in Figure 3.12 beautifully highlights this rapid process where high concentrations of AMP are observed during the early stages of the incubation. This is associated with the formation of an exceptionally large pool of FBP with a maximum concentration measured at about 5 mM.

The IP-RPLC analytical data compares favourably with the well-established method of quantifying glycolytic intermediates using coupled enzyme assay techniques as shown in Figure 3.13. The concentrations of ATP, DHAP and FBP were independently quantified via the IP-RPLC method and via enzyme coupled assays and the resulting data compared well. This

suggests that the quantifiability of the IP-RPLC method developed here is comparable to the quantifiability of coupled enzyme assay techniques. There are some limitations to the applicability of this novel IP-RPLC metabolomics technique. The availability and quality of ^{14}C-GLC starting material is an obstacle to consider. ^{14}C-impurities are present in the commercially obtained ^{14}C-GLC starting material that should be accounted for when correlating peak area to concentration in the analysis of the IP-RPLC radiolabelled data. Furthermore, the limited commercial availability of ^{14}C-glycolytic intermediates limits the identification of chemical species present in the chromatographic traces. Here we have resorted to convert the commercially available ^{14}C-GLC, ^{14}C-GLY and ^{14}C-PYR enzymatically to the other ^{14}C-glycolytic intermediates. However, this cumbersome process limits confidence in our assignment of some of the ^{14}C-glycolytic intermediates.

The novel IP-RPLC technique developed for the quantification of glycolytic intermediates and cofactors address some of the disadvantages associated with metabolomic studies performed using NMR or MS analysis. The strengths of this metabolomics method lie in the robustness of the separation technique and that the radiolabelled detection is free from matrix effects. This allows for routine analysis to be performed in complex cell matrices with limited sample preparation required. Furthermore, the higher sensitivity of radio-isotope detection compared to the sensitivity of NMR allows for quantitative analysis on small cell samples. The quantifiability of this method is comparable to that of enzyme coupled assays. This novel metabolomics technique can separate the majority of the glycolytic intermediates and quantify all cofactors in a single HPLC run of 20 mins, making this technique ideal for targeted studies of glycolysis in combination with modelling studies.

Reliance on the limited availability and quality of ^{14}C-starting material available, is one of the weaknesses associated with this technique. Furthermore, the ^{14}C-starting material and analysis via radiolabelled detection is costly in comparison to other metabolomic techniques, such as MS or NMR. However, it should be noted that the cost of equipment required for the establishment of NMR or MS analysis is far greater in comparison to the cost requirements of establishing this technique. Peak overlap and the limited number of metabolites that can be separated using this technique are also drawbacks that needs to be considered. This limits the usefulness of this technique to targeted metabolomic analysis of glycolytic intermediates for bottom-up studies of glycolysis.

In this chapter we have discussed the development of a novel IP-RPLC metabolomic technique and application in yeast extract. However, the applicability of the technique is not limited to yeast extracts. Metabolomic analysis of cell lines using this technique depends on the pre-analysis preparation of time-course samples and not on modification of the IP-RPLC analytical technique. Therefore, cellular extract of any cell line can be analysed via the IP-RPLC technique discussed here. We aim to employ this metabolomics technique in Chapter 5 of this thesis for the metabolomic analysis of C_2C_{12} skeletal muscle extract as a technique for validating a detailed kinetic model describing glycolysis in C_2C_{12} skeletal muscle extract, constructed in Chapter 4 of this thesis.

3.6 Conclusion

A novel IP-RPLC technique with UV-Vis and radio-labelled detection was developed here for the separation of the glycolytic intermediates and cofactors. The novel metabolomics technique was successfully applied to determine the concentration of glycolytic intermediates and cofactors in yeast extract. Furthermore, the quantifiability of this technique was shown to be comparable to that of enzyme coupled assays. The ability to follow the dynamic behaviour of the glycolytic intermediates and cofactors is of great value to system biology studies focusing on the characterisation of glycolysis, as this method enables the comparison of model simulations to experimental concentration profiles for a large number for metabolites.

3.7 References

1 **Schaub J and Reuss M.**, In Vivo Dynamics of Glycolysis in Escherichia coli Shows Need for Growth-Rate Dependent Metabolome Analysis., *Biotechnol. Prog.* 24:1402-1406, 2008

2 **Goodacre R, Vaidyanathan S, Dunn WB, Harrigan GG and Kell DB.**, Metabolomics by numbers: acquiring and understanding global metabolite data., *Trends Biotechnol*. 22:245-252, 2004

3 **Nielsen J.**, It is all about metabolic fluxes., *J. Bacteriol.* 185:7031–7035, 2003

4 **Krömer JO, Sorgenfrei O, Klopprogge K, Heinzle E and Wittmann C.**, In-depth profiling of lysine-producing Corynebacterium glutamicum by combined analysis of the transcriptome, metabolome, and fluxome., *J. Bacteriol*. 186:1769–1784, 2004.

5 **Dunn WB, Broadhurst DI, Atherton HJ, Goodacre R and Griffin JL.**, Systems level studies of mammalian metabolomes: the roles of mass spectrometry and nuclear magnetic resonance spectroscopy., *Chem. Soc. Rev*. 40:387-426, 2011

6 **Nielsen J.**, Metabolic engineering., *Appl. Microbiol. Biotechnol*. 55:263–283, 2001

7 **Chassagnole C, Noisommit-Rizzi N, Schmid JW, Mauch K and Reuss M.**, Dynamic modeling of the central carbon metabolism of Escherichia coli., *Biotechnol. Bioeng*. 79:53–73, 2002

8 **Visser D, Schmid JW, Mauch K, Reuss M and Heijnen JJ.**, Optimal re-design of primary metabolism in Escherichia coli using linlog kinetics,. *Metab. Eng*. 6:378–390, 2004

9 **Tweeddale H, Notley-McRobb L and Ferenci T.**, Effect of slow growth on metabolism of *Escherichia coli*, as revealed by global metabolite pool ("Metabolome") analysis., *J. Bacteriol*. 180:5109-5116, 1998

10 **Maharjan RP and Ferenci T.**, Global metabolite analysis: the influence of extraction methodology on metabolome profiles of *Escherichia coli., Anal. Biochem*. 313:145-154, 2003

11 **Tang H, Wang Y, Nicholson JK and Lindon JC.**, Use of relaxation-edited one-dimensional and two-dimensional nuclear magnetic resonance spectroscopy to improve detection of small metabolites in blood plasma., *Anal. Biochem*. 32:260-272, 2004

12 **Raamsdonk LM, Teusink B, Broadhurst D, Zhang N, Hayes A, Walsh MC, Berden JA, Brindle KM, Kell DB, Rowland JJ, Westerhoff HV, van Dam K and Oliver SG.**, A functional genomics strategy that uses metabolome data to reveal the phenotype of silent mutations., *Nat. Biotechnol*. 19:45-50, 2001

13 **Mesnard F and Ratcliffe RG.**, NMR analysis of plant nitrogen metabolism., *Photosynth. Res*. 83:163-180, 2005

14 **Sato S, Soga T, Nishioka and Tomita M.**, Simultaneous determination of the main metabolites in rice leaves using capillary electrophoresis mass spectrometry and capillary electrophoresis diode array detection., *Plant. J*. 40:151-163, 2004

15 **Wang W, Zhou H, Lin H, Roy S, Shaler TA, Hill LR, Norton S, Kumar P, Anderle M and Becker CH.**, Quantification of proteins and metabolites by mass spectrometry without isotopic labeling or spiked standards., *Anal. Chem.* 75:4818-4826, 2003

16 **Lafaye A, Labarre J, Tabet JC, Ezan E and Junot C.**, Liquid chromatography-mass spectrometry and ^{15}N metabolic labeling for quantitative metabolic profiling., *Anal. Chem.* 77:2026-2033, 2005

17 **Wu L, Mashego MR, van Dam JC, Proell AM, Vinke JL, Ras C, van Winden WA, van Gulik WM and Heijnen JJ.**, quantitative analysis of the microbial metabolome by isotope dilution mass spectrometry using uniformly ^{13}C-labeled cell extracts as internal standards., *Anal. Biochem.* 336:164-171, 2005

18 **Mashego MR, Jansen MLA, Vinke JL, van Gulik WM and Heijnen JJ.**, Changes in the metabolome of Saccharomyces cerevisiae associated with evolution in aerobic glucose-limited chemostats., *FEMS Yeast Res*. 5:419-430, 2005

19 **Fiehn O, Kopka J, Dormann P, Altmann T, Trethewey RN and Willmitzer L.**, Metabolite profiling for plant functional genomics., *Nat. Biotechnol.* 18:1157-1161, 2000

20 **Bajad SU, Lu W, Kimball EH, Yuan J, Peterson C and Rabinowitz JD.**, Separation and quantitation of water soluble cellular metabolites by hydrophilic interaction chromatography-tandem mass spectrometry., *J. Chromatogr. A* 1125:76-88, 2006

21 **Guo Y and Gaiki S.,** Retention behavior of small polar compounds on polar stationary phases in hydrophilic interaction chromatography., *J. Chromatogr. A* 1074:71-80, 2005

22 **Lu W, Clasquin MF, Melamud E, Amador-Noguez D, Caudy AA and Rabinowitz JD.**, Metabolomic analysis via reversed-phase ion-pairing liquid chromatography coupled to a stand alone orbitrap mass spectrometer., *Anal. Chem*. 82:3212-3221, 2010

23 **Balani SK, Xu X, Pratha V, Koss MA, Amin RD, Dufresne D, Miller RR, Arison BH, Doss GA, Chiba M, Freeman A, Holland SD, Schwartz JI, Lasseter KC, Gertz BJ, Isenberg JI, Rogers JD, Lin JH and Baillie TA.**, Metabolic profiles of montelukast sodium (singulair), a potent cysteinyl leukotreine$_1$ receptor antagonist, in human plasma and bile., *Drug Metab. Dispos.* 25:1282-1287, 1997

24 **Alivisatos SGA, Ungar F and Abraham GJ.**, Spontaneous reactions of 1,3-substituted 1,4-dihydropyridines with acids in water at neutrality. I. Kinetic analysis and mechanism of the reactions of dihydronicotinamide-adenine dinucleotide with orthophosphates., *Biochemistry* 4:2616-2630, 1965

25 **Oppenheimer NJ and Kaplan NO.**, Structure of the primary acid rearrangement product of reduced nicotinamide adenine dinucleotide (NADH)., *Biochemistry* 11:4675-4685, 1974

26 **Tewari YB, Steckler DK and Goldberg RN.**, Thermodynamics of isomerization reactions involving sugar phosphates., *J. Biol. Chem*. 263:3664-3669, 1988

27 **Hofmann E and Kopperschlaeger G.**, Phosphofructokinase from yeast., *Methods Enzymol*. 90:49-60, 1982

28 **Imamura K and T. Tanaka T.**, Pyruvate kinase isozymes from rat., *Methods Enzymol*. 90:150–165, 1982

29 **Teusink B, Passarge J, Reijenga CA, Esgalhado E, van der Weijden CC, Schepper M, Walsh MC, Bakker BM, van Dam K, Westerhoff HV and Snoep JL.**, Can yeast glycolysis be understood in terms of in vitro kinetics of the constituent enzymes? Testing biochemistry., *Eur. J. Biochem.* 267:5313-5329, 2000

30 **Konrad M.**, Analysis and *in vivo* disruption of the gene coding for adenylate kinase (ADK1) in the yeast *Saccharomyces cerevisiae*., *J. Biol. Chem.* 263:19468-19474, 1988

Chapter 4
Constructing a detailed mechanistic model of glycolysis in differentiated C_2C_{12} muscle cells

4.1. Preamble

In this chapter the construction of a detailed kinetic model describing glycolysis in differentiated C_2C_{12} skeletal muscle cells using a bottom-up modelling approach is presented.

4.2. Introduction

Skeletal muscle cells play a major role in maintaining blood glucose homeostasis within the body. Dietary glucose introduced into the body is metabolised mainly in skeletal muscle[1,2]. Glycolysis is a central catabolic pathway and results in the production of ATP and forms lactate as a by-product[3,4]. Defects within the glycolytic pathway of muscle cells will have a direct impact on the regulation of blood glucose homeostasis, which can lead to chronic hyperglycaemia, the predominant metabolic state attributed to type 2 diabetes mellitus. A mechanistic model of glycolysis in skeletal muscle is important to understand metabolic defects that may arise from dysfunctional glucose regulation. The current metabolic understanding of skeletal muscle focusses on describing metabolism under exercise conditions[5 - 8]. Literature points out that the major determining factor regulating metabolism in skeletal muscle is based on a high demand for ATP to drive muscle activity. However, it is of importance to consider how glucose metabolism in skeletal muscle behaves under conditions where there is a low demand for ATP and a high supply of glucose. Under insulin stimulated conditions it is postulated that the rate of glycolysis in skeletal muscle will not be dictated by the rate of ATP consumption. Therefore, we seek to investigate how glycolysis will behave when there is an oversupply of both glucose and ATP.

Insulin stimulation of skeletal muscle leads to an increased influx of glucose into the cell due to the activation of GLUT4 translocation from the cytosol to the cell membrane. Once glucose enters the cell, glycolysis converts it through a series of linearly connected enzyme catalysed reactions to form lactate, referred to as the glycolytic pathway[9]. There are 11 main reactions that make up the glycolytic pathway converting glucose to lactate. Each glucose molecule yields in total 2 molecules of ATP and 2 molecules of lactate, if no branches of

glycolysis are active. Apart from the 10 main reactions, adenylate kinase interconverts the adenosine moieties via the reversible reaction 2 ADP ↔ ATP + AMP. It is of importance to note that the upper part of glycolysis uses ATP as a substrate, whereas the lower part of glycolysis yields ATP as a product. This results in interesting metabolic behaviours that are strongly dependent on the concentrations of the adenosine metabolites present and their relative ratios. When considering the dynamics of muscle cell metabolism under insulin stimulated conditions it is important to consider the basal demand for ATP to drive cellular maintenance processes. In the model an ATPase rate is used to describe the basal conversion of ATP to ADP caused by the presence of ATP-dependent reactions associated with cellular maintenance and muscle contraction. A schematic illustration representing the glycolytic pathway considered in this chapter is given in Figure 4.1.

Lambeth and Kushmeric noted that a lack of standardised kinetic data in a specified cell line is a limiting factor that needs to be addressed to improve the existing models available for glycolysis in skeletal muscle[6]. Van Eunen *et. al.*[10] discussed in detail how to systematically investigate glycolysis under physiologically representative conditions. This includes measuring enzyme activity at a physiological pH and temperature, in a buffer matrix that mimics the chemical composition of the cytosol. Similarly, Teusink *et. al.*[11] investigated glycolysis in yeast through a series of enzyme coupled reactions which enabled them to measure the activity of specific enzymes photometrically at 340 nm by observing the change in NADH concentration. In short, the enzyme under investigation is coupled to excess amounts of subsequent enzymes until a reaction that is dependent on a nicotinamide is reached. It is important to ensure that the enzyme under investigation is rate limiting so that the change in concentration of the nicotinamide moiety is equivalent to the rate of the enzyme under investigation.

The investigation of glycolysis in skeletal muscle will be conducted in differentiated C_2C_{12} skeletal muscle cells as model cell line. The C_2C_{12} cell line is an immortalised mouse skeletal muscle cell line extensively used to research muscle development, differentiation, myofibrilogenesis and sarcomere development and the procedures for culturing and differentiating C_2C_{12} skeletal muscles are well established[12] - [16]. Furthermore, Kanzaki and Nedachi[17] have shown that the glucose transport machinery required for insulin induced GLUT4 translocation is present in C_2C_{12} muscle myofibers. Therefore, C_2C_{12} skeletal muscle cells are a good representative cell line to investigate the insulin dependent metabolism of skeletal muscle. However, significant differences in the metabolic behaviour of cultured C_2C_{12}

myotubes vs human tissue are expected. Preliminary measurements of the glucose and lactate flux (data not shown) in glucose starved cells suggests a stoichiometric relationship of 2 molecules of lactate formed per molecule of glucose consumed, suggesting that little to no glycogen is produced during the 48-hour timeframe measured. Furthermore, the reported rate of glycogen synthesis in differentiated C_2C_{12} muscle cells is 11 nmol of glucose units.h^{-1}. mg total protein^{-1}, compared to a glucose uptake and phosphorylation rate of approximately 250 nmol.h^{-1}.mg total protein^{-1} under basal conditions[18]. The maximal outflow of glucose to glycogen synthesis can be estimated to be lower than 5 %, which is small enough to be excluded in this study. Therefore, the production and consumption of glycogen will not be included in the model.

To investigate the behaviour of glycolysis in skeletal muscle cells a detailed kinetic model describing glycolysis in C_2C_{12} myofibers will be constructed. The activity of each enzyme in the glycolytic pathway will be measured at varying concentrations of its substrates to derive a mathematical equation that describes the activity of the enzyme. A bottom-up modelling approach was employed by setting up a series of ordinary differential equations (ODE's) from the mathematically derived rate equations. The glycolytic model was then used to predict the behaviour of glycolysis in differentiated C_2C_{12} muscle extract under various conditions.

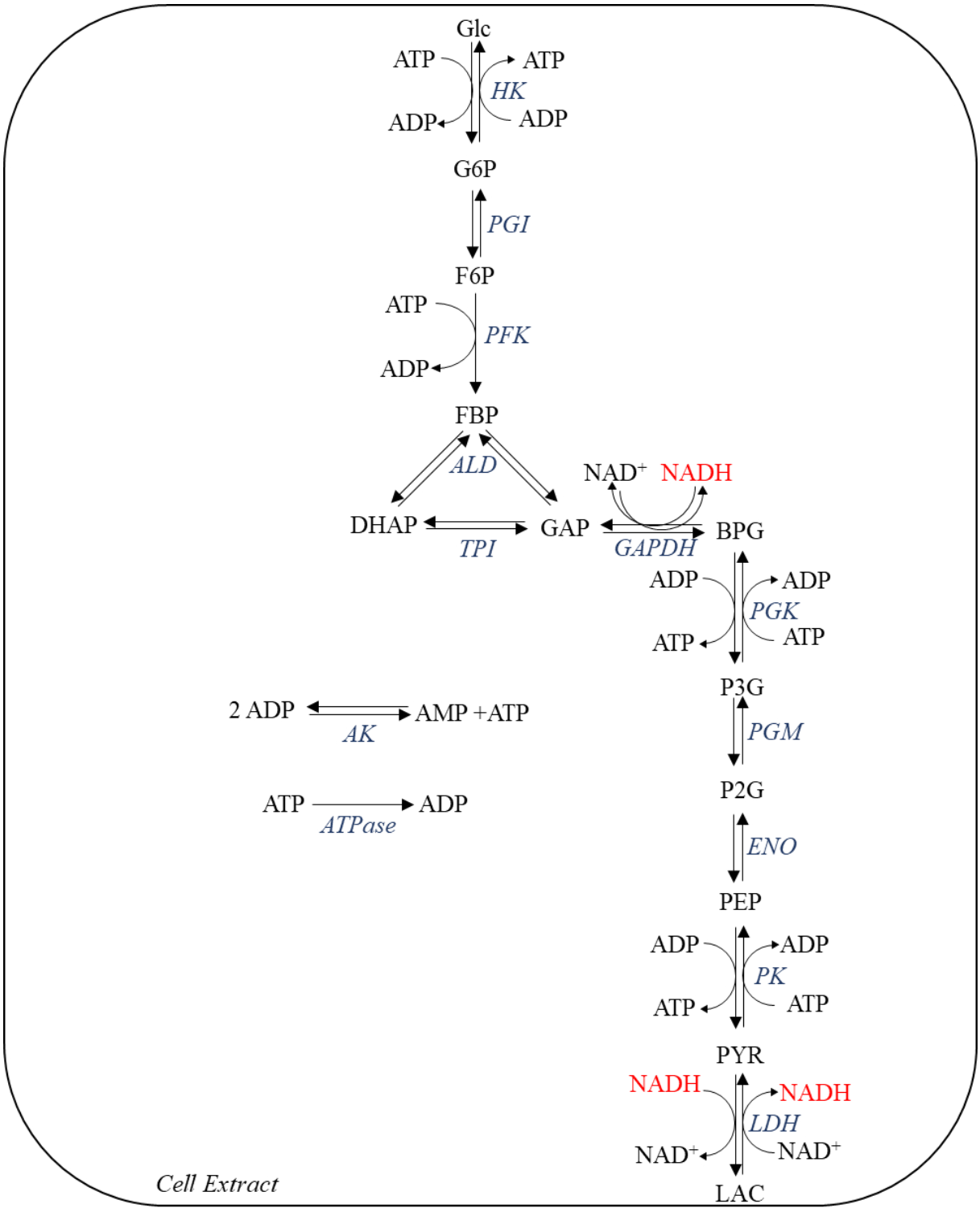

***Figure 4.1**: Schematic representation of glycolysis in C_2C_{12} skeletal muscle extract. The enzymes marked in blue notes the enzymes of interest in this study and will form the 13 reactions used to construct a detailed kinetic model of glycolysis in C_2C_{12} skeletal muscle extract. NADH marked in red can be visualised spectrophotometrically at 340 nm to quantify the rate of each enzyme of interest.*

4.3. *Materials and Methods*

4.3.1. *C_2C_{12} Culturing Protocol*

C_2C_{12} myocyte freezer stocks were obtained from *ATCC*[i] and was stored under liquid nitrogen. The C_2C_{12} freezer stocks were seeded in a T75 culturing flask (Nest Biotech Co., nonpyrogenic polystyrene flasks) and maintained in Delbecco's modified Eagle's medium (DMEM, *gibco*) containing 1 g/L (5.55 mM) glucose, L-glutamine and sodium pyruvate. For proliferation of the C_2C_{12} myocytes, the DMEM was augmented with 10% fetal calf serum (FBS, *gibco*), 100 U/mL penicillin and 100 µg/mL streptomycin (penstrep, *Sigma-Aldrich*). Initial growth in low glucose DMEM (LG-DMEM) containing 1 g/L glucose, resulted in very slow growth rates. Furthermore, differentiation was found to be poor and unreliable. Much better growth rates and differentiation was obtained when the proliferation media (LG-DMEM, 10% FBS, penstrep) was augmented with 1% of a 100 g/L glucose solution (*Sigma-Aldrich*) to give a final glucose concentration of 10 mM, abbreviated as MG-DMEM. Cells were grown at 37 ºC under a humidified atmosphere maintained at 5% CO_2 in an incubator. Proliferation conditions were maintained until a confluence of between 70 – 80% was reached (*approx*. 2 – 3 days). The cell cultures were kept below a confluence of 80% to ensure that the cultured cells remained in the log growth phase. Once the cultured cells had reached a confluence of 70 – 80%, the cultured cells were split by treating the cells with trypsin (*Sigma-Aldrich*) and equal fractions of the suspended cells were transferred into 3 new T75 flasks. The cultured cells were again grown to 70 – 80% confluence and each T75 were split into three T175 culturing flasks. The T175 culturing flasks were grown to 95% confluence upon which the culturing media was changed to differentiation media consisting of MG-DMEM augmented with penstrep and 2% horse serum (*Sigma-Aldrich*). The cells were grown under differentiation media for a total of 7 days. Images of the progression of differentiation are shown in Figure 4.2. On day 7 C_2C_{12} myofibers were clearly visible and the cells were harvested stored in an assay buffer that mimics of skeletal muscle cytosolic conditions.

4.3.2. *Deriving a standardised buffer to mimic cytosolic conditions*

To ensure that the enzyme activities measured *in vitro* reflect activities within the cell, it was important to measure the enzyme activities in a matrix that mimics the cytosolic conditions

[i] Special thanks to Dr. Annadie Krygsman for supplying the C_2C_{12} freezer stocks.

in which the enzymes function. Therefore, an approach similar to the approach taken by van Eunen *et. al.*[10] was taken to construct a cytosolic representative buffer system. The buffer system was constructed from the elemental analysis performed on the cytosol of frog toe muscle and consisted of the following chemical components: 50 mM Tris-HCl, 30 mM KH_2PO_4, 10 mM NaCl, 130 mM KCl and 10 mM $MgCl_2$[19]. The assay buffer was heated to 37 ºC and the pH was adjusted to 7.4 at the operating temperate of the buffer. Harvesting of the C_2C_{12} myofibers along with all assays performed of the C_2C_{12} myofibers were performed in this buffer.

4.3.3. Harvesting and preparation of differentiated C_2C_{12} cell lysate

Once a large amount of differentiated C_2C_{12} myofibers were visible in the culturing flasks (approx. 7 days of differentiation, refer to Figure 4.2 G and H) the C_2C_{12} myofibers were serum starved overnight by refreshing the fibres with LG-DMEM. After overnight serum starvation the cells were washed 3 times with assay buffer by adding an approximate 5 mL of assay buffer to the flask, swirling the flask to ensure that the LG-DMEM is rinsed off and then discarding the assay buffer. After the final wash step 1mL of a harvesting buffer was added. The harvesting buffer was prepared by adding a protease inhibitor cocktail to 10 mL of the assay buffer. The cells were scraped from the surface of each flask, suspended in the harvesting buffer and aliquoted into 3 cryovials for storage at -80ºC until required, typically within 3 months.

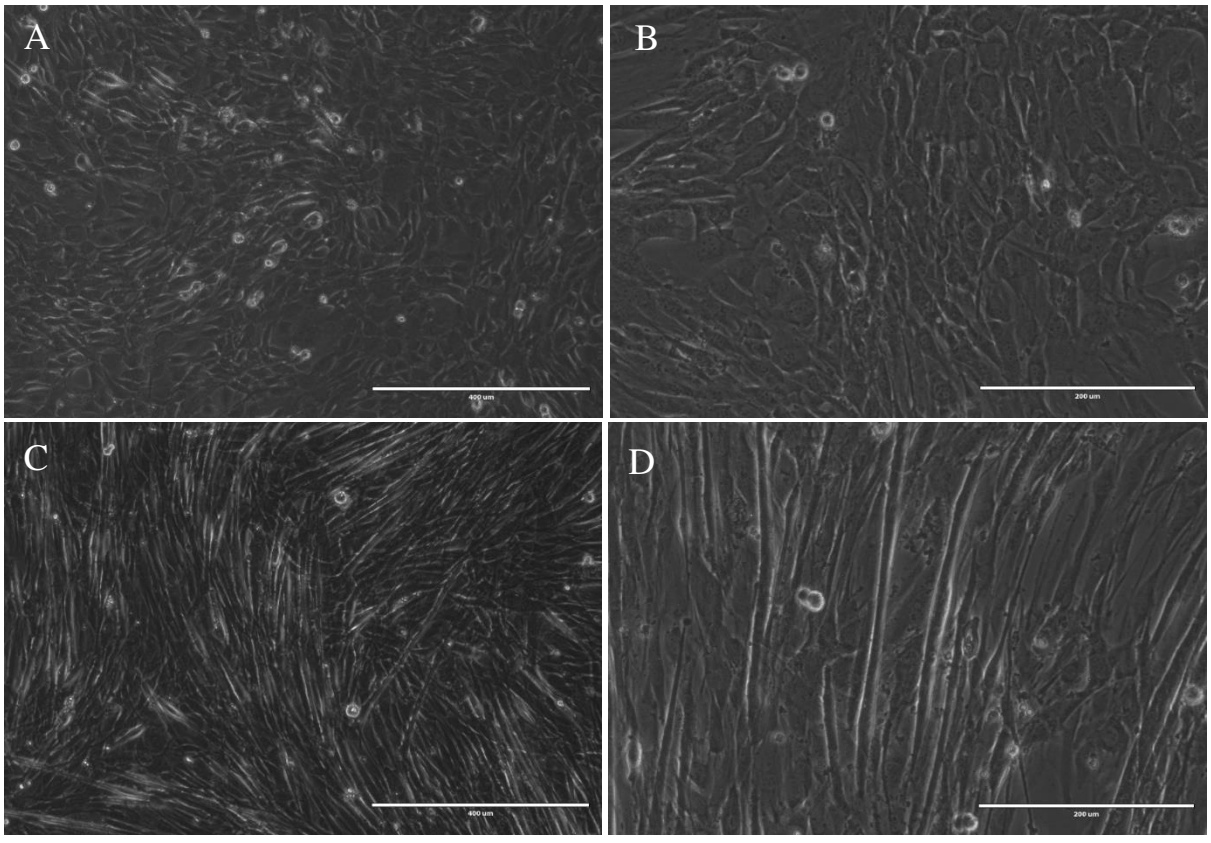

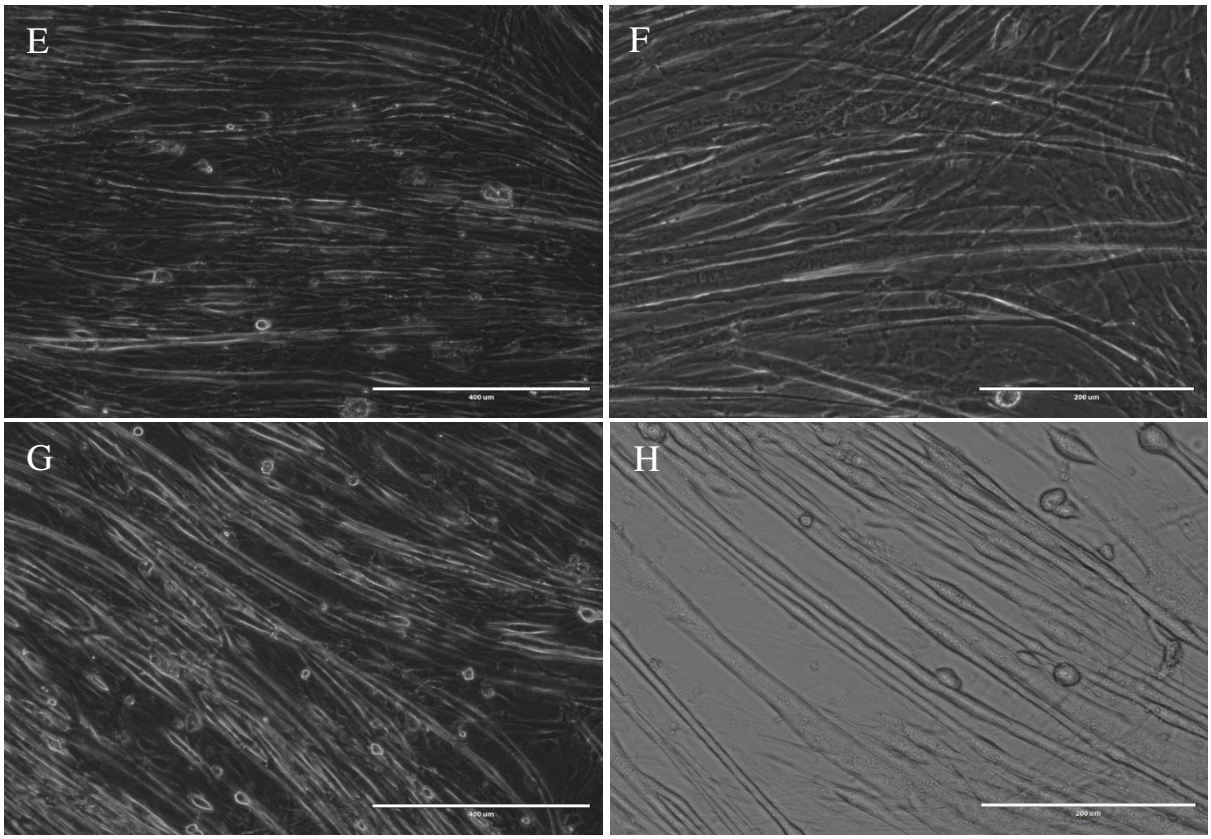

Figure 4.2**: Images of the C_2C_{12} muscle cells during differentiation;* **A: Image on day 0 of differentiation at 400 µm scale.* **B***: Image on day 0 of differentiation at 200 µm scale.* **C***: Image on day 2 of differentiation at 400 µm scale.* **D***: Image on day 2 of differentiation at 200 µm scale.* **E***: Image on day 4 of differentiation at 400 µm scale.* **F***: Image on day 4 of differentiation at 200 µm scale.* **G***: Image on day 7 of differentiation at 400 µm scale.* **H***: Image on day 7 of differentiation at 200 µm scale.*

When required the cells were thawed to prepare lysate. 2 protocols for the preparation were attempted and will briefly be discussed here: **(1)** the thawed aliquot of cells was added to fine glass beads (≤ 106 µm diameter, *Sigma-Aldrich*) at a ratio of 25 mg glass beads to 1 mL of cell suspension. Lysis was performed by vortexing the cell suspension for 1 minute followed by resting the suspension on ice for 15 seconds and repeating this cycle 6 times. The cell solution was then centrifuged at 20 800 x *g* at 4ºC for 15 minutes to pellet the cell debris. After centrifugation the supernatant was removed and stored on ice. **(2)** 20µL of a 10% solution of Triton X-100 (*Unitek*) was added to the thawed aliquot of harvested C_2C_{12} fibres and left to react on ice for 30 minutes, shaking every 5 minutes. Triton X-100 is a non-ionic surfactant that is widely used to lyse cells by disrupting the integrity of the cell membrane to release the cytosolic content[20]. After the 30-minute treatment with Triton X-100 is done the cell solution was then centrifuged at 20 800 x *g* at 4ºC for 15 minutes to pellet the cell debris. After centrifugation the supernatant was removed and stored on ice. The supernatant prepared from the differentiated C_2C_{12} muscle cells was used for the kinetic characterisation of the glycolytic

enzymes. Preliminary investigation of the enzyme activity of hexokinase (HK) and Phosphoglucoisomerase (PGI) showed little difference in the results obtained from the 2 lysis protocols (data not shown). However, lysing the cells with Triton X-100 resulted in a higher recovery of the volume of supernatant containing the cell lysate. Therefore, all enzyme assays were performed on lysate obtained via Triton X-100 treatment of the C_2C_{12} fibres. Coupled enzyme assays for the determination of glycolytic enzyme rates.

4.3.4. Kinetic characterisation of the glycolytic enzymes using coupled enzyme assays

The glycolytic enzymes were characterised in terms of their maximal specific activity (Vmax) and affinity for each substrate and product (Km) in cell lysate. Characterisation of the kinetic parameters (Vmax, Km) for each glycolytic enzyme was done in a cytosolic representative assay buffer at a pH of 7.4 and temperature of 37 ºC to mimic the physiological operating conditions of the glycolytic enzymes. The kinetic parameters were determined by linking each glycolytic enzyme to the production or formation of NADH or NADPH, adapted from Teusink *et. al.*[11], and measuring the change in NADH or NAPDH concentration spectrophotometrically at 340 nm on a *BioTek PowerWave 340* or *BMG Labtech SPECTROstar*^{Nano} spectrophotometer. Measurement of glycolytic enzyme activity was done in a 96-well plate (*Greiner bio-one F-Bottom* microtiter plate) with a total volume of 100 µL.

To ensure that the enzyme under investigation is rate limiting, each of the coupling enzymes were used at a final concentration of 5 U/mL. Furthermore, the activity of the linking enzymes was tested by performing an assay in the absence of the rate limiting enzyme and in the presence of its product to ensure that the activity of the series of linking enzymes are much faster than the enzyme under investigation. All enzymes and reactants were sourced from *Sigma-Aldrich*. Enzyme assays were performed under varying concentrations of enzyme substrates as 3 technical repeats to account for experimental and instrumental error. In the case of bi-substrate reactions, assays were performed under saturating concentrations of one substrate while varying the concentration of the other substrate. Concerning the coupled assays that are ATP or ADP dependent, a magnesium concentration equal to double the ATP or ADP concentration was added to ensure that the active MgATP or MgADP complex was present. The resulting rate obtained from the coupled assays represents the change in absorbance as a function of time. However, for modelling purposes it is necessary to convert this rate to describe the change in substrate as a function of time per protein concentration (µmol/ min. mg total protein^{-1}). The relationship between concentration and absorbance is described by the Beer-

Lambert law where the total protein concentration is determined by means a Bradford reaction. It is important to note that the pathlength of the sample is dependent on the volume in each well. Therefore, the relationship between absorbance and the concentration of substrate was rather established by means of a NADH calibration curve. The response factor representing the extinction coefficient of NADH and the pathlength of the assay was determined for the wells in the 96 well plate. The experimental description for the measurement of the enzyme activity for each enzyme investigated in this study is discussed below:

Hexokinase (HK) catalyses the phosphorylation of glucose (GLC) to form glucose-6-phosphate (G6P) through the transfer of phosphate from ATP. In so doing, ATP is converted to ADP as a product of this reaction. The activity of hexokinase was determined with various concentrations of the substrates and potential activators or inhibitors. The rate of hexokinase was quantified using a coupled assay technique and observing the formation of NADPH at 340 nm as a function of time. To visualize the activity of hexokinase the enzyme was coupled to an excess amount of commercially obtained G6PDH to ensure that the rate of G6PDH vastly exceeds that of the hexokinase under investigation. G6PDH catalyses the conversion of the hexokinase product, G6P, to phosphor-D-glucono-1,5-lactone (PGL) accompanied with a conversion of $NADP^+$ to NADPH. Therefore, the change in concentration of NADPH is stoichiometrically equivalent to the change in glucose concentration and reflects the activity of hexokinase.

Phosphoglucoisomerase (PGI) catalyses the isomerization of G6P to fructose -6-phosphate (F6P). The kinetic activity of PGI was determined in both the forward and reverse directions. Measurement of PGI in the forward direction was done by measuring the conversion of NADH to NAD^+ by coupling the enzymatic reaction via phosphofructokinase (PFK), Aldolase (ALD) and Triosephosphate isomerase (TPI) to glycerol-3-phosphate dehydrogenase (G3PDH). G3PDH converts dihydroxyacetone phosphate (DHAP), a product of ALD, to glycerol-3-phosphate (G3P). The conversion of DHAP to G3P is associated with a conversion of NADH to NAD^+, which is utilized to visualize the consumption of G6P by PGI. Therefore, an excess amount of the commercially obtained enzymes of PFK, ALD, TPI and G3PDH was added to each well to ensure that the conversion of F6P to G3P was always faster than the conversion of G6P to F6P through PGI supplied by the lysate of C_2C_{12} muscle myotubes. It is important to note the 1:2 stoichiometric relationship between G6P consumption and NAD^+ production and this relationship was taken into account when determining the rate of the

forward reaction of PGI. The kinetic activity of PGI in the reverse direction was measured by coupling the enzyme to an excess amount of commercially obtained G6PDH. Therefore, the conversion of F6P to G6P is measured spectrophotometrically at 340 nm by the conversion of $NADP^+$ to NADPH.

Phosphofructokinase (PFK) catalyses the phosphorylation of F6P to form fructose -1,6-bisphosphate (FBP), via the transfer of a phosphate from ATP, yielding ADP as a product. The kinetic activity of PFK was measured by coupling the enzyme to G3PDH via ALD and TPI. Excess amounts of commercially obtained ALD, TPI and G3PDH was used to ensure that PFK obtained from the lysate of C_2C_{12} muscle myofibers was rate limiting. Therefore, the activity of PFK will be equal to half the conversion of NADH to NAD^+ via G3PDH due to the stoichiometric relationship between FBP and G3P. PFK is monitored directly by measuring the consumption of NADH spectrophotometrically at 340 nm.

Aldolase (ALD) catalyses the dissociation of FBP into dihydroxyacetone phosphate (DHAP) and glyceraldehyde -3- phosphate (GAP). The kinetic activity of ALD was measured in the forward direction under varying FBP concentrations by coupling the enzyme to G3PDH and measuring the conversion of NADH to NAD^+. Excess amounts of commercially acquired G3PDH and TPI was added to ensure that the aldolase obtained from the lysate of C_2C_{12} muscle myofibers is the rate limiting reaction. This will ensure that the conversion of NADH to NAD^+ reflects 2 times the consumption rate of FBP. ALD is monitored directly by measuring the consumption of NADH spectrophotometrically at 340 nm.

Glyceraldehyde-3-phosphate dehydrogenase (GAPDH) catalyses the conversion of GAP to 1,3-bisphosphoglycerate (BPG) accompanied with the conversion of NAD^+ to NADH. This entails incorporation of an additional phosphate group into GAP from the inorganic phosphate present in the matrix. Therefore, this reaction is expected to be dependent on the inorganic phosphate concentration of the matrix. However, the effect of inorganic phosphate concentration on GAPDH activity was not tested, and we assumed that the inorganic phosphate concentration in skeletal muscle cells remains saturating over time under non-exercising conditions. Since GAPDH activity entails the conversion of NAD^+ to NADH, this reaction can be monitored directly by measuring the formation or consumption of NADH spectrophotometrically at 340 nm.

3-phosphoglycerate kinase (PGK) catalyses the conversion of BPG to P3G through the transfer of a phosphate from BPG to ADP. Therefore, the reaction is dependant on the availability of ADP and results in the production of ATP. The activity of PGK was measured in the reverse direction by coupling the enzyme to GAPDH. This reaction can be monitored directly by measuring the consumption of NADH spectrophotometrically at 340 nm.

Pyruvate kinase (PK) catalyses the conversion of phosphoenol pyruvate (PEP) to pyruvate through the transfer of a phosphate from PEP to ADP resulting in the formation of ATP as a product of the reaction. The activity of PK was measured in the forward direction under varying concentrations of the substrates PEP and ADP as well as under varying concentrations of the product ATP to determine the inhibitory effect of ATP. The activity of PK was measured by coupling the PK obtained from the C_2C_{12} myofiber extract to an excess amount of commercially obtained lactate dehydrogenase (LDH) to ensure that PK is the rate limiting enzyme. LDH converts the PK product, PYR, to LAC along with the conversion of NADH to NAD^+ and the activity of PK can be monitored by measuring the consumption of NADH spectrophotometrically at 340 nm.

Lactate dehydrogenase (LDH) catalyses the conversion of pyruvate (PYR) to lactate (LAC). This reaction is dependent on the availability of NADH as a substrate of the reaction and yields NAD^+ as a product. Activity was measured by monitoring the change in the concentration of NADH spectrophotometrically at 340 nm as a function of time.

Adenylate kinase (AK) catalyses the conversion of ADP to ATP and AMP via the transfer of a phosphate group from one ADP molecule to another ADP molecule. The activity of AK was measured in the forward, and the reverse direction at varying concentrations of ATP, ADP and AMP. AK activity was measured in the forward direction by coupling the enzyme to excess amounts of HK and G6PDH in the presence of excess amounts of GLC. This allows for the conversion of the product ATP to ADP, yielding an equivalent amount of G6P which gets converted by G6PDH along with the conversion of NAD^+ to NADH. Activity was measured by monitoring the change in the concentration of NADH as a function of time. AK activity was measured in the reverse direction by coupling the enzyme to excess amounts of PK and LDH. This allowed for the conversion of ADP, as product of the reverse direction, along with the conversion of PEP to PYR. PYR will then rapidly be converted to LAC along with the conversion of NADH to form NAD^+. Activity was measured by monitoring the change in the concentration of NADH spectrophotometrically at 340 nm as a function of time.

The **ATPase** reaction describes the time dependent conversion of ATP to ADP by cellular maintenance and reactions and muscle contraction in C_2C_{12} skeletal muscle myotubes. The ATPase activity in cell extract is expected to be significantly less compared to intact muscle fibres due to the removal of the membrane fraction. The activity of ATPase was measured at varying ATP concentrations by coupling the reaction to commercially obtained PK and LDH in the presence of 10 mM PEP and 0.5 mM NADH. The time dependent conversion of ATP to ADP drives the conversion of PEP to PYR followed by the conversion of PYR to LAC. The conversion of PYR to LAC corresponds with an equivalent conversion of NADH to NAD^+. Therefore, the decrease in NADH concentration is equivalent to the decrease in ATP concentration. Activity was measured by monitoring the change in the concentration of NADH spectrophotometrically at 340 nm as a function of time.

The resulting series of initial rates obtained for each glycolytic enzyme at varying product and substrate concentrations form an experimental dataset describing the activity of each enzyme. Each glycolytic enzyme was described with a single rate equation. Therefore, the complete dataset for a specific enzyme was used as a single data array for fitting its rate equation. The *NonLinearModelFit* function of *Wolfram Mathematica* was performed on the combined multidimensional dataset to determine the optimal kinetic parameters describing the activity of each enzyme. The resulting kinetic parameters obtained for each enzyme was compared to kinetic parameters in literature. It should be noted that a direct comparison cannot be made since the values obtained for the kinetic parameters will be different if different rate equations are used. Therefore, our criteria for considering the comparison of kinetic parameter values to published values as good, is when the values are within the same order of magnitude, acceptable when the values are within 2 orders of magnitude and not good when the difference between values are further than 2 orders of magnitude apart.

4.3.5. Constructing a glycolytic model of differentiated C_2C_{12} extract

The resulting rate equations were arranged in a series of ordinary differential equations (ODE's) describing the change in concentration of each variable (chemical species) as a function of time. The set of ODE's was solved using the *NDSolve* function of *Wolfram Mathematica* and the steady state was calculated using the *FindRoot* function.

4.4. Results

4.4.1. Kinetic characterisation of HK

Hexokinase activity was measured in the forward direction, as discussed in Section 4.3.4 with various concentrations of the substrates; glucose and ATP as well as with varying AMP concentrations. A non-reversible bi-substrate reaction with allosteric inhibition by AMP and ATP, described by Eq.4.1, was found to describe the activity of hexokinase well. The *non-linear model fit* function of *mathematica* was used to fit Eq.4.1 to the complete experimental dataset acquired with the coupled enzyme assays. The *non-linear model fit* function determines the best set of kinetic parameters (Vf_{HK}, *K*atp, *K*glc, *Ki*amp and *Ki*atp) to mathematically describe the activity of hexokinase within the experimental boundaries tested, shown in Figure 4.3. A summary of the kinetic parameters is given in Table 4.1.

$$v\mathrm{HK} = \frac{Vf_{\mathrm{HK}} \cdot \mathrm{atp} \cdot \mathrm{glc}}{(1+\frac{\mathrm{atp}}{K\mathrm{atp}}) \cdot K\mathrm{atp} \cdot (1+\frac{\mathrm{glc}}{K\mathrm{glc}}) \cdot K\mathrm{glc} \cdot (1+\frac{\mathrm{amp}}{Ki\mathrm{amp}}) \cdot (1+\frac{\mathrm{atp}}{Ki\mathrm{atp}}) \cdot (1+\frac{\mathrm{atp}^2}{Ki\mathrm{atp}^2})} \quad \text{(Eq. 4.1)}$$

***Table 4.1**: Summary of the kinetic parameters determined for the forward reaction of hexokinase in C_2C_{12} mouse muscle myotubes. Eq.4.1 was fitted to the experimental dataset obtained for hexokinase. The fitted values (±standard error) are compared to values reported in literature for similar tissue types where values are available. (U = µmol/min)*

Parameter	Fitted Value	Units	Literature Value	Reference
Vf_{HK}	0.0129 ± 0.0019	U/mg total protein	-	
*K*atp	3.0646 ± 0.7116	mM	0.5 - 1.0	21
*K*glc	0.0663 ± 0.0168	mM	0.003 - 0.3	21
*Ki*atp	21.0749 ± 3.3200	mM		
*Ki*amp	2.3713 ± 0.2604	mM	2.5	22
Keq			3800	11

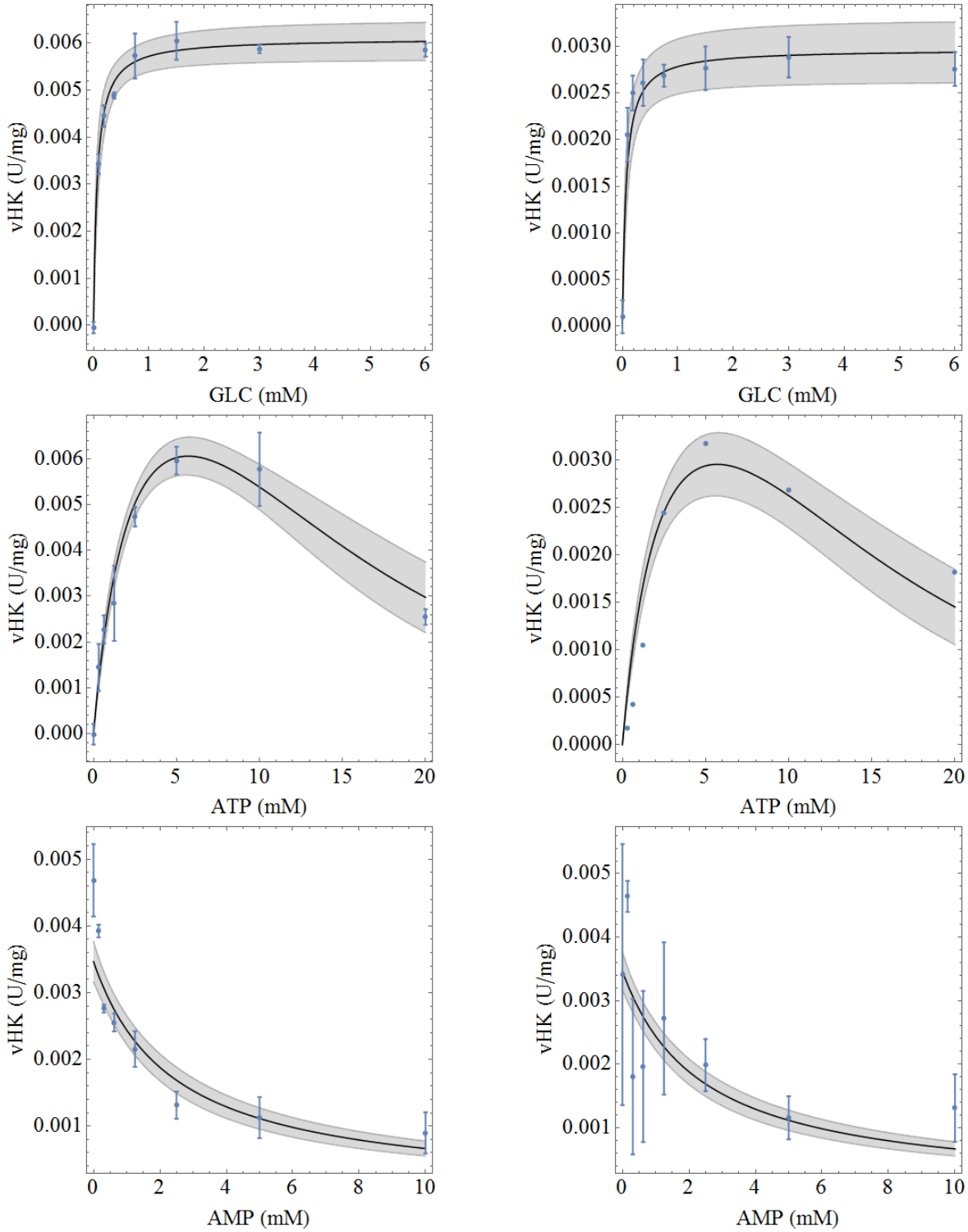

Figure 4.3**: Kinetic characterisation of hexokinase in C_2C_{12} muscle myotubes under varying substrate concentrations:* ***(top-left) - *Saturation of hexokinase with glucose at 5 mM ATP and 0 mM AMP.* ***(top-right) -*** *Saturation of hexokinase with glucose at 5 mM ATP and 2.5 mM AMP.* ***(centre-left) -*** *Saturation of hexokinase with ATP at 6 mM glucose and 0 mM AMP.* ***(centre-right) -*** *Saturation of hexokinase with ATP at 6 mM glucose and 2.5 mM AMP.* ***(bottom-left) -*** *Inhibition of hexokinase with AMP at 6 mM glucose and 1.25 mM ATP.* ***(bottom-right) -*** *Inhibition of hexokinase with AMP at 6 mM glucose and 1.25 mM ATP. The blue dots represent the experimental data obtained; the black line represents the simulated fit of the complete dataset (95% confidence represents by the shaded area).*

The mathematical description of hexokinase illustrated in Eq.4.1 describes a non-reversible bi-substrate reaction with allosteric inhibition by AMP and ATP. The inhibitory effect of AMP was well described assuming a single binding site on the enzyme. However, the inhibition afforded by ATP assumes one active site and 3 inhibitory sites for ATP on the enzyme. This mechanism resulted in a better description of the experimental dataset compared to either one or four inhibitory binding sites for ATP. Overall, Eq.4.1 accurately described the kinetic data and a good correlation between the kinetic data and the mathematical description given by Eq.4.1 is obtained as shown in Figure 4.3. Limited data is available in literature for comparison of the kinetic parameters and the values obtained are dependent on the rate equation used, and comparison should be made with care. The value reported for *K*atp is lower in literature compared to our determination, but within the same order of magnitude. The value for *K*glc compares very well with what is reported in literature.

4.4.2. Kinetic characterisation of PGI

PGI activity was measured in the forward and reverse direction as discussed in Section 4.3.4, with varying concentrations of its substrate (G6P) and product (F6P). The *non-linear model fit* function of *Mathematica* was used to fit a reversible Michealis-Menten equation shown in Eq.4.2 to determine the kinetic parameters (Vf_{PGI}, Vr_{PGI}, *K*g6p, *K*f6p) that best describe the experimental dataset used for PGI in C_2C_{12} muscle myotubes. The *non-linear model fit* of the experimental dataset is shown in Figure 4.4 and the determined parameters are listed in Table 4.2.

$$v\mathrm{PGI} = \frac{\frac{Vf_{\mathrm{PGI}} \cdot \mathrm{g6p}}{K\mathrm{g6p}} - \frac{Vr_{\mathrm{PGI}} \cdot \mathrm{f6p}}{K\mathrm{f6p}}}{1 + \frac{\mathrm{g6p}}{K\mathrm{g6p}} + \frac{\mathrm{f6p}}{K\mathrm{f6p}}} \qquad \text{(Eq. 4.2)}$$

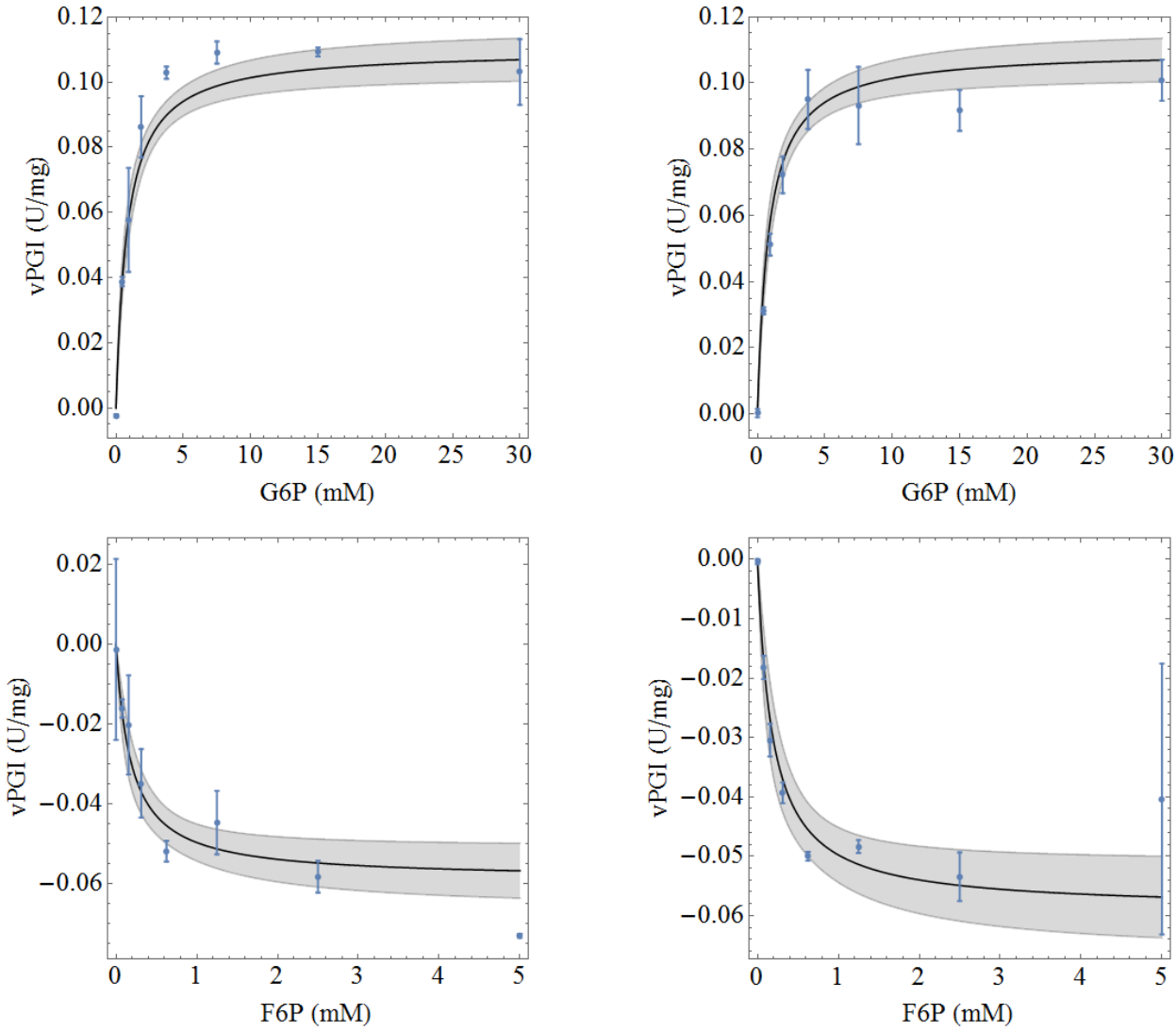

***Figure 4.4**: Kinetic characterisation of PGI in C_2C_{12} muscle myotubes under varying substrate concentrations.* ***(top-left) -** Saturation of PGI in the forward direction with G6P.* ***(top-right) -** Saturation of PGI in the forward direction with G6P.* ***(bottom-left) -** Saturation of PGI in the reverse direction with F6P.* ***(bottom-right) -** Saturation of PGI in the reverse direction with F6P. The blue dots represent the experimental data obtained; the black line represents the simulated fit of the complete dataset (95% confidence represents by the shaded area).*

***Table 4.2**: Summary of the kinetic parameters determined for the forward and reverse reactions of PGI in C_2C_{12} mouse muscle myotubes. Eq.4.2 was fitted to the experimental dataset obtained for PGI. The fitted values (± standard error) are compared to values reported in literature for similar tissue types where values are available. (U = µmol/min)*

Parameter	Fitted Value	Units	Literature Value	Reference
Vf_{PGI}	0.1098 ± 0.0036	U/mg total protein		
Vr_{PGI}	0.0589 ± 0.0039	U/mg total protein		
*K*g6p	0.8353 ± 0.1282	mM	0.48	23
*K*f6p	0.1845 ± 0.0523	mM	0.031	24
Keq	0.3607 - 0.4437		0.314	25

The rate equation for PGI is a reversible Michealis-Menten equation. The negative rate observable in Figure 4.4 denotes the rate of the reaction in the reverse direction. The reversible Michealis-Menten equation given in Eq.4.2 accurately describes the kinetic data as shown in Figure 4.4. The parameters determined for PGI summarised in Table 4.2, can be used to determine the equilibrium constant (*Keq*) for the species G6P and F6P by using the Haldane relation. Given that the *Keq* is equal to the ratio of the product and the substrate at equilibrium for a given reaction, the equilibrium constant can be calculated with Eq.4.3.

$$Keq(\mathrm{PGI}) = \frac{Vf_{\mathrm{PGI}} \cdot K\mathrm{f6p}}{Vr_{\mathrm{PGI}} \cdot K\mathrm{g6p}} \qquad \text{(Eq. 4.3)}$$

The *Keq* for PGI as determined using the Haldane relation yields a slightly higher, but comparable value as compared to the referenced value for the *Keq* of PGI in literature (Table 4.2).

4.4.3. Kinetic characterisation of PFK

The PFK activity was measured in the forward direction, as discussed in Section 4.3.4, with varying F6P and ATP concentrations. A non-reversible bi-substrate Michealis-Menten equation shown in Eq.4.4 was used to describe the experimental dataset and a *non-linear model fit* function was fitted to the complete experimental dataset to determine the kinetic parameters (V_{PFK}, Katp, Kf6p) that best describe the data obtained. The *non-linear model fit* to the experimental data is shown in Figure 4.5 and the determined kinetic parameter are listed in Table 4.3.

$$v\mathrm{PFK} = \frac{V_{\mathrm{PFK}} \cdot \mathrm{atp} \cdot \mathrm{f6p}}{(1 + \frac{\mathrm{atp}}{K\mathrm{atp}}) \cdot K\mathrm{atp} \cdot (1 + \frac{\mathrm{f6p}}{K\mathrm{f6p}}) \cdot K\mathrm{f6p}} \qquad \text{(Eq. 4.4)}$$

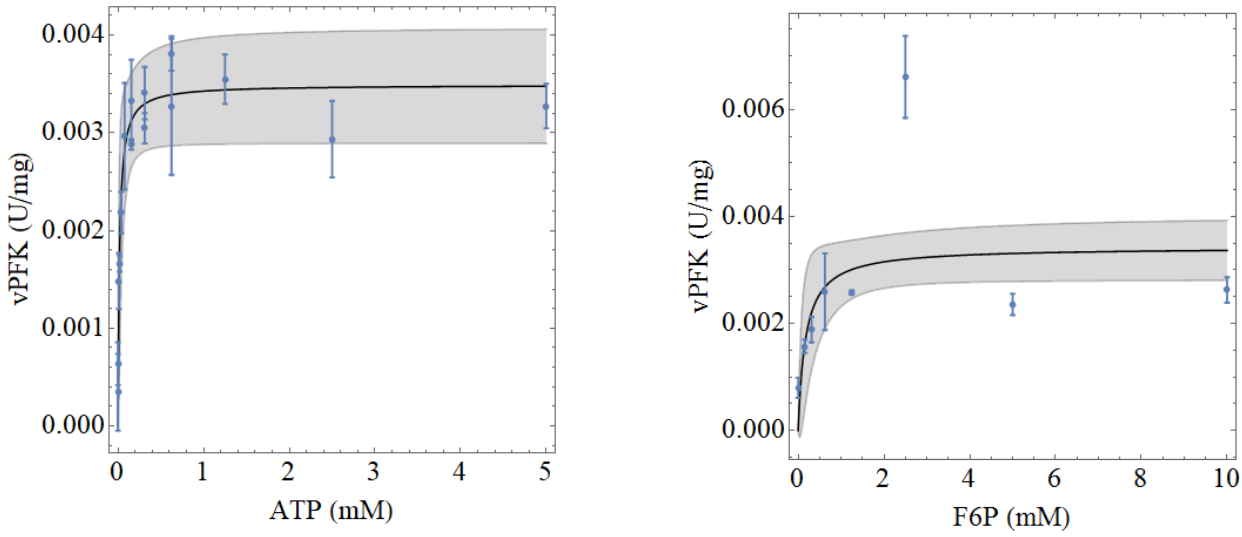

***Figure 4.5**:Kinetic characterisation of PFK in C_2C_{12} muscle myotubes under varying substrate concentrations.**(left)** - Saturation of PFK with ATP at a F6P concentration of 10 mM. **(right)** - Saturation of PFK with F6P at an ATP concentration of 10 mM. The blue dots represent the experimental data obtained; the black line represents the non-linear model fit simulation of the complete dataset (95% confidence represents by the shaded area).*

***Table 4.3**: Summary of the kinetic parameters determined for the non-reversible Michaelis-Menten equation describing PFK activity in C_2C_{12} muscle myotubes. Eq.4.3 was fitted to the complete experimental dataset obtained for PFK. The fitted values (± standard error) are compared to values reported in literature for similar tissue types where values are available. (U = µmol/min)*

Parameter	Fitted Value	Units	Literature Value	Reference
Vf_{PFK}	0.0036 ± 0.0003	U/mg total protein		
*K*atp	0.01827 ± 0.0116	mM	0.02654	26
*K*f6p	0.1926 ± 0.1351	mM	0.06849	26
Keq			800	27

The rate equation for PFK given in Eq.4.3 describes a non-reversible bi-substrate Michealis-Menten type of mechanism and gives a good fit to the data. Furthermore, comparison of the kinetic parameters obtained for PFK with the parameters given in literature is within the same order of magnitude.

4.4.4. Kinetic characterisation of ALD

ALD activity was measured in the forward direction, as discussed in Section 4.3.4, with varying FBP concentrations .A non-reversible mono-substrate Michealis-Menten equation given in Eq.4.5 was used to fit the activity of ALD in C_2C_{12} muscle myofibers. A *non-linear model fit* function was fitted to the complete experimental dataset to determine the kinetic parameters (V_{ALD}, *K*fbp) that best describe the data obtained. The experimental data and the

non-linear model fit of the experimental data is shown in Figure 4.6 and the determined kinetic parameter are listed in Table 4.4.

$$v\text{ALD} = \frac{Vf_{\text{ALD}} \cdot \text{fbp}}{\left(1 + \frac{\text{fbp}}{K\text{fbp}}\right) \cdot K\text{fbp}} \qquad \text{(Eq. 4.5)}$$

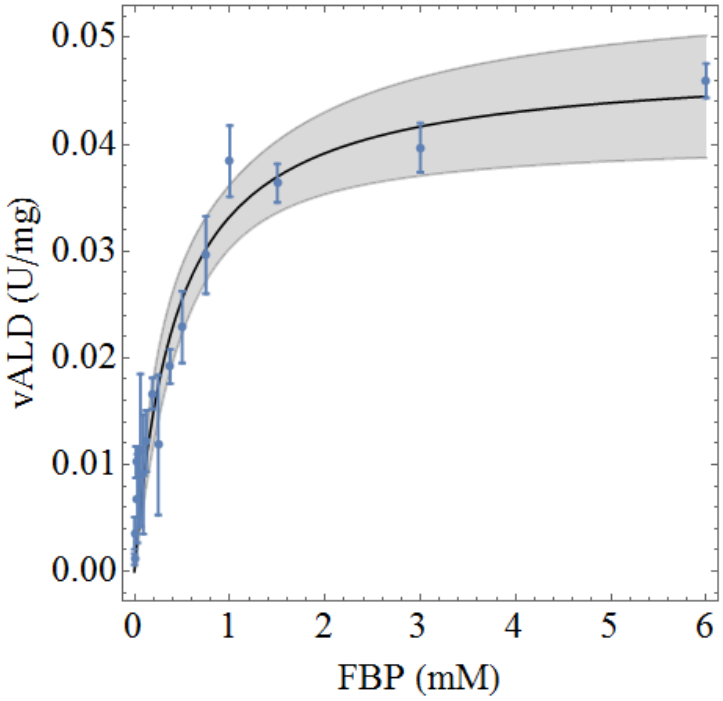

***Figure 4.6**: Kinetic characterisation of ALD in C_2C_{12} muscle myotubes under varying substrate concentrations. The experimental data gives the activity of ALD as a function of FBP concentration. The blue dots represent the experimental data obtained; the black line represents the non-linear model fit simulation of the complete dataset (95% confidence represents by the shaded area).*

***Table 4.4**: Summary of the kinetic parameters determined for the Michaelis-Menten equation describing ALD activity in C_2C_{12} muscle myotubes in the forward direction. Eq.4.5 was fitted to the complete experimental dataset obtained for ALD. The fitted values (± standard error) are compared to values reported in literature for similar tissue types where values are available. (U = µmol/min)*

Parameter	Fitted Value	Units	Literature Value	Reference
Vf_{ALD}	0.0477±0.0034	U/mg total protein		
Kfbp	0.4353±0.0933	mM	0.05	6
Keq			0.052	28

The mono-substrate Michealis-Menten equation given in Eq.4.5. accurately describes the kinetic data and a good fit is obtained between the experimental data set and the predicted fit as shown in Figure 4.6. The optimized parameters for ALD are summarised in Table 4.4. A

literature comparison for the kinetic parameters obtained in this study shows that our value for *K*fbp is 10-fold larger compared to what is reported in literature.

4.4.5. Kinetic characterisation of GAPDH

The activity of GAPDH was measured in the reverse direction under varying concentrations of the substrates. BPG is not commercially available and to measure GAPDH in the reverse direction the reaction was coupled to an excess amount of the enzyme phosphoglycerate kinase (PGK) and the reaction was initialised with 3-phosphoglycerate (P3G) as substrate in the presence of excess ATP. GAPDH activity in the forward direction can be measured with the same experimental setup in the presence of NAD^+ and GAP, however this experiment was not performed. In the presence of excess PGK, the conversion of P3G to BPG is assumed to be at equilibrium. The *Keq* for PGK is equal to 3 200[11] and the corresponding initial concentration of BPG can be determined using Eq. 4.6.

$$[\mathrm{BPG}] = \frac{[\mathrm{P3G}] \cdot [\mathrm{ATP}]}{[\mathrm{ADP}] \cdot Keq} \qquad \text{(Eq. 4.6)}$$

A non-reversible bi-substrate Michealis-Menten equation, given in Eq.4.7, was used to fit the GAPDH activity. A *non-linear model fit* function was fitted to the complete experimental dataset to determine the kinetic parameters (Vr_{GAPDH}, *K*bpg, *K*nadh) that best describe the data obtained. The experimental data and the *non-linear model fit* of the experimental data is shown in Figure 4.7 and the determined kinetic parameter are listed in Table 4.5.

$$v\mathrm{GAPDH} = \frac{-Vr_{\mathrm{GAPDH}} \cdot \mathrm{bpg} \cdot \mathrm{nadh}}{K\mathrm{bpg} \cdot \left(1 + \frac{\mathrm{bpg}}{K\mathrm{bpg}}\right) \cdot K\mathrm{nadh} \cdot \left(1 + \frac{\mathrm{nadh}}{K\mathrm{nadh}}\right)} \qquad \text{(Eq. 4.7)}$$

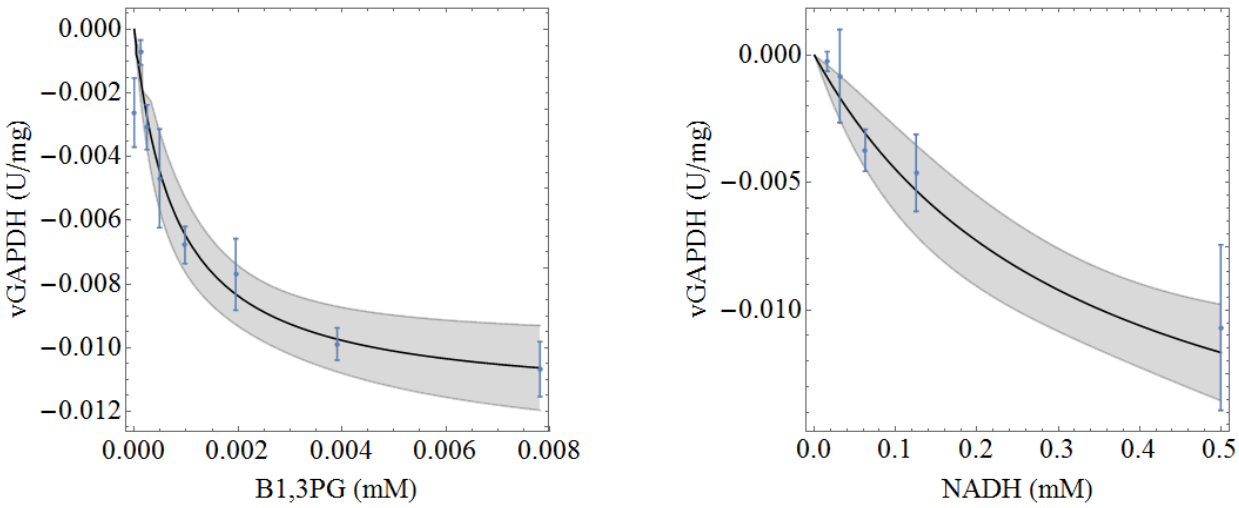

***Figure 4.7**: Kinetic characterisation of GAPDH in C_2C_{12} muscle myotubes in the reverse direction under varying substrate concentrations.* ***(left) -** Saturation of GAPDH with BPG (25 mM P3G) at a NADH concentration of 0.5 mM and an ATP concentration of 10 mM. the effective concentration of BPG was determined using Eq.4.6.* ***(right)** – Activity profile of GAPDH under varying concentrations of NADH at a P3G concentration of 25 mM and an ATP concentration of 10 mM. The blue dots represent the experimental data obtained; the black line represents the non-linear model fit simulation of the complete dataset (95% confidence represents by the shaded area).*

***Table 4.5**: Summary of the kinetic parameters determined for the Michaelis-Menten equation describing GAPDH activity in C_2C_{12} muscle myotubes in the reverse direction. Eq.4.7 was fitted to the complete experimental dataset obtained for GAPDH. The fitted values (± standard error) are compared to values reported in literature for similar tissue types where values are available. (U = µmol/min)*

Parameter	Fitted Value	Units	Literature Value	Reference
Vr_{GAPDH}	0.0195 ± 0.0047	U/mg total protein		
*K*bpg	0.0008 ± 0.0002	mM	0.0008	29
*K*nadh	0.3333 ± 0.1586	mM	0.0033	29
Keq			0.0056	30

The rate equation for GAPDH in Eq.4.7 describes a non-reversible bi-substrate mechanism in the reverse direction. A good correlation between the mathematical description of GAPDH and the experimental dataset is obtained as illustrated in Figure 4.7. The optimised parameters of GAPDH are listed in Table 4.5. The fitted parameter estimations for *K*bpg corresponds very well with what is reported in literature, but the fitted parameter for *K*nadh is much higher than reported in literature.

4.4.6. Kinetic characterisation of PGK

PGK activity was measured in the reverse direction, as discussed in Section 4.3.4, under varying concentrations of the substrates, P3G and ATP, and under varying concentrations of ADP to determine the inhibitory effect of ADP on the activity of the enzyme. The activity of PGK was measured by coupling the enzyme to an excess amount of commercially obtained GAPDH and monitoring the consumption of NADH. This also ensured that the product BPG does not increase to inhibitory levels. A Michealis-Menten equation, given in Eq.4.8, was used to mathematically describe the activity profile of PGK. A *non-linear model fit* function was fitted to the complete experimental dataset to determine the kinetic parameters (Vr_{PGK}, Kp3g, Katp, Kiadp) that best describe the data obtained. The experimental data and the *non-linear model fit* of the experimental data is shown in Figure 4.8 and the determined kinetic parameter are listed in Table 4.6.

$$v\mathrm{PGK} = \frac{-Vr_{\mathrm{PGK}} \cdot \mathrm{p3g} \cdot \mathrm{atp}}{K\mathrm{atp} \cdot \left(1 + \frac{\mathrm{atp}}{K\mathrm{atp}}\right) \cdot K\mathrm{p3g} \cdot \left(1 + \frac{\mathrm{p3g}}{K\mathrm{p3g}}\right) \cdot \left(1 + \frac{\mathrm{atp}}{Ki\mathrm{atp}}\right) \cdot \left(1 + \frac{\mathrm{adp}}{Ki\mathrm{adp}}\right)} \qquad \text{(Eq. 4.8)}$$

Table 4.6*: Summary of the kinetic parameters determined for the Michaelis-Menten equation describing PGK activity in C_2C_{12} muscle myotubes in the reverse direction. Eq.4.8 was fitted to the complete experimental dataset obtained for PGK. The fitted values (± standard error) are compared to values reported in literature for similar tissue types where values are available. (U = µmol/min)*

Parameter	Fitted Value	Units	Literature Value	Reference
Vr_{PGK}	0.5889 ± 0.07176	U/mg total protein		
Kp3g	1.0116 ± 0.1716	mM	1.37	31
Katp	0.4932 ± 0.1602	mM	0.42	31
Kiatp	39.7968 ± 22.2315	mM		
Kiadp	1.994 ± 0.3839	mM		
Keq			3200	11

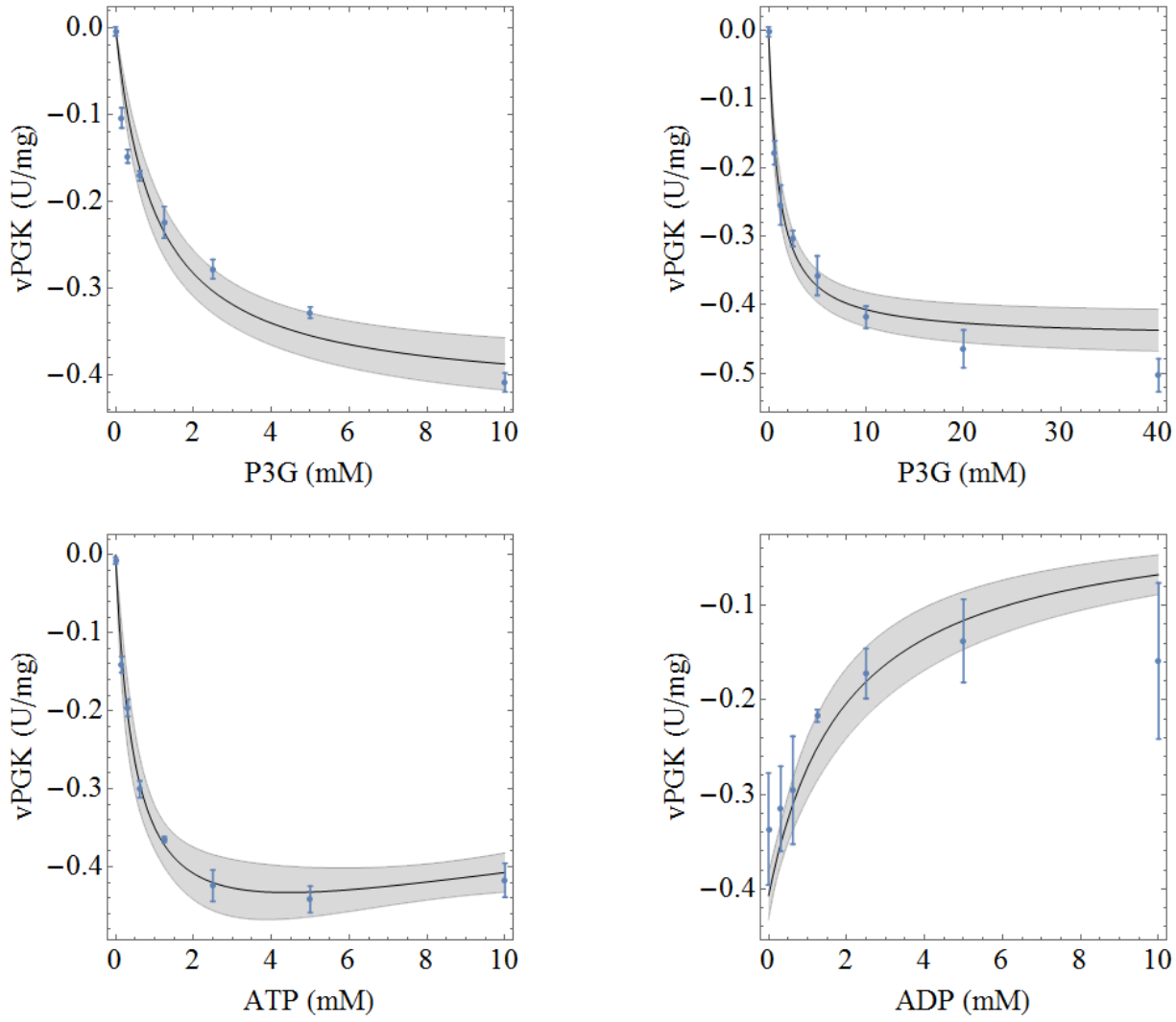

***Figure 4.8**: Kinetic characterisation of PGK in C_2C_{12} muscle myotubes in the reverse direction under varying substrate concentrations.* ***(top-left) -** Saturation of PGK with P3G at an ATP concentration of 1.5 mM.* ***(top-right) -** Saturation of PGK with P3G at an ATP concentration of 10 mM.* ***(bottom-left) -** Saturation of PGK with ATP at a P3G concentration of 10 mM.* ***(bottom-right)** – Evaluation of ADP product inhibition at a P3G concentration of 10 mM and an ATP concentration of 10 mM. The blue dots represent the experimental data obtained; the black line represents the non-linear model fit simulation of the complete dataset (95% confidence represents by the shaded area).*

The rate equation for PGK given in Eq.4.8 describes a non-reversible bi-substrate mechanism for the reverse direction. A good correlation between the mathematical fit and the experimental datasets are obtained and is illustrated in Figure 4.8. The fitted kinetic parameters for the PGK reverse reaction correspond well to the values reported in literature as summarised in Table 4.6.

4.4.7. Kinetic characterisation of PK

PK activity was measured in the forward direction, as discussed in Section 4.3.4, under varying concentrations of its substrates (PEP and ADP) and under varying concentrations of ATP to determine the inhibitory effect of ATP on PK activity. A non-reversible bi-substrate Michealis-Menten equation with allosteric inhibition by ATP and PEP is given in Eq.4.9 was fitted to the experimental dataset and the kinetic parameters (Vf_{PK}, *K*pep, *K*adp, *Ki*pep, *Ki*atp) were determined. The experimental data and the *non-linear model fit* of the experimental data is shown in Figure 4.9 and the determined kinetic parameter are listed in Table 4.7.

$$v\mathrm{PK} = \frac{Vf_{\mathrm{PK}} \cdot \mathrm{pep} \cdot \mathrm{adp}}{K\mathrm{pep} \cdot \left(1 + \frac{\mathrm{pep}}{K\mathrm{pep}}\right) \cdot K\mathrm{adp} \cdot \left(1 + \frac{\mathrm{adp}}{K\mathrm{adp}}\right) \cdot \left(1 + \frac{\mathrm{pep}}{Ki\mathrm{pep}}\right) \cdot \left(1 + \frac{\mathrm{atp}}{Ki\mathrm{atp}}\right)} \qquad \text{(Eq. 4.9)}$$

Table 4.7*: Summary of the kinetic parameters determined for the Michaelis-Menten equation describing PK activity in C_2C_{12} muscle myotubes in the forward direction. Eq.4.9 was fitted to the complete experimental dataset obtained for PK. The fitted values (± standard error) are compared to values reported in literature for similar tissue types where values are available. (U = µmol/min)*

Parameter	Fitted Value	Units	Literature Value	Reference
Vf_{PK}	0.4732 ± 0.0301	U/mg total protein		
*K*pep	0.1254 ± 0.0287	mM	0.08	32
*K*adp	0.3039 ± 0.0483	mM	0.3	32
*Ki*pep	30.6690 ± 11.2451	mM		
*Ki*atp	5.1256 ± 1.6347	mM		
Keq			6 500	33

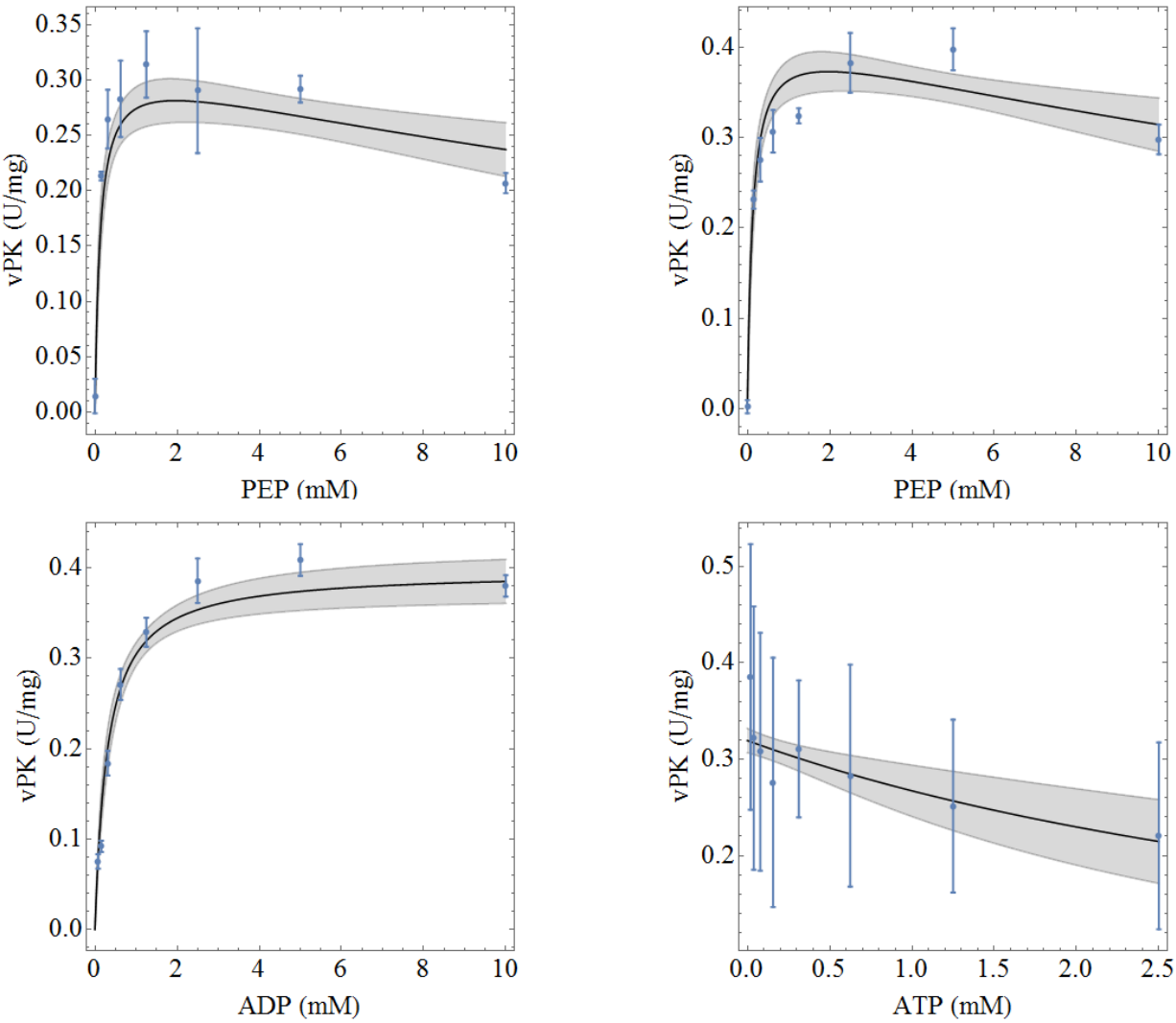

***Figure 4.9**: Kinetic characterisation of PK in C_2C_{12} muscle myotubes in the forward direction under varying substrate concentrations.* ***(top-left) -** Saturation of PK with PEP at an ADP concentration of 0.625 mM.* ***(top-right) -** Saturation of PK with PEP at an ADP concentration of 2.5 mM.* ***(bottom-left) -** Saturation of PK with ADP at a PEP concentration of 5 mM.* ***(bottom-right)** – Evaluation of ATP product inhibition at a PEP concentration of 5 mM and an ATP concentration of 1.25 mM. The blue dots represent the experimental data obtained; the black line represents the non-linear model fit simulation of the complete dataset (95% confidence represents by the shaded area).*

The rate equation for PK given in Eq.4.9 describes a non-reversible bi-substrate Michealis-Menten equation with allosteric inhibition by ATP and PEP for the forward direction. A good correlation between the mathematical fit and the experimental datasets are obtained as illustrated in Figure 4.9. The fitted kinetic parameters for the PK reaction are summarised in Table 4.7. The fitted value determined for *K*adp correlates very well with what is reported in literature. The optimised value obtained for *K*pep is slightly higher compared to literature.

4.4.8. Kinetic characterisation of LDH

The activity of LDH was measure in the forward and reverse direction, as discussed in Section 4.3.4, at varying concentrations of the substrates, PYR and NADH and varying concentrations of the products, LAC and NAD^+. A reversable bi-substrate Michealis-Menten equation with allosteric inhibition by PYR and NADH, given in Eq.4.10, was fitted to the experimental dataset and the kinetic parameters (Vf_{LDH}, Vr_{LDH}, *K*pyr, *K*lac, *K*nadh, *K*nad, *Ki*pyr, *Ki*nadh) were determined. The experimental data and the *non-linear model fit* of the experimental data is shown in Figure 4.10 and the determined kinetic parameter are listed in Table 4.8.

$$v\mathrm{LDH} = \frac{Vf_{\mathrm{LDH}} \cdot \frac{\mathrm{pyr}}{K\mathrm{pyr}} \cdot \frac{\mathrm{nadh}}{K\mathrm{nadh}} - Vr_{\mathrm{LDH}} \cdot \frac{\mathrm{lac}}{K\mathrm{lac}} \cdot \frac{\mathrm{nad}}{K\mathrm{nad}}}{\left(1 + \frac{\mathrm{lac}}{K\mathrm{lac}} + \frac{\mathrm{pyr}}{K\mathrm{pyr}}\right) \cdot \left(1 + \frac{\mathrm{nad}}{K\mathrm{nad}} + \frac{\mathrm{nadh}}{K\mathrm{nadh}}\right) \cdot \left(1 + \frac{\mathrm{pyr}}{Ki\mathrm{pyr}}\right) \cdot \prod_{n=1}^{4} \left(1 + \frac{\mathrm{nadh}}{Ki\mathrm{nadh}}\right)^{n}} \quad \text{(Eq. 4.10)}$$

Table 4.8*: Summary of the kinetic parameters determined for the Michaelis-Menten equation describing LDH activity in C_2C_{12} muscle myotubes in the forward and reverse directions. Eq.4.10 was fitted to the complete experimental dataset obtained for LDH. The fitted values (± standard error) are compared to values reported in literature for similar tissue types where values are available. (U = µmol/min)*

Parameter	Fitted Value	Units	Literature Value	Reference
Vf_{LDH}	26.8931 ± 8.0206	U/mg total protein		
Vr_{LDH}	3.1797 ± 0.3903	U/mg total protein		
*K*pyr	0.3469 ± 0.0821	mM	0.1 - 0.35	34
*K*lac	12.4493 ± 6.6165	mM	9.34 - 23.0	34
*K*nadh	0.5678 ± 0.2166	mM	0.008	35
*K*nad	0.6489 ± 0.2528	mM	0.253	36
*Ki*pyr	4.3823 ± 1.0727	mM		
*Ki*nadh	2.1107 ± 0.2765	mM		
Keq	168 - 500		150 - 430	11

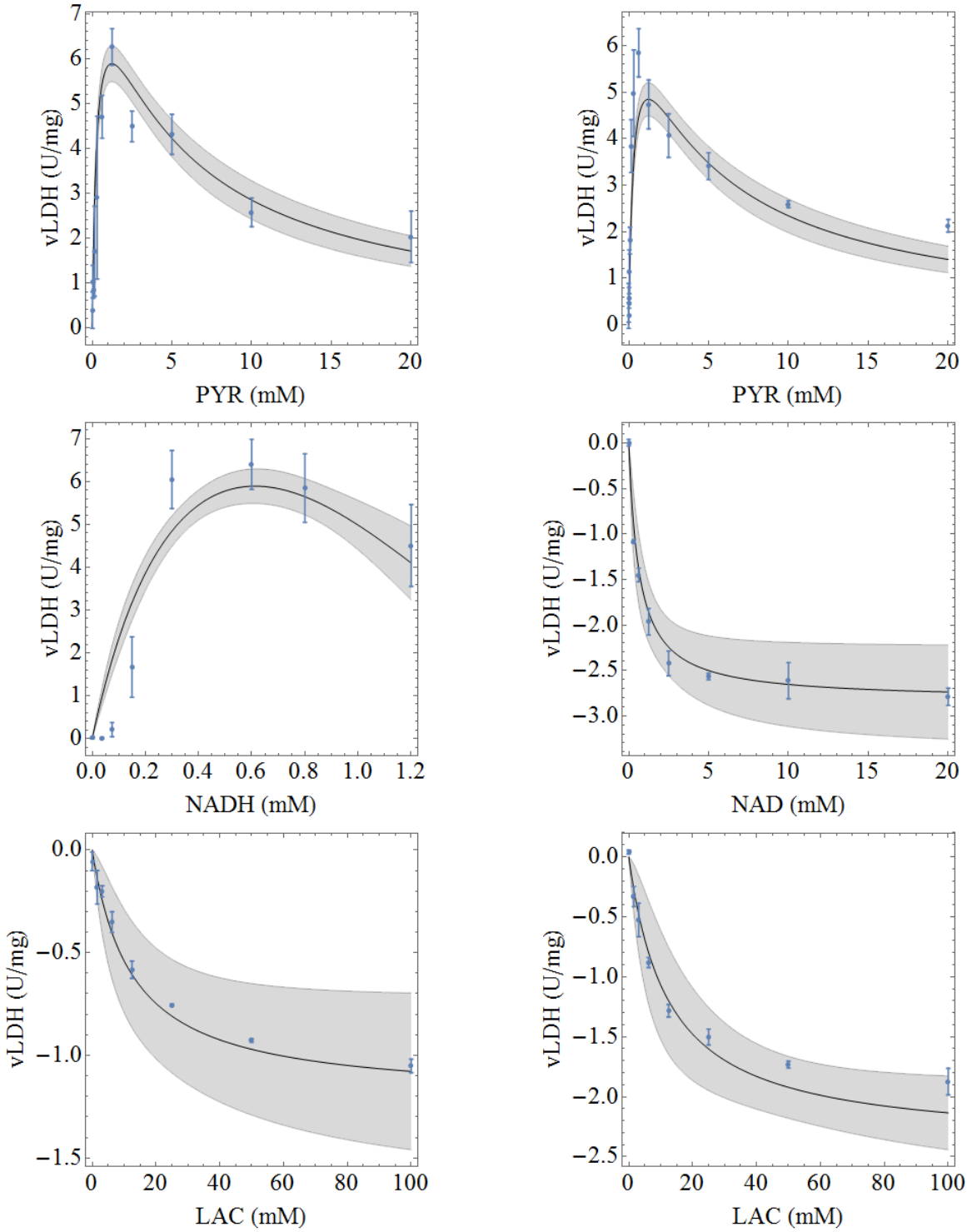

***Figure 4.10**: Kinetic characterisation of LDH in C_2C_{12} muscle myotubes in the forward and reverse directions under varying substrate concentrations.* ***(top) -** Saturation of LDH with PYR at a NADH concentration of 0.6 mM (left) and 0.3 mM (right) respectively.* ***(center-left) -** Saturation of LDH with NADH at a PYR concentration of 1.25 mM.* ***(center-right) -** Saturation of LDH with NAD^+ at a LAC concentration of 100 mM.* ***(bottom) -** Saturation of LDH with LAC at a NAD^+ concentration of 0.4 mM (left) and 2 mM (right) respectively. The blue dots represent the experimental data obtained; the black line represents the non-linear model fit simulation of the complete dataset (95% confidence represents by the shaded area).*

The rate equation for LDH given in Eq.4.10 describes a reversable bi-substrate Michealis-Menten equation with allosteric inhibition by PYR and NADH for the forward and reverse directions. A good correlation between the mathematical fit and the experimental datasets are obtained as illustrated in Figure 4.10. The fitted kinetic parameters for the LDH reaction correspond very well to the values reported in literature as summarised in Table 4.8. The values determined for *K*pyr and *K*lac falls within the range reported in literature. The values determined for *K*nadh and *K*nad are higher as compared to the values reported in literature with 2 orders of magnitude difference in the case of *K*nadh.

$$Keq(\mathrm{LDH}) = \frac{Vf_{\mathrm{LDH}} \cdot K\mathrm{lac} \cdot K\mathrm{nad}}{Vr_{\mathrm{LDH}} \cdot K\mathrm{pyr} \cdot K\mathrm{nadh}} \qquad \text{(Eq. 4.11)}$$

Using the Haldane relation represented by Eq.4.11, we can determine the estimated *Keq* for LDH from the optimized parameters given in Table 4.8. This yields a value range between 168 - 500 which falls within the range determined by Teusink *et al.*[11] for LDH in yeast.

4.4.9. Kinetic characterisation of AK

The activity of AK was measure in the forward and reverse direction, as discussed in Section 4.3.4, at varying concentrations of the substrate ADP and varying concentrations of the products, ATP and AMP.A reversible Michealis-Menten equation given in Eq.4.12 was fitted to the experimental dataset and the kinetic parameters (Vf_{AK}, Vr_{AK}, *K*adp, *K*atp, *K*amp, *Ki*adp, *Ki*atp) were determined. The experimental data and the *non-linear model fit* of the experimental data is shown in Figure 4.11 and the determined kinetic parameter are summarised in Table 4.9.

$$v\mathrm{AK} = \frac{Vf_{\mathrm{AK}} \cdot \frac{\mathrm{adp}^2}{K\mathrm{adp}^2} - Vr_{\mathrm{AK}} \cdot \frac{\mathrm{atp}}{K\mathrm{atp}} \cdot \frac{\mathrm{amp}}{K\mathrm{amp}}}{\left(1 + \frac{\mathrm{adp}}{K\mathrm{adp}} + \frac{\mathrm{amp}}{K\mathrm{amp}}\right) \cdot \left(1 + \frac{\mathrm{adp}}{K\mathrm{adp}} + \frac{\mathrm{atp}}{K\mathrm{atp}}\right) \cdot \left(1 + \frac{\mathrm{adp}}{Ki\mathrm{adp}}\right) \cdot \left(1 + \frac{\mathrm{atp}}{Ki\mathrm{atp}}\right)} \qquad \text{(Eq. 4.12)}$$

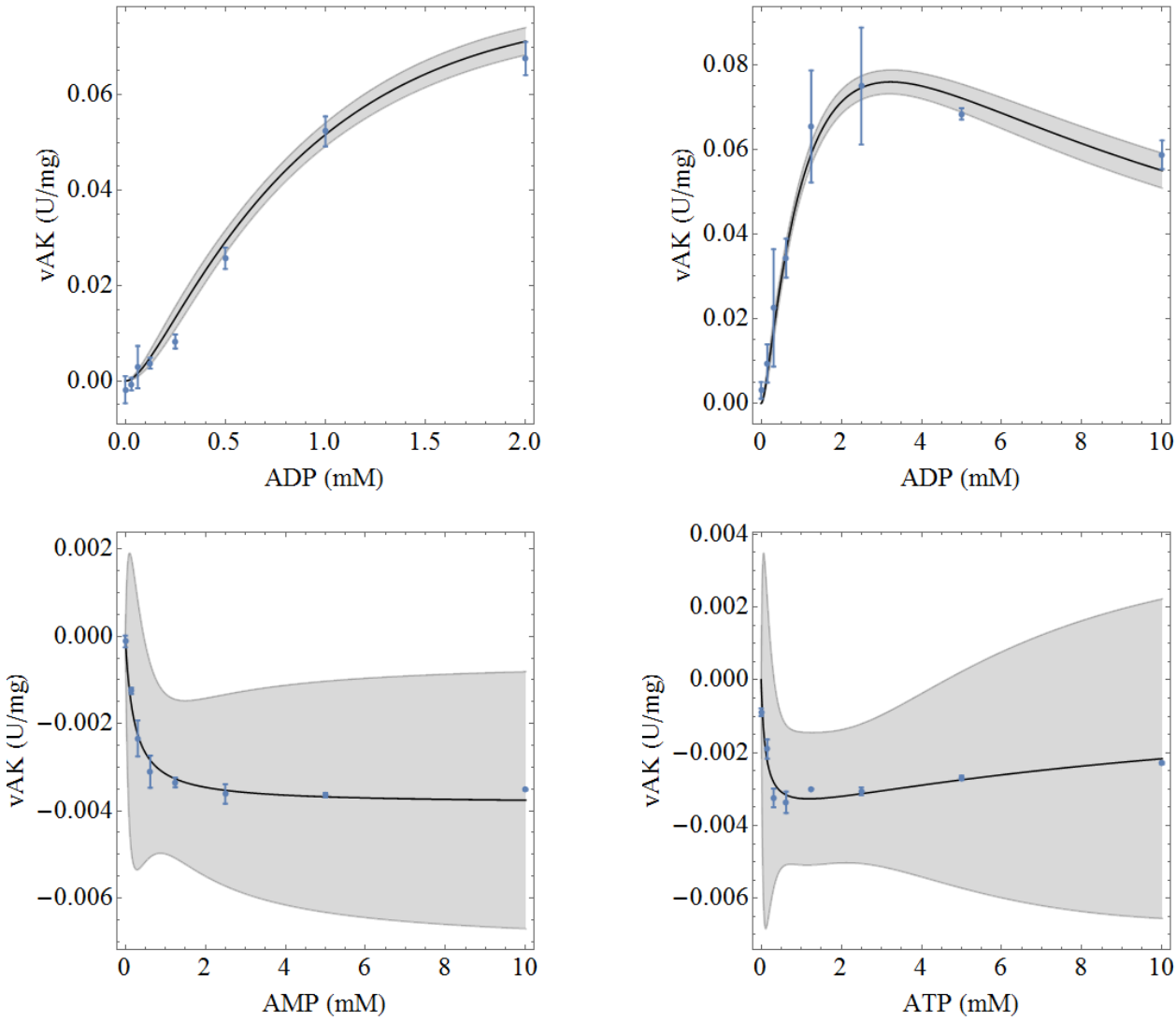

***Figure 4.11**: Kinetic characterisation of AK in C_2C_{12} muscle myotubes in the forward and reverse directions under varying substrate concentrations.* ***(top-left)** – incomplete saturation of AK with ADP* ***(top-right)** - Saturation of AK with ADP.* ***(bottom-left)** - Saturation of AK with AMP at an ATP concentration of 1.25 mM.* ***(bottom-right)** – Saturation of AK with ATP at an AMP concentration of 1.25 mM. The blue dots represent the experimental data obtained; the black line represents the non-linear model fit simulation of the complete dataset (95% confidence represents by the shaded area).*

***Table 4.9**: Summary of the kinetic parameters determined for the Michaelis-Menten equation describing AK activity in C_2C_{12} muscle myotubes in the forward and reverse directions. Eq.4.12 was fitted to the complete experimental dataset obtained for AK. The fitted values (± standard error) is compared to values reported in literature for similar tissue types where values are available. (U = µmol/min)*

Parameter	Fitted Value	Units	Literature Value	Reference
Vf_{AK}	0.1522 ± 0.0134	U/mg total protein		
Vr_{Ak}	0.0046 ± 0.0018	U/mg total protein		
*K*adp	0.5967 ± 0.0549	mM	0.35	37
*K*atp	0.1116 ± 0.2054	mM	0.27	37
*K*amp	0.2193 ± 0.2609	mM	0.32	37
*Ki*adp	7.1708 ± 1.2167	mM		
*Ki*atp	12.7666 ± 22.7975	mM		
Keq	0.66 - 9.28		0.45	33

The rate equation for AK given in Eq.4.12 describes a random order mechanism for the forward and reverse directions. A good correlation between the mathematical fit and the experimental datasets are obtained as illustrated in Figure 4.11. The fitted kinetic parameters for the AK reaction are summarised in Table 4.9. The correlation between the kinetic parameters determined in this study and values reported in literature is fair.

$$Keq(\mathrm{AK}) = \frac{Vf_{\mathrm{AK}} \cdot K\mathrm{atp} \cdot K\mathrm{amp}}{Vr_{\mathrm{AK}} \cdot K\mathrm{adp}^2} \qquad (\mathrm{Eq.}\,4.13)$$

Using the Haldane relation represented by Eq.4.13, we can determine the estimated Keq for AK from the optimized parameters given in Table 4.9. This yields a value range between 0.66 – 9.28 which is higher than the value reported by Bergmeyer[33] for AK. There are large uncertainties in the optimised values of *K*atp and *K*amp which can be addressed by increasing the amount of dataset used for parameter optimisation.

4.4.10. Kinetic characterisation of ATPase

ATPase activity was measured, as discussed in Section 4.3.4, under varying concentrations of ATP. The ATPase reaction was described by an irreversible mass action rate equation given in Eq. 4.14 was fitted to the experimental dataset and the rate constant (Vf_{ATPase}) was determined. The experimental data and the fitted function are shown in Figure 4.12.

$$v\mathrm{ATPase} = Vf_{\mathrm{ATPase}} \cdot \mathrm{atp} \qquad (\mathrm{Eq.}\,4.14)$$

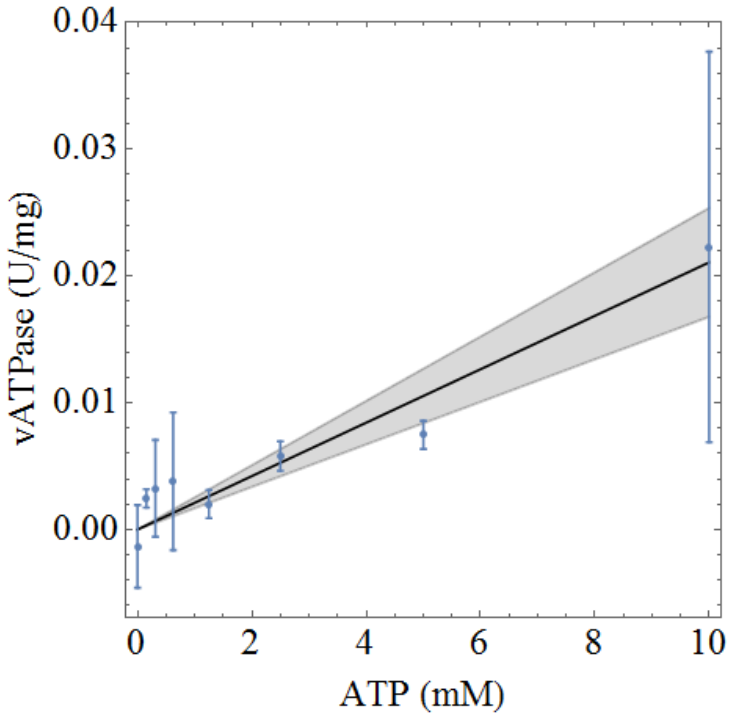

Figure 4.12: *Kinetic characterisation of ATPase in C_2C_{12} muscle myotubes under varying ATP concentrations. The blue dots represent the experimental data obtained; the black line represents the non-linear model fit simulation of the complete dataset (95% confidence represents by the shaded area).*

The rate equation for ATPase given in Eq. 4.14 describes an irreversible mass action relation. A good correlation between the mathematical fit and the experimental data is obtained as illustrated in Figure 4.12. The fitted rate constant is Vf_{ATPase} = 0.0021 ± 0.0002 U/mg total protein. This rate constant is significantly lower compared to the value reported by Lambeth *et. al.* in resting skeletal muscle (ATPase coefficient = 0.075)[6]. However, it is expected that C_2C_{12} skeletal muscle cell extract have significantly lower ATPase activity when compared to active human skeletal muscle. The value reported here is representative of skeletal muscle extract and is not directly comparable to skeletal muscle.

4.4.11. Measuring the biological variance in enzyme activity

The maximal activity for each enzyme, measured as µmol/ min/ mg total protein, gives the activity of each enzyme as measured within the cell extract. However, significant difference in the maximal activity of specific enzymes can be expected amongst different batches of cultured cells. The extent of differentiation of the C_2C_{12} skeletal muscle cells cannot be quantified and only a qualitative estimate can be made based on a microscopic visualisation of the differentiated cells. Therefore, the maximal activity measured within a given batch of differentiated C_2C_{12} skeletal muscle cells is a combination of the fractional maximal activity of

differentiated cells and a fractional maximal activity of undifferentiated cells, the fraction sizes of which cannot be determined. Furthermore, the level of enzyme expression in different culturing batches of the C_2C_{12} skeletal muscle cells can also vary.

Several batches of C_2C_{12} skeletal muscle cells were grown and differentiated to determine the range of biological variation in the activity of the glycolytic enzymes. The activity of the glycolytic enzymes was measured via enzyme coupled assays with substrate concentrations at saturating or near saturating conditions for each enzyme in the different batches. The biological variance obtained is summarised in Table 4.10.

Table 4.10: *Comparison of the enzyme activities measured for the glycolytic enzymes in C_2C_{12} muscle myotubes. The maximal specific activities of each enzyme were measured in several cultured batched of differentiated C_2C_{12} myotubes (n = 3 – 5) to determine the expected biological variance of each enzyme. The biological variance was determined by measuring enzyme activity at saturating or near saturating substrate concentrations. The error bars represent the standard error to the mean (SEM) the annotation fwd and rev refer to the forward and reverse reactions respectively.*

Enzyme	Average Measured Activity (µmol. min^{-1} .mg total $protein^{-1}$)	Biological Variance (SEM)
HK_{fwd}	0.0132	0.0017
PGI_{fwd}	0.1090	0.0027
PGI_{rev}	0.0545	0.0129
PFK_{fwd}	0.0023	0.0007
ALD_{fwd}	0.0278	0.0097
$GAPDH_{rev}$	0.0133	0.1284
PGK_{rev}	0.3051	0.1511
PK_{fwd}	0.4542	0.0657
LDH_{fwd}	24.0229	2.1102
LDH_{rev}	1.5496	0.8191

4.4.12. Constructing a mechanistic model describing glycolysis in C_2C_{12} myofibers

The glycolytic model describing glycolysis in C_2C_{12} skeletal muscle myofibers consist of 13 reaction steps. The model describes the conversion of GLC to the product LAC in C_2C_{12} cell extract and therefore does not account for a whole cell with the transport of GLC into the cell or the transport of LAC out of the cell. This model also includes the conserved adenosine (ATP, ADP, AMP) and nicotinamide (NAD^+, NADH) moieties. In the above section kinetic rate equations were derived for each reaction steps in the model. The kinetic model was constructed from the kinetic parameters determined by performing a fit of the specified rate equation on the

experimental data set. In the case where rate equations were described for only the forward or reverse reaction, the rate equation was modified to describe a reversible rate equation by using the *Keq* of the specific reaction. The rate equations used to construct the model is given below: (Eq 4.15 – Eq. 4.27).

$$v\mathrm{HK} = \frac{\left(Vf_{HK} \cdot \frac{\mathrm{atp}[t]}{K\mathrm{atp}} \cdot \frac{\mathrm{glc}[t]}{K\mathrm{glc}}\right) \cdot \left(1 - \frac{\mathrm{adp}[t] \cdot \mathrm{g6p}[t]}{\mathrm{atp}[t] \cdot \mathrm{glc}[t] \cdot Keq_{\mathrm{HK}}}\right)}{\left(1 + \frac{\mathrm{atp}[t]}{K\mathrm{atp}} + \frac{\mathrm{adp}[t]}{K\mathrm{adp}}\right) \cdot \left(1 + \frac{\mathrm{glc}[t]}{K\mathrm{glc}} + \frac{\mathrm{g6p}[t]}{K\mathrm{g6p}}\right) \cdot \left(1 + \frac{\mathrm{amp}[t]}{Ki\mathrm{amp}}\right) \cdot \left(1 + \frac{\mathrm{atp}[t]}{Ki\mathrm{atp}}\right) \cdot \left(1 + \frac{\mathrm{atp}[t]^2}{Ki\mathrm{atp}^2}\right)} \quad \text{(Eq. 4.15)}$$

$$v\mathrm{PGI} = \frac{\frac{Vf_{\mathrm{PGI}} \cdot \mathrm{g6p}[t]}{K\mathrm{g6p}} - \frac{Vr_{\mathrm{PGI}} \cdot \mathrm{f6p}[t]}{K\mathrm{f6p}}}{1 + \frac{\mathrm{g6p}[t]}{K\mathrm{g6p}} + \frac{\mathrm{f6p}[t]}{K\mathrm{f6p}}} \quad \text{(Eq. 4.16)}$$

$$v\mathrm{PFK} = \frac{V_{\mathrm{PFK}} \cdot \mathrm{atp}[t] \cdot \mathrm{f6p}[t]}{\left(1 + \frac{\mathrm{atp}[t]}{K\mathrm{atp}} + \frac{\mathrm{adp}[t]}{K\mathrm{adp}}\right) \cdot K\mathrm{atp} \cdot \left(1 + \frac{\mathrm{f6p}[t]}{K\mathrm{f6p}} + \frac{\mathrm{fbp}[t]}{K\mathrm{fbp}}\right) \cdot K\mathrm{f6p}} \quad \text{(Eq. 4.17)}$$

$$v\mathrm{ALD} = \frac{\left(Vf_{\mathrm{ALD}} \cdot \frac{\mathrm{fbp}[t]}{K\mathrm{fbp}}\right) \cdot \left(1 - \frac{\mathrm{gap}[t] \cdot \mathrm{dhap}[t]}{\mathrm{fbp}[t] \cdot Keq_{\mathrm{ALD}}}\right)}{1 + \frac{\mathrm{gap}[t]}{K\mathrm{gap}} + \frac{\mathrm{dhap}[t]}{K\mathrm{dhap}} + \frac{\mathrm{fbp}[t]}{K\mathrm{fbp}} + \frac{\mathrm{gap}[t] \cdot \mathrm{dhap}[t]}{K\mathrm{gap} \cdot K\mathrm{dhap}}} \quad \text{(Eq. 4.18)}$$

$$v\mathrm{TPI} = \frac{\frac{Vf_{\mathrm{TPI}} \cdot \mathrm{gap}[t]}{K\mathrm{gap}} \cdot \left(1 - Keq_{\mathrm{TPI}} \cdot \frac{\mathrm{dhap}[t]}{\mathrm{gap}[t]}\right)}{1 + \frac{\mathrm{gap}[t]}{K\mathrm{gap}} + \frac{\mathrm{dhap}[t]}{K\mathrm{dhap}}} \quad \text{(Eq. 4.19)}$$

$$v\mathrm{GAPDH} = \frac{-Vr_{\mathrm{PGK}} \cdot \frac{\mathrm{bpg}[t]}{K\mathrm{bpg}} \cdot \frac{\mathrm{nadh}[t]}{K\mathrm{nadh}} \cdot \left(Keq_{\mathrm{GAPDH}} \cdot \frac{\mathrm{gap}[t] \cdot \mathrm{nad}[t]}{\mathrm{bpg}[t] \cdot \mathrm{nadh}[t]} - 1\right)}{\left(1 + \frac{\mathrm{nad}[t]}{K\mathrm{nad}} + \frac{\mathrm{nadh}[t]}{K\mathrm{nadh}}\right) \cdot \left(1 + \frac{\mathrm{bpg}[t]}{K\mathrm{bpg}} + \frac{\mathrm{gap}[t]}{K\mathrm{gap}}\right)} \quad \text{(Eq. 4.20)}$$

$$v\mathrm{PGK} = \frac{-Vr_{\mathrm{PGK}} \cdot \frac{\mathrm{p3g}[t]}{K\mathrm{p3g}} \cdot \frac{\mathrm{atp}[t]}{K\mathrm{atp}} \cdot \left(Keq_{\mathrm{PGK}} \cdot \frac{\mathrm{bpg}[t] \cdot \mathrm{adp}[t]}{\mathrm{p3g}[t] \cdot \mathrm{atp}[t]} - 1\right)}{\left(1 + \frac{\mathrm{atp}[t]}{K\mathrm{atp}} + \frac{\mathrm{adp}[t]}{K\mathrm{adp}}\right) \cdot \left(1 + \frac{\mathrm{p3g}[t]}{K\mathrm{p3g}} + \frac{\mathrm{bpg}[t]}{K\mathrm{bpg}}\right) \cdot \left(1 + \frac{\mathrm{atp}[t]}{Ki\mathrm{atp}}\right) \cdot \left(1 + \frac{\mathrm{adp}[t]}{Ki\mathrm{adp}}\right)} \quad \text{(Eq. 4.21)}$$

$$v\mathrm{PGM} = \frac{\frac{Vf_{\mathrm{PGM}} \cdot \mathrm{p3g}[t]}{K\mathrm{p3g}} \cdot \left(1 - \cdot \frac{\mathrm{p2g}[t]}{\mathrm{p3g}[t] \cdot Keq_{\mathrm{PGM}}}\right)}{1 + \frac{\mathrm{p3g}[t]}{K\mathrm{p3g}} + \frac{\mathrm{p2g}[t]}{K\mathrm{p2g}}} \quad \text{(Eq. 4.22)}$$

$$v\mathrm{ENO} = \frac{\frac{Vf_{\mathrm{ENO}} \cdot \mathrm{p2g}[t]}{K\mathrm{p2g}} \cdot \left(1 - \cdot \frac{\mathrm{pep}[t]}{\mathrm{p2g}[t] \cdot Keq_{\mathrm{ENO}}}\right)}{1 + \frac{\mathrm{p2g}[t]}{K\mathrm{p2g}} + \frac{\mathrm{pep}[t]}{K\mathrm{pep}}} \quad \text{(Eq. 4.23)}$$

$$v\mathrm{PK} = \frac{Vf_{\mathrm{PK}} \cdot \frac{\mathrm{pep}[t]}{K\mathrm{pep}} \cdot \frac{\mathrm{adp}[t]}{K\mathrm{adp}} \cdot \left(1 - \frac{\mathrm{pyr}[t] \cdot \mathrm{atp}[t]}{\mathrm{pep}[t] \cdot \mathrm{adp}[t] \cdot Keq_{\mathrm{PK}}}\right)}{\left(1 + \frac{\mathrm{pep}[t]}{K\mathrm{pep}} + \frac{\mathrm{pyr}[t]}{K\mathrm{pyr}}\right) \cdot \left(1 + \frac{\mathrm{adp}[t]}{K\mathrm{adp}} + \frac{\mathrm{atp}[t]}{K\mathrm{atp}}\right) \cdot \left(1 + \frac{\mathrm{pep}[t]}{Ki\mathrm{pep}}\right) \cdot \left(1 + \frac{\mathrm{atp}[t]}{Ki\mathrm{atp}}\right)} \qquad \text{(Eq. 4.24)}$$

$$v\mathrm{LDH} = \frac{Vf_{\mathrm{LDH}} \cdot \frac{\mathrm{pyr}[t]}{K\mathrm{pyr}} \cdot \frac{\mathrm{nadh}[t]}{K\mathrm{nadh}} - Vr_{\mathrm{LDH}} \cdot \frac{\mathrm{lac}[t]}{K\mathrm{lac}} \cdot \frac{\mathrm{nad}[t]}{K\mathrm{nad}}}{\left(1 + \frac{\mathrm{lac}[t]}{K\mathrm{lac}} + \frac{\mathrm{pyr}[t]}{K\mathrm{pyr}}\right) \cdot \left(1 + \frac{\mathrm{nad}[t]}{K\mathrm{nad}} + \frac{\mathrm{nadh}[t]}{K\mathrm{nadh}}\right) \cdot \left(1 + \frac{\mathrm{pyr}[t]}{Ki\mathrm{pyr}}\right) \cdot \prod_{n=1}^{4}\left(1 + \frac{\mathrm{nadh}[t]}{Ki\mathrm{nadh}}\right)^{n}} \qquad \text{(Eq. 4.25)}$$

$$v\mathrm{AK} = \frac{Vf_{\mathrm{AK}} \cdot \frac{\mathrm{adp}[t]^2}{K\mathrm{adp}^2} - Vr_{\mathrm{AK}} \cdot \frac{\mathrm{atp}[t]}{K\mathrm{atp}} \cdot \frac{\mathrm{amp}[t]}{K\mathrm{amp}}}{\left(1 + \frac{\mathrm{adp}[t]}{K\mathrm{adp}} + \frac{\mathrm{amp}[t]}{K\mathrm{amp}}\right) \cdot \left(1 + \frac{\mathrm{adp}[t]}{K\mathrm{adp}} + \frac{\mathrm{atp}[t]}{K\mathrm{atp}}\right) \cdot \left(1 + \frac{\mathrm{adp}[t]}{Ki\mathrm{adp}}\right) \cdot \left(1 + \frac{\mathrm{atp}[t]}{Ki\mathrm{atp}}\right)} \qquad \text{(Eq. 4.26)}$$

$$v\mathrm{ATPase} = Vf_{\mathrm{ATPase}} \cdot \mathrm{atp}[t] \qquad \text{(Eq. 4.27)}$$

The parameterised rate equations dictate the rate of change of the specified variables (chemical species). A summary of the kinetic parameters used for the construction of the kinetic model describing glycolysis in differentiated C_2C_{12} skeletal muscle extract is given in Table 4.11 and Table 4.12. The rate measured for GAPDH in the reverse direction is significantly lower than is expected for GAPDH. Lambeth and Kushmerick[6] noted an activity for GAPDH that is comparable to that of PGK. Therefore, we have decided to increase the activity of GAPDH to reflect the relationship with PGK (Vr_{GAPDH} = 1.13 x Vr_{PGK}) as noted by Lambeth and Kushmerick[6] yielding a value of Vr_{GAPDH} = 0.6651 U/mg total protein^{-1}. The activity of the glycolytic enzymes of TPI, PGM and ENO was not determined experimentally. Values for the activity of these enzymes (Vf_{TPI}, Vf_{PGM} and Vf_{ENO}) were obtained from similar published studies in rat and mice skeletal muscle as M/min[38,39]. If we assume an average density of 1.06 kg/ L[40] for skeletal muscle, the values can be converted to µmol. min^{-1}. mg total protein^{-1} The kinetic parameters (*Km* values) pertaining to the half-reactions that were not experimentally characterised (*e.g.* *K*adp for HK) were obtained from literature sources as indicated in Table 4.12. The same literature sources as the study performed by Lambeth and Kushmeric[6] were used for the required *Km* values.

During model construction, it is important to indicate the relationship between the specified variable and its relevant rate equations that. This is done by setting up a series of ordinary differential equations (ODE's) as illustrated by Eq. 4.28 – 4.44. The ODE's comprise of three factors, namely; a direction that dictates an increase or decrease in concentration noted as a negative sign for a decrease and positive sign for an increase, a stoichiometric factor

indicating the relative amount of the variable formed or consumed by the reaction, and the specified rate equation that determines the change in variable concentration.

***Table 4.11**: Summary of the maximal specific activities measured as µmol.min^{-1}.mg total protein^{-1} used for the construction of a detailed kinetic model describing glycolysis is C_2C_{12} skeletal muscle myotubes. The maximal specific activities for each enzyme was determined by performing a fit of the relevant rate equation on the experimentally obtained kinetic data where possible. In the cases where data was not obtained for certain enzymes, maximal specific activities were obtained from literature for similar cell types.*

	Maximal Specific Activity (µmol.min^{-1}.mg total protein^{-1})				
Enzyme	Forward	Value	Reverse	Value	*Keq*
HK	Vf_{HK}	0.0129	Vr_{HK}	-	3800[11]
PGI	Vf_{PGI}	0.1098	Vr_{PGI}	0.0589	0.36 - 0.44
PFK	Vf_{PFK}	0.0036			800[27]
ALD	Vf_{ALD}	0.0477	Vr_{ALD}	-	0.052[28]
TPI	Vf_{TPI}	0.726[38]	Vr_{TPI}	-	0.089[28]
GAPDH	Vf_{GAPDH}	-	Vr_{GAPDH}	0.6651†	0.0056[30]
PGK	Vf_{PGK}	-	Vr_{PGK}	0.5889	0.18[28]
PGM	Vf_{PGM}	0.434[38]	Vr_{PGM}	-	0.49[28]
ENO	Vf_{ENO}	0.070[39]	Vr_{ENO}	-	6.7[33]
PK	Vf_{PK}	0.4732	Vr_{PK}	-	6500[33]
LDH	Vf_{LDH}	26.8931	Vr_{LDH}	3.1797	168 - 500
AK	Vf_{AK}	0.1522	Vr_{AK}	0.0046	0.66 - 9.28
ATPase	Vf_{ATPase}	0.0021			

† - The activity of GAPDH was increased to reflect the relationship between the activities of GAPDH and PGK as given by Lambeth and Kushmerick[6]. This results in a Vr_{GAPDH} value that is slightly higher than Vr_{PGK}.

***Table 4.12**: Summary of the Michealis-Menten constant (Km) values used for the construction of a detailed kinetic model describing glycolysis is C_2C_{12} skeletal muscle myotubes. The Km values for each enzyme was determined by performing a fit of the relevant rate equation on the experimentally obtained kinetic data where possible. In the cases where data was not obtained for certain enzymes, Km values were obtained from literature for similar cell types.*

	Kinetic Parameters			
Enzyme	Parameter	Value (mM)	Parameter	Value (mM)
HK	*K*glc	0.0663	*K*atp	3.0646
	*K*adp	1.9[41]	*K*g6p	0.065[41]
	*Ki*atp	21.0749	*Ki*amp	2.3713
PGI	*K*g6p	0.8353		
	*K*f6p	0.1827		
PFK	*K*f6p	0.1926	*K*atp	0.0159
	*K*fbp	4.02[42]	*K*adp	2.71[42]
ALD	*K*fbp	0.4353		
	*K*gap	1.1[43]	*K*dhap	2.1[43]
TPI	*K*gap	0.32[44]		
	*K*dhap	0.61[45]		
GAPDH	*K*gap	0.0025[29]	*K*nad	0.09[29]
	*K*bpg	0.0008	*K*nadh	0.3333
PGK	*K*bpg	0.0022[31]	*K*adp	0.05[46]
	*K*p3g	1.0116	*K*atp	0.4932
	*Ki*atp	39.7968	*Ki*adp	1.994
PGM	*K*p3g	0.2[47]		
	*K*p2g	0.014[47]		
ENO	*K*p2g	0.12[48]		
	*K*pep	0.37[48]		
PK	*K*pep	0.1254	*K*adp	0.3039
	*K*pyr	7.05[49]	*K*atp	0.82–1.13[49]
	*Ki*pep	30.6690	*Ki*atp	5.1256
LDH	*K*pyr	0.3469	*K*nadh	0.5678
	*K*lac	12.4493	*K*nad	0.6489
	*Ki*pyr	4.3823	*Ki*nadh	2.1107
AK	*K*adp	0.5967		
	*K*amp	0.2193	*K*atp	0.1116
	*Ki*adp	7.1708	*Ki*atp	12.7666

$$\mathrm{GLC}'[t] = -1.0 * v\mathrm{HK} \quad \text{(Eq. 4.28)}$$

$$\mathrm{G6P}'[t] = +1.0 * v\mathrm{HK} - 1.0 * v\mathrm{PGI} \quad \text{(Eq. 4.29)}$$

$$\mathrm{F6P}'[t] = +1.0 * v\mathrm{PGI} - 1.0 * v\mathrm{PFK} \quad \text{(Eq. 4.30)}$$

$$\mathrm{FBP}'[t] = +1.0 * v\mathrm{PFK} - 1.0 * v\mathrm{ALD} \quad \text{(Eq. 4.31)}$$

$$\mathrm{DHAP}'[t] = +1.0 * v\mathrm{ALD} + 1.0 * v\mathrm{TPI} \quad \text{(Eq. 4.32)}$$

$$\mathrm{GAP}'[t] = +1.0 * v\mathrm{ALD} - 1.0 * v\mathrm{TPI} - 1.0 * v\mathrm{GAPDH} \quad \text{(Eq. 4.33)}$$

$$\mathrm{BPG}'[t] = +1.0 * v\mathrm{GAPDH} - 1.0 * v\mathrm{PGK} \quad \text{(Eq. 4.34)}$$

$$\mathrm{P3G}'[t] = +1.0 * v\mathrm{PGK} - 1.0 * v\mathrm{PGM} \quad \text{(Eq. 4.35)}$$

$$\mathrm{P2G}'[t] = +1.0 * v\mathrm{PGM} - 1.0 * v\mathrm{ENO} \quad \text{(Eq. 4.36)}$$

$$\mathrm{PEP}'[t] = +1.0 * v\mathrm{ENO} - 1.0 * v\mathrm{PK} \quad \text{(Eq. 4.37)}$$

$$\mathrm{PYR}'[t] = +1.0 * v\mathrm{PK} - 1.0 * v\mathrm{LDH} \quad \text{(Eq. 4.38)}$$

$$\mathrm{LAC}'[t] = +1.0 * v\mathrm{LDH} \quad \text{(Eq. 4.39)}$$

$$\mathrm{ATP}'[t] = -1.0 * v\mathrm{HK} - 1.0 * v\mathrm{PFK} + 1.0 * v\mathrm{PGK} + 1.0 * v\mathrm{PK} + 1.0 * v\mathrm{AK} - 1.0 * v\mathrm{ATPase} \quad \text{(Eq. 4.40)}$$

$$\mathrm{ADP}'[t] = +1.0 * v\mathrm{HK} + 1.0 * v\mathrm{PFK} - 1.0 * v\mathrm{PGK} - 1.0 * v\mathrm{PK} - 2.0 * v\mathrm{AK} + 1.0 * v\mathrm{ATPase} \quad \text{(Eq. 4.41)}$$

$$\mathrm{AMP}'[t] = +1.0 * v\mathrm{AK} \quad \text{(Eq. 4.42)}$$

$$\mathrm{NADH}'[t] = +1.0 * v\mathrm{GAPDH} - 1.0 * v\mathrm{LDH} \quad \text{(Eq. 4.43)}$$

$$\mathrm{NAD}'[t] = -1.0 * v\mathrm{GAPDH} + 1.0 * v\mathrm{LDH} \quad \text{(Eq. 4.44)}$$

The model consists of 17 ODE's describing the change in concentration of the 17 variables in the model. The ODE's are constructed from 13 rate equations corresponding to the 13 enzymatic reactions involved in the glycolytic pathway. Each ODE gives the change in concentration of each of the corresponding variables as a function of time. This yields a dynamic concentration profile for each of the 17 chemical species of interest. The initial concentrations of each of the 17 variables are assigned as an input value in the model. The initial concentrations generally correspond to the concentration of each chemical species as measured experimentally within a sample of cells.

4.4.13. Steady state analysis

To compare the model constructed here with the model published by Schmitz *et. al.*[50] the same set of initial concentrations were used as an input to the model and the steady state values were compared to the published values[50]. The model published by Schmitz *et. al.*[50] described the conversion of glycogen to LAC in skeletal muscle, whereas we are investigating the conversion of GLC to LAC in skeletal muscle extract. Their study investigated the behaviour of glycolysis *in silico* under various scenarios pertaining to the effect of PFK and PK inhibition[50]. The steady state value determined for the model constructed here was compared to the steady state values determined in the scenario where PFK and PK inhibition is included.

The initial concentration of GLC was set to the initial value of G1P in the Schmitz model. All other initial values were set to the same value. Steady state concentrations of the glycolytic intermediates and cofactors were determined by fixing the concentrations of GLC and LAC to 0.059 mM and 1.3 mM respectively and allowing the model to reach a steady state. The current model was not able to reach a steady state since all adenosine metabolites would convert to AMP. Therefore, we decreased the value describing the ATPase activity (Vf_{ATPase} = 0.0021 U/mg) to 12% of the original value to reach a steady state. This ATPase rate gave the best comparison to the steady state values reported by Schmitz *et. al.*[50]. The comparison of the steady state values calculated by the model constructed here with the steady state values published by Schmitz *et. al.*[50] is given in Table 4.13.

***Table 4.13**: Comparison of the steady state values calculated by the model constructed here (van Dyk 2019) and the steady state values published by Schmitz et. al. (Schmitz 2009)[50]. The initial values of the variables described in the model was set to the same values reported by Schmitz et. al. to reflect an accurate comparison of the two models.*

Chemical Species	Initial (mM)	Schmitz (2009)[50]	van Dyk (2019)
		Steady-State (mM)	Steady-State (mM)
GLC	0,059	-	-
G1P	0,059	0,025	-
G6P	0,75	0,41	0.205
F6P	0,23	0,18	0.079
FBP	0,072	0,18	0.266
DHAP	0,076	0,02	0.506
GAP	0,036	0,39	0.044
BPG	0,065	0,0032	0.001
P3G	0,052	0,2	0.034
P2G	0,005	0,036	0.016
PEP	0,019	0,018	0.076
PYR	0,099	0,012	0.128
LAC	1,3	0,84	-
ATP	8,2	8,2	8.106
ADP	0,013	0,0098	0.104
AMP	1.13×10^{-6}	6.49×10^{-6}	0.003
NAD	0,5	0,47	0.485
NADH	0	-	0.015

Comparison of the steady state concentrations calculated by the van Dyk (2019) model and the Schmitz (2009)[50] model predict similar values for the adenosine moieties. The steady state concentrations of AMP and ADP as predicted by the van Dyk (2019) model is higher in comparison to the steady state concentrations predictions of the Schmitz (2009)[50] model. The steady state concentrations of FBP, DHAP, PEP and PYR as predicted to be higher and the steady state concentrations of G6P, F6P, GAP, BPG, P3G and P2G are predicted to be lower in comparison to the steady state concentrations predictions of the Schmitz (2009)[50] model. However, there is less than an order of magnitude difference for half of the steady state concentrations predicted by the 2 models and most of the steady state values are predicted within the same 2 orders of magnitude.

4.5. Discussion

In recent years, several research groups have focussed their attention on describing the metabolic behaviours observed for skeletal muscle[5,6,26,51]. These studies were predominantly

focussed on understanding the dynamic interplay between muscle contraction and glucose consumption. This has led to the construction of several *in silico* models describing the regulatory effect that increased ATP demand has on glycolysis. It was found that the predominant driving force dictating the metabolic activity of skeletal muscle is the generation of ATP for muscle activity[6]. Furthermore, a minimal mechanistic model describing the cellular energy balance regulatory process in individuals transitioning from a resting state to an activated state and back to a resting state has been constructed by Vicini and Kushmerick[5]. Their model successfully described the time dependent concentrations of PCR and Pi by focussing on the interplay between oxidative phosphorylation, ATP utilization and creatine kinase activity. However, there has been a universal agreement that kinetic parameters, determined under standardised physiologically relevant conditions, is lacking in order to further improve our understanding on the regulatory characteristics of glycolysis in skeletal muscle[5,6,51].

For our model construction, emphasis was placed on studying enzyme activities under conditions that mimic cytosolic conditions. A standardised buffer system was derived from knowledge of the molecular make-up of the skeletal muscle cytosol and all enzyme activities were measured in this buffer. Furthermore, all enzyme activities were measured at a physiological pH (7.4) and physiological temperature (37ºC) to ensure that the activities measured were representative of the enzyme activities expected inside the intact cell. The glycolytic enzyme activities were described by Michealis-Menten type kinetics, which were fitted to the data. This resulted in the characterisation of the glycolytic enzymes in terms of their maximal specific activities (*Vmax*) and affinity for each substrate and product (*Km*) in differentiated C_2C_{12} extract. We were not so interested in the best fit observed for each individual experimental dataset, but rather for the best set of kinetic parameters that describe the total dataset for an enzyme the best. By employing a larger dataset and measurements of enzyme activities under various substrate and product concentrations, a better description of the enzyme from a mechanistic point of view can be obtained albeit at the cost of perfect fits to the data. In the cases of PGI, LDH and AK, experimental data were obtained for both the forward and the reverse half reactions and the fitted rate equation described both the forward and reverse half reactions. Experimental data for only the forward half reaction of HK, PFK, ALD and PK was obtained, and the fitted rate equations described only the forward half reaction of these enzymes. Similarly, experimental data for GAPDH and PGK were obtained for only the reverse half reaction and the fitted rate equation only described the reverse half reaction for these 2

enzymes. We were unable to obtain experimental data for the enzymes; TPI, PGM and ENO and literature data were used to model these enzymes. It should be noted that these enzymes are generally very active and are often described by equilibrium reactions in modelling studies. Overall, the fitted kinetic parameters compared fairly well with what is reported in literature, with the exceptions of the *K*nadh value obtained for GAPDH (0.333 ± 0.1586) and the *K*nadh value obtained for LDH (0.5678 ± 0.2166) where a 2 orders of magnitude difference is seen between our results and what is reported in literature. GAPDH was measured in the reverse direction by coupling GAPDH to the downstream enzyme PGK and initialising the reaction with P3G. In this study the activity of GAPDH could only be measured up to a concentration of 8 µM of BPG, which corresponds to the *K*bpg value obtained for this enzyme. Lambeth and Kushmeric[6] have used a value comparable to the rate of PGK for the activity of GAPDH and this was considered in the construction of our model. The value was determined by correlating the relative activities of PGK and GAPDH in the Lambeth and Kushmeric[6] model with the activity measured for PGK. This yielded a value of Vr_{GAPDH} = 0.6651 U/mg total protein, which is slightly higher than the value for Vr_{PGK} = 0.5889 U/ mg total protein. The assumption regarding GAPDH activity will be evaluated in Chapter 5.

HK was inhibited by both its substrate ATP (at high concentrations), as well as by AMP. The finding that AMP inhibits HK was surprising since one would expect that HK should be activated under high energy demands where AMP concentrations are elevated. AMP inhibition has been reported to be present in cerebral-cortex hexokinase[22]. Other inhibitory behaviours of note are; ADP inhibition of PGK in the reverse direction, ATP inhibition of PK in the forward direction and substrate inhibition of LDH by PYR. The rate equations were modified to describe these inhibitory behaviours where applicable and the inhibitory behaviours were described very well by the fitted rate equations. Choi et. al.[52] hypothesised feedback inhibition of glycolysis by LAC results in insulin resistance, associated with a decreased activity in the glycolytic enzyme PFK. Therefore, we have tested whether PFK is directly inhibited by the presence of LAC by measuring the activity of PFK at a constant concentration of F6P and ATP and varying the concentration of LAC present. However, no difference in the activity of PFK was observed at varying concentrations of LAC (data not shown) and therefore conclude that LAC does not directly inhibit PFK.

The resulting rate equations describing the activity of the glycolytic enzymes obtained from the cell extract of differentiated C_2C_{12} muscle were compiled into a bottom-up mechanistic

model. In this manner we can investigate the functional properties of glycolysis that arise from different environmental constraints experienced by skeletal muscle. By having a high level of mechanistic detail about the molecular processes involved in the glycolytic system and the interactions thereof, the behaviour of the system can be replicated *in silico* and then compared to what is observed in the laboratory. Our purpose to the construction of a detailed mechanistic model is two-fold; **(1)** to understand the underlying principles that constrains the system to behave as it does, and **(2)** to be able to replicate the glycolysis in differentiated C_2C_{12} extract to a modest degree of accuracy. However, some modifications to the descriptions of the experimental data were necessary to construct this mechanistic model. With the exception of PFK, all enzymatic reactions in the model were described as reversible reactions. The rate equations for the enzymes where experimental data was obtained for only the forward or reverse reaction was modified to describe the reaction as a reversible reaction. This was done by modifying the fitted rate equations with the use of the Haldane relationship to describe the rate equations as reversible reactions (Eq.4.14-4.26). Furthermore, shortages in the experimental determination of kinetic parameters were addressed by obtaining values for these kinetic parameters from literature sources of studies done on mammalian cell lines. We have treated the conserved adenosine and nicotinamide moieties as free metabolic variables rather than parameters to monitor the changes in concentration of the species under different conditions as well as to better describe the model on a mechanistic foundation. This results in 17 ODE's to describe the changes in variable concentrations as a function of time. The ODE's were constructed from the 13 rate equations describing the activities of the 12 enzymes present in the glycolytic pathway along with a rate equation describing ATPase.

Steady state analysis of the kinetic model describing glycolysis in C_2C_{12} skeletal muscle extract was performed to compare the resulting steady state concentrations of the glycolytic intermediates and cofactors to the steady state concentrations published by Schmitz *et. al.*[50]. Although, there are significant differences in the construction and purpose of the models, comparison of the steady state concentrations calculated by the van Dyk model and the Schmitz model[50] are satisfactory when the ATPase rate is adjusted.

The mechanistic model describing glycolysis in differentiated C_2C_{12} muscle extract showed some interesting results. The most prominent is the low activity observed for HK and PFK. HK and PFK are present in upper glycolysis and require ATP for catalytic activity. The restriction of glucose influx into glycolysis by HK and PFK regulates the concentration of

glycolytic intermediates present in the system. In contrast, the rates associated with lower glycolysis, specifically PGK and PK, are more than an order of magnitude larger in comparison. This results in a phenomenon where the flux through the upper glycolysis, that utilises ATP as a substrate, is much slower than the flux through lower glycolysis, that produces ATP as a product. This is contradictory to what is observed in other cell types such as yeast where the flux through upper glycolysis is much faster and high concentrations of FBP are observed[11]. Another observation of importance is the regulatory behaviours exerted on the glycolytic pathway by the adenosine metabolites. The initial concentrations of ATP, ADP and AMP have a significant effect on the model predicted concentrations of the glycolytic intermediates. This is in line with the findings of other research groups[5,6,8,26,51,53] who found that the flux control through glycolysis regulated by the demand for ATP could be as high as 99%[53]. Metabolic control analysis for the glycolytic model constructed in this chapter will be performed and compared to related models in chapter 5.

The mechanistic model constructed here predicts the time dependent concentration profiles of glycolytic intermediates as a result of how glycolysis operates in differentiated C_2C_{12} muscle extract. One of the aims in the construction of the model was to replicate the behaviour of glycolysis in this cell line. Therefore, the question put forth is how well this mechanistic model can predict the time dependent trends of the glycolytic intermediates. To determine this the model needs to be validated. This entails comparing the model predictions to experimental data obtained for the same set of initial conditions. This will be discussed in the subsequent chapters of this thesis.

4.6. Conclusion

We have determined a complete set of kinetic parameters for glycolytic enzymes in differentiated C_2C_{12} muscle fibres. These findings address some of the concerns expressed in literature[5,6,51]. The kinetic description of the glycolytic enzymes was compiled into a bottom-up model of the glycolytic pathway. The low activity of the ATP dependent enzymes of upper glycolysis have shown comparatively low activity even under conditions where high levels of ATP is present, whereas the activity of lower glycolytic enzymes, such as PGK and PK are significantly higher.

4.7. References

1 **DeFronzo RA, Jacot E, Jequier E, Maeder E, Wahren J and Felber JP.**, The effect of insulin on the disposal of intravenous glucose. Results from indirect calorimetry and hepatic and femoral venous catheterization., *Diabetes* 30:1000–1007, 1981

2 **Nuutila P, Knuuti MJ, Raitakari M, Ruotsalainen U, Teras M, Voipio-Pulkki LM, Haaparanta M, Solin O, Wegelius U and Yki-Jarvinen H.**, Effect of antilipolysis on heart and skeletal muscle glucose uptake in overnight fasted humans., *Am. J. Physiol. Endocrinol. Metab.* 267:E941–E946, 1994

3 **Fothergill-Gilmore LA and Michels PA.**, Evolution of glycolysis., *Prog. Biophys. Mol. Biol.* 59:105–235, 1993

4 **Romano AH and Conway T.**, Evolution of carbohydrate metabolic pathways., *Res. Microbiol.* 147:448–455, 1996

5 **Vicini P and Kushmerick MJ.**, Cellular energetics analysis by a mathematical model of energy balance: estimation of parameters in human skeletal muscle. *Am. J. Physiol. Cell. Physiol.* 279:C213–C224, 2000

6 **Lambeth MJ and Kushmerick MJ.**, A Computational Model for Glycogenolysis in Skeletal Muscle., *Ann. Biomed. Eng.* 30:808–827, 2002

7 **Dash RK, Li Y, Kim J, Beard DA, Saidel GM and Cabrera ME.**, Metabolic dynamics in skeletal muscle during acute reduction in blood flow and oxygen supply to mitochondria: in-silico studies using a multi-scale, top-down integrated model., *Plos One* 3:e3168, 2008

8 **Selivanov VA, de Atauri P, Centelles JJ, Cadefau J, Parra J, Cuss oR, Carreras J and Cascante M.**, The changes in the energy metabolism of human muscle induced by training., *J. Theor. Biol.* 252:402–410, 2008

9 **Barnett JA.**, A history of research on yeast 5: the fermentation pathway., *Yeast* 20:509-543, 2003

10 **van Eunen K, Bouwman J, Daran-Lapujade P, Postmus J, Canelas AB, Mensonides FIC, Orij R, Tuzuns I, van den Brink J, Smits GJ, van Gulik WM, Brul S, Heijnen JJ, de Winde JH, de Mattoss MJT, Kettner C, Nielsen J, Westerhoff HV and Bakker BM.**, Measuring enzyme activities under standardized in vivo-like conditions for systems biology., *FEBS Journal* 277:749–760, 2010

11 **Teusink B, Passarge J, Reijenga CA, Esgalhado E, van der Weijden CC, Schepper M, Walsh MC, Bakker BM, van Dam K, Westerhoff HV and Snoep JL.**, Can yeast glycolysis be understood in terms of in vitro kinetics of the constituent enzymes? Testing biochemistry., *Eur. J. Biochem.* 267:5313-5329, 2000

12 **Cooper ST, Maxwell AL, Kizana E, Ghoddusi M, Hardeman EC, Alexander IE, Allen DG and North KN.**, C2C12 co-culture on a fibroblast substratum enables sustained survival of contractile, highly differentiated myotubes with peripheral nuclei and adult fast myosin expression., *Cell. Motil. Cytoskel.* 58:200–211, 2004

13 **Kislinger T, Gramolini AO, Pan Y, Rahman K, Maclennan DH and Emili A.**, Proteome dynamics during C2C12 myoblast differentiation., *Mol. Cell Proteomics* 4:887–901, 2005

14 **Moran JL, Li Y, Hill AA, Mounts WM and Miller CP.**, Gene expression changes during mouse skeletal myoblast differentiation revealed by transcriptional profiling., *Physiol. Genomics* 10:103–111, 2002

15 **Tsuchiya Y, Hatakeyama H, Emoto N, Wagatsuma F, Matsushita S and Kanzaki M.**, Palmitate-induced down-regulation of sortilin and impaired GLUT4 trafficking in C2C12 myotubes., *J. Biol. Chem.* 285:34371–34381, 2010

16 **Pandurangan M and Hwang I.**, Application of cell co-culture system to study fat and muscle cells., *Appl. Microbiol. Biotechnol.* 98:7359–7364, 2014

17 **Nedachi T and Kanzaki M.**, Regulation of glucose transporters by insulin and extracellular glucose in C2C12 myotubes., *Am. J. Physiol. Endocrinol. Metab.* 291: E817–E828, 2006

18 **Schmitz-Peiffer C, Craig DL and Biden TJ.**, Ceramide generation is sufficient to account for the inhibition of the insulin-stimulated PKB pathway in C_2C_{12} skeletal muscle cells pre-treated with palmitate., *J. Biol. Chem.* 274:24202-24210, 1999

19 **Somlyo AV, Shuman H and Somlyo AP.**, Elemental distribution in straited muscle and effects of hypertonicity., *J. Cell Biol.* 74: 828-857, 1977

20 **Koley D and Bard AJ.**, Triton X-100 concentration effects on membrane permeability of a single HeLa cell by scanning electrochemical microscopy (SECM)., *Proc. Natl. Acad. Sci. USA* 107:16783-16787, 2010

21 **Wilson JE.**, Isozymes of mammalian hexokinase: structure, subcellular localization and metabolic function., *J. Exp. Biol.* 206:2049-2057, 2003

22 **Clark AD, Bachelard HS and Thompson MF.**, Cerebral-cortex hexokinase: Elucidation of reaction mechanisms by substrate and dead-end inhibitor kinetic analysis., *Biochem. J.* 123:707-715, 1971

23 **Puigjaner J. Rais B, Burgos M, Comin B, Ovadi J and Cascante M.**, Comparison of control analysis data using different approaches: Modeling and experiments with muscle extract., *FEBS Lett.* 418:47–52, 1997

24 **Kahana SF, Lowry OH, Schulz DW, Passoneau JV and Crawford EJ.**, The kinetics of phosphoglucoisomerase., *J. Biol. Chem.* 235:2178–2184, 1960

25 **Tewari YB, Steckler DK and Goldberg RN.**, Thermodynamics of isomerization reactions involving sugar phosphates., *J. Biol. Chem.* 263:3664-3669, 1988

26 **Schmitz JPJ, Groenendaal W, Wiseman RW, Hilbers PAJ, Nicolay K, Pompers JJ, Jeneson JAL and van Riel NAW.**, Combined in vivo and in silico investigations of activation of glycolysis in contracting skeletal muscle., *Am. J. Physiol. Cell Physiol.* 304:C180–C193, 2013

27 **Hofmann E and Kopperschlaeger G.**, Phosphofructokinase from yeast., *Methods Enzymol.* 90:49-60, 1982

28 **Johnson MJ.**, Enzyme equilibria and thermodynamics. In: The Enzymes, 4, edited by H. Lardy, P. D. Boyer and K. Myrback., New York: Academic, 1959, pp. 407–441.

29 **Velick SF and Furfine C.**, Glyceraldehyde 3-phosphate dehydrogenase. In: The Enzymes, 7, edited by P. D. Boyer, H. Lardy, and K. Myrback. New York: Academic, 1963, Vol. 7, Chap. 12.

30 **Byers LD, She HS, Alayoff A.**, Interaction of phosphate analogues with glyceraldehyde-3-phosphate dehydrogenase., *Biochemistry* 18:2471-2480, 1979

31 **Krietsch WK and Bucher T.**, 3-phosphoglycerate kinase from rabbit sceletal muscle and yeast., *Eur. J. Biochem.* 17:568–580, 1970

32 **Imamura K and T. Tanaka T.**, Pyruvate kinase isozymes from rat., *Methods Enzymol.* 90:150–165, 1982

33 **Bergmeyer HU.**, Methods of Enzymatic Analysis., *Verlag Chemie*, Weinheim, Germany, 1974

34 **Stambaugh R and Post D.**, Substrate and product inhibition of rabbit muscle lactic dehydrogenase heart (H_4) and Muscle (M_4) isozymes., *J. Biol. Chem.* 241:1462-1467, 1966

35 **Sempere S, Cortes A and Bozal J.**, Kinetic mechanism of guinea-pig skeletal muscle lactate dehydrogenase (M_4) with oxaloacetate-NADH and pyruvate-NADH as substrates., *Int. J. Biochem.* 13:727-731, 1981

36 **Zewe V and Fromm HJ.**, Kinetic studies of rabbit muscle lactate dehydrogenase., *J. Biol. Chem.* 237:1668-1675, 1962

37 **Thuma E, Schirmer RH and Schirmer I.**, Preparation and characterization of a crystalline human ATP: AMP phosphotransferase., *Biochim. Biophys. Acta.* 268:81–91, 1972

38 **Riol-Cimas JM and Melendez-Hevia E.**, Distribution of metabolic fluxes towards glycerol phosphate and L-lactate from fructose-1,6-bisphosphate *in vitro*: effect of glycerol phosphate dehydrogenase., *Int. J. Biochem. Cell Biol.* 18:853-856, 1986

39 **Petell JK, Marshall NA and Lebherz HG.**, content and synthesis of several abundant glycolytic enzymes in skeletal muscles of normal and dystrophic mice., *Int. J. Biochem.* 16:61-67, 1984

40 **Urbancheka M, Picken E, Kallianen L and Kuzon W.**, Specific force deficit in skeletal muscles of old rats is partially explained by the existence of denervated muscle fibers., *J. Gerontol. A. Biol. Sci. Med. Sci.* 56:B191-B197, 2001

41 **Rees BB, Ropson IJ and Hand SC.**, Kinetic Properties of Hexokinase under Near-physiological Conditions., *J. Biol. Chem.* 264:15410-15417, 1989

42 **Merry S and Britton HG.**, The mechanism of rabbit muscle phosphofructokinase at pH8., *Biochem. J.* 226:13–28, 1985

43 **Penhoet EE, Kochman M and Rutter WJ.**, Isolation of fructose diphosphate aldolases A, B, and C., *Biochemistry* 8:4391–4395, 1969

44 **Krietsch WK, Pentchev PG, Klingenburg H, Hofstatter T and Bucher T.**, The isolation and crystallization of yeast and rabbit liver triose phosphate isomerase and a comparative characterization with the rabbit muscle enzyme., *Eur. J. Biochem.* 14:289–300, 1970

45 **Dabrowska A, Kamrowska I and Baranowski T.**, Purification, crystallization, and properties of triosephosphate isomerase from human skeletal muscle., *Acta Biochim. Pol.* 25:247–256, 1978

46 **Molnar M and Vas M.**, Mg^{2+} affects the binding of ADP but not ATP to 3-phosphoglycerate kinase. Correlation between equilibrium dialysis binding and enzyme kinetic data., *Biochem. J.* 293:595–599, 1993

47 **Rose ZB and Dube S.**, Phosphoglycerate mutase. Kinetics and effects of salts on the mutase and bisphosphoglycerate phosphatase activities of the enzyme from chicken breast muscle., *J. Biol. Chem.* 253:8583–8592, 1978

48 **Rider CC and Taylor CB.**, Enolase isoenzymes in rat tissues. Electrophoretic, chromatographic, immunological, and kinetic properties., *Biochim. Biophys. Acta* 365:285–300, 1974

49 **Dyson RD, Cardenas JM and Barsotti RJ.**, The reversibility of skeletal muscle pyruvate kinase and an assessment of its capacity to support glyconeogenesis., *J. Biol. Chem.* 250:3316–3321, 1975

50 **Schmitz JPJ, van Riel NAW, Nicholay K, Hilbers PAJ and Jeneson JAL.**, Silencing of glycolysis in muscle: experimental observation and numerical analysis., *Exp. Physiol.* 95:380–397, 2009

51 **Vinnakota KC, Joshua Rusk J, Palmer L, Shankland E and Kushmerick MJ.**, Common phenotype of resting mouse extensor digitorum longus and soleus muscles: equal ATPase and glycolytic flux during transient anoxia., *J. Physiol.* 588:1961–1983, 2010

52 **Choi SC, Kim Y, Lee FN, Zabolotny JM, Kahn BB and Youn JH.**, Lactate induces insulin resistance in skeletal muscle by suppressing glycolysis and impairing insulin signalling., *Am. J. Physiol. Endocrinol. Metab.* 283:E233–E240, 2002

53 **Lambeth MJ, Kushmerick MJ, Marcinek DJ and Conley KE.**, Basal glycogenolysis in mouse skeletal muscle: in vitro model predicts in vivo fluxes., *Mol. Biol. Rep.* 29:135-139, 2002

Chapter 5
Validation and analysis of the mechanistic model describing glycolysis in differentiated C_2C_{12} muscle extract

5.1 Preamble

In this chapter we apply the IP-RPLC method developed in Chapter 3 to quantify the time-dependent concentrations of glycolytic intermediates and cofactors in C_2C_{12} skeletal muscle extracts. For model validation we compare the model simulations to time-dependent concentrations of glycolytic intermediates and cofactors. Metabolic control analysis of the detailed kinetic model describing glycolysis in skeletal muscle was performed to evaluate which reaction steps have control over the pathway.

5.2 Introduction

Bottom-up modelling approaches aim to combine the mechanistic knowledge of the isolated components of a system into a mathematical model and test its ability to make predictions for the system`s behaviour. Therefore, one of the main concerns faced by bottom-up modelling approaches is to consider how accurate the model predicts what is observed experimentally[1]. The need for and conceptualisation of how models in both natural and social sciences ought to be validated has been a controversial topic for many years[2]. Tropsha *et. al.*[3] stated in their research on the essential need for validation of quantitative structure property relationship (QSPR) models that a prerequisite for QSPR models to be reliable is that these models should be statistically significant and robust, and should be accurate in predicting external data sets that were not used in model development. Furthermore, the application boundaries of these models should be limited to the areas that they have been validated in. Estimating the true predictive capabilities of a model necessitates the comparison of model predictions to observed trends of a sufficiently large set of external tests that were not used in model construction[3]. The complexity of bottom-up modelling often requires incorporation of kinetic parameters from various sources. Due to limited availability of experimental data to determine kinetic parameters under a standardised set of cytosolic representative conditions, gaps are filled by relying on studies performed under non-cytosolic representative conditions, or by fitting kinetic parameters to simplified catalytic mechanisms.

Determining the predictive accuracy of bottom-up models relies on the availability of analytical techniques that can quantify variables specified and predicted in the model. In the context of metabolic models, these analytical techniques need to construct a metabolomic picture of the biological system being simulated. Metabolome analysis allows for the direct access to the phenotype expressed under specific environmental conditions. The outcome of cellular regulatory processes present at different levels of expression is reflected in the metabolomic phenotype of the system[4,5]. In essence, a picture of the whole is obtained without any information of the mechanisms that lead to the formation of the whole. This can then be compared to the outcomes of the mechanistic layout described in the model. Metabolomic techniques hold significant value to molecular systems biologists to compare bottom-up mechanistic model predictions with metabolome data. The ability to utilise a metabolomic approach in tandem with dynamic metabolic modelling approaches have further benefits. Employing an iterative approach between mechanistic modelling and experimental metabolomic analysis allows for the identification and elucidation of new metabolic pathways as well as a better understanding of regulatory processes involved in existing metabolic pathways[6,7].

There are several examples in literature of how metabolomic data were used to validate the predictive accuracy of mechanistic models of glycolysis. Penkler et. al.[8] constructed a detailed kinetic model of glycolysis in *Plasmodium falciparum*. In total the model described the change in concentration of 17 chemical species including the conserved adenosine and nicotinamide moieties. The detailed kinetic model was validated by quantifying the time dependent concentrations of GLC, LAC, PYR and GLY enzymatically and via HPLC-MS analysis and comparing the resulting data to model predictions. 4 out of the 17 variables described by the model were correlated to dynamic experimental data and several other metabolites were determined under steady state conditions. Similarly, Lambeth and Kushmeric[9,10] constructed a bottom-up computational model of glycogenolysis in skeletal muscle relying on kinetic parameters obtained from literature sources. The computational model described 19 variables in total and the model was validated by obtaining quantitative concentrations of PCr and Pi as a function of time by performing ^{31}P-NMR analysis on anesthetised male Swiss Webster mice. This resulted in validating the model by correlating 2 variables to the total 19 described in the model. Schmitz *et. al.*[11] further investigated the predictive accuracy of the computational model constructed on glycogenolysis in skeletal muscle, by Lambeth and Kushmeric[9]. ^{31}P-NMR measurements of hexose monophosphates were

performed on human leg muscle. ^{31}P-NMR is a powerful technique for the *in vivo* determination of metabolites in whole organisms. In contrast, the metabolomics method developed in Chapter 3 is more applicable for targeted metabolomic studies in *in vitro* samples The endeavours pointed out here indicate the need for the development of analytical metabolomic techniques that can quantify a large amount of corresponding chemical species in a time dependent manner in *in vitro* biochemical samples.

Once a mathematical model has been constructed and validated, metabolic control analysis can be performed. Metabolic control analysis is a powerful tool for investigating the systematic properties of a pathway, such as steady state fluxes and metabolite concentrations in terms of enzyme rates and kinetic parameters. The degree to which a small change in a local rate property exerts a change in the systematic properties of the pathway can be investigated by deriving flux and concentration control coefficients. Metabolic control analysis determines which reaction in the pathway exerts most control over the flux through and concentrations of metabolites in the pathway. Modelling studies on the metabolic activity of skeletal muscle performed by Lambeth *et. al.*[9] and Choi *et. al.*[12] demonstrated that the flux control in glycolysis lies largely with the demand for ATP (ATPase) with a contribution of between 95% and 99%.

In Chapter 3 of this thesis we developed an ion-pairing reverse phase liquid chromatographic (IP-RPLC) method coupled to UV/Vis detection in tandem with radiolabelled isotope detection for the separation and quantification of glucose derived intermediates formed in glycolysis along with the separation and quantification of the adenosine and nicotinamide moieties. This chapter will focus on utilising this newly developed technique to quantify the glycolytic intermediates and adenosine and nicotinamide moieties formed by the glycolytic pathway in differentiated C_2C_{12} muscle extract under various experimental conditions as a function of time. The resulting time dependent concentration traces will then be compared to model predictions using the glycolytic model constructed in Chapter 4 of this thesis. Construction and validation of the glycolytic model describing glycolysis in C_2C_{12} muscle fibre extract was limited to investigating the pathway in extracts and not to whole muscle fibres. This has the benefit that a series of different starting conditions can be selected to provide rigorous and thorough testing of model capabilities. Whole cells are limited by the rate of glucose uptake. In contrast, with cellular extracts the glycolytic pathway can be initialised with different initial concentrations of the adenosine and nicotinamide moieties or any of the glycolytic intermediates available. The disadvantage of the *in vitro* analysis is that the physiological

relevance is not as good compared to *in vivo* intact cell or organism approaches. The predictive accuracy of the glycolytic model describing glycolysis in C_2C_{12} muscle fibre extract will be validated here using 3 different sets of initial conditions. Model predictions and experimentally obtained data, determined for the same set of initial conditions will be overlaid to determine how well the model predicts the experimental data.

5.3 Materials and Methods

5.3.1. C_2C_{12} muscle fibre lysis protocol

Extract of differentiated C_2C_{12} muscle fibres were prepared by lysing the cells with Triton X-100 as per the protocol given in Chapter 4 of this thesis. In short: an aliquot of differentiated C_2C_{12} muscle fibres were thawed and treated with 20µL of a 10% Triton X-100 solution. The cell suspension was left to rest on ice for 30 min. After the 30 min treatment the cell suspension was centrifuged at 20 800 x *g* at 4ºC for 15 minutes to pellet the cell debris. After centrifugation the supernatant was removed and stored on ice.

5.3.2. HPLC methodology

HPLC analysis was done using the method developed in Chapter 3 of this thesis. In short, low pressure mixing of mobile phase A, consisting of 25 mM TBA in water adjusted to a pH of 7.3 (± 0.1) and mobile phase B consisting of 97.5% acetonitrile and 2.5% water at a ratio of 95% A and 5% B. a gradient was employed to expedite the analysis of higher retaining chemical species. The gradient is a follow: at 0 min 95% A and 5% B; 5 min 70% A and 30% B; 12 min 95% A and 5% B. The column eluent was detected by UV/Vis detection at 254 nm followed by radiolabelled detection.

5.3.3. Time-course sampling protocol

Differentiated C_2C_{12} extract was prepared in assay buffer for the time dependent quantification of the glycolytic intermediates and adenosine and nicotinamide moieties by means of HPLC analysis. A cocktail containing the specified concentrations of ATP and NAD^+ was added to the C_2C_{12} muscle fibre extract, the sample was heated to 37ºC and was kept at 37ºC for the duration of the experiment. A mixture of ^{14}C-glucose and non-radiolabelled glucose (cold-glucose) was added to the cell extract to initialise the incubation and a 50 µL sample was taken at this timepoint (t = 0 min). Further sampling was performed at the specified

timepoints. Directly after the acquisition of each sample it was treated with 7.5 µL 50% PCA, neutralised with 42.5 µL of a 1M K_2CO_3 solution and stored on ice. This resulted in the deactivation and precipitation of the glycolytic enzymes, along with the precipitation of $KClO_4$. The precipitate was removed via centrifugation at 20 800 x *g* for 15 min at 4ºC. 5µL of each sample was injected into the HPLC column and quantified.

The resulting chromatographic traces obtained from the radiolabelled detector were integrated using an in-house developed script (described below). The chromatographic traces obtained from the UV/Vis detector corresponds to the adenosine and nicotinamide moieties and were quantified by means of a calibration curve.

5.3.4. Integration of chromatographic traces and data analysis

The concentrations of the adenosine and nicotinamide metabolites in the time-course samples were determined by integration of the UV/Vis chromatographic traces as described in Section 3.4.1 of Chapter 3 in this thesis. In short, calibration curves for the metabolites ATP, ADP, AMP, NAD^+, and NADH were constructed. The concentrations of the adenosine and nicotinamide metabolites were determined by correlating the integrated area of the chromatographic traces obtained for the time-course experiments to the calibration function.

The concentrations of the glycolytic intermediates in the time-course samples were determined by integration of the radiolabelled chromatographic traces as described in Section 3.3.3 of Chapter 3 in this thesis. In short, a response factor correlating the integrated area of the GLC chromatographic trace to concentration was determined for each time-course incubation. Data analysis entailed fitting a series of skewed normal distribution functions to the chromatograms using an in-house developed script in *Wolfram Mathematica*. The integration of each skewed normal distribution function yielded the area under the peak. In cases where excessive tailing was present the peak was described by fitting 2 skewed normal distribution functions and summing the resulting areas. The data was normalised to the total counts in each run, and a baseline subtraction was performed to eliminate the contribution of the radiolabelled impurities present in the starting material.

5.3.5. Performing metabolic control analysis.

Metabolic control analysis was performed on the detailed kinetic model describing glycolysis in differentiated C_2C_{12} skeletal muscle. To obtain a steady state the ATPase activity

was decreased 10-fold as explained in Section 4.4.13. The concentration of GLC was clamped at 10 mM to reflect the culturing conditions of the C_2C_{12} cells (see Section 4.3.1), and the LAC was clamped at 1.3 mM in correspondence with Schmitz *et al.*[11] Metabolic control analysis was performed in *Wolfram Mathematica 12.0* by perturbing each Vmax by 0.1 % and evaluating the effect on flux and concentrations.

5.4 Results

5.4.1. Validating the predictive accuracy of the glycolytic model in differentiated C_2C_{12} muscle extract

To validate the detailed kinetic model describing glycolysis in differentiated C_2C_{12} skeletal muscle extract, model predictions were compared to experimental data obtained via IP-RPLC analysis of C_2C_{12} muscle extracts. Three time-course experiments (named Exp 1, Exp 2 and Exp 3) were conducted at different initial conditions to see how the model behaves in different scenarios. Exp 1 and Exp 2 are very similar in setup. Exp 1 and Exp 2 were performed in different cell lysates and differ in the initial concentrations of GLC, ATP and NAD^+.

1. Exp 1 (Section 5.4.2) was initiated with 0.815 mM GLC, 2.616 mM ATP and 1.110 mM NAD^+. This allows for the presence of excess cofactors to ensure complete consumption of GLC.
2. Exp 2 (Section 5.4.3) was initiated with approximately 0.5 mM GLC, 4 mM ATP and 2 mM NAD^+. The experiment was designed to observe how the system behaves in the presence of excess cofactors, in comparison with what is required to consume the amount of GLC present.
3. Exp 3 (Section 5.4.4) was initiated with approximately 3.077 mM FBP, 0.644 mM ADP and 1.010 mM NAD^+. The experiment was designed to observe how the system behaves when initialised in the middle of the glycolytic pathway.

The initial metabolite concentrations of Exp 1, Exp 2 and Exp 3 are listed in Table 5.1 and these values were used as input value for model simulations, which were compared to the experimentally obtained time-course data. Time-course incubations of differentiated C_2C_{12} muscle fibres were carried out at 37ºC in duplicate by dividing the cell extract in 2 equal parts and performing the time-course experiment in both fractions simultaneously. The adenosine and nicotinamide cofactors were added to the incubations prior to initialisation with GLC or FBP. This resulted in the conversion of some of the ATP to ADP and AMP in the cases of Exp1

and Exp 2. Regarding Exp 1 and Exp 2, the initial GLC concentration was determined via a coupled assay technique by adding commercially obtained HK and G6PDH as described in Section 3.4.5 of this thesis. The time-course incubation was initialised by adding the glucose to the differentiated C_2C_{12} muscle extract containing the adenosine and nicotinamide cofactors and samples were prepared and injected onto the column for HPLC analysis as described in Section 5.3.3.

For Exp 3, ^{14}C-glucose was reacted with commercially obtained HK and PGI in the presence of ATP and NAD^+ to convert the ^{14}C-GLC to ^{14}C-FBP. The extend of conversion was tested by injecting a representative sample into the HPLC, which indicated that the conversion has reached completion. Cold FBP was added to the ^{14}C-FBP sample and the total FBP concentration was determined by a coupled assay technique by adding commercially obtained ALD, TPI and G3PDH. The time-course incubation was initialised by adding the FBP stock solution to the differentiated C_2C_{12} muscle extract and samples were prepared and injected into the column for HPLC analysis as described in Section 5.3.3.

It was not possible to determine the concentrations of AMP and NADH via HPLC-UV/Vis detection in the time-course samples of Exp 2 and Exp 3, due to significant peak overlap between AMP and NADH. Therefore, the concentrations of NADH and AMP was estimated by using Eq.5.1 and Eq.5.2 which assumes that the total adenosine and nicotinamide moieties remain constant overtime

$$\text{Adenosine}_{\text{Total}} = \text{ATP} + \text{ADP} + \text{AMP} \qquad \text{(Eq. 5.1)}$$

$$\text{Nicotinamide}_{\text{Total}} = \text{NADH} + \text{NAD}^+ \qquad \text{(Eq. 5.2)}$$

***Table 5.1**: Summary of the initial concentrations as obtained from the chromatographic analysis of the time-course incubation of differentiated C_2C_{12} muscle extract taken at 0 min for the time course experiments Exp 1, Exp 2 and Exp 3. The initial concentrations served as the input values for the model predictions correlated to the experimentally obtained time dependent traces.*

	Initial concentrations (mM)		
Metabolite	Exp 1	Exp 2	Exp 3
GLC	0.815	0.471	0,005
G6P	0.026	0.010	0.000
F6P	0.008	0.005	0.000
FBP	0.000	0.000	3,077
LAC	0.002	0.026	0,089
NAD^+	1.110	1.710	0,771
NADH	0.000	0.290	0,239
ATP	1.468	2.220	0,263
ADP	1.148	1.390	0,226
AMP	0	0.390	0,155
Tprot (mg)	3.893	2.184	1,878
Tvol (mL)	0.6	0.6	0,6

The model constructed in Chapter 4 of this thesis was compared to the time dependent concentration trends obtained from the HPLC analysis of the time-course samples. The initial concentrations of each variable in the model was determined from the first chromatographic result at time point 0 min. With regards to Exp 3 the chromatographic peak corresponding to GLC at 0 min was large and does not compare to the GLC concentrations observed in the later time points. Therefore, the initial concentration of GLC was set to the chromatographic peak corresponding to GLC at 5 min .To correlate model predictions to the time course experimental data we needed to modify the model to describe enzyme activities as *mM/ min* as opposed to $\mu mol.min^{-1}.mg\ total\ protein^{-1}$ in the model constructed in Chapter 4. Therefore, the kinetic parameter describing the maximal specific activity (*Vmax*) for each enzyme was modified by multiplying it by the protein concentration (determined via a Bradford assay) and dividing by the total volume of the incubation. This effectively creates a cell unit that is the size of the incubation.

5.4.2. Comparing the glycolytic model in differentiated C_2C_{12} muscle extract with IP-RPLC time-course data initialised with GLC (Exp 1)

Exp 1 was carried out as discussed in Section 5.4.1. The experimentally obtained chromatographic traces were obtained via IP-RPLC analysis of differentiated C_2C_{12} skeletal muscle extract in duplicate, and was correlated with model predictions and are given in Figure 5.1. The integrated chromatographic traces of Exp 1 are shown in the attached Appendix (Figure A.1 and Figure A.2)

In total 15 variables present in the model describing glycolysis in differentiated C_2C_{12} muscle extract were compared to experimentally determined time-course data. There is a good correlation between the model predicted and experimentally obtained time dependent concentration traces of GLC, G6P, F6P and FBP. With regards to the LAC and PYR trends, the predictive trends show a similar shape as compared to the experimental data. However, there is an overestimation of the concentration of LAC and an underestimation of the concentration of PYR by the model. The predictions for the adenosine moieties show similar trends compared with the experimental data but does not perfectly describe the experimental data. The experimentally determined trends of the nicotinamide moieties suggests that there are other reactions present that influence the concentrations of these chemical species. Furthermore, the model significantly underpredicts the concentrations of the intermediates in the bottom part of glycolysis, *i.e.* P3G, P2G and PEP.

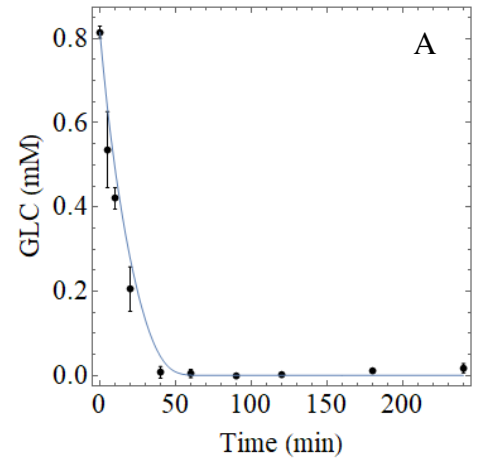

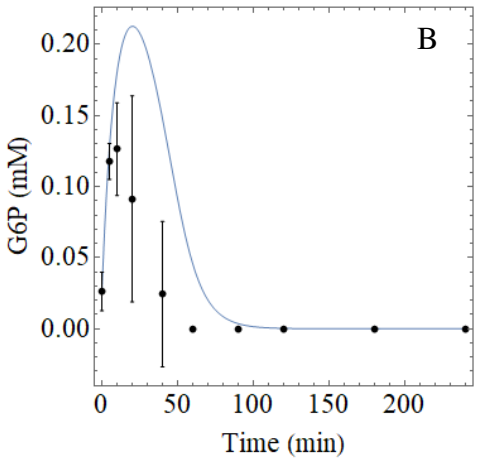

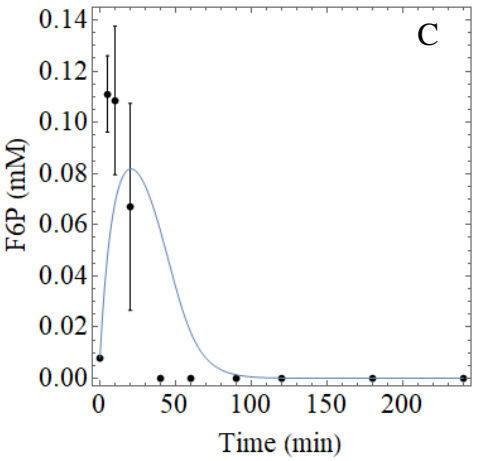

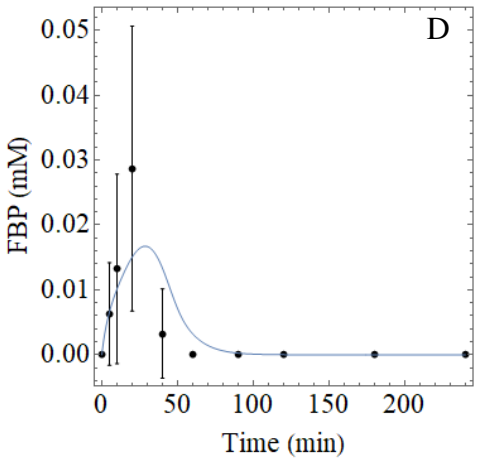

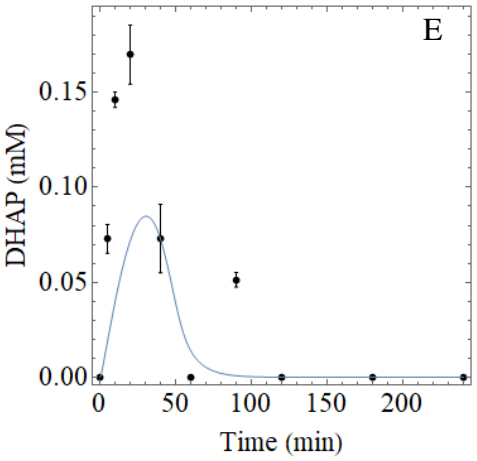

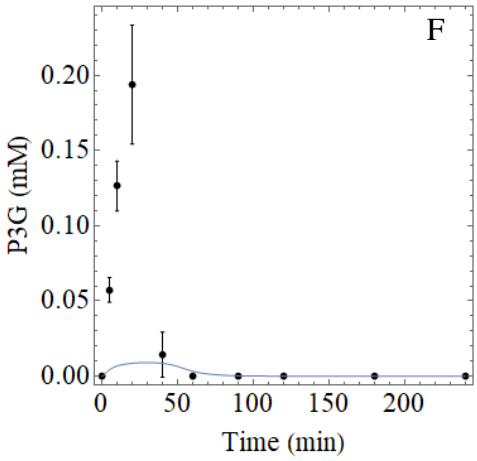

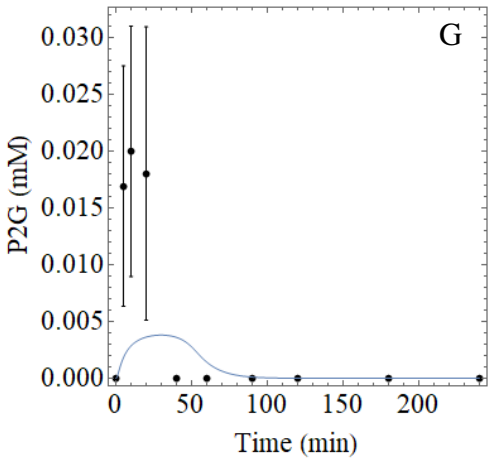

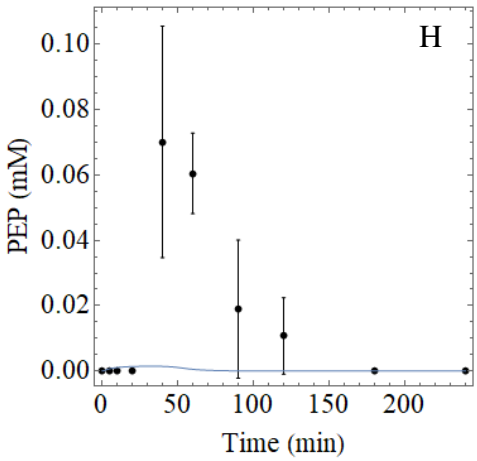

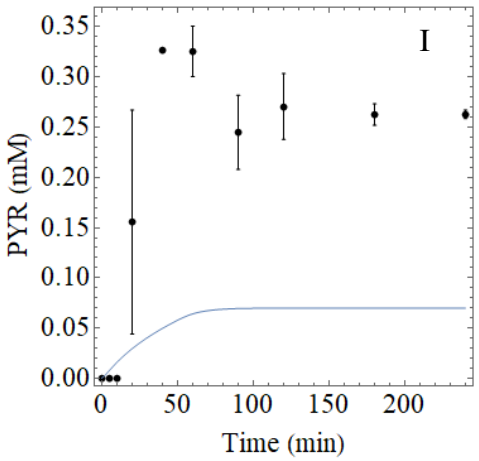

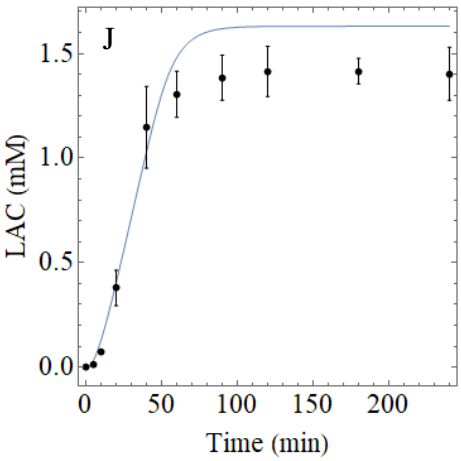

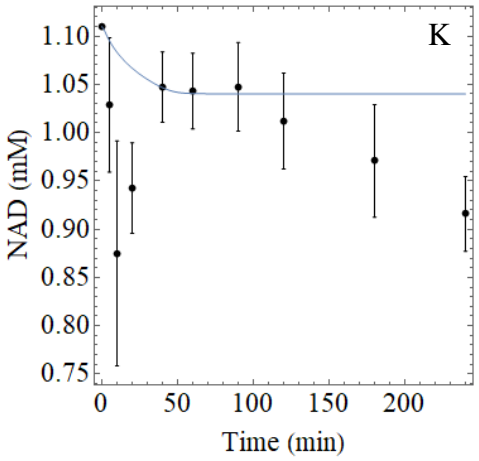

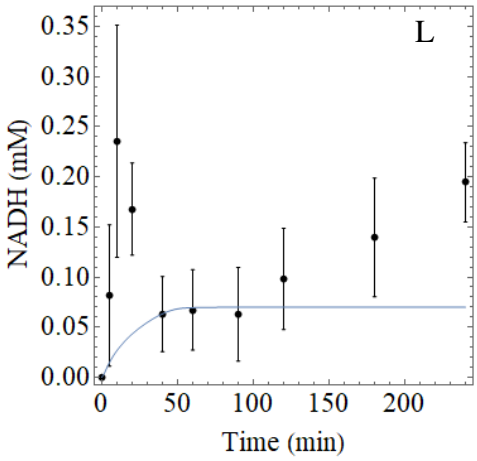

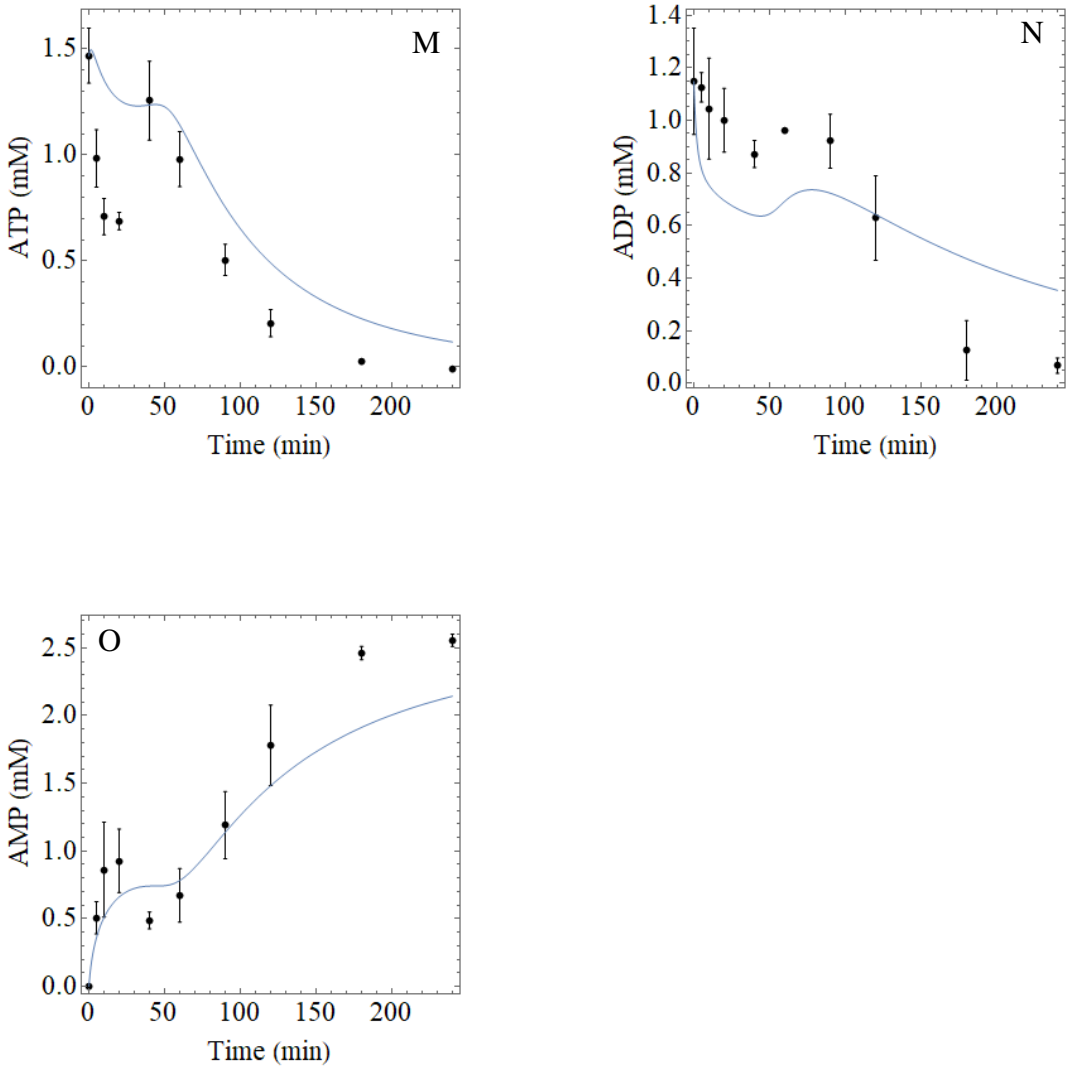

***Figure 5.1**: Correlation of model predictions to the experimentally determined time dependent concentrations as obtained via IP-RPLC analysis of the time-course experiment initialised with 0.853 mM GLC, 2.616 mM ATP and 1.11 mM NAD^+. The data points represent the concentrations as determined via IP-RPLC analysis. The blue line represents the model predictions using the model constructed in chapter 4 of this thesis describing glycolysis in differentiated C_2C_{12} muscle extract. The subfigures represent the model predicted flux and experimentally measured flux of the variables. **A:** experimental data and model simulation of GLC, **B:** experimental data and model simulation of G6P, **C:** experimental data and model simulation of F6P, **D:** experimental data and model simulation of FBP, **E:** experimental data and model simulation of DHAP, **F:** experimental data and model simulation of P3G, **G:** experimental data and model simulation of P2G, **H:** experimental data and model simulation of PEP, **I:** experimental data and model simulation of PYR, **J:** experimental data and model simulation of LAC,**K:** experimental data and model simulation of NAD^+, **L:** experimental data and model simulation of NADH, **M:** experimental data and model simulation of ATP, **N:** experimental data and model simulation of ADP and **O:** experimental data and model simulation of AMP.*

5.4.3. Comparing the glycolytic model in differentiated C_2C_{12} muscle extract with IP-RPLC time-course data initialised with GLC (Exp 2)

Exp 2 was carried out as discussed in Section 5.4.1. The experimentally obtained chromatographic traces were obtained via IP-RPLC analysis of differentiated C_2C_{12} skeletal muscle extract in duplicate, and was correlated with model predictions and are given in Figure 5.2. The integrated chromatographic traces of Exp 1 are shown in the attached Appendix (Figure A.3 and Figure A.4)

The model describing glycolysis in differentiated C_2C_{12} muscle fibre extract was compared with the experimentally determined concentrations. The time dependent concentrations of 15 variables were quantified via IP-RPLC analysis and compared to the corresponding model predictions. The experimentally obtained traces for GLC, G6P, F6P, FBP and DHAP correlates well with model predictions. The model predictions overestimate the concentration of LAC and underestimates the concentration of PYR, similar to the previous experiment. The initial trends in the adenosine moieties as predicted by the model, correlate well with experimental data, however model predictions deviate from the experimental data in the latter half of the reaction.

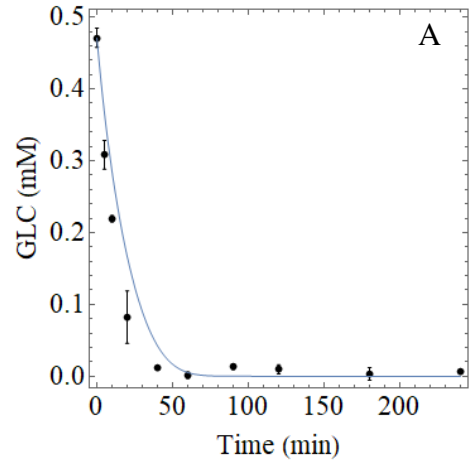

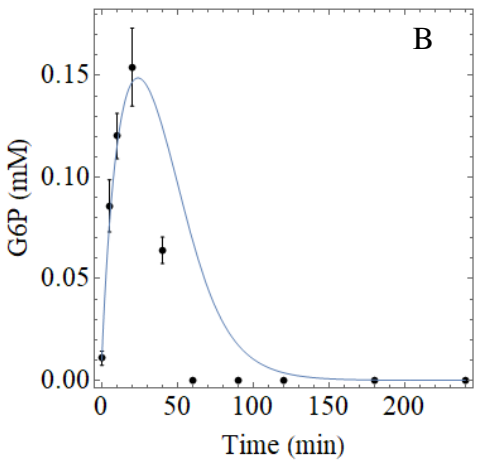

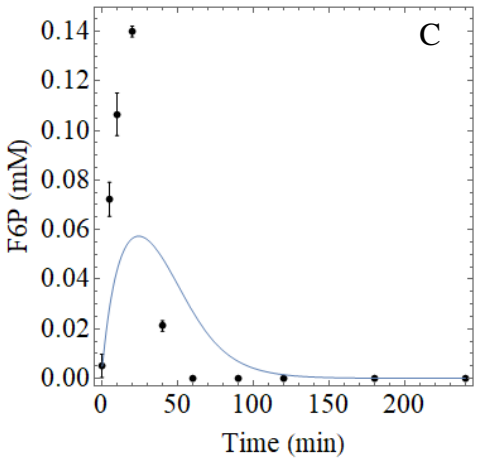

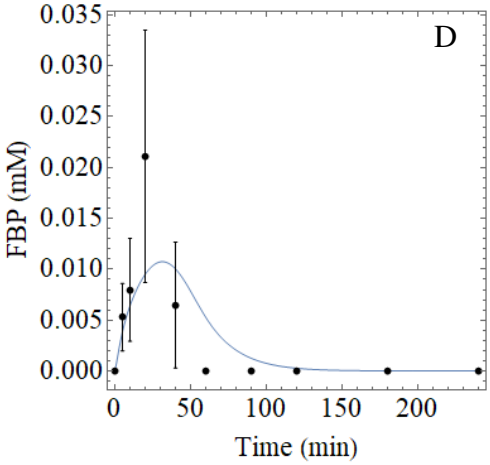

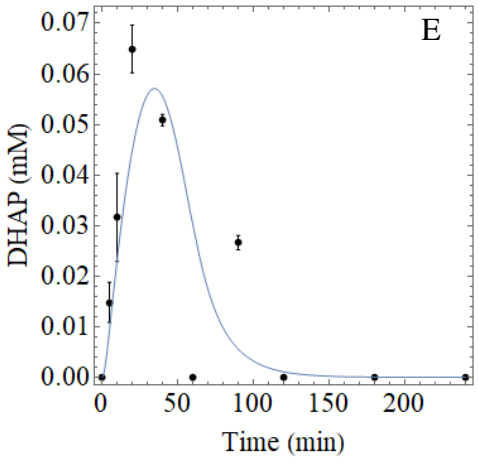

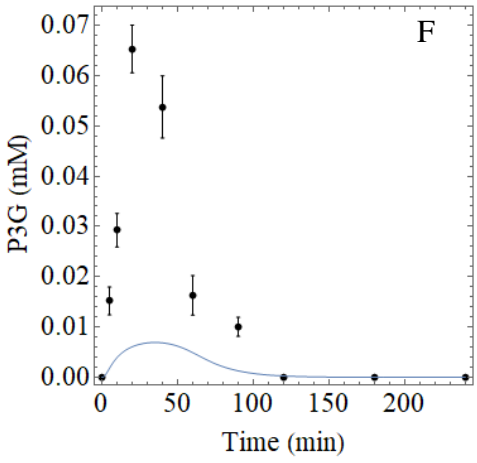

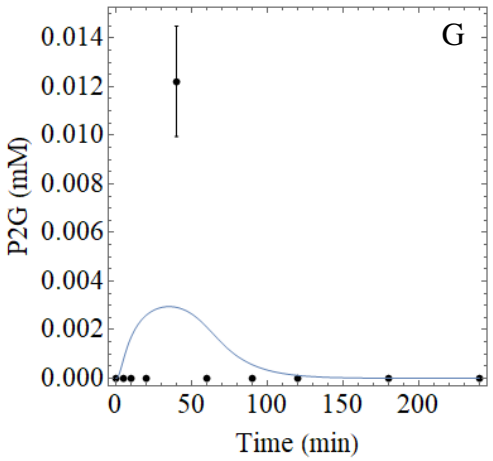

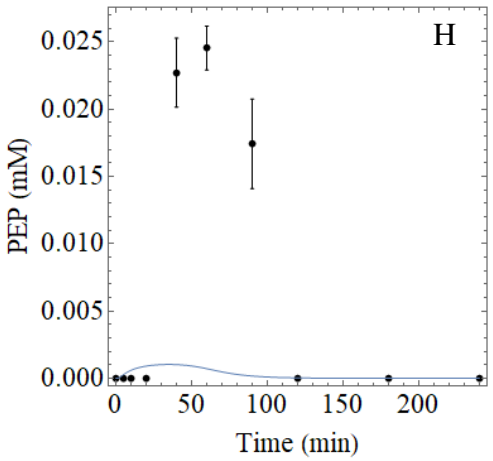

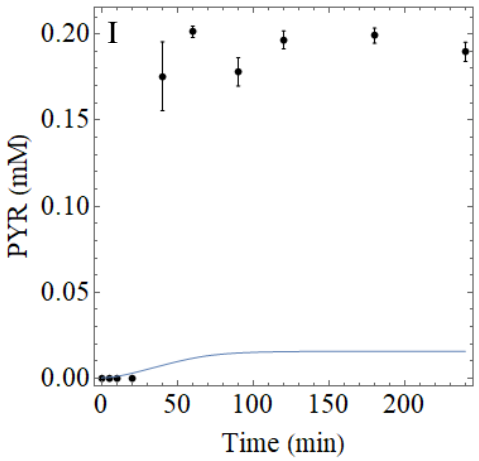

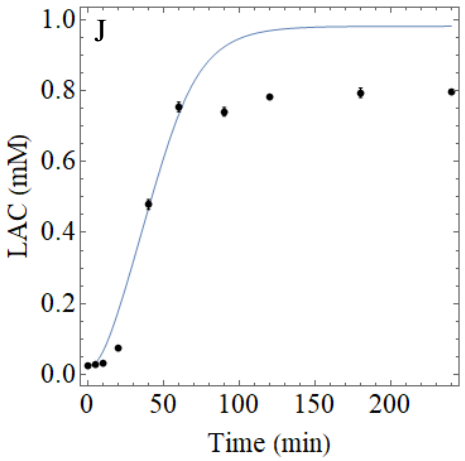

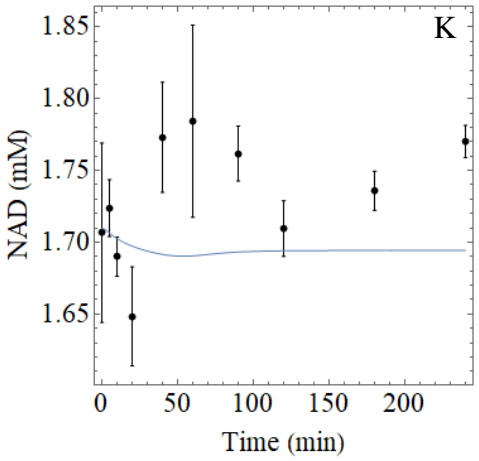

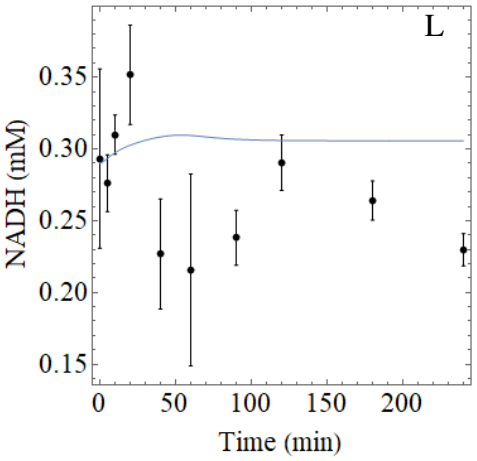

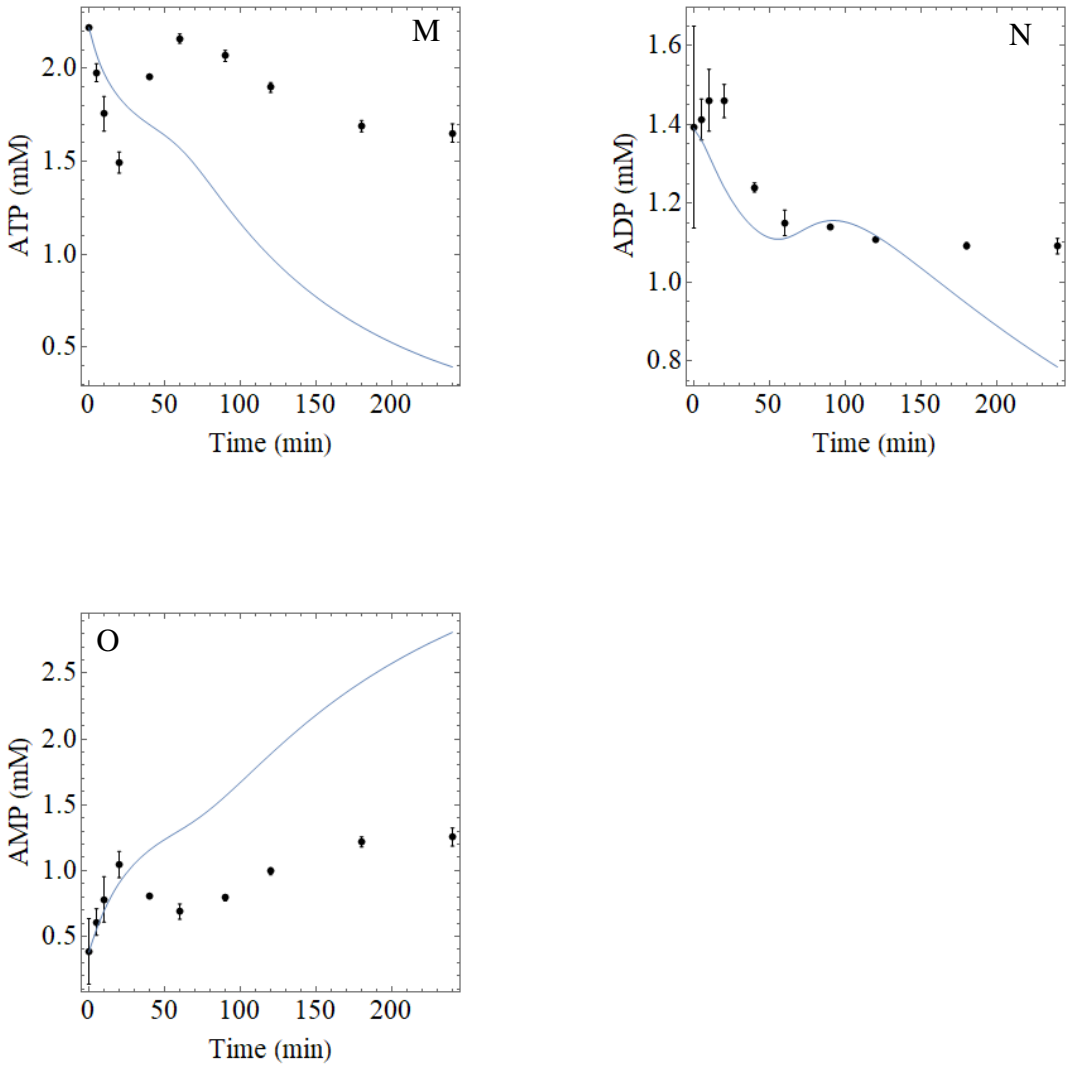

***Figure 5.2**: Correlation of model predictions to the experimentally determined time dependent concentrations as obtained via IP-RPLC analysis of the time-course experiment initialised with 0.512 mM GLC, 4 mM ATP and 2 mM NAD⁺. The data points represent the concentrations as determined via IP-RPLC analysis. The blue line represents the model predictions using the model constructed in chapter 4 of this thesis describing glycolysis in differentiated C_2C_{12} muscle extract. The subfigures represent the model predicted flux and experimentally measured flux of the variables: **A:** experimental data and model simulation of GLC, **B:** experimental data and model simulation of G6P, **C:** experimental data and model simulation of F6P, **D:** experimental data and model simulation of FBP, **E:** experimental data and model simulation of DHAP, **F:** experimental data and model simulation of P3G, **G:** experimental data and model simulation of P2G, **H:** experimental data and model simulation of PEP, **I:** experimental data and model simulation of PYR, **J:** experimental data and model simulation of LAC,**K:** experimental data and model simulation of NAD⁺, **L:** experimental data and model simulation of NADH, **M:** experimental data and model simulation of ATP, **N:** experimental data and model simulation of ADP and **O:** experimental data and model simulation of AMP.*

5.4.4. Comparing the glycolytic model in differentiated C_2C_{12} muscle extract with IP-RPLC time-course data initialised with FBP (Exp 3)

Exp 3 was carried out as discussed in Section 5.4.1. The experimentally obtained chromatographic traces were obtained via IP-RPLC analysis of differentiated C_2C_{12} skeletal muscle extract in duplicate, and was correlated with model predictions and are given in Figure 5.3. The integrated chromatographic traces of Exp 1 are shown in the attached Appendix (Figure A.5 and Figure A.6)

The model describing glycolysis in differentiated C_2C_{12} muscle fibre extract was compared with the experimentally determined concentrations. The time dependent concentrations of 10 variables were quantified via IP-RPLC analysis and compared to the corresponding model predictions. There is a good comparison between the model predicted trends and experimentally obtained traces for FBP and LAC. Due to the absence of G6P and F6P, the GAP peak was clearly visible and could easily be quantified. However, the model significantly underestimates the concentration of GAP and overestimates the concentration of DHAP. Comparison of the model predicted trends and experimental traces for the adenosine moieties show similar behaviour. The traces corresponding to P3G, P2G, PEP and PYR were too low in the chromatographic traces to quantify.

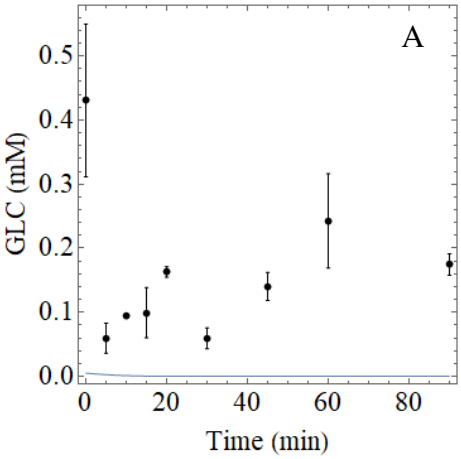

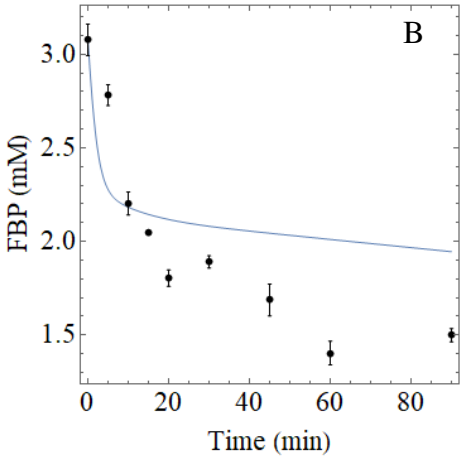

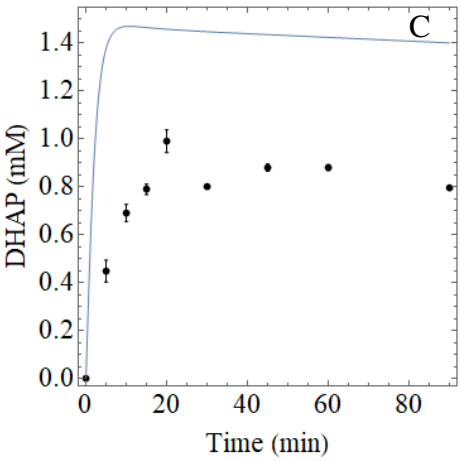

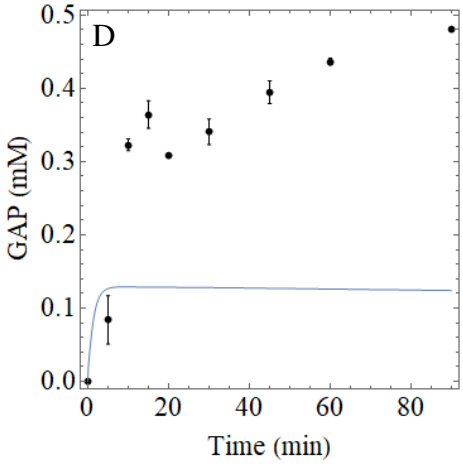

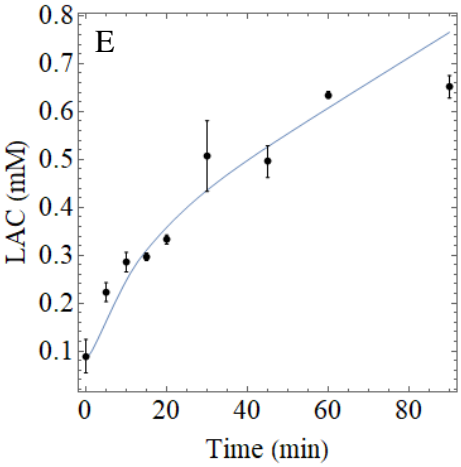

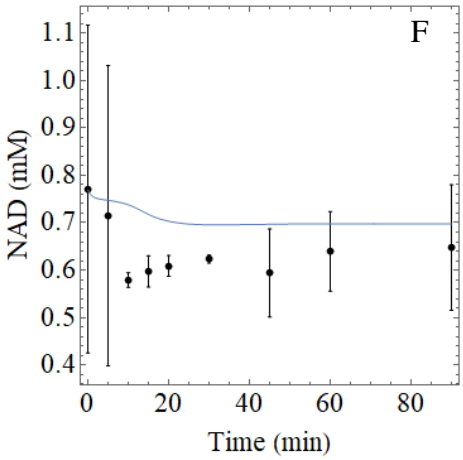

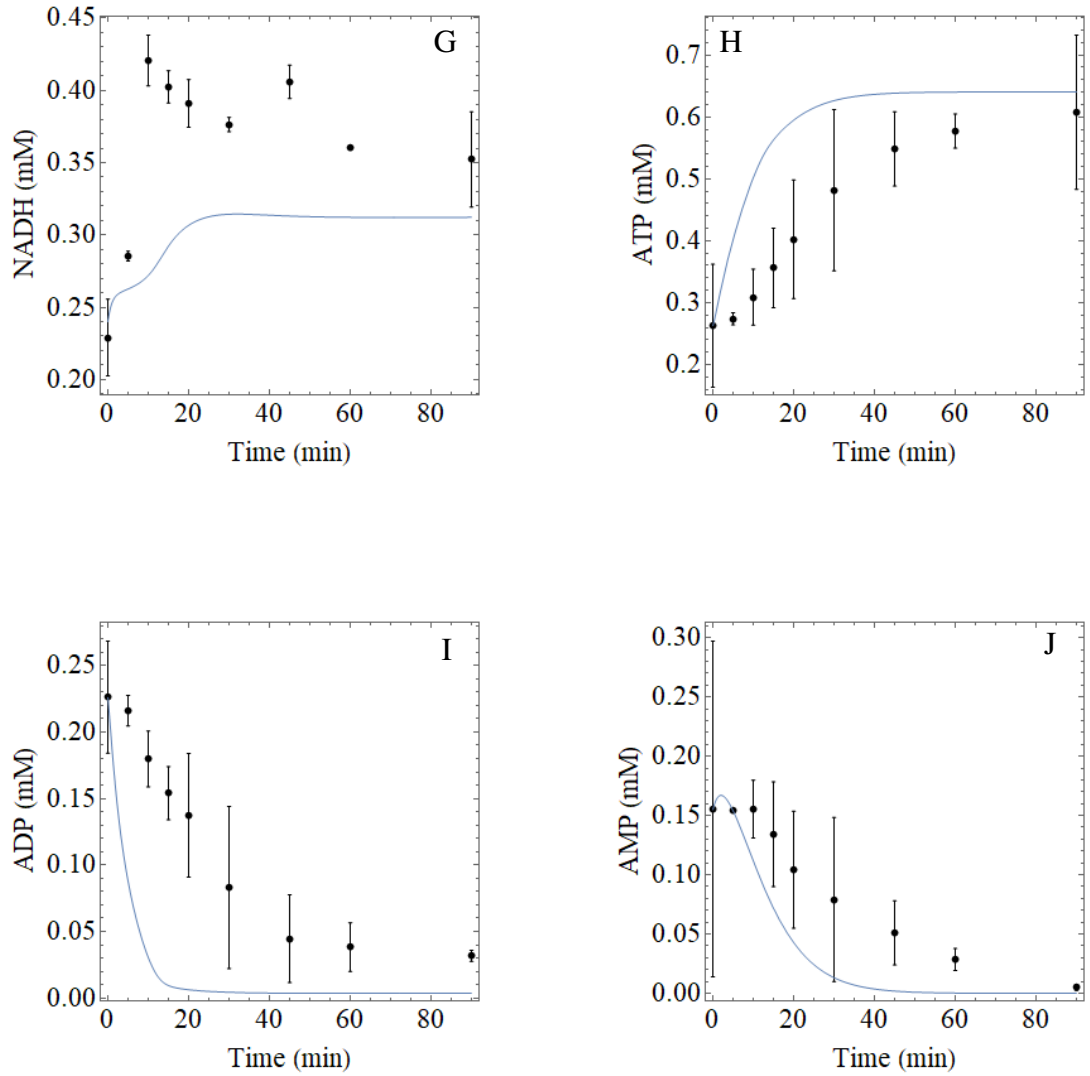

***Figure 5.3**: Correlation of model predictions to the experimentally determined time dependent concentrations as obtained via IP-RPLC analysis of the time-course experiment initialised with 3.596 mM FBP, 0.263 mM ATP, 0.226 mM ADP and 0.771 mM NAD⁺. The data points represent the concentrations as determined via IP-RPLC analysis. The blue line represents the model predictions using the model constructed in chapter 4 of this thesis describing glycolysis in differentiated C_2C_{12} muscle extract. The subfigures represent the model predicted flux and experimentally measured flux of the variables: **A:** experimental data and model simulation of GLC, **B:** experimental data and model simulation of FBP, **C:** experimental data and model simulation of DHAP, **D:** experimental data and model simulation of GAP, **E:** experimental data and model simulation of LAC, **F:** experimental data and model simulation of NAD⁺, **G:** experimental data and model simulation of NADH, **H:** experimental data and model simulation of ATP, **I:** experimental data and model simulation of ADP, **J:** experimental data and model simulation of AMP.*

5.4.5. Model analysis and metabolic control analysis

Metabolic control analysis was performed on the kinetic model describing glycolysis in differentiated C_2C_{12} skeletal muscle cells to quantify the control that each enzyme has over the system. The concentrations of GLC and LAC were clamped at 10 mM and 1.3 mM respectively to simulate the physiological blood concentrations of these compounds in mice. To obtain a steady state the ATPase activity was decrease 10-fold as discussed in Section 4.4.13. The complete matrix of flux and concentration control coefficients are given in Table 5.2 and Table 5.3. The ATPase reaction has most of the flux control at 99.4 % whereas minor control over the flux of the system is held by PK (0.5 %) and GAPDH (0.1 %). This corresponds to the findings of published in literature[9,11] stating that ATPase has between 95 % and 99 % of the flux control through the system.

Table 5.2: *Complete set of flux control coefficients as determined for the kinetic model describing glycolysis in differentiated C_2C_{12} skeletal muscle extract. ATPase accounts for most of the flux control, with minor flux control by GAPDH and PK, highlighted in Bold. The flux control coefficients were determined in Wolfram Mathematica 12.0, through a perturbation method.*

	v_{HK}	v_{PGI}	v_{PFK}	v_{ALD}	v_{TPI}	v_{GAPDH}	v_{PGK}	v_{PGM}	v_{ENO}	v_{PK}	v_{LDH}	v_{AK}	v_{ATPase}
J_{HK}	0.000	0.000	0.000	0.000	0.000	**0.001**	0.000	0.000	0.000	**0.005**	0.000	0.000	**0.994**
J_{PGI}	0.000	0.000	0.000	0.000	0.000	**0.001**	0.000	0.000	0.000	**0.005**	0.000	0.000	**0.994**
J_{PFK}	0.000	0.000	0.000	0.000	0.000	**0.001**	0.000	0.000	0.000	**0.005**	0.000	0.000	**0.994**
J_{ALD}	0.000	0.000	0.000	0.000	0.000	**0.001**	0.000	0.000	0.000	**0.005**	0.000	0.000	**0.994**
J_{TPI}	0.000	0.000	0.000	0.000	0.000	**0.001**	0.000	0.000	0.000	**0.005**	0.000	0.000	**0.994**
J_{GAPDH}	0.000	0.000	0.000	0.000	0.000	**0.001**	0.000	0.000	0.000	**0.005**	0.000	0.000	**0.994**
J_{PGK}	0.000	0.000	0.000	0.000	0.000	**0.001**	0.000	0.000	0.000	**0.005**	0.000	0.000	**0.994**
J_{PGM}	0.000	0.000	0.000	0.000	0.000	**0.001**	0.000	0.000	0.000	**0.005**	0.000	0.000	**0.994**
J_{ENO}	0.000	0.000	0.000	0.000	0.000	**0.001**	0.000	0.000	0.000	**0.005**	0.000	0.000	**0.994**
J_{PK}	0.000	0.000	0.000	0.000	0.000	**0.001**	0.000	0.000	0.000	**0.005**	0.000	0.000	**0.994**
J_{LDH}	0.000	0.000	0.000	0.000	0.000	**0.001**	0.000	0.000	0.000	**0.005**	0.000	0.000	**0.994**
J_{AK}	0.000	0.000	0.000	0.000	0.000	**0.001**	0.000	0.000	0.000	**0.005**	0.000	0.000	**0.994**
J_{ATPase}	0.000	0.000	0.000	0.000	0.000	**0.001**	0.000	0.000	0.000	**0.005**	0.000	0.000	**0.994**

Table 5.3: *Complete set of concentration control coefficients as determined for the kinetic model describing glycolysis in differentiated C_2C_{12} skeletal muscle extract. Concentration control coefficients with a value above 0.5 or below -0.5 are highlighted in bold. The concentration control coefficients were determined in Wolfram Mathematica 12.0.*

	v_{HK}	v_{PGI}	v_{PFK}	v_{ALD}	v_{TPI}	v_{GAPDH}	v_{PGK}	v_{PGM}	v_{ENO}	v_{PK}	v_{LDH}	v_{AK}	v_{ATPase}
ATP	0.000	0.000	0.000	0.000	0.000	0.001	0.000	0.000	0.000	0.005	0.000	0.000	-0.006
AMP	-0.008	0.000	-0.010	0.000	0.000	-0.320	-0.003	0.000	0.000	**-1.978**	0.000	0.000	**2.320**
NADH	0.030	0.001	0.034	0.000	0.000	**1.142**	0.008	0.000	0.000	-0.062	0.000	0.000	**-1.153**
G6P	**1.174**	0.000	0.000	0.000	0.000	0.000	0.000	0.000	0.000	0.000	0.000	0.000	**-1.173**
F6P	**1.174**	0.022	0.000	0.000	0.000	0.000	0.000	0.000	0.000	0.000	0.000	0.000	**-1.196**
FBP	**1.177**	0.022	**1.342**	0.000	0.000	-0.001	0.000	0.000	0.000	-0.008	0.000	0.000	**-2.532**
DHAP	**0.588**	0.011	0.671	0.009	0.000	-0.001	0.000	0.000	0.000	-0.004	0.000	0.000	**-1.275**
GAP	**0.588**	0.011	0.671	0.009	0.000	-0.001	0.000	0.000	0.000	-0.004	0.000	0.000	**-1.275**
P3G	0.017	0.000	0.019	0.000	0.000	**0.630**	0.007	0.000	0.000	-0.050	0.000	0.000	**-0.623**
P2G	0.017	0.000	0.019	0.000	0.000	**0.630**	0.007	0.000	0.000	-0.050	0.000	0.000	**-0.623**
PEP	0.017	0.000	0.019	0.000	0.000	**0.630**	0.007	0.000	0.000	-0.050	0.000	0.000	**-0.623**
PYR	-0.067	-0.001	-0.076	-0.001	0.000	**-2.543**	-0.018	0.000	0.000	0.139	-0.034	0.000	**2.601**
LAC	x	x	x	x	x	x	x	x	x	x	x	x	x

5.5 Discussion

The aim of this chapter was to use this newly developed metabolomic technique to validate the predictive accuracy of the mechanistic model describing glycolysis in C_2C_{12} muscle fibre extract, constructed in Chapter 4. The model describing glycolysis in differentiated C_2C_{12} muscle extract predicts the time dependent concentrations of 17 variables. The variables comprise of GLC and the glycolytic intermediates, as well as the conserved adenosine and nicotinamide moieties. The IP-RPLC method developed during this study and described in Chapter 3 allows for the quantification of the conserved adenosine and nicotinamide moieties via UV/Vis detection, along with the quantification of the GLC and glycolytic intermediates via a radiolabelled detector. In total, all species described in the model, with the exception of BPG, were separated and quantified with this method. This enabled the comparison of 15, out of the total 17 species described in the model, to be compared to experimentally obtained time courses. The ability to compare most of the variables predicted by the model with experimental data allowed for a rigorous scrutiny of the behaviour of the glycolytic model. Furthermore, observation of the time dependent concentration trends of the glycolytic intermediates and conserved moieties under several different initial sets of conditions were performed (Exp 1, Exp 2 and EXP 3). It should be noted that the model predictions are obtained independent of the experimental data. The model predictions do not result from fitting the data, but by using the initial conditions and simulating the model in the absence of any experimental input. The resulting comparison (Figure 5.1, Figure 5.2 and Figure 5.3) are then generated by overlaying the experimentally obtained concentration trends with the corresponding model predictions.

Establishing the criteria for whether a model is validated or invalidated is not a trivial endeavour. A model can never be fully validated since it is experimentally impossible to test the validity of all parameters used in model construction. Therefore, it is more accurate to consider a model as partially validated. A prerequisite for a reliable and useful model is that it should be able to accurately predict external datasets that were not used in model development[3], and it is more accurate to state that we are evaluating the predictive accuracy of the glycolytic model constructed in C_2C_{12} skeletal muscle. The process of assessing the predictive accuracy of a model requires a subjective or objective estimation of how closely the model simulates the behaviour in comparison to observations[13]. In the case presented here, considerations regarding the quality of the comparison between experimental data and model predictions were made subjectively as any objective measure of predictive accuracy would be meaningless without a

standard measure of what constitutes a good or bad result. Objective measures are only useful when comparing the predictive accuracy of several models to the same experimental dataset. In light of this, we can state that the predictive accuracy of the model constructed in C_2C_{12} skeletal muscle is satisfactory, as explained below.

The overlay of the model predicted trace and experimentally obtained trace for GLC compare very well for both Exp 1 and Exp 2 (Section 5.4.2 and Section 5.4.3). The change in concentration of GLC is catalysed by the enzyme HK. The good correlation between the experimentally obtained trace and model predicted trace suggests that the model description of HK dynamics accurately describes what happens experimentally. The comparison of model simulated fluxes of G6P and F6P and experimental measurements shows that the model slightly overestimates the concentration of G6P and underestimates the concentration of F6P. However, there is extensive overlap of the chromatographic peaks for G6P and F6P and deconvolution of these peaks are required during the analysis of the chromatographic traces. The respective difference observed between model simulation and experimental quantification could be due to inaccurate deconvolution of the chromatographic traces. The model simulation for FBP is in fair agreement, but slightly lower that what is observed in the experimentally obtained traces of Exp1 and Exp 2 in Section 5.4.2 and Section 5.4.3. The model simulated concentrations of FBP obtained for Exp 3 (Section 5.4.4) compares well with the experimentally obtained trace. The concentration of FBP towards the end of the reaction is estimated to be higher than the experimentally obtained results. However, this is most likely due to the inaccurate description of the DHAP and GAP traces, resulting in feedback inhibition in the model simulation that does not reflect the experimental reality. The relationship dictating the concentrations of DHAP and GAP is governed by TPI and the experimental results suggest that the activity of TPI is overestimated in the model. The model predicted flux of P3G is underestimated in comparison with the experimentally obtained data. This is likely due to the high activity attributed to PGM and ENO in the model. Integration of the P2G peak in the chromatographic traces is difficult due to the low area obtained for this species, resulting in large standard deviations among the measurements. Therefore, the experimentally obtained concentration traces cannot be assumed to accurately reflect reality. Regarding Exp 1 and Exp 2, there is a discrepancy between the model simulations and experimentally obtained traces of PYR and LAC (Figure 5.1 and Figure 5.2). LAC is overpredicted and PYR is under predicted in the final half of the reaction. The conversion of PYR to LAC is determined by LDH activity. Comparison of the experimental and model simulated traces suggests that the equilibrium state described by the rate equation

for LDH is inaccurate and a higher concentration of PYR should be favoured in the description of the reaction. Overall, the model simulated trends of the conserved adenosine and nicotinamide moieties correlate well with the experimentally obtained concentration traces. The model simulated concentrations of NAD^+ and NADH correlates well with the experimental data. It should be noted that the concentrations of NAD^+ and NADH in several measured samples (Figure 5.1L and Figure 5.2L in the case of NADH and Figure 5.3G in the case of NAD^+) are below the LOQ determined for these species, with LOQ values of 0.683 and 0.582 for NAD^+ and NADH respectively. Therefore, these measurements should be considered as unreliable and any observations corresponding to these measurements are made considering this. The model simulations of the adenosine moieties correlate well with the experimentally obtained traces, with the exception of the data obtained for Exp 3 in Section 5.4.4. Comparison of the model simulations and experimentally obtained adenosine traces in Section 5.4.3. suggests that the equilibrium state described by AK in the model does not accurately reflect what happens in the experimental setup.

Metabolic control analysis was performed on the kinetic model describing glycolysis in C_2C_{12} muscle extract and showed that ATPase has a 99% control over the flux through the pathway. This finding is in line with published results[9,12] stating and ATPase flux control of between 95% and 99%.

The simulations of the bottom-up model describing glycolysis in C_2C_{12} muscle extract correlates well with the experimentally obtained data. This suggests that a degree of confidence can be placed on the predictive accuracy of the model. The glycolytic pathway is relatively small and linear when compared to other biological pathways. For future research we will expand on the mechanistic model describing glycolysis in C_2C_{12} muscle extract to incorporate the insulin response and study insulin sensitivity.

5.6 Conclusion

3 time-course experiments were done under different sets of initial concentrations and compared to the corresponding model prediction traces. The model predicted the metabolite concentration changes to a satisfactory degree of accuracy.

5.7 References

1 **Bruggeman FJ and Westerhoff HV.**, The nature of systems biology., *Trends Microbiol.* 15:45–50, 2006

2 **Barlas Y and Carpenter S.**, Phylosophical roots of model validation: two paradigms., *Syst. Dyn. Rev.* 6:148-166, 1990

3 **Tropsha A, Gramatica P and Gombar VK.**, The importance of being earnest: Validation is the absolute essential for successful application and interpretation of QSPR models., *QSAR Comb. Sci.* 22:69-77, 2003

4 **Nielsen J.**, It is all about metabolic fluxes., *J. Bacteriol*. 185:7031–7035, 2003

5 **Krömer JO, Sorgenfrei O, Klopprogge K, Heinzle E and Wittmann C.**, In-depth profiling of lysine-producing Corynebacterium glutamicum by combined analysis of the transcriptome, metabolome, and fluxome., *J. Bacteriol*. 186:1769–1784, 2004

6 **Chassagnole C, Noisommit-Rizzi N, Schmid JW, Mauch K and Reuss M.**, Dynamic modeling of the central carbon metabolism of Escherichia coli., *Biotechnol. Bioeng*. 79:53–73, 2002

7 **Visser D, Schmid JW, Mauch K, Reuss M and Heijnen JJ.**, Optimal re-design of primary metabolism in Escherichia coli using linlog kinetics., *Metab. Eng*. 6:378–390, 2004

8 **Penkler G, du Toit F, Adams W, Rautenbach M, Palm DC, van Niekerk DD and Snoep JL.**, Construction and validation of a detailed kinetic model of glycolysis in *Plasmodium falciparum*., *FEBS Journal* 282:1481-1511, 2015

9 **Lambeth MJ and Kushmerick MJ.**, A Computational Model for Glycogenolysis in Skeletal Muscle., *Ann. Biomed. Eng*. 30:808–827, 2002

10 **Lambeth MJ, Kushmerick MJ, Marcinek DJ and Conley KE.**, Basal glycogenolysis in mouse skeletal muscle: in vitro model predicts in vivo fluxes., *Mol. Biol. Rep.* 29:135-139, 2002

11 **Schmitz JPJ, van Riel NAW, Nicholay K, Hilbers PAJ and Jeneson JAL.**, Silencing of glycolysis in muscle: experimental observation and numerical analysis., *Exp. Physiol.* 95:380–397, 2009

12 **Choi SC, Kim Y, Lee FN, Zabolotny JM, Kahn BB and Youn JH.**, Lactate induces insulin resistance in skeletal muscle by suppressing glycolysis and impairing insulin signalling., *Am. J. Physiol. Endocrinol. Metab.* 283:E233–E240, 2002

13 **Krause P, Boyle DP and Bäse F.**, comparison of different efficiency criteria for hydrological model assessment., *ADGEO* 5:89-97, 2005

Chapter 6
General discussion and concluding remarks

Several *in silico* models to describe the *in vivo* and *in vitro* behaviours of glycolysis in skeletal muscle, and the development of metabolic syndrome, have been developed[1] - [6]. Access to models capable of describing the metabolic changes and pathophysiological symptoms associated with the development of metabolic diseases aid in the clinical identification of such diseases. Understanding the biochemical mechanisms that give rise to the development of metabolic diseases is of critical importance for the development of treatment and precautionary intervention.

Extensive *in silico* analysis on the *in vivo* behaviours of skeletal muscle glycolysis has been performed by Rozendaal *et. al.*[1,2] on the development of metabolic syndrome, with great success. Furthermore, metabolomic analysis via the use of ^{31}P-NMR on intact tissue and even living organisms, has the advantage of obtaining dynamic concentration profiles that accurately reflects the physiological state. However, making perturbations to analyse the underlying principles that give rise to the physiological state is very difficult. In contrast, *in vitro* analysis of a model cell-line, as presented in this thesis, generally gives an inaccurate description of *in vivo* observations, but is much easier to make perturbations for detailed analysis.

The thesis presented here, focussed on the *in vitro* kinetic characterisation of the enzymes present in glycolysis under *in vivo* like conditions, and the construction of a mathematical model describing glycolysis is skeletal muscle cells using a bottom-up systems biology approach. C_2C_{12} mouse skeletal muscle cells were used as model cell-line for investigating muscle cell glycolysis. A bottom-up systems biology approach to the characterisation of skeletal muscle glycolysis under basal conditions (the metabolic reference state) has value in understanding and analysing the regulatory behaviours of this pathway. The validation and determination of the predictive accuracy of mathematical models are key to the successful implementation of such models[7]. As discussed in Chapter 5 (Section 5.5), establishing criteria for whether a model is validated or invalidated is not trivial, since model validation relies on experimentally testing the validity of every single parameter used in model construction, which is an impossible endeavour. In actuality, a model can only be partially validated with regards to some of the parameters used in model construction model. Therefore, it is more accurate to state that we evaluated the predictive accuracy of the glycolytic model constructed in C_2C_{12} skeletal muscle.

The process of assessing the predictive accuracy of a model requires a subjective or objective estimation of how closely the model simulates the behaviours observed in experiments[8]. One of the novel outcomes of this study was the development of an IP-RPLC metabolomics technique for the dynamic determination of glycolytic intermediate and cofactor concentrations. The dynamic concentration profiles of C_2C_{12} muscle extract time-course experiments were compared to model simulations in Chapter 5 to determine the predictive accuracy to the mathematical model constructed in this thesis (Chapter 4). The similarities in the model simulations and the experimentally determined concentration profiles (see Figure 5.1, Figure 5.2 and Figure 5.3) illustrates how accurately the model describes glycolysis in C_2C_{12} skeletal muscle extract and the model describes the data to a satisfactory degree. The targeted metabolomics technique developed here enables quantification of glycolytic intermediates and cofactors in cellular extracts with minimal sample preparation. The strengths of this metabolomics method lie in the robustness of the separation technique and detection of glycolytic intermediates free from matrix effects. Using a reverse phase C_{18} column (Phenomenex Luna C_{18} column) for RPLC analysis makes this a robust separation technique. Furthermore, the ^{14}C-tag of glycolytic intermediates is detected via radio-labelled detection and the resulting signal is not influenced by a change in the sample matrix. The IP-RPLC metabolomics technique developed here, have become a powerful and routine analytical technique in our laboratory for similar systems biology studies on glycolysis in different cell-lines.

Having constructed a mathematical model of glycolysis in skeletal muscle that can predict glycolytic behaviour to a satisfactory degree of accuracy, we can perform *in silico* investigations into the control mechanisms regulating glycolysis in skeletal muscle. Metabolic control analysis of the glycolytic model indicate that ATPase hold most of the control over the flux through glycolysis with a flux control coefficient of 99.4 %. These findings are in line with the findings of other *in silico* studies of glycolysis in skeletal muscle[3,6]. The control exerted by ATPase is subtle and operates largely by controlling the concentrations of the adenosine moieties. The relative concentrations of ATP regulate the activity the enzymes HK and PFK (using ATP as substrate) in upper glycolysis, and PGK and PK (Producing ATP as product) in lower glycolysis. As explained by Hofmeyr *et. al.*[9] cellular metabolism can be functionally organised into supply and demand block that are linked by metabolic products and cofactors. With regards to the scenario described in skeletal muscle, glycolysis can be broken down into an ATP supply block (PGK and PK) and a demand block (HK, PFK and ATPase) with ATP

regulating the supply-demand dynamics. This approach was used by du Preez *et. al.*[10] to compare kinetic models of erythrocytes and beautifully highlights the regulatory mechanisms of ATP supply-demand dynamics.

The functionality of skeletal muscle relies on rapid changes in the activity of ATPase to allow for muscle movement (*i.e*. ATPase activity increases during exercise). This increase in the demand block will require an increase in the supply block to take place to accommodate a higher demand for ATP. An increase in the ATP demand block can partly be explained by an increase in glucose metabolism afforded by higher GLC transport activity. As discussed in Section 2.5 of the literature review in this thesis, The AMPK signalling cascade facilitates GLUT4 translocation to the cell membrane. AMPK is activated by low concentrations of ATP and high concentrations of AMP, the dynamics of which is regulated by AK. However, supply of ATP via an influx of GLC is throttled by the relative low activity of HK under high levels of AMP (refer to Section 4.4.1 for details). The increase supply of ATP most likely comes from an increased consumption of glycogen inside skeletal muscle cells, this will be discussed in more detail below.

On the other side of ATP supply-demand dynamics, an increased supply of ATP facilitated by an increased need to dispose of excess GLC (*i.e.* insulin stimulation after a meal) will require an increase in the ATP demand block to accommodate a higher supply of ATP. Insulin stimulation of skeletal muscle facilitates an increase in GLC transport over the cell membrane facilitated by insulin mediated GLUT4 translocation, as discussed in Section 2.4 of the literature review (Chapter 2). The need for an increase in ATP demand is most likely accommodated by an increase in glycogen synthesis. A 2-fold increase in the production of glycogen was observed during insulin stimulation of C_2C_{12} skeletal muscle cells[11] and this supports the above-mentioned hypothesis. Glycogen is produced via the glycogen synthesis pathway that branches from glycolysis after GLC has been phosphorylated by HK. Therefore, glycogen can be perceived as phosphorylated GLC. The ATP demand required to metabolise glycogen is less compared to GLC and only relies on phosphorylation by PFK before it can enter the ATP supply block (see Figure 6.1). In contrast, phosphorylation of GLC to form glycogen increases the demand block when ATP supply is high, and this corresponds with a slow and gradual production of glycogen when ATPase activity is low and a rapid consumption of glycogen when ATPase activity is high.

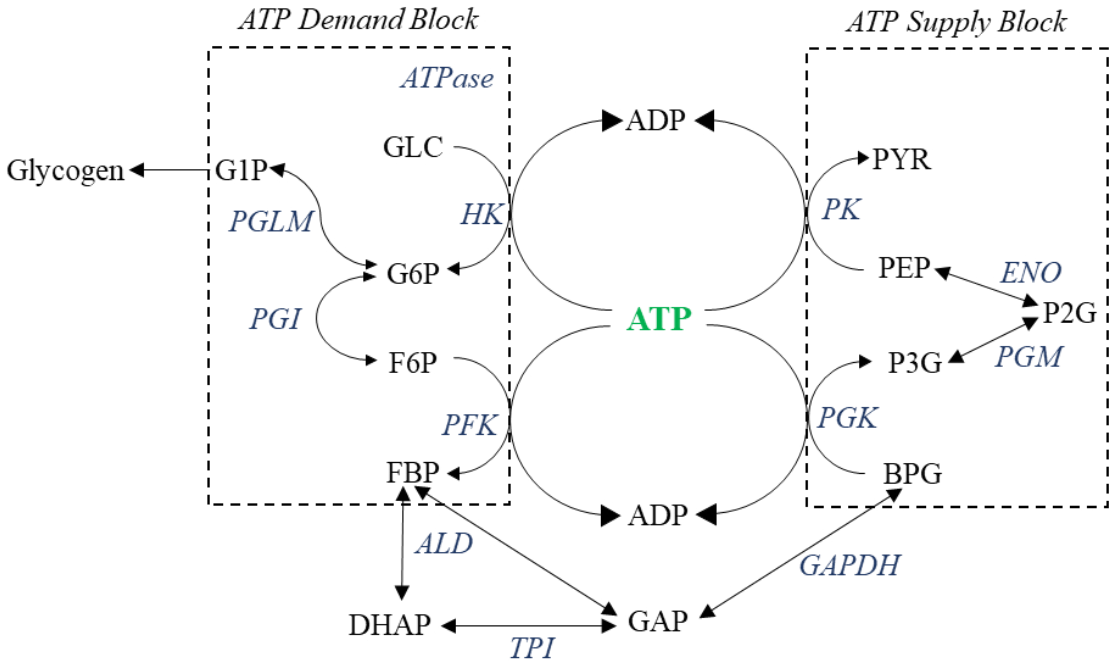

Figure 6.1: *Schematic representation describing skeletal muscle glycolysis in terms of ATP supply-demand dynamics. The enzymatic reactions of HK, PFK and ATPase form part of the ATP demand block. The enzymatic reactions of PGK and PK form part of the ATP supply block. The 2 blocks are connected via ATP.*

The study lined out in this thesis was performed in partnership with a sister-study performed by Stefan Kuhn on characterising the insulin signalling pathway, and GLC transport under insulin stimulated conditions. The combined endeavours of these 2 studies will improve our understanding of skeletal muscle glycolysis under basal and insulin stimulated conditions.

With regards to this combined research endeavour, we consider how an individual's physiological state will impact muscle glycolysis, we will postulate 4 hypothetical modes in which ATP supply-demand dynamics in skeletal muscle glycolysis can operate, as listed below:

1. The glycolytic activity of skeletal muscle at rest can be described as muscle glycolysis operating under normal (physiological) GLC levels with low (basal) glucose transport (GT) activity and low ATPase activity.
2. The glycolytic activity of insulin stimulated skeletal muscle at rest can be described as muscle glycolysis operating under high GLC levels with high GT activity and low ATPase activity.
3. The glycolytic activity of skeletal muscle during exercise can be described as muscle glycolysis operating under normal (physiological) GLC levels with low (basal) GT activity and high ATPase activity.

4. The glycolytic activity of insulin stimulated skeletal muscle during exercise can be described as muscle glycolysis operating under high GLC levels with high GT activity and high ATPase activity.

Analysing the ATP supply-demand dynamics of the 4 hypothetical modes lined out here will form part of our future research endeavours. We speculate that the flux control of glycolysis in the 4 hypothetical modes will differ significantly, with high flux control by ATPase in mode 2and possibly mode 1, and high flux control by GLC transport in modes 3 and 4 and possibly in mode 1. A description of skeletal muscle metabolism under basal, insulin stimulated and exercise conditions[3,6] will greatly improve our understanding of how skeletal muscle metabolism behaves in healthy individuals. Understanding this behaviour in terms of ATP supply-demand dynamics could potentially lead to a descriptive understanding of the underlying mechanisms that give rise to metabolic disorders such as insulin resistance.

6. 1. Future studies

As described above, future endeavours will entail the combination of the study presented here with the sister-study performed by Stefan Kuhn for a description of GLC metabolism under basal and insulin stimulated conditions. Including glycogen production and consumption in the model and analysing the model in terms flux control and ATP supply-demand dynamics under basal and insulin stimulated conditions will need to be performed

Future studies pertaining to the study presented here should focus on expanding the kinetic characterisation of the glycolytic enzymes in differentiated C_2C_{12} skeletal muscle cells. Characterisation of the enzymes TPI, PGM and ENO will aid to a better understanding of glycolysis in skeletal muscle. Furthermore, testing the effect of well-known inhibitors (*e.g.* AMP, fructose-2,6-bisphosphate and citrate as inhibitors of PFK, inorganic phosphate as inhibitor of GAPDH) will aid in improving the glycolytic model of C_2C_{12} skeletal muscle.

6. 2. References

1 **Rozendaal YJW, Wang Y, Paalvast Y, Tambyrajah LL, Li Z, Willems van Dijk K, Rensen PCN, Kuivenhoven JA, Groen AK, Hilbers PAJ and van Riel NAW.**, *in vivo* and *in silico* dynamics of the development of metabolic syndrome., *PLoS Comput. Biol.* 14:e1006145, 2018

2 **Rozendaal YJW, Wang Y, Hilbers PAJ and van Riel NAW.**, Computational modelling of energy balance in individuals with metabolic syndrome., *MBC Syst. Biol.* 13:24, 2019

3 **Lambeth MJ and Kushmerick MJ.**, A Computational Model for Glycogenolysis in Skeletal Muscle., *Ann. Biomed. Eng.* 30:808–827, 2002

4 **Dash RK, Li Y, Kim J, Beard DA, Saidel GM and Cabrera ME.**, Metabolic dynamics in skeletal muscle during acute reduction in blood flow and oxygen supply to mitochondria: in-silico studies using a multi-scale, top-down integrated model., *Plos One* 3:e3168, 2008

5 **Selivanov VA, de Atauri P, Centelles JJ, Cadefau J, Parra J, Cuss oR, Carreras J and Cascante M.**, The changes in the energy metabolism of human muscle induced by training., *J. Theor. Biol.* 252:402–410, 2008

6 **Schmitz JPJ, van Riel NAW, Nicolay K, Hilbers PAJ and Jeneson JAL.**, Silencing of glycolysis in muscle: experimental observation and numerical analysis., *Exp. Physiol*. 95:380-397, 2010

7 **Tropsha A, Gramatica P and Gombar VK.**, The importance of being earnest: Validation is the absolute essential for successful application and interpretation of QSPR models., *QSAR Comb. Sci.* 22:69-77, 2003

8 **Krause P, Boyle DP and Bäse F.**, Comparison of different efficiency criteria for hydrological model assessment., *ADGEO* 5:89-97, 2005

9 **Hofmeyr JS and Cornish-Bowden A.**, Regulating the cellular economy of supply and demand., *FEBS Lett.* 476:47-51, 2000

10 **du Preez FB, Conradie R, Penkler GP, Holm K, van Dooren FLJ and Snoep JL.**, A comparative analysis of kinetic models of erythrocyte glycolysis., *J. Theor. Biol*. 252:488-496, 2008

11 **Schmitz-Peiffer C, Craig DL, Biden TJ.**, Ceramide generation is sufficient to account for the inhibition of the insulin-stimulated PKB pathway in C_2C_{12} skeletal muscle cells pre-treated with palmitate., *J. Biol. Chem.* 274:24202-24210, 1999

Appendix

Chromatographic Traces of the time-course experiments presented in Chapter 5

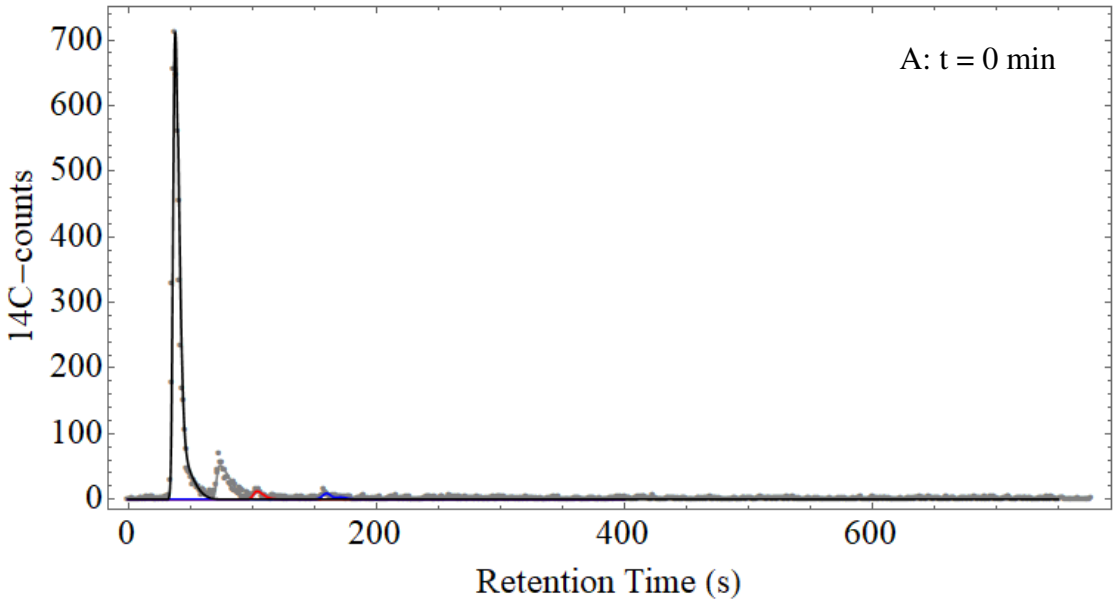

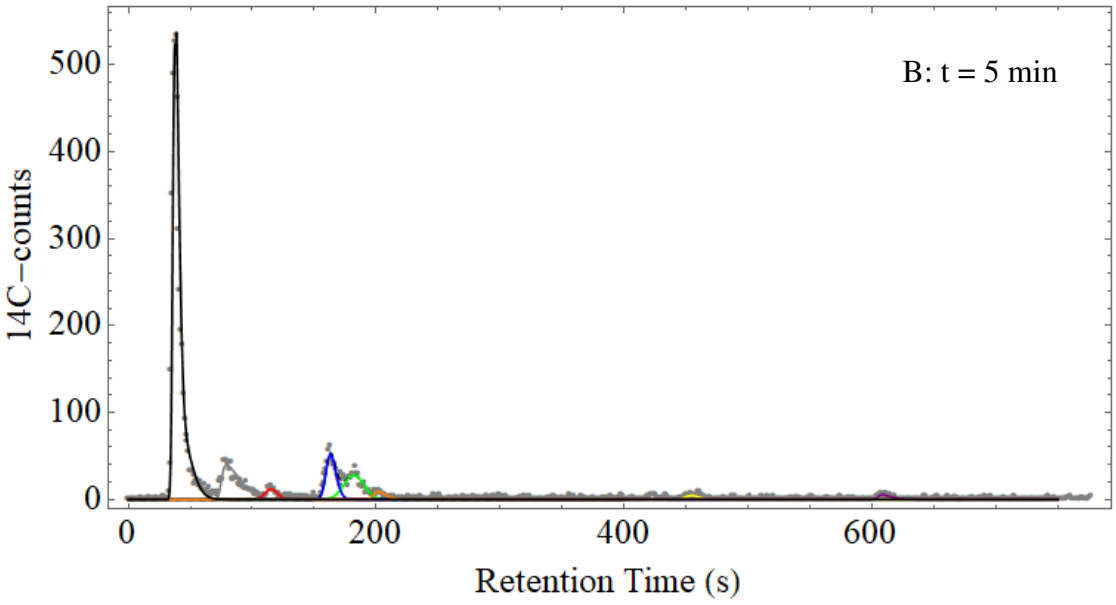

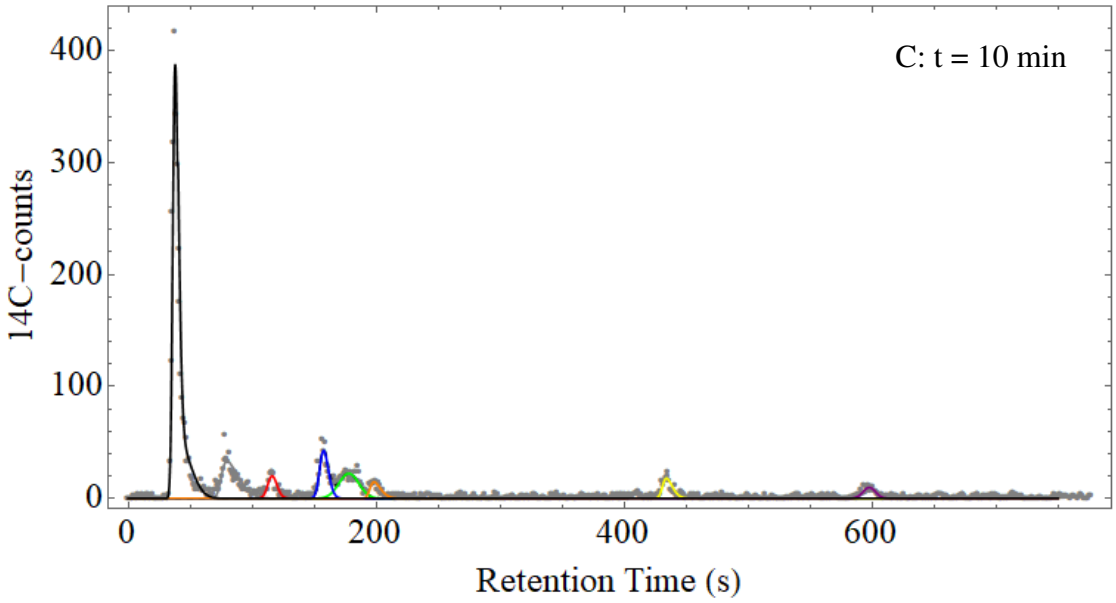

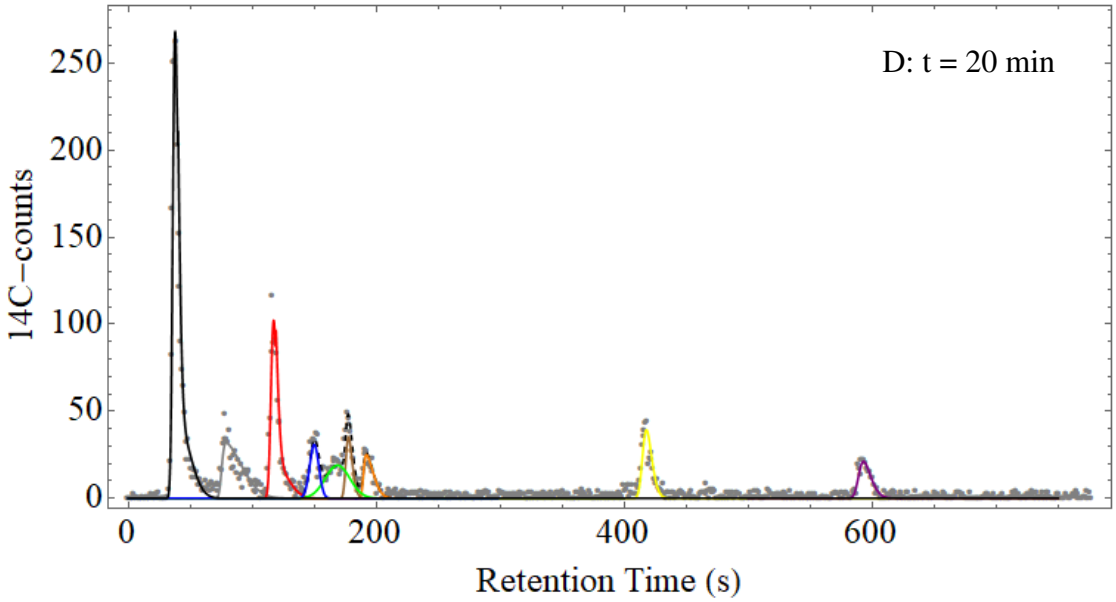

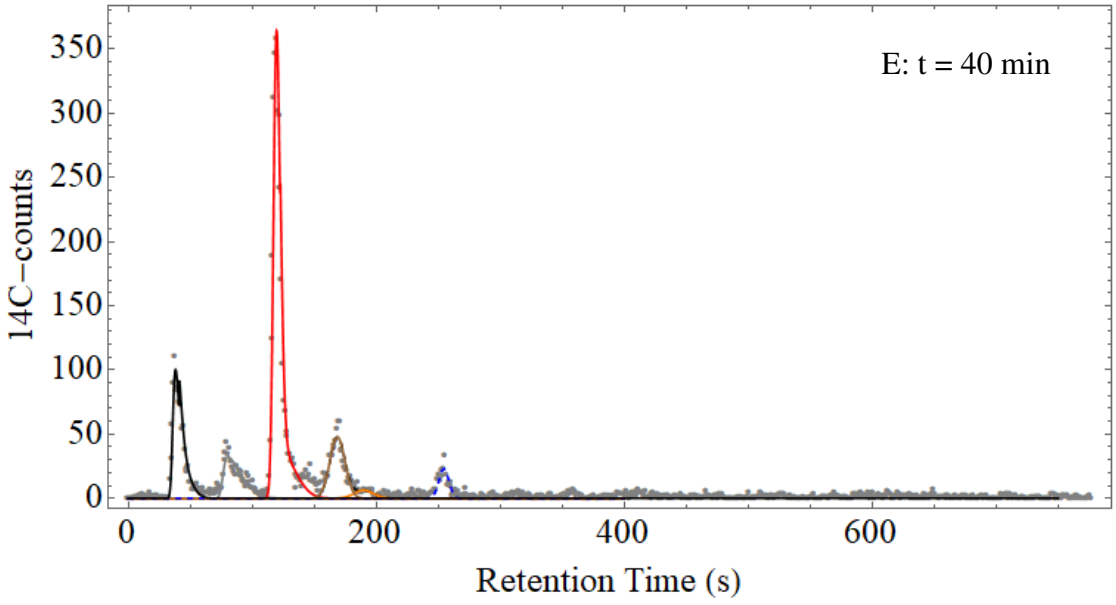

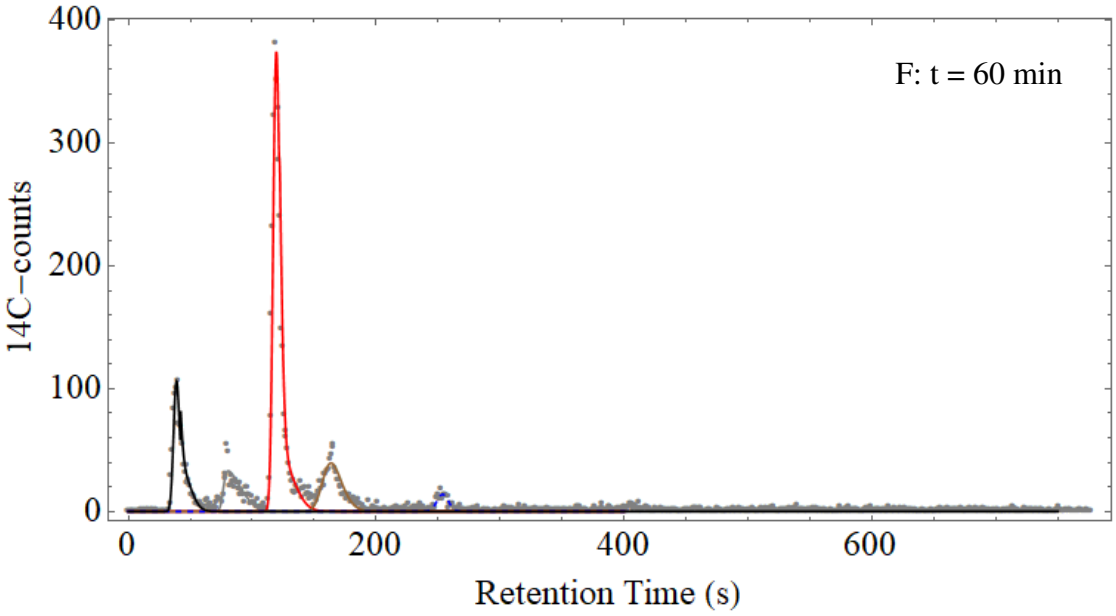

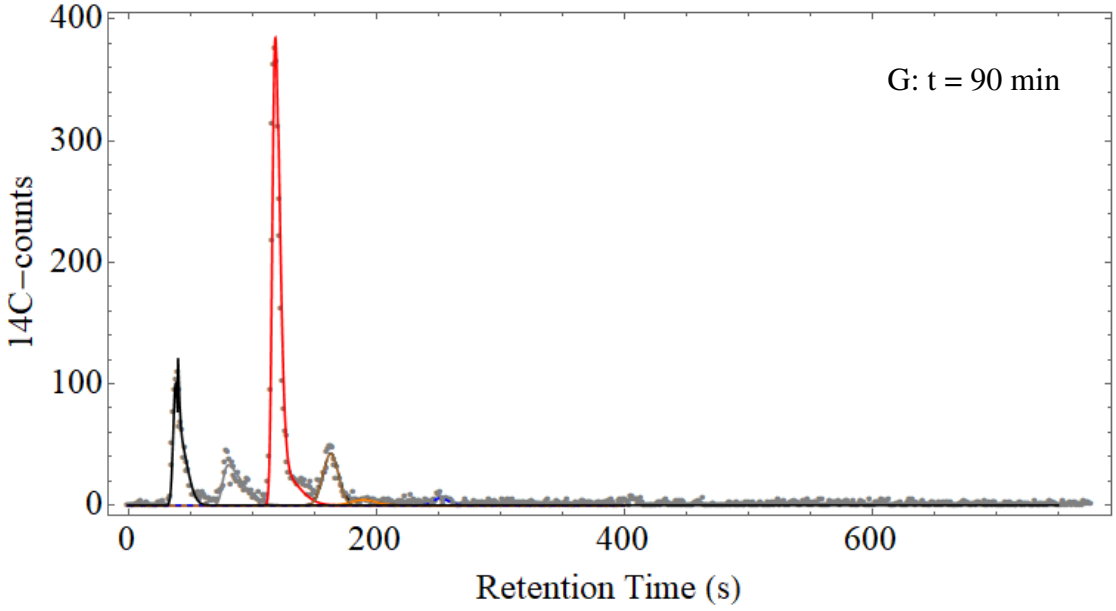

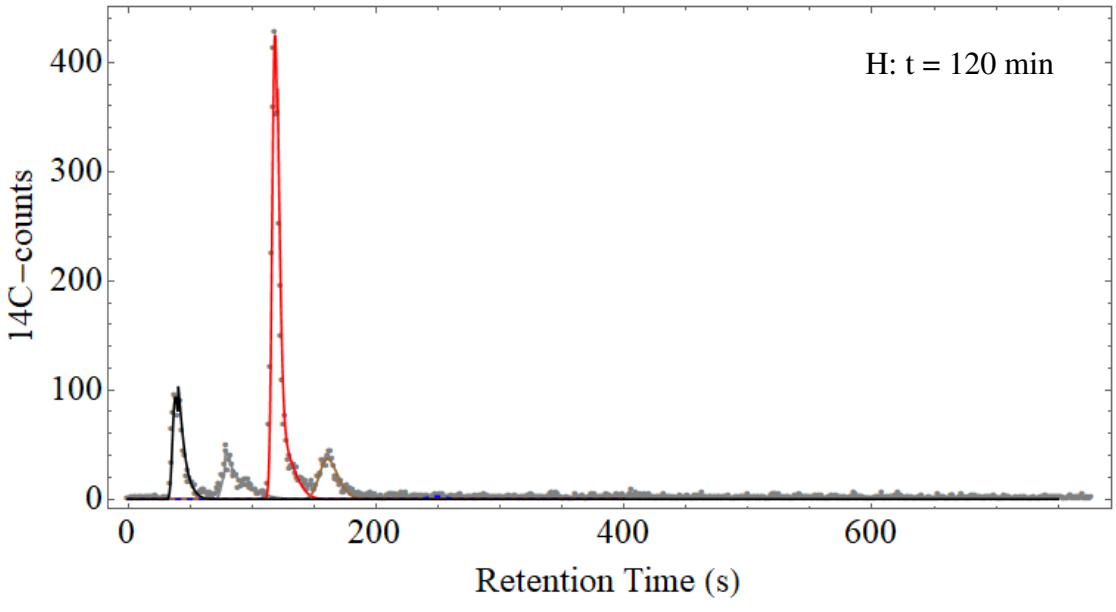

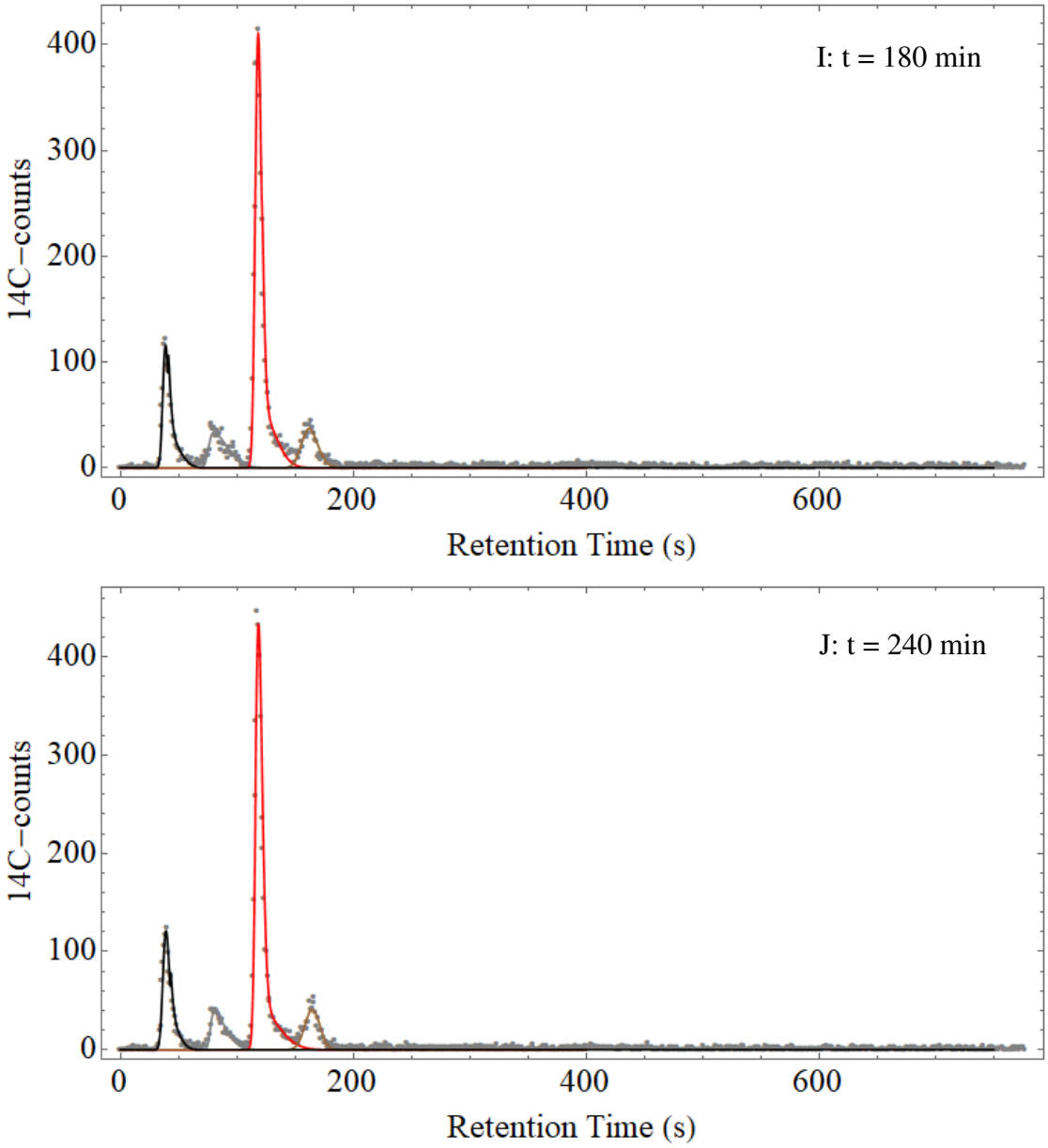

Figure A. 1: *The integrated chromatographic traces of the time-course experiment discussed in Section 5.4.2 of this thesis (Exp 1).The experiment was carried out in duplicate and the chromatographic traces shown here is from the first repeat. The grey dots represent the chromatographic data, the Black line represents GLC, Grey represents the Impurity, Blue represents G6P, Green Represents F6P, Purple represents FBP, Orange represents DHAP, Yellow represents P3G, Blue-Dash represents PEP, Brown represents PYR, Red represents LAC, A: analysis performed at t = 0 min, B: analysis performed at t = 5 min, C: analysis performed at t = 10 min, D: analysis performed at t = 20 min, E: analysis performed at t = 40 min, F: analysis performed at t = 60 min, G: analysis performed at t = 90 min, H: analysis performed at t = 120 min, I: analysis performed at t = 180 min, J: analysis performed at t = 240 min.*

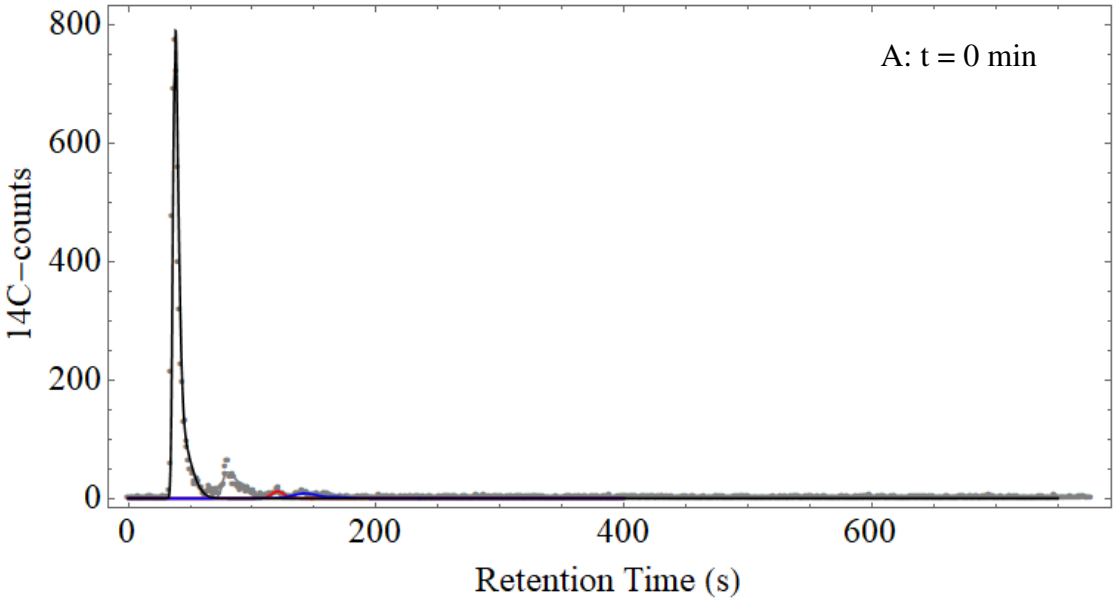

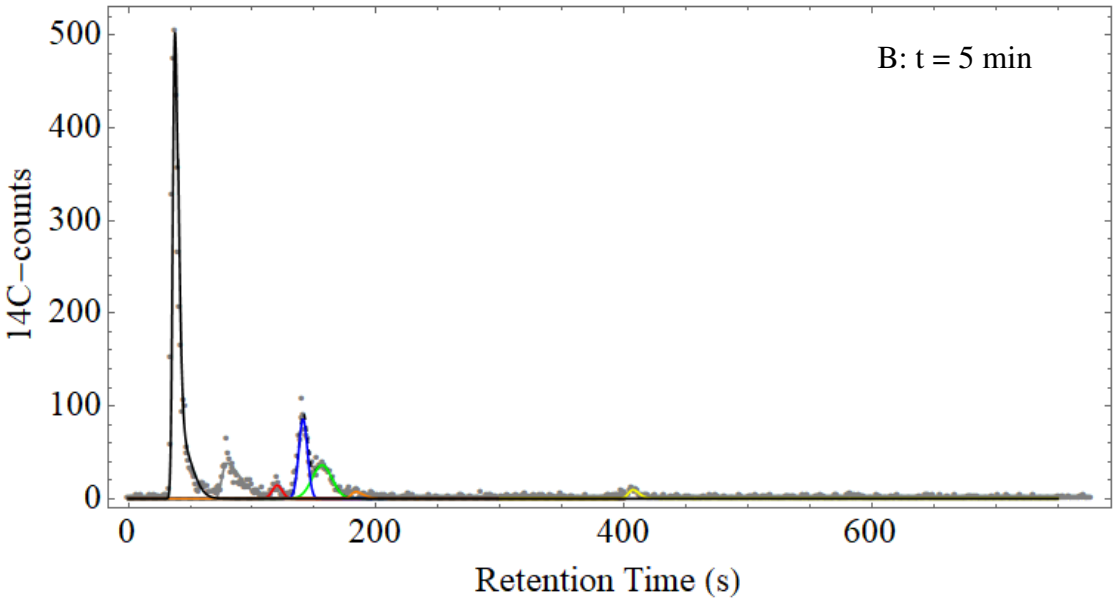

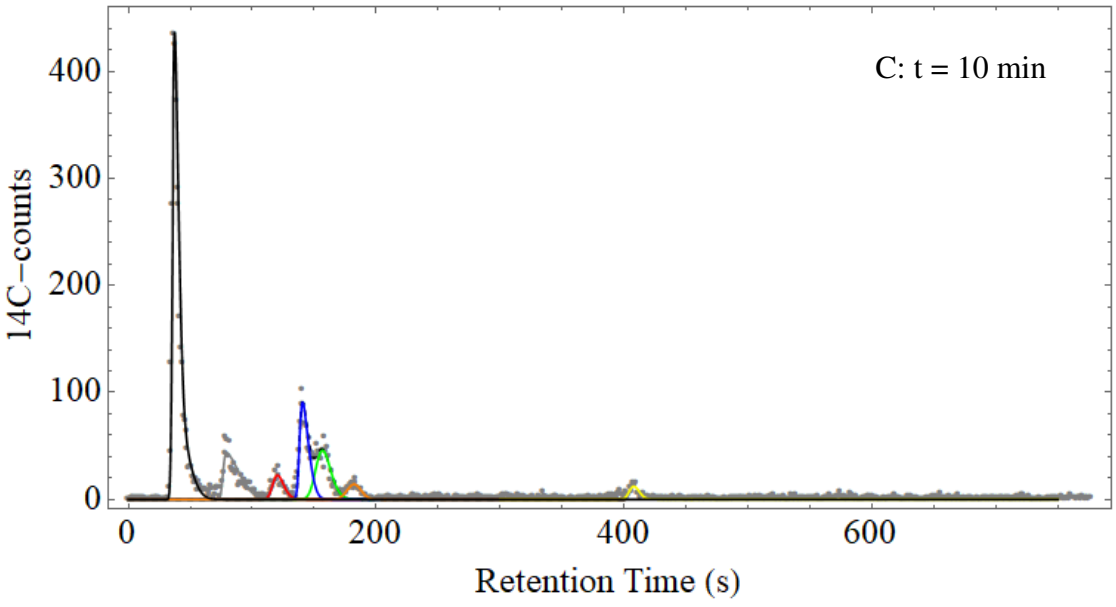

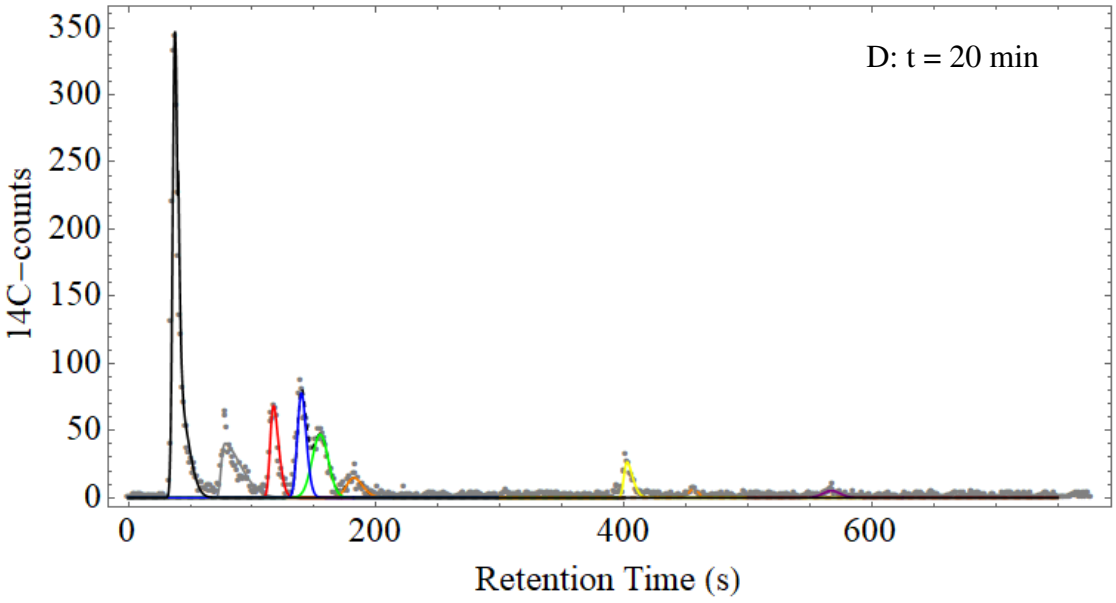

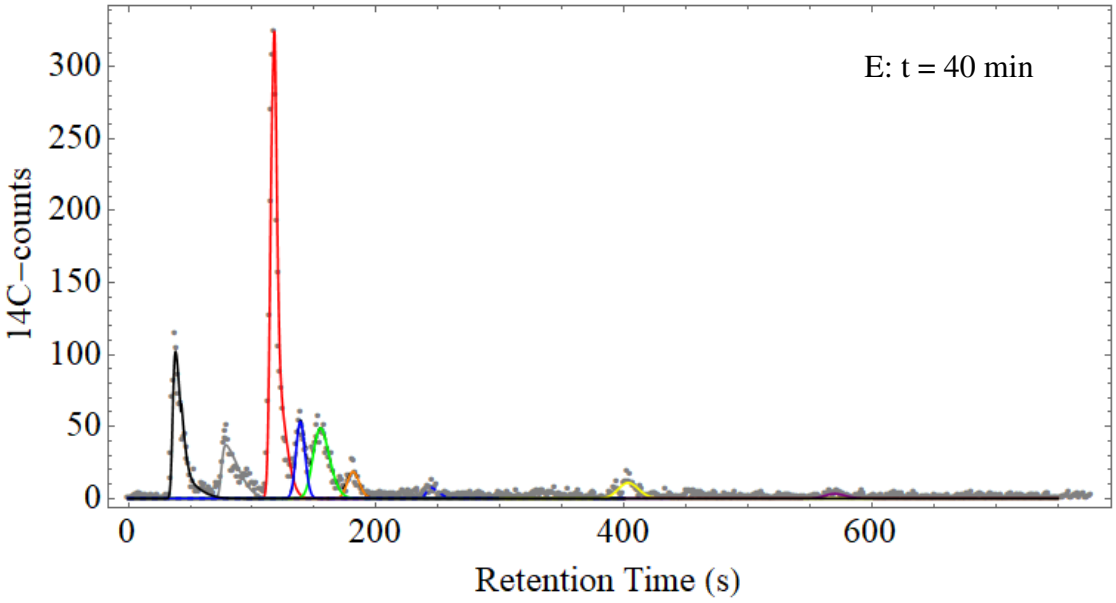

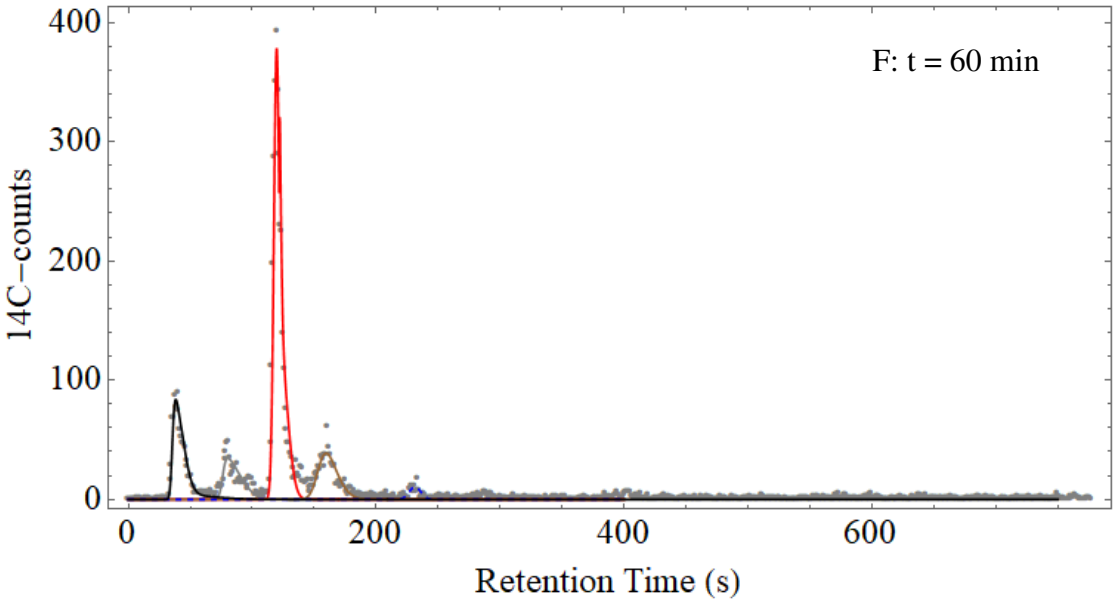

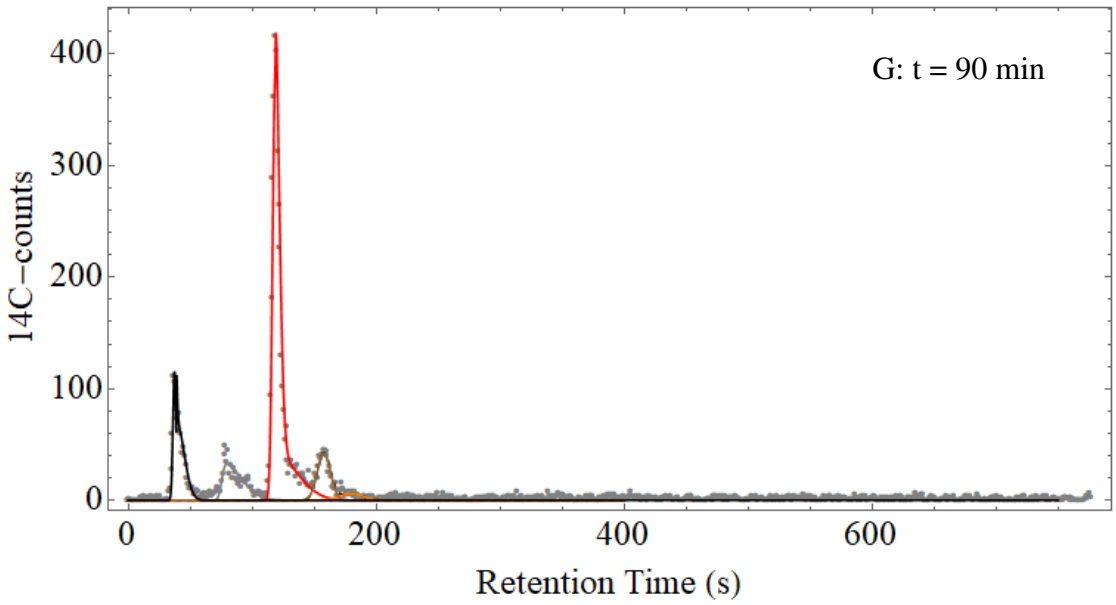

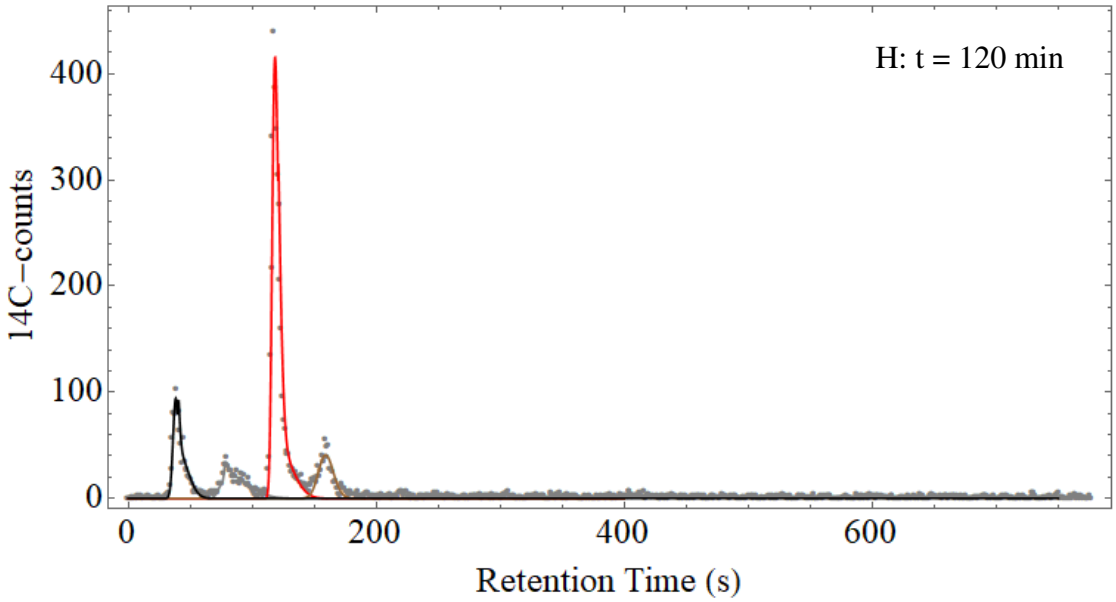

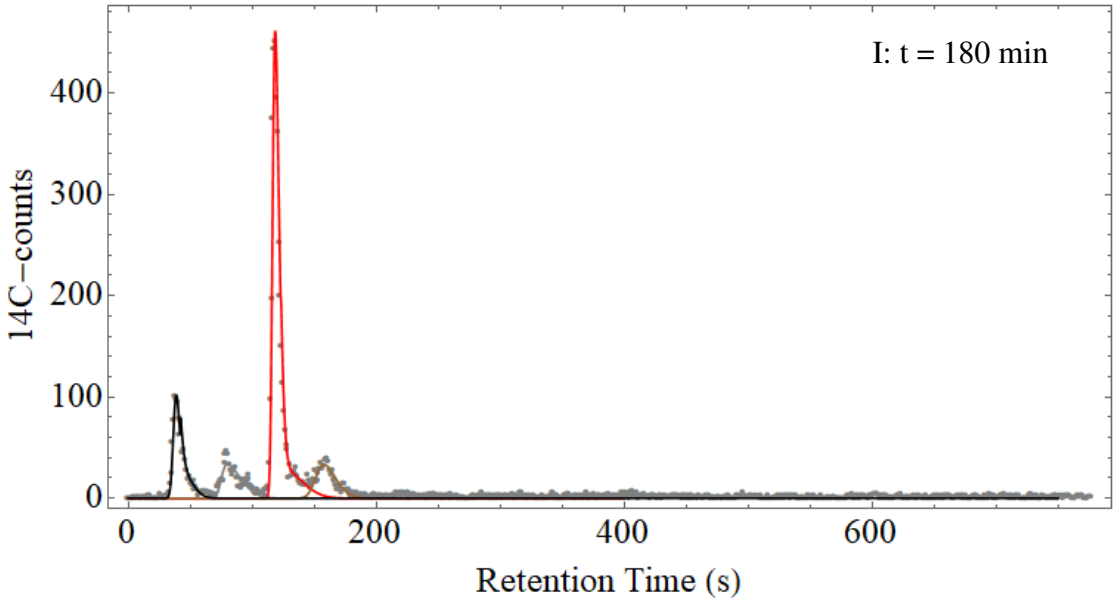

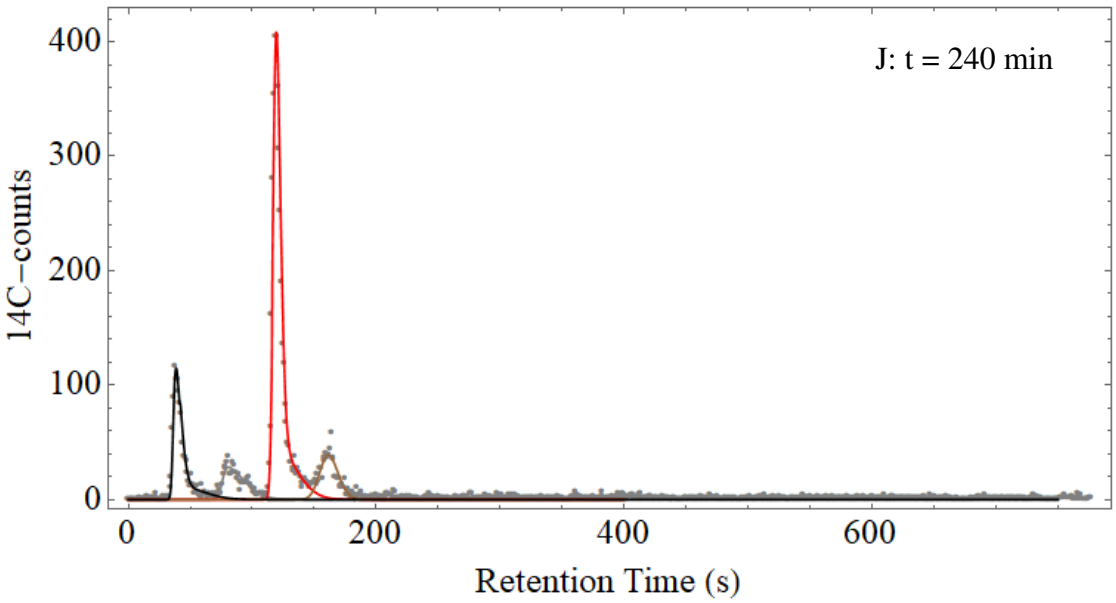

Figure A. 2: *The integrated chromatographic traces of the time-course experiment discussed in Section 5.4.2 of this thesis (Exp 1). The experiment was carried out in duplicate and the chromatographic traces shown here is from the second repeat. The grey dots represent the chromatographic data, the Black line represents GLC, Grey represents the Impurity, Blue represents G6P, Green Represents F6P, Purple represents FBP, Orange represents DHAP, Yellow represents P3G, Orange-Dash represents P2G, Blue-Dash represents PEP, Brown represents PYR, Red represents LAC, A: analysis performed at t = 0 min, B: analysis performed at t = 5 min, C: analysis performed at t = 10 min, D: analysis performed at t = 20 min, E: analysis performed at t = 40 min, F: analysis performed at t = 60 min, G: analysis performed at t = 90 min, H: analysis performed at t = 120 min, I: analysis performed at t = 180 min, J: analysis performed at t = 240 min.*

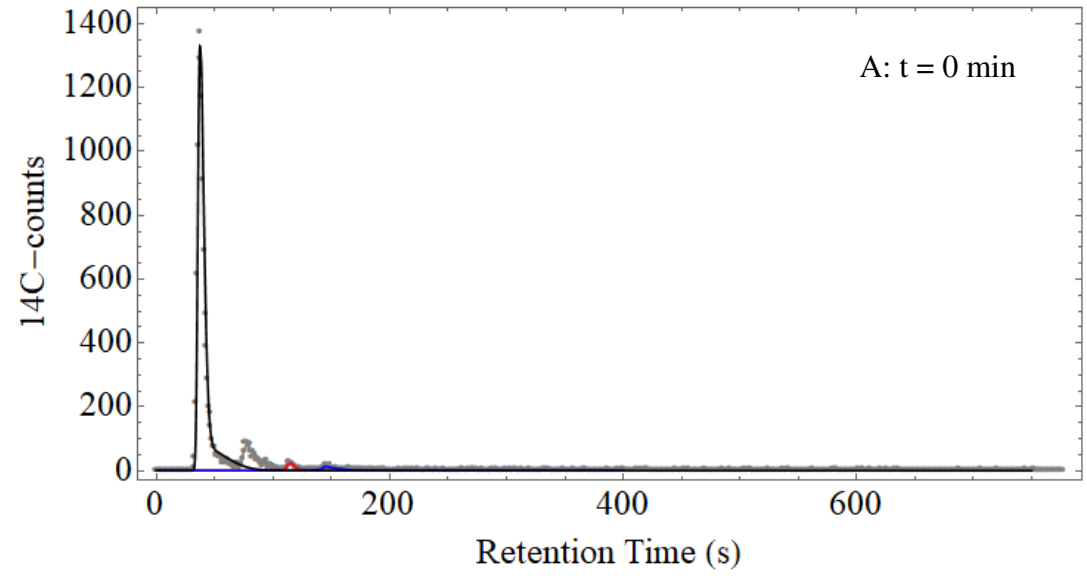

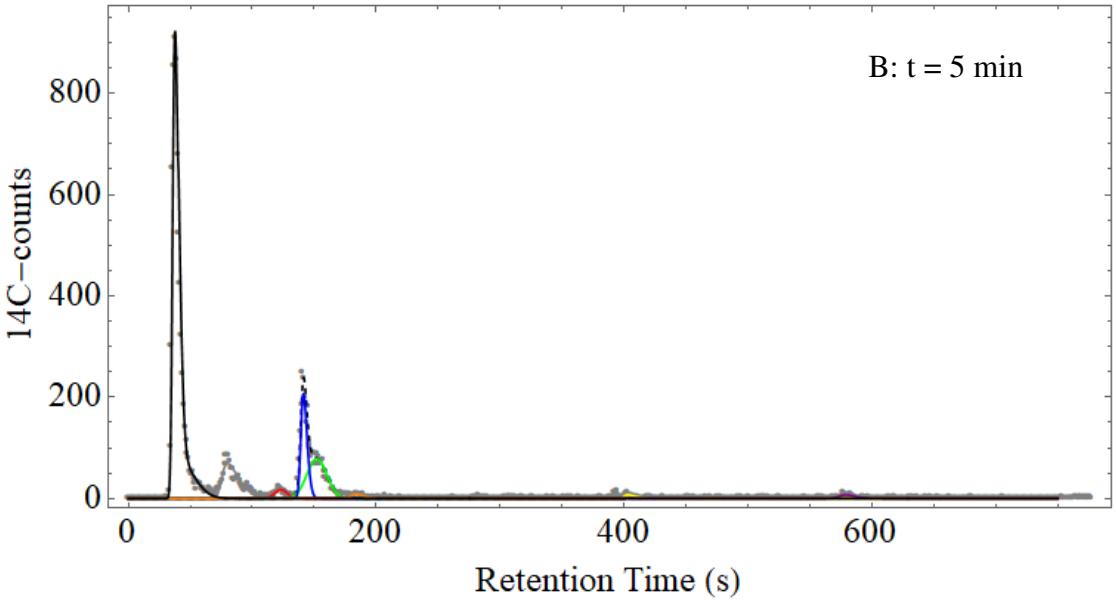

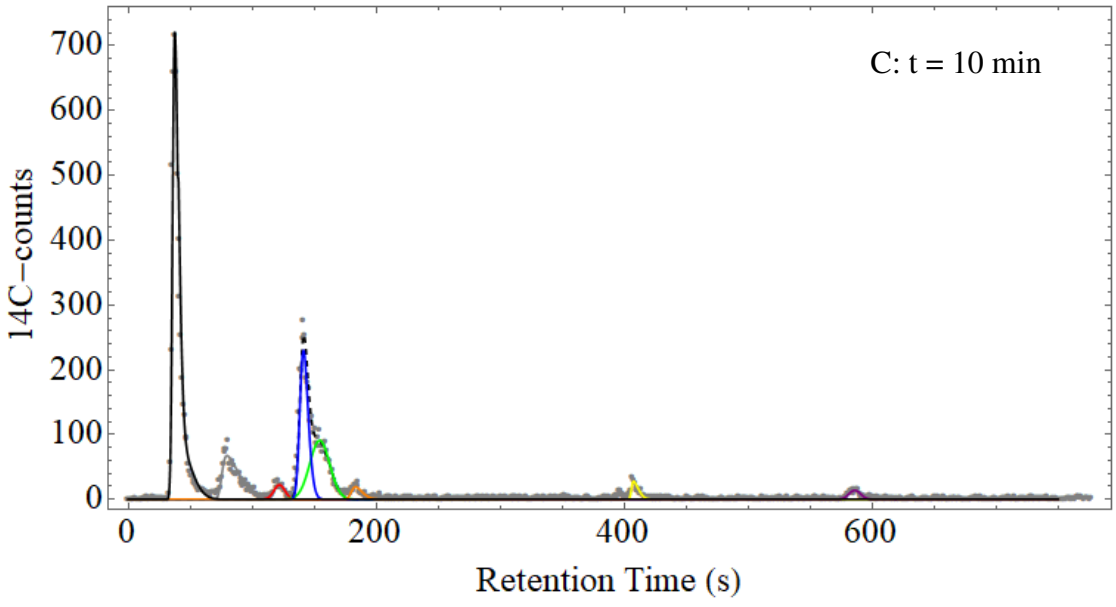

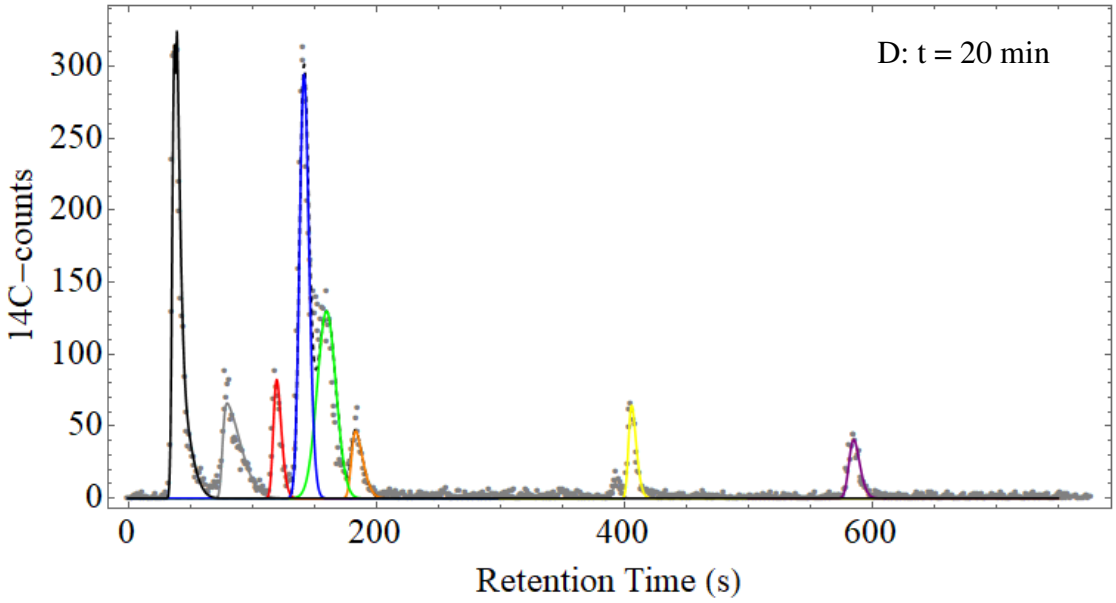

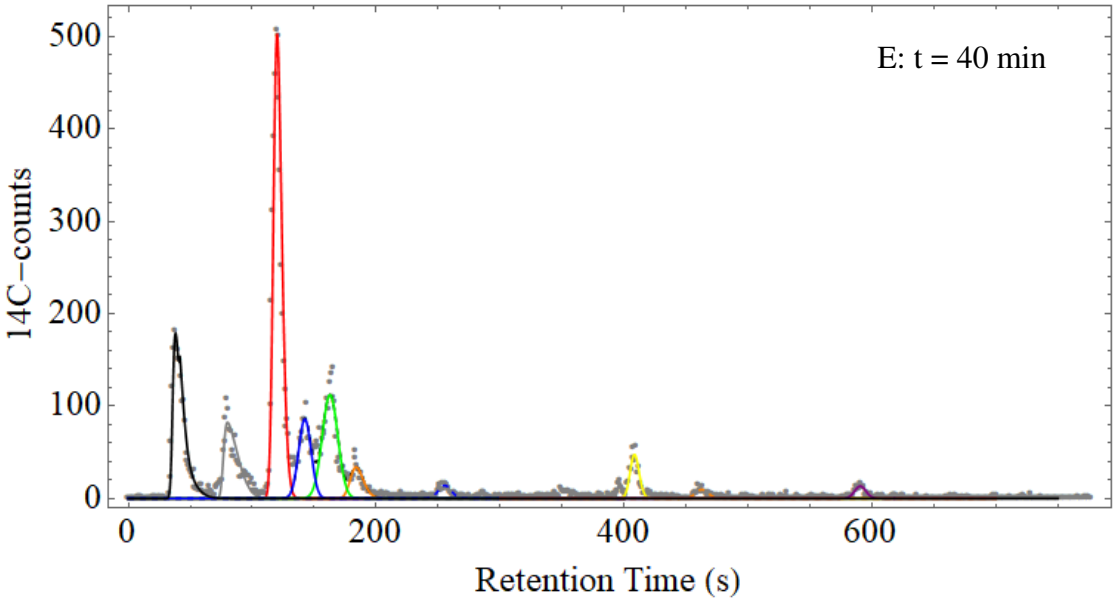

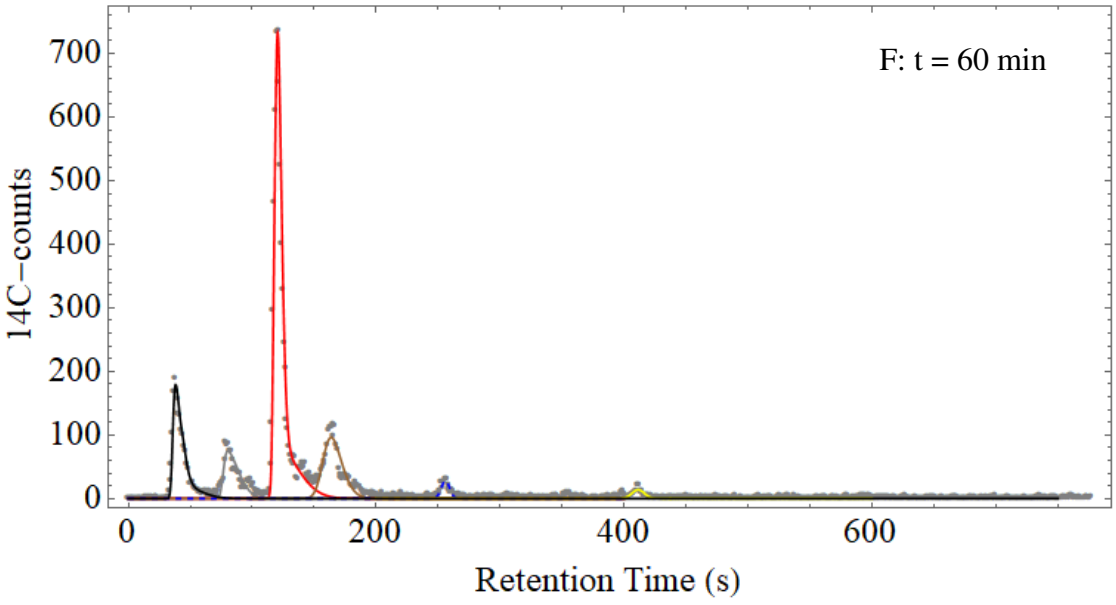

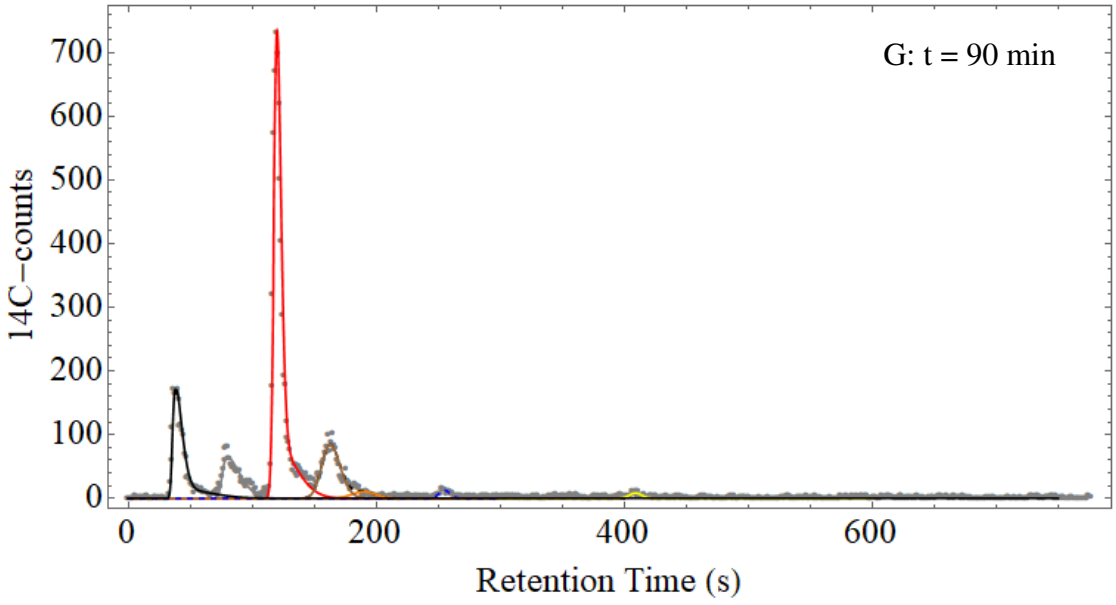

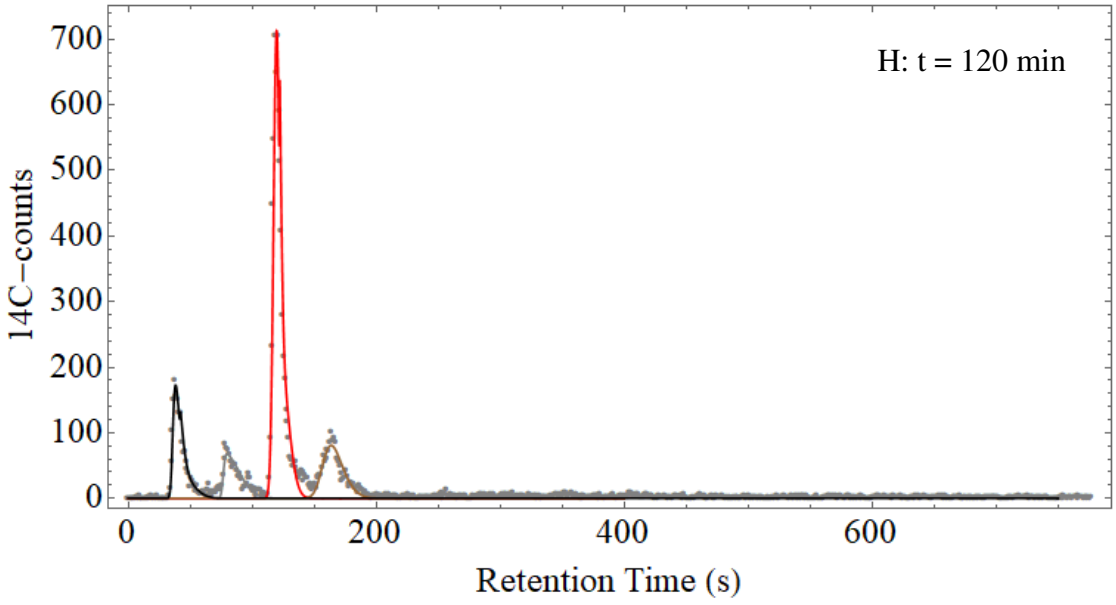

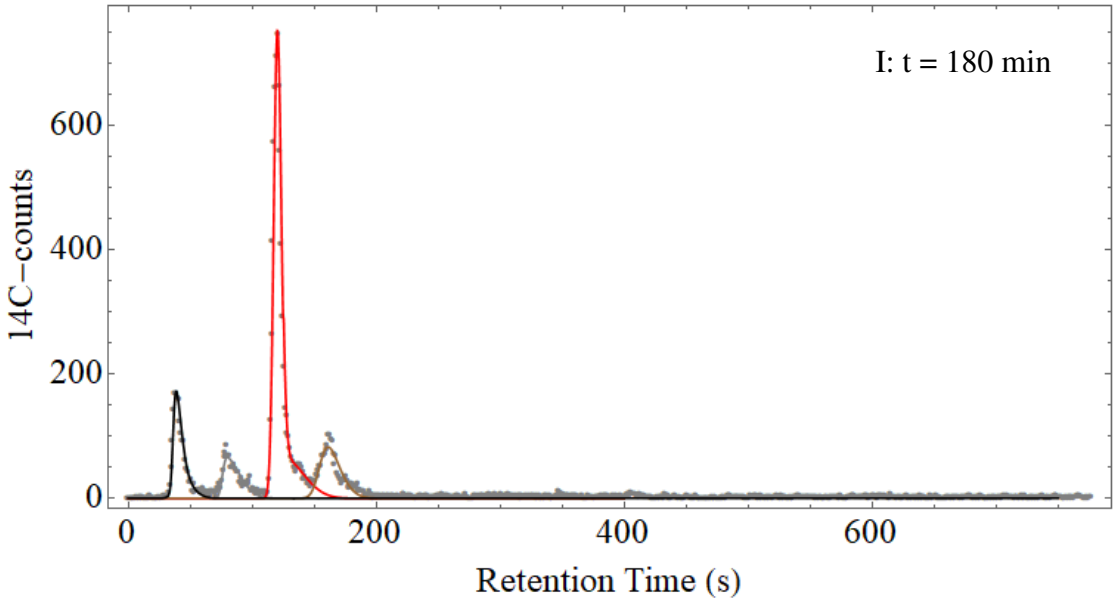

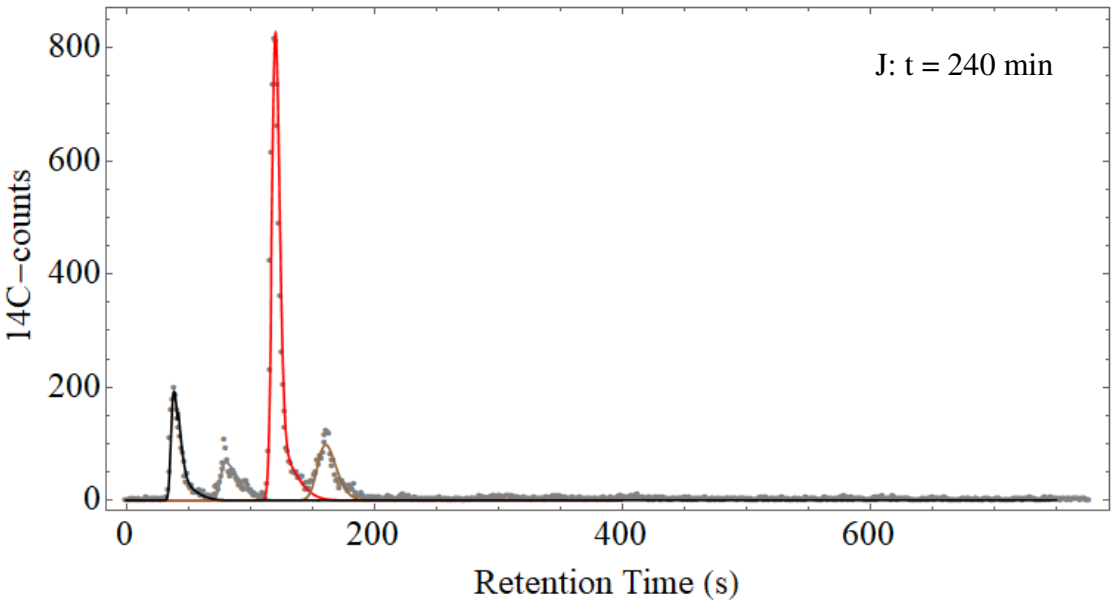

Figure A. 3: *The integrated chromatographic traces of the time-course experiment discussed in Section 5.4.3 of this thesis (Exp 2). The experiment was carried out in duplicate and the chromatographic traces shown here is from the first repeat. The grey dots represent the chromatographic data, the Black line represents GLC, Grey represents the Impurity, Blue represents G6P, Green Represents F6P, Purple represents FBP, Orange represents DHAP, Yellow represents P3G, Orange-Dash represents P2G, Blue-Dash represents PEP, Brown represents PYR, Red represents LAC, A: analysis performed at t = 0 min, B: analysis performed at t = 5 min, C: analysis performed at t = 10 min, D: analysis performed at t = 20 min, E: analysis performed at t = 40 min, F: analysis performed at t = 60 min, G: analysis performed at t = 90 min, H: analysis performed at t = 120 min, I: analysis performed at t = 180 min, J: analysis performed at t = 240 min.*

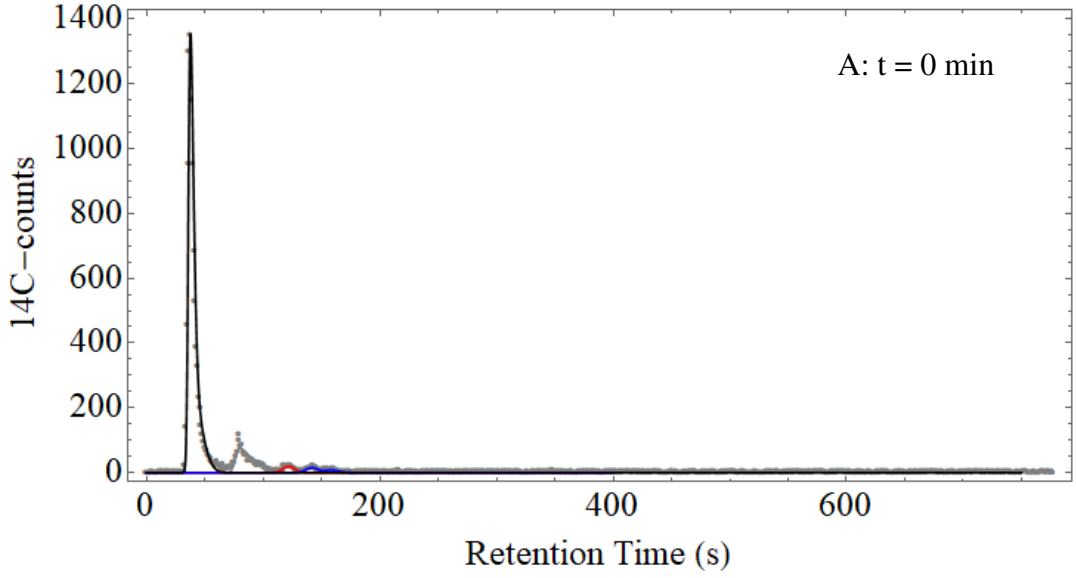

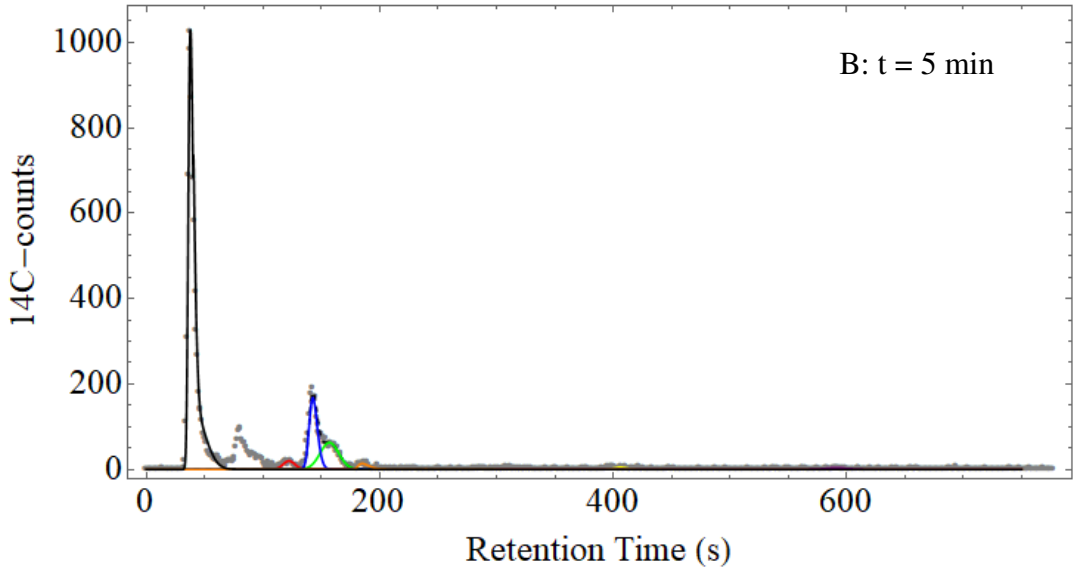

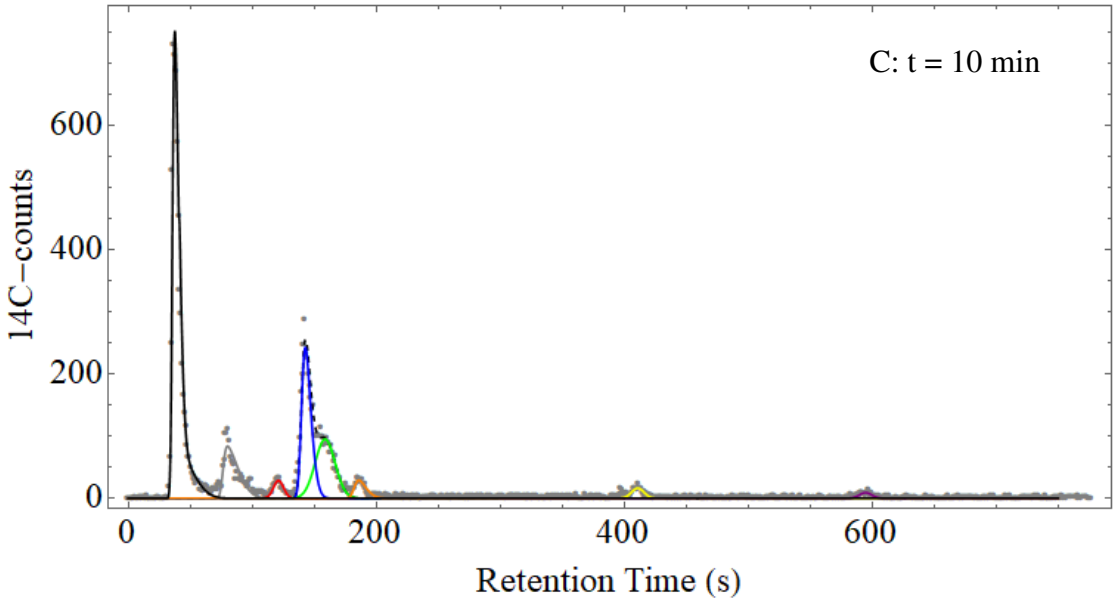

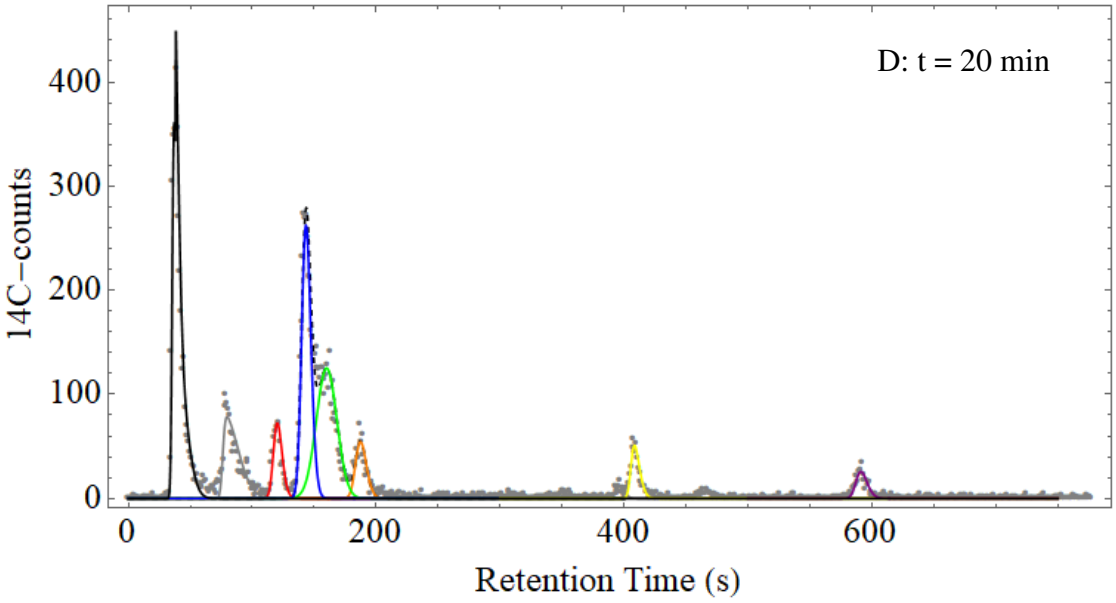

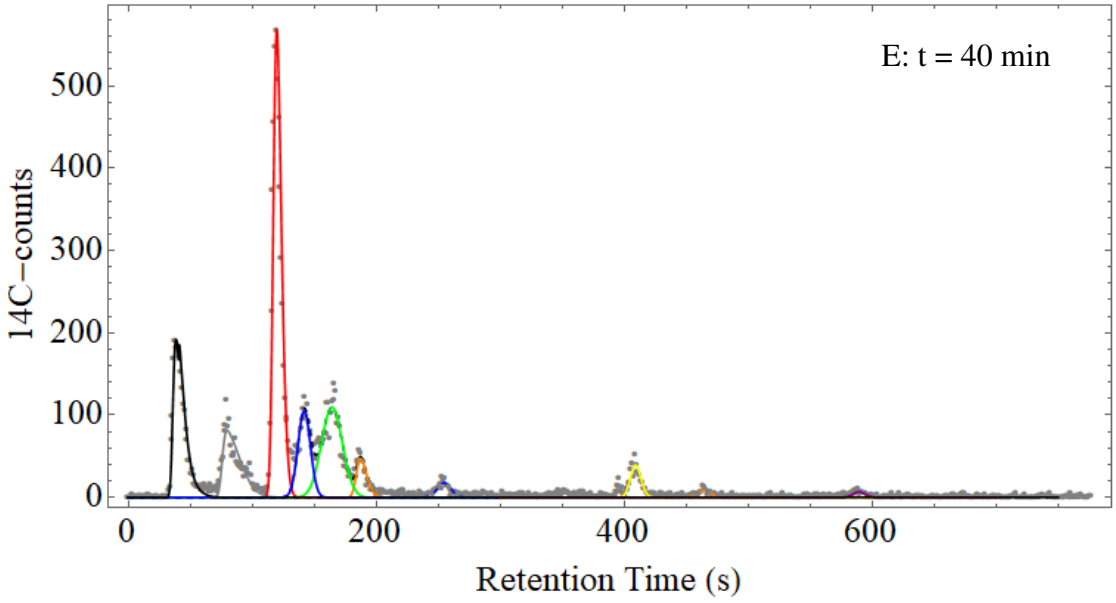

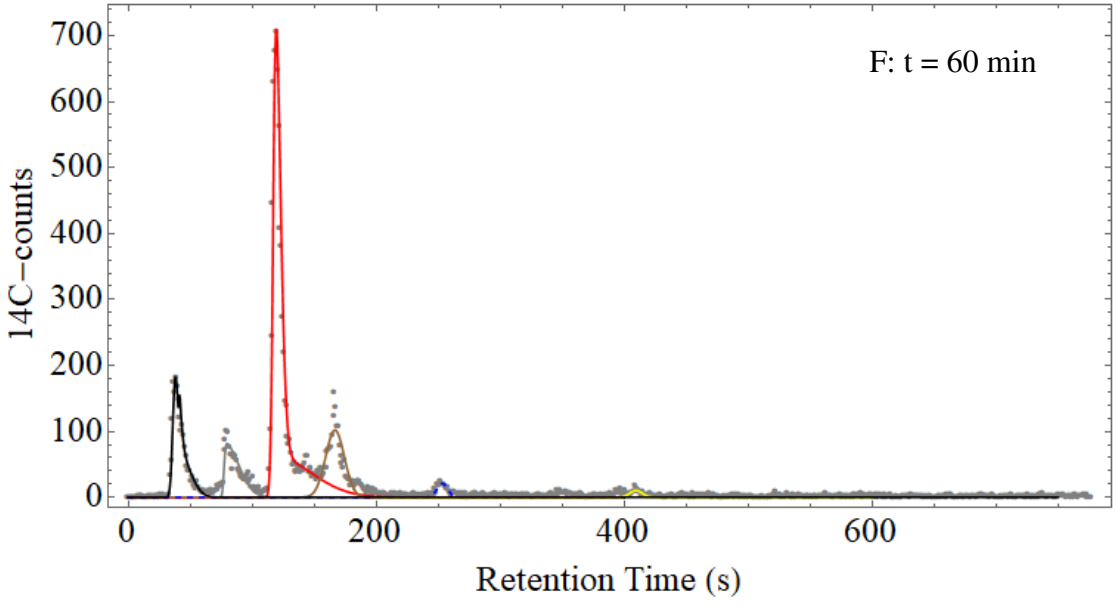

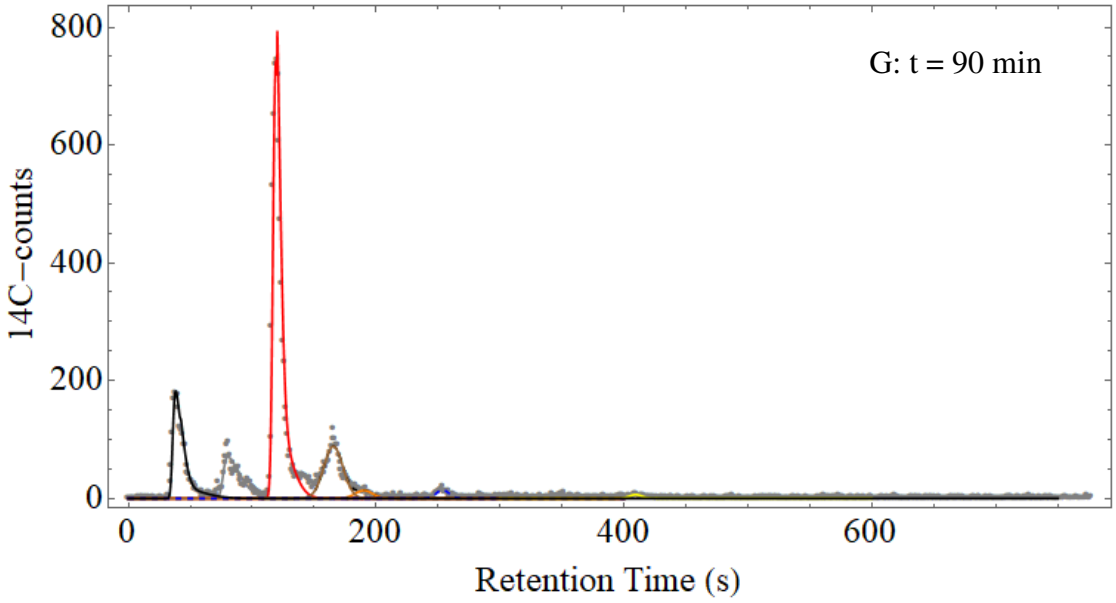

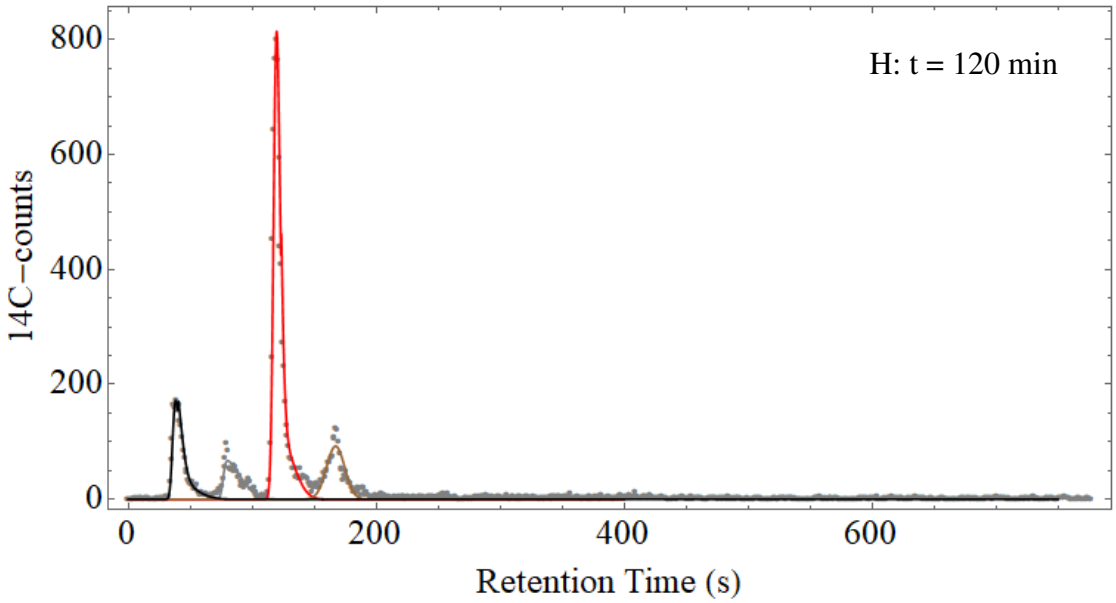

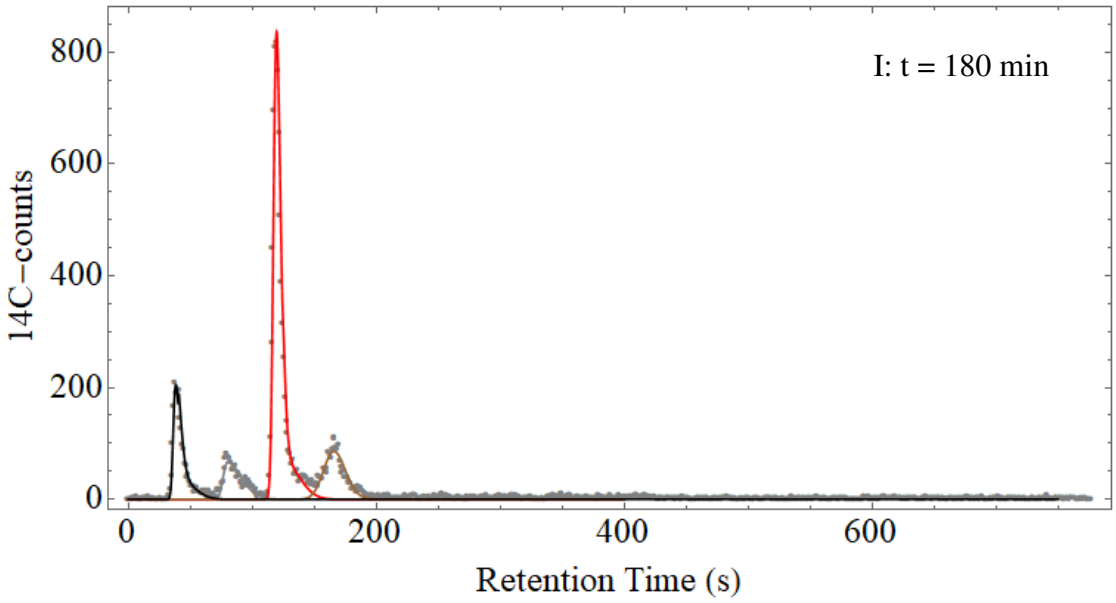

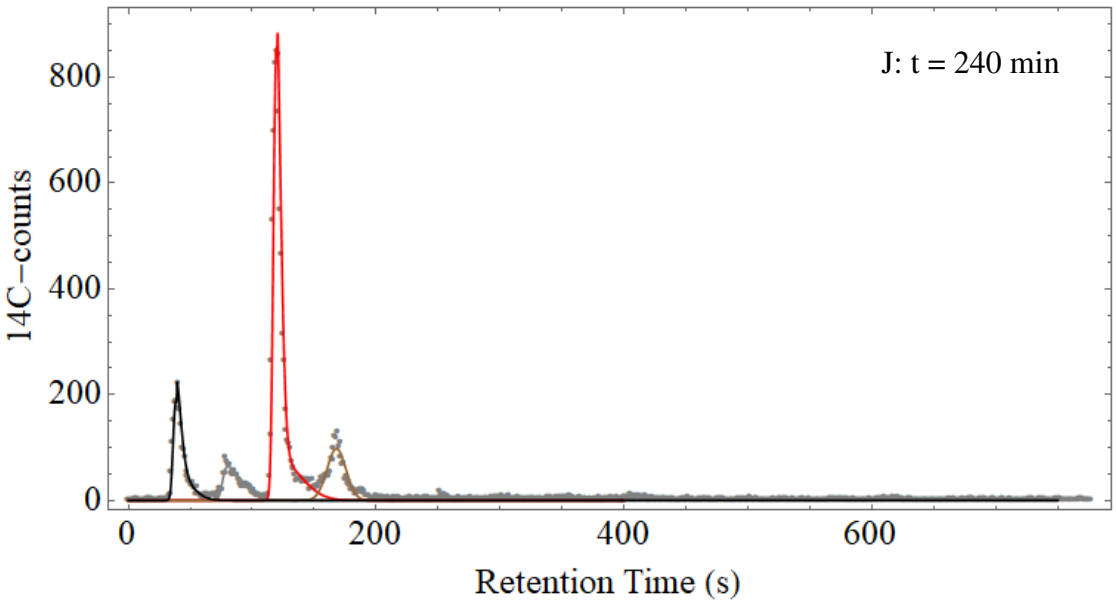

Figure A. 4: *The integrated chromatographic traces of the time-course experiment discussed in Section 5.4.3 of this thesis (Exp 2). The experiment was carried out in duplicate and the chromatographic traces shown here is from the second repeat. The grey dots represent the chromatographic data, the Black line represents GLC, Grey represents the Impurity, Blue represents G6P, Green Represents F6P, Purple represents FBP, Orange represents DHAP, Yellow represents P3G, Orange-Dash represents P2G, Blue-Dash represents PEP, Brown represents PYR, Red represents LAC, A: analysis performed at t = 0 min, B: analysis performed at t = 5 min, C: analysis performed at t = 10 min, D: analysis performed at t = 20 min, E: analysis performed at t = 40 min, F: analysis performed at t = 60 min, G: analysis performed at t = 90 min, H: analysis performed at t = 120 min, I: analysis performed at t = 180 min, J: analysis performed at t = 240 min.*

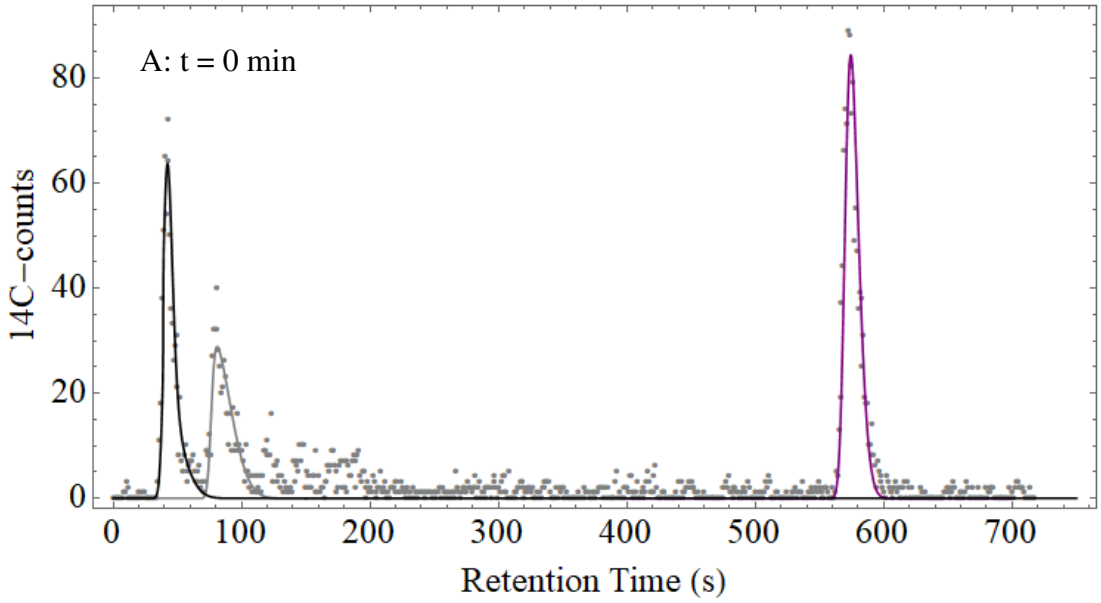

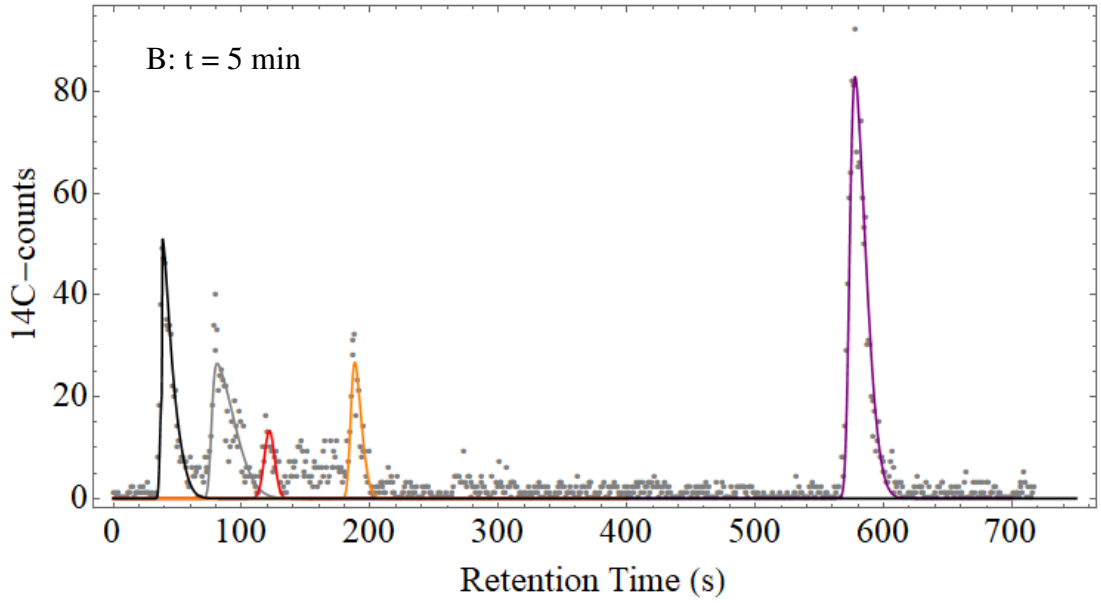

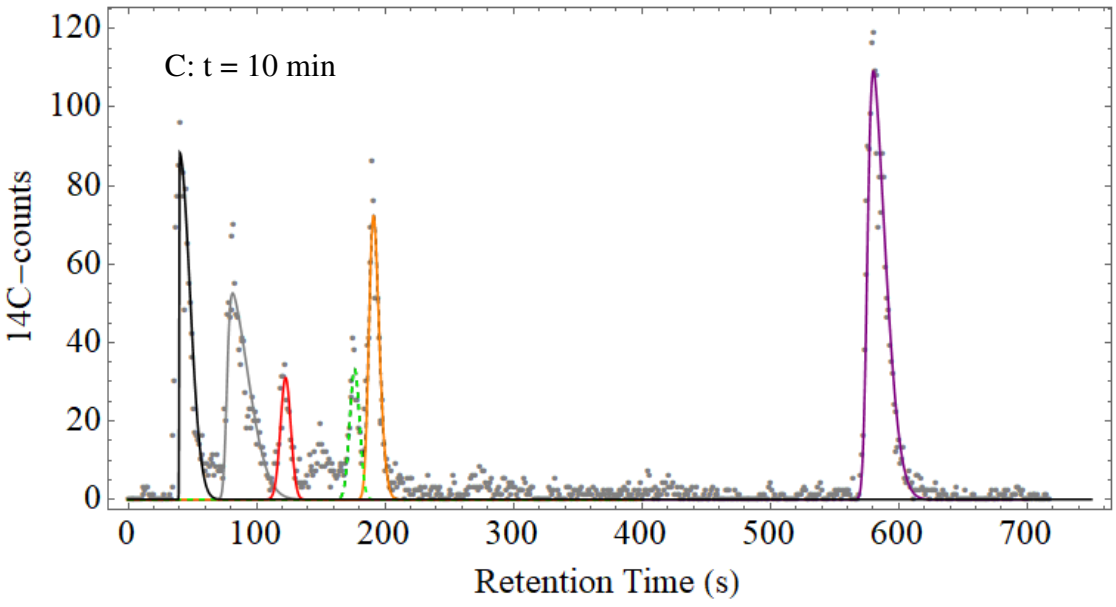

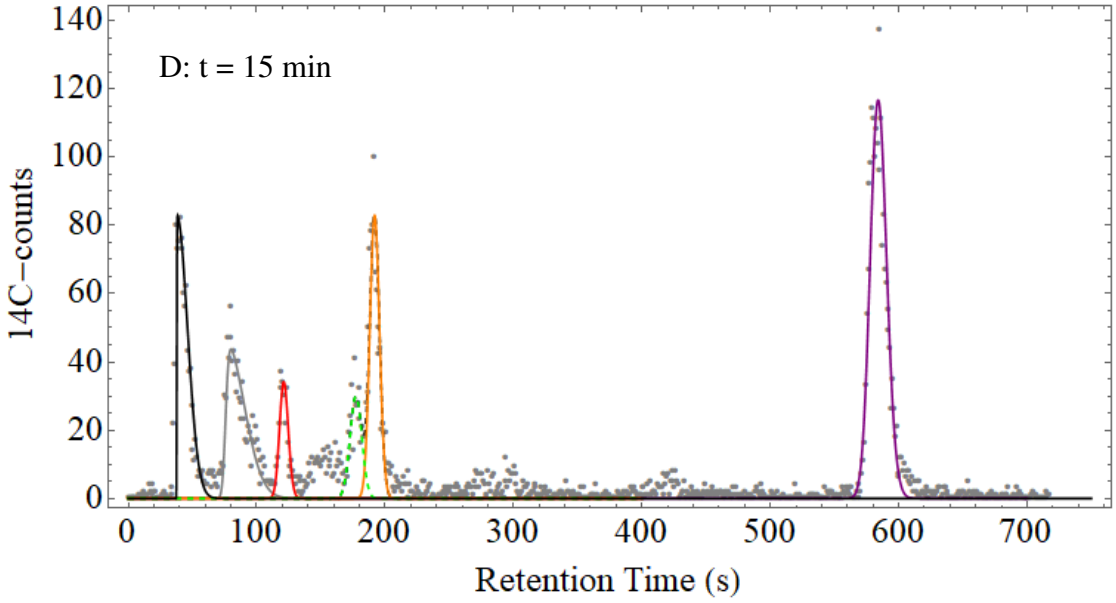

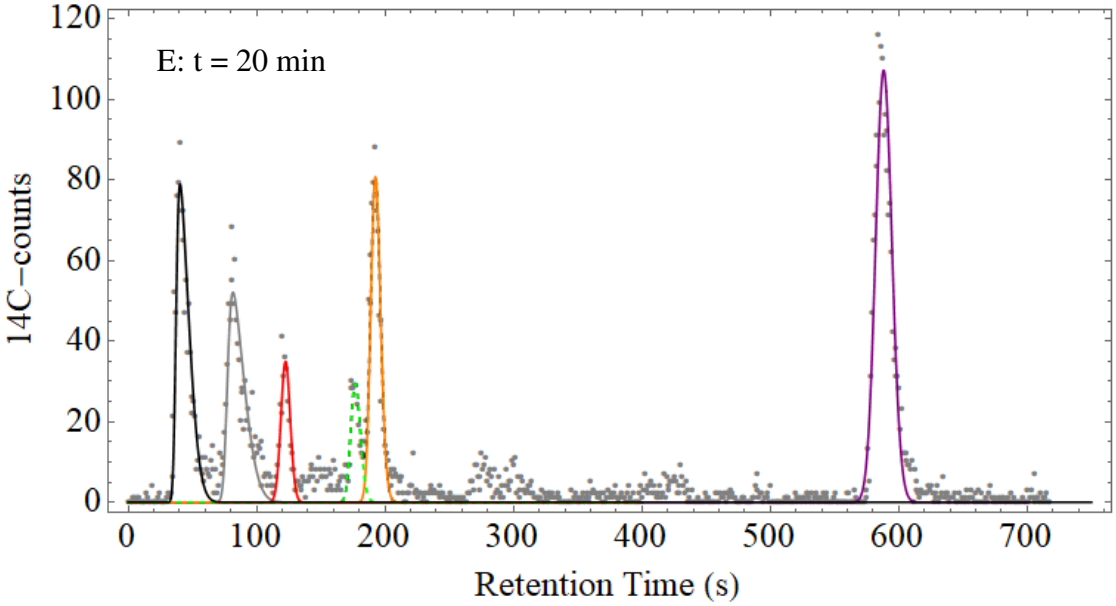

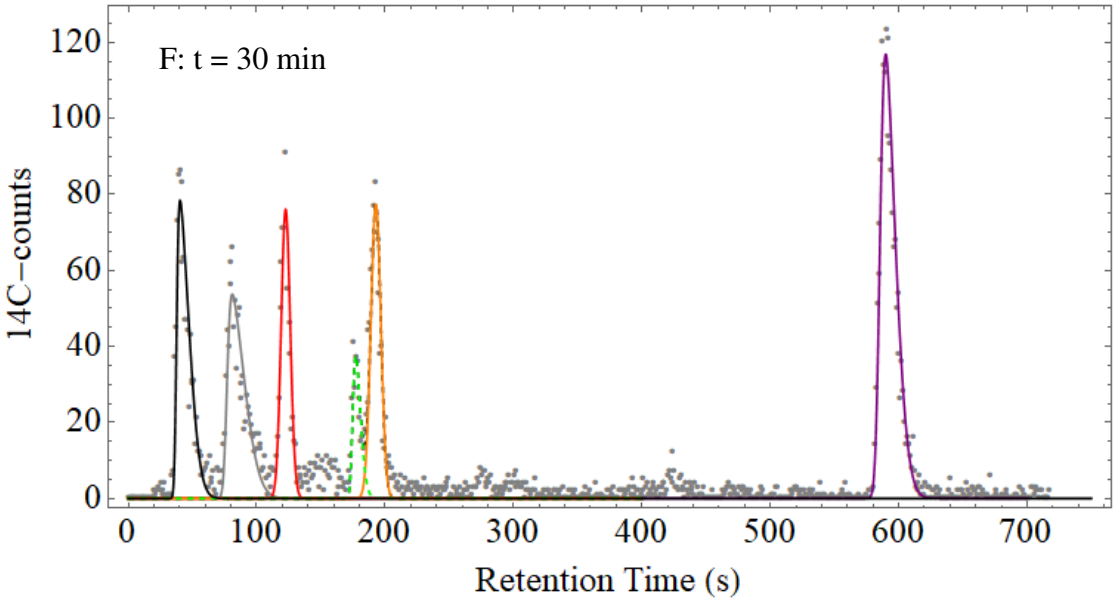

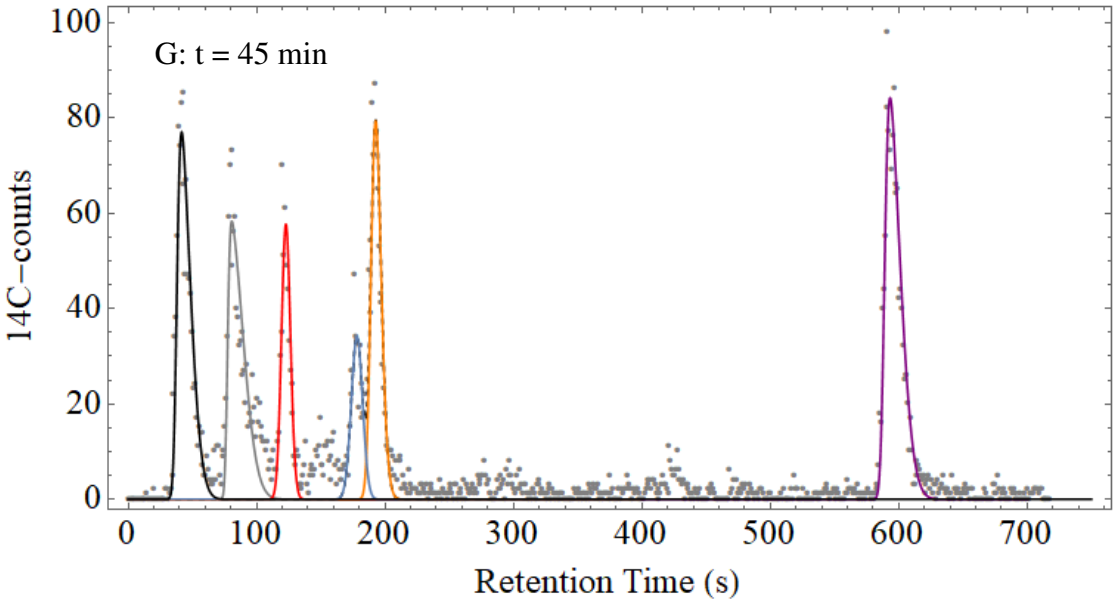

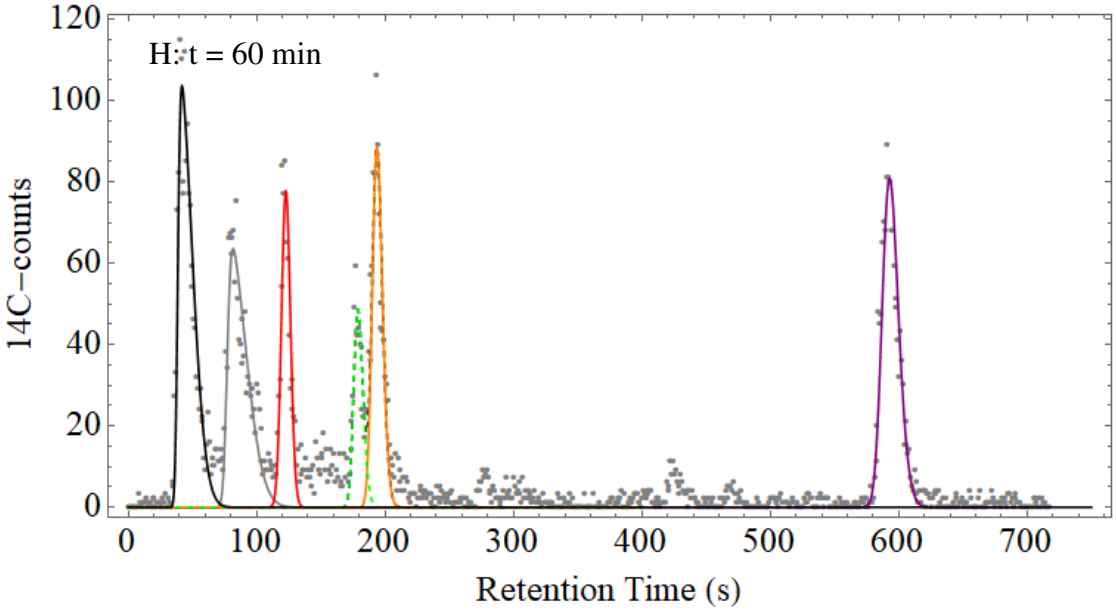

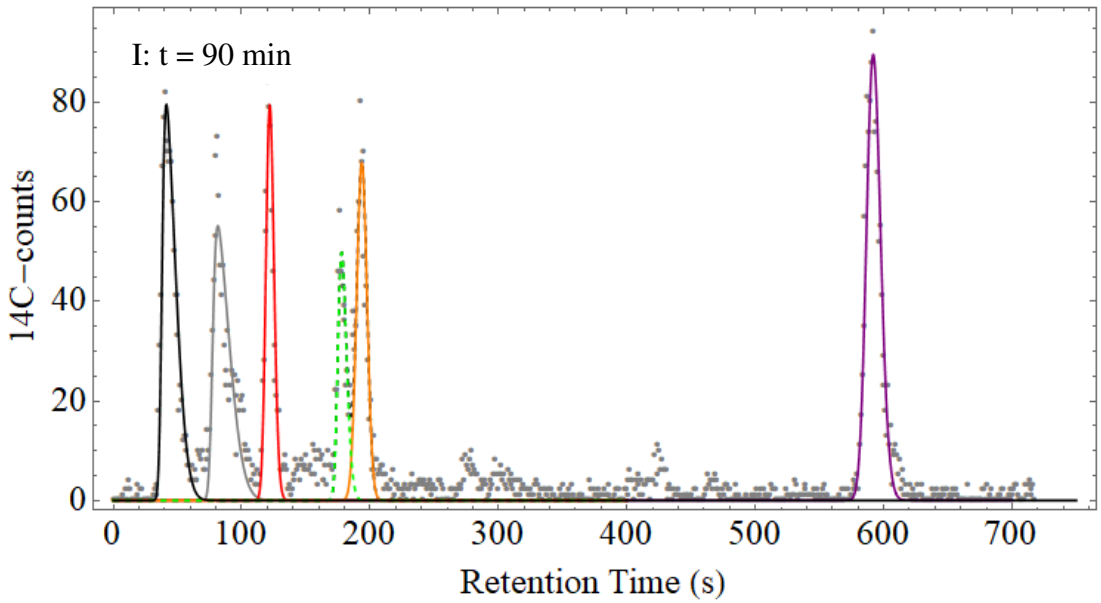

Figure A. 5: *The integrated chromatographic traces of the time-course experiment discussed in Section 5.4.4 of this thesis (Exp 3). The experiment was carried out in duplicate and the chromatographic traces shown here is from the first repeat. The grey dots represent the chromatographic data, the Black line represents GLC, Grey represents the Impurity, Purple represents FBP, Orange represents DHAP, Green-Dash represents GAP, Red represents LAC, A: analysis performed at t = 0 min, B: analysis performed at t = 5 min, C: analysis performed at t = 10 min, D: analysis performed at t = 15 min, E: analysis performed at t = 20 min, F: analysis performed at t = 30 min, G: analysis performed at t = 45 min, H: analysis performed at t = 60 min, I: analysis performed at t = 90 min.*

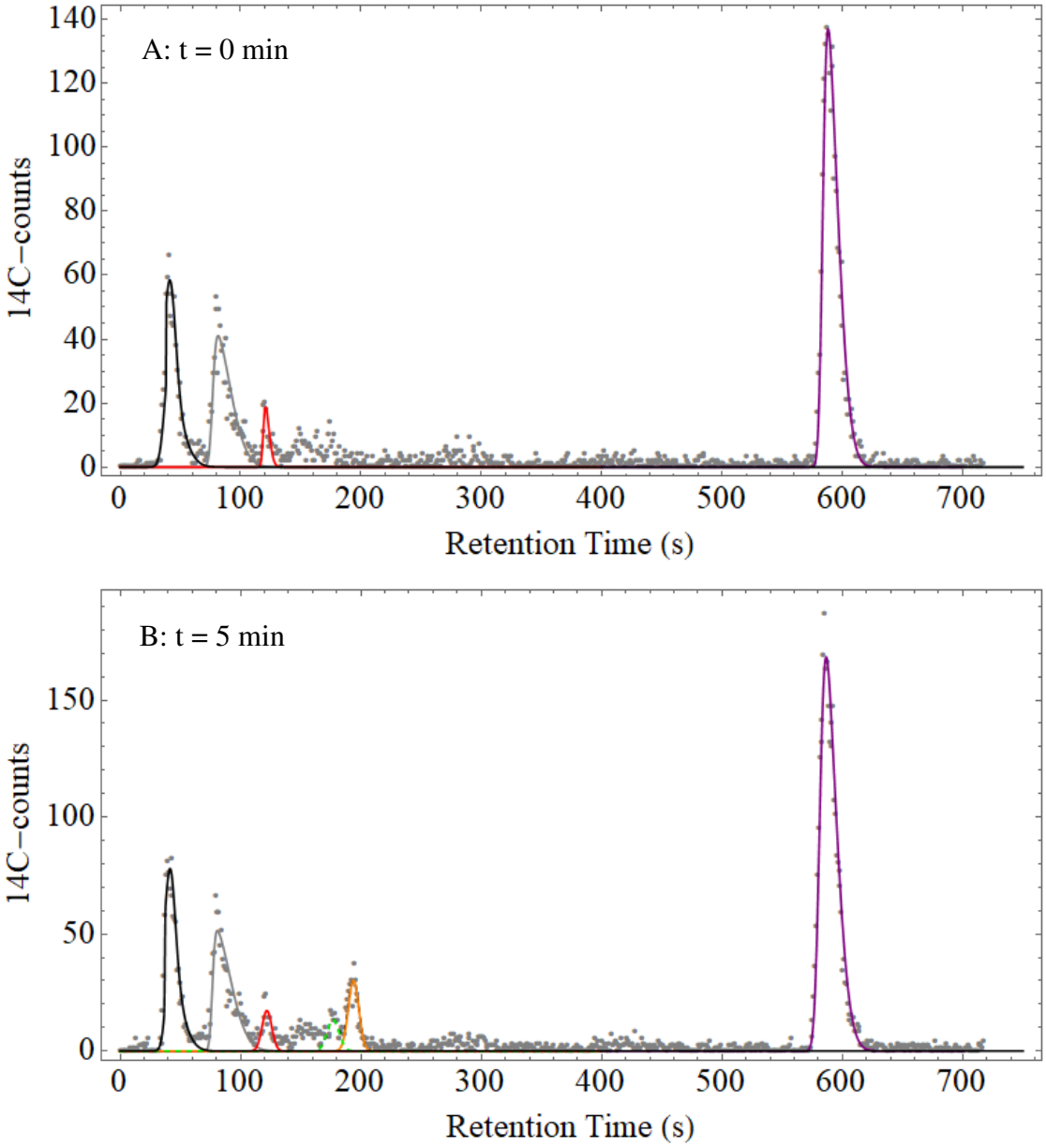

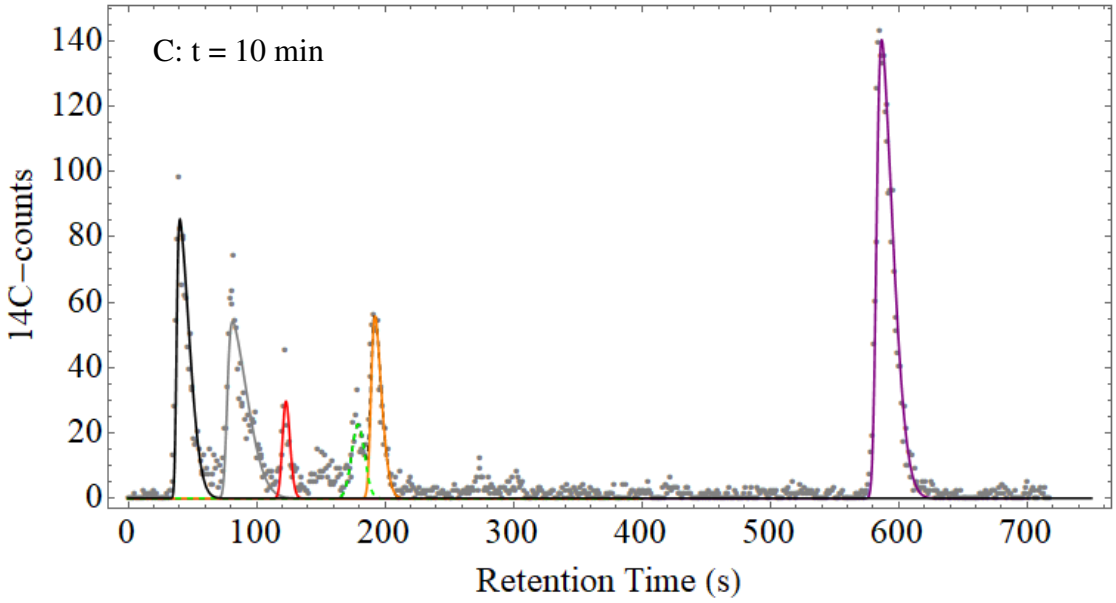

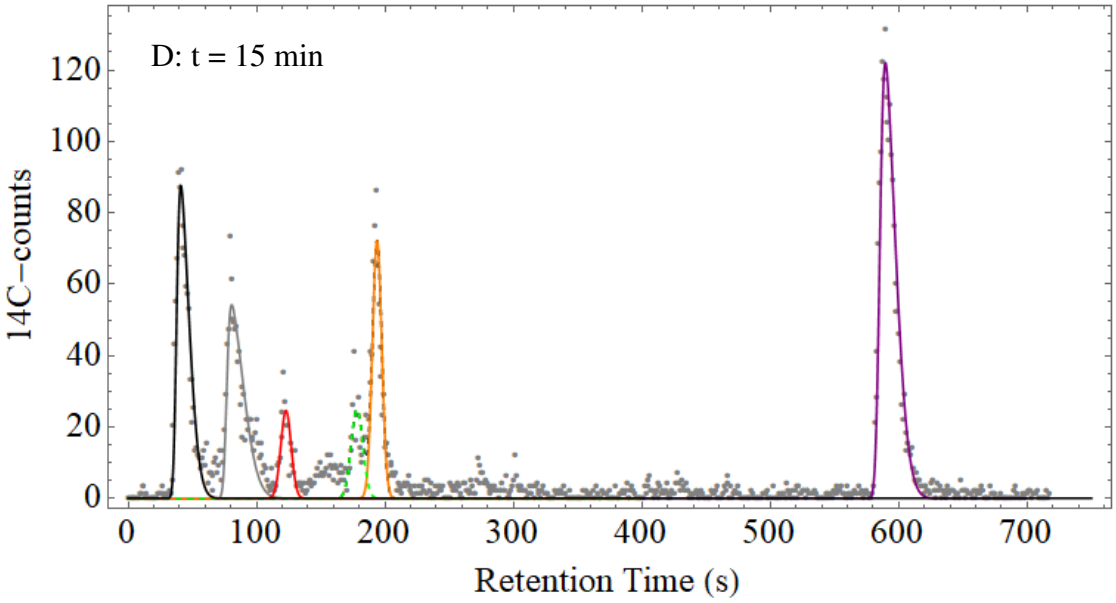

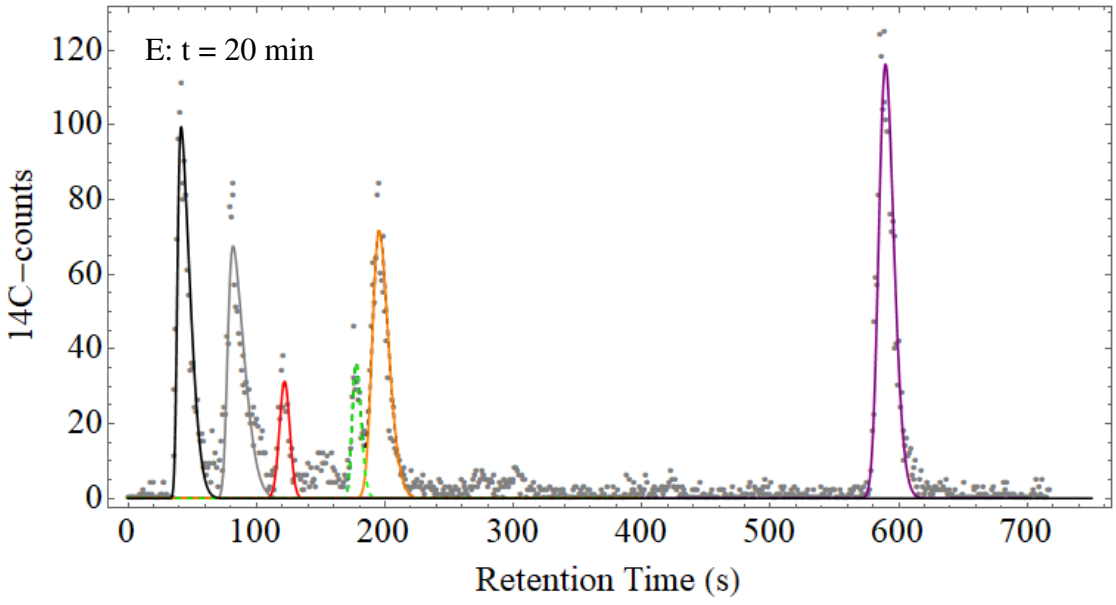

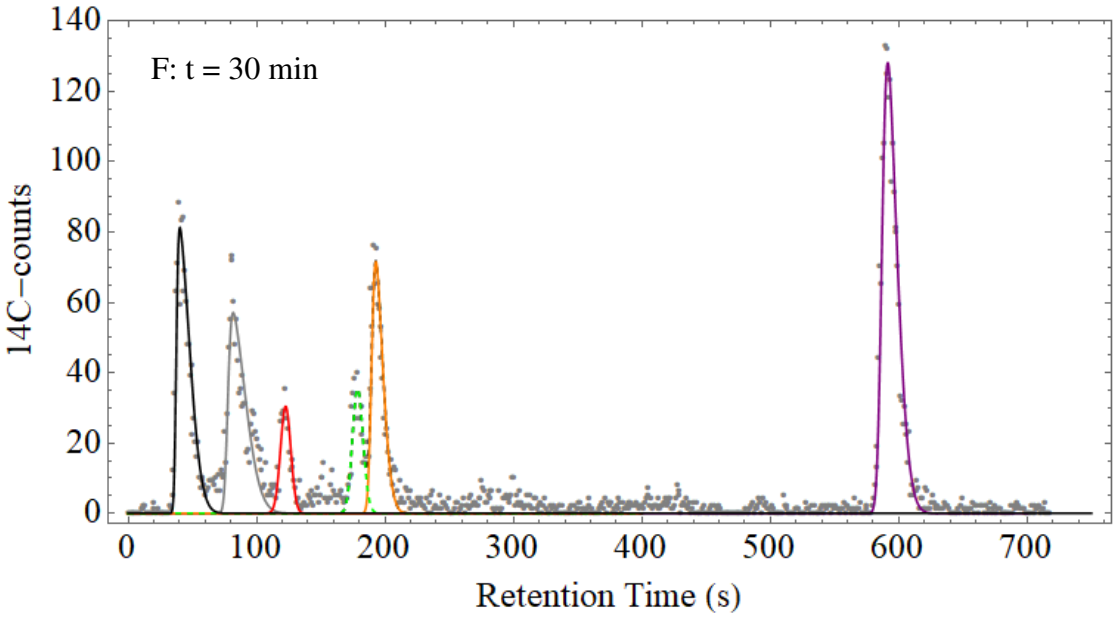

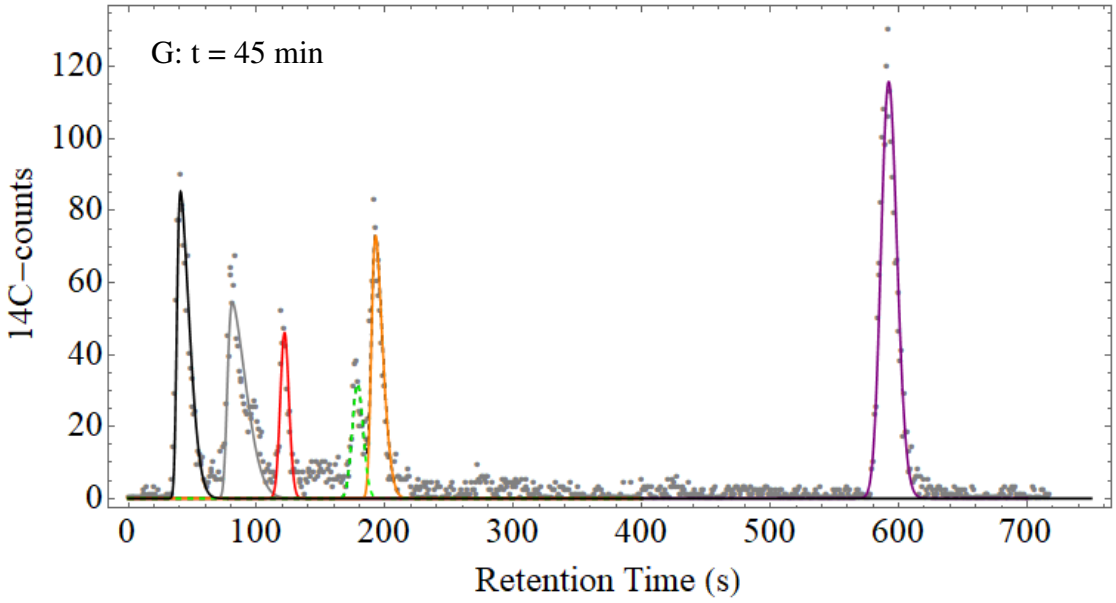

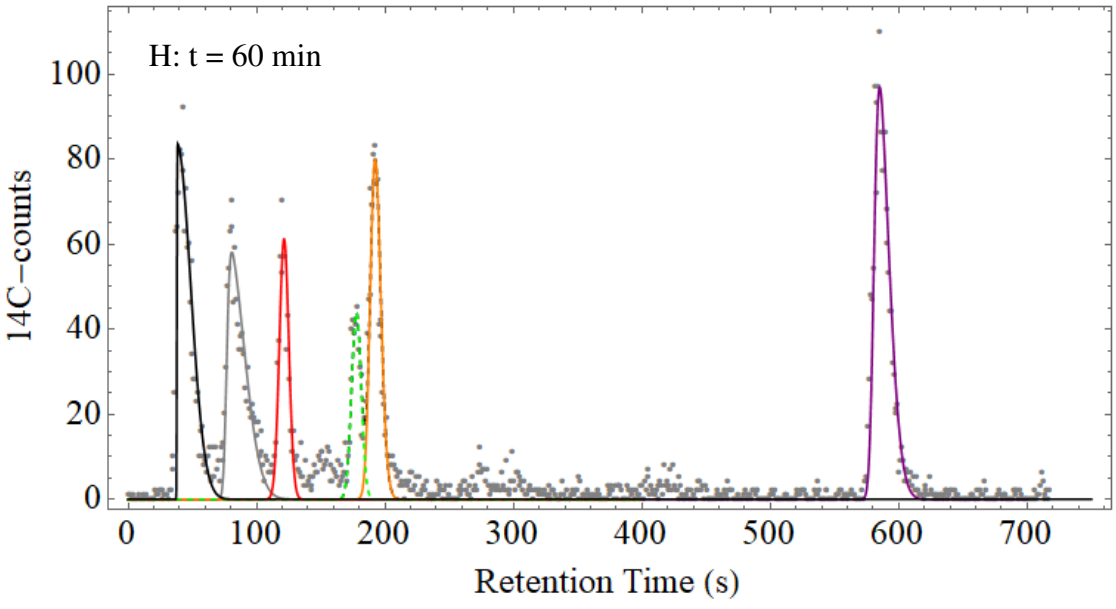

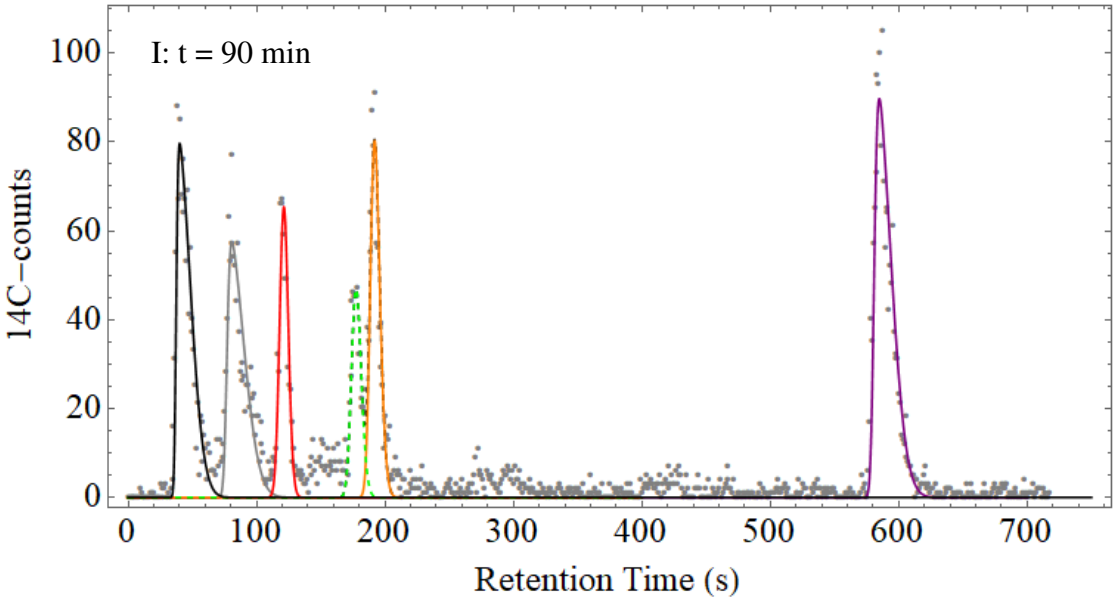

Figure A. 6: *The integrated chromatographic traces of the time-course experiment discussed in Section 5.4.4 of this thesis (Exp 3). The experiment was carried out in duplicate and the chromatographic traces shown here is from the second repeat. The grey dots represent the chromatographic data, the Black line represents GLC, Grey represents the Impurity, Purple represents FBP, Orange represents DHAP, Green-Dash represents GAP, Red represents LAC, A: analysis performed at t = 0 min, B: analysis performed at t = 5 min, C: analysis performed at t = 10 min, D: analysis performed at t = 15 min, E: analysis performed at t = 20 min, F: analysis performed at t = 30 min, G: analysis performed at t = 45 min, H: analysis performed at t = 60 min, I: analysis performed at t = 90 min.*